



HAL
open science

Optimal Helical Tube Design for Intensified Heat / Mass Exchangers

Omran Abushammala

► **To cite this version:**

Omran Abushammala. Optimal Helical Tube Design for Intensified Heat / Mass Exchangers. Chemical and Process Engineering. Université de Lorraine, 2020. English. NNT: 2020LORR0091 . tel-02969949

HAL Id: tel-02969949

<https://hal.univ-lorraine.fr/tel-02969949>

Submitted on 17 Oct 2020

HAL is a multi-disciplinary open access archive for the deposit and dissemination of scientific research documents, whether they are published or not. The documents may come from teaching and research institutions in France or abroad, or from public or private research centers.

L'archive ouverte pluridisciplinaire **HAL**, est destinée au dépôt et à la diffusion de documents scientifiques de niveau recherche, publiés ou non, émanant des établissements d'enseignement et de recherche français ou étrangers, des laboratoires publics ou privés.



AVERTISSEMENT

Ce document est le fruit d'un long travail approuvé par le jury de soutenance et mis à disposition de l'ensemble de la communauté universitaire élargie.

Il est soumis à la propriété intellectuelle de l'auteur. Ceci implique une obligation de citation et de référencement lors de l'utilisation de ce document.

D'autre part, toute contrefaçon, plagiat, reproduction illicite encourt une poursuite pénale.

Contact : ddoc-theses-contact@univ-lorraine.fr

LIENS

Code de la Propriété Intellectuelle. articles L 122. 4

Code de la Propriété Intellectuelle. articles L 335.2- L 335.10

http://www.cfcopies.com/V2/leg/leg_droi.php

<http://www.culture.gouv.fr/culture/infos-pratiques/droits/protection.htm>

Optimal Helical Tube Design for Intensified Heat / Mass Exchangers

THÈSE

présentée et soutenue publiquement le 18 Septembre 2020

pour l'obtention du

Doctorat de l'Université de Lorraine

(Spécialité: Génie des procédés, des produits et des molécules)

par

Omran Abushammala

Composition du jury

<i>Rapporteurs :</i>	Glenn LIPSCOMB	Professeur, University Toledo, Ohio, USA
	Catherine XUEREB	Directrice de recherches CNRS, LGC Toulouse, France
<i>Examineurs :</i>	Christophe SERRA	Professeur, Université Strasbourg, Strasbourg, France
	Cécile LEMAITRE	Maître de conférences, Université Lorraine, Nancy, France
<i>Invites :</i>	Denis FUNFSCHILLING	Chargé de recherches CNRS, Strasbourg, France
	Talib DBOUK	Professeur, University of Nicosia, Nicosia, Cyprus
<i>Encadrants :</i>	Eric FAVRE	Professeur, Université Lorraine, Nancy, France
	Rainier HREIZ	Maître de conférences, Université Lorraine, Nancy, France

Remerciements

Firstly, I would like to express my sincere gratitude to my supervisors **Eric Favre**, **Rainier Hreiz** and **Cecile Lemaitre** for the continuous support of my PhD study and the related research, for their patience, motivation, and immense knowledge. Their guidance helped me in all the time of research and writing of this thesis. I could not have imagined having a better supervisors and mentors for my PhD study.

My sincere thanks also goes to my thesis committee: **Glenn Lipscomb**, **Catherine Xuereb**, **Christophe Serra**, **Denis Funfschilling**, and **Talib Dbouk** for their insightful comments and encouragement, but also for their question which incanted me to widen my research from various perspectives.

Besides all, I would like to thank my friends in the **PRISM** team for a lovely working atmosphere and also the administration staff in LRGP and ENSIC Nancy Grand-Est for making our daily activities going smoothly.

I am grateful to the academic and research staff in the LRGP for their support and help. Thanks to **Neila Djoudi**, **Karima Gahfif**, **Feriel Yahiat**, **Amira Doggaz**, **Divyesh Arora**, **Mohd-Faidzul Adnan** and a particular thank go to **Jean-Francois Portha** and **Jean-Marc Commenge** for enlightening me the first glance of research.

I would like to thank my closest friends, **Ahmed Qabbaa**, **Mohammad Abu Taha**, **Mohammed Abuoudeh**, **Wazen Shbair**, **Ahmed Aldahdooh** and **Adham Anaka** and their lovely families.

My family has always played a great part in my life specially during these years. **My dad** is my best friend and greatest hero. **My Mum**, you inspire me a great deal, your dedication makes every thing else pale in comparison. **My brothers and sisters**, I am blessed to have you. I owe my deepest gratitude to you all.

Thanks to all of you. I will remain indebted for you forever.

Synthèse et objectifs de la thèse

Les membranes sont largement utilisées pour la séparation de mélanges homogènes et multiphasiques. Les contacteurs membranaires sont prometteurs pour l'intensification des procédés, en particulier pour les procédés d'absorption gaz-liquide. Par ailleurs, les échangeurs de chaleur sont un procédé efficace pour transférer de la chaleur entre deux fluides et sont utilisés dans de nombreuses applications industrielles, telles que la réfrigération, la climatisation, les centrales électriques, les usines chimiques, les raffineries de pétrole, et le traitement des eaux usées. La conception et le fonctionnement des séparateurs membranaires et des échangeurs de chaleur ont été l'objet d'un grand nombre de recherches scientifiques visant à améliorer l'efficacité de la séparation/du transfert. Dans ce contexte, la mécanique des fluides numériques ('Computational Fluid Dynamics', CFD, en anglais) se révèle comme un outil puissant pour aider et assister les ingénieurs dans la détermination de la forme optimale des séparateurs membranaires et des échangeurs de chaleur. Dans cette thèse, une étude numérique approfondie des performances des échangeurs de chaleur/matière de forme hélicoïdale est conduite. L'objectif est de déterminer les effets de la géométrie des tubes hélicoïdaux (pas et rayon de l'hélice et diamètre interne des tubes) sur :

- + L'efficacité du transfert de matière/chaleur obtenue (généralement exprimée par le nombre de Sherwood/Nusselt).
- + Les pertes de charge induites (généralement caractérisées par le coefficient de frottement) étant donné que l'énergie de pompage nécessaire pour les compenser représente un coût de fonctionnement important.
- + La compacité maximale possible dans le cas d'échangeurs de matière/chaleur intégrant un grand nombre de tubes hélicoïdaux, c.à.d. la surface spécifique d'échange par unité de volume la plus élevée possible pour une géométrie de tubes donnée.

Les prochains chapitres portent d'abord sur le développement de corrélations exprimant l'efficacité du transfert de chaleur/matière dans les tubes hélicoïdaux. Ces corrélations sont ensuite utilisées pour déterminer la géométrie optimale des échangeurs de chaleur/matière à tubes hélicoïdaux, c'est-à-dire celle permettant le meilleur compromis entre l'intensification du transfert et l'augmentation des coûts de pompage.

Structure de la thèse

L'intensification des transferts de matière et de chaleur entre deux fluides au sein d'un échangeur constitue un des objectifs emblématiques du génie des procédés. Le chapitre I du présent manuscrit de thèse présente un état de l'art des solutions hydrodynamiques utilisées pour intensifier les processus de séparation et / ou pour améliorer les techniques de transfert de chaleur. Dans la première partie, les concepts de base des procédés de filtration, de séparation membranaire et de transfert de chaleur sont définis, et les principaux types de modules de séparation et d'échangeurs de chaleur sont présentés. Les polarisations de concentration et de température sont expliquées comme étant l'une des principales limitations de l'efficacité du transfert. Ensuite, une étude bibliographique de sept techniques basées sur l'hydrodynamique pour contrer ces effets est présentée. Une première technique consiste à utiliser des moteurs de turbulence qui sont des obstacles (pariétaux ou placés dans le volume) que le fluide doit contourner et qui produisent des recirculations favorables au mélange. Une autre solution consiste à faire vibrer la paroi du module, ce qui limite le dépôt de particules. L'application d'ultrasons est une méthode très efficace pour décolmater les filtres encrassés. Du gaz (souvent de l'air) peut également être injecté dans le liquide : le passage de bouchons gazeux (grosses bulles à gaz) perturbe efficacement l'écoulement de la phase liquide. Les systèmes cylindriques ou à disques rotatifs tirent parti des instabilités hydrodynamiques qui apparaissent dans ces géométries et qui induisent des recirculations avec des coûts énergétiques relativement faibles. Enfin, l'utilisation de dispositifs de formes complexes est présentée. C'est une technique passive qui induit des tourbillons de type Dean ou qui conduit à un comportement d'écoulement chaotique, ce qui se traduit par un mélange extrêmement efficace pour une faible consommation d'énergie. Dans ce travail de mémoire, nous nous focaliserons notamment sur l'utilisation de techniques passives de type conduite hélicoïdale dans le but de produire des écoulements secondaires intenses au sein de l'écoulement primaire. L'utilisation de tubes hélicoïdaux (réalisables par impression 3D), permettant de combiner une grande aire interfaciale spécifique et une importante augmentation des coefficients de transferts par génération de tourbillons de Dean a été étudiée pour évaluer les performances maximales de transfert de chaleur/matière qu'ils permettent d'atteindre.

Le chapitre II du présent manuscrit se focalise sur les pertes de charge régulières ou linéiques dans les conduites de forme hélicoïdale. En effet, les tuyaux hélicoïdaux fortement incurvés offrent des potentialités attractives pour des performances intensifiées de matière et / ou de transfert de chaleur car ils génèrent des tourbillons intenses de type Dean. Cependant, ces écoulements secondaires induisent également une perte de charge plus élevée par rapport aux tubes droits, et donc, génèrent des besoins énergétiques spécifiques plus importants. Par conséquent, l'évaluation du coefficient de frottement dans ce type de géométries est d'un intérêt majeur afin d'évaluer de manière fiable, pour une conception donnée, le compromis possible entre l'augmentation du taux de transfert volumique (c'est-à-dire la réduction possible du volume des échangeurs de chaleur et de matière) et les besoins

énergétiques spécifiques associés (c'est-à-dire les coûts de pompage). Malheureusement, dans la littérature, de telles données font défaut pour les hélices fortement incurvées, probablement en raison de la difficulté à fabriquer ces géométries par des techniques de fabrication traditionnelles. Dans ce chapitre, des simulations CFD sont effectuées pour déterminer le coefficient de frottement linéique dans les tuyaux hélicoïdaux, en particulier ceux fortement courbés et incurvés. L'accent est mis sur le régime d'écoulement laminaire qui est couramment rencontré dans les membranes à fibres creuses, les réacteurs catalytiques à monolithe ainsi que dans les applications d'échangeurs de chaleur microstructurés. Diverses conceptions d'hélice et une large gamme de valeurs de nombre de Reynolds ont été étudiées numériquement. Pour une validation expérimentale des résultats numériques, une hélice fortement courbée a été construite par impression 3D. On montre que les corrélations existantes échouent à prédire de manière précise le coefficient de frottement dans les hélices fortement courbées et incurvées. Sur la base de ces nouveaux résultats, une corrélation originale a été ainsi développée et proposée. Les mesures expérimentales de perte de charge acquises sur le modèle imprimé en 3D et les prédictions de la corrélation proposée étaient en excellent accord, l'erreur relative étant inférieure à 8% pour toutes les conditions étudiées. De plus, la nouvelle corrélation s'avère efficace et prédictive car elle estime correctement les données de la littérature obtenues avec des conditions géométriques et opérationnelles au-delà de celles étudiées dans le chapitre (et sur lesquelles la corrélation a été construite).

Les tuyaux hélicoïdaux fortement courbés (HCHP) offrent d'énormes potentialités pour des performances intensifiées de transfert de chaleur / matière car ils génèrent des tourbillons intenses de type Dean. Cependant, ces conceptions n'ont pas été explorées jusqu'à présent dans la littérature, probablement parce qu'elles sont difficiles à construire en utilisant des techniques de fabrication traditionnelles. De nos jours, grâce aux progrès constatés dans l'impression 3D, la fabrication de HCHP est devenue réalisable. Par conséquent, étudier leurs performances en termes d'intensification de chaleur et de transfert de matière présente un intérêt significatif tant du point de vue académique qu'industriel. En effet, la conception et le fonctionnement des séparateurs à membrane et des échangeurs de chaleur ont été d'un grand intérêt pour de nombreuses recherches scientifiques visant à améliorer l'efficacité de séparation / transfert. Dans ce contexte, la CFD (Computational Fluid Dynamics ou Mécanique des Fluides Numérique) se révèle être un outil puissant pour assister et accompagner les ingénieurs dans la détermination de la forme optimale des modules à membrane et échangeur de chaleur. Ainsi, le chapitre III de ce manuscrit explore les deux stratégies qui peuvent être appliquées afin de pousser l'intensification du processus de transfert : maximiser les coefficients de transfert de chaleur / matière et maximiser la surface spécifique membrane / échangeur de chaleur (c'est-à-dire la compacité des tubes) du module. La génération de tourbillons est l'une des méthodes les plus efficaces mais nécessite des tuyaux de forme hélicoïdale, qui ne peuvent pas être aussi densément emboîtés que des tubes droits. C'est pour cette raison qu'une étude combinée de densité de tassement et de transfert de

chaleur / matière est menée dans ce chapitre afin d'évaluer les performances optimales des modules à membrane hélicoïdale et des échangeurs de chaleur.

En particulier, la performance des tuyaux hélicoïdaux fortement courbés (HCHP) est étudiée. Le facteur d'amélioration du transfert de chaleur / matière est introduit : il est égal à $Nu_H^\infty / Nu_S^\infty$ (respectivement $Sh_H^\infty / Sh_S^\infty$) - le rapport entre les coefficients de transfert de chaleur (respectivement de matière) dans les tubes hélicoïdaux et droits - multiplié par $\phi_{(H,max)} / \phi_{(S,max)}$ - le rapport entre la surface spécifique des tuyaux hélicoïdaux et droits. Ce facteur représente l'augmentation du taux de transfert volumétrique que les tuyaux hélicoïdaux permettent d'obtenir lorsqu'ils sont utilisés dans des modules garnis, c'est-à-dire qu'il correspond à la réduction de volume unitaire maximale (de réacteurs catalytiques, échangeurs de chaleur ou contacteurs à membranes) que de telles conceptions permettent d'atteindre.

Des simulations CFD ont été réalisées pour étudier le transfert de chaleur / matière dans les tubes hélicoïdaux, en particulier ceux très courbés, qui n'ont pas été étudiés dans la littérature antérieurement. Les simulations CFD couvraient des géométries hélicoïdales extrêmes dans des conditions d'écoulement laminaire (nombre de Reynolds compris entre 10 et 2 000). D'autre part, un logiciel de CAO (Conception Assistée par Ordinateur) a été utilisé pour déterminer la compacité maximale des hélices en fonction de leur géométrie. Les résultats numériques obtenus par CFD ont révélé que les HCHPs permettent d'atteindre des taux de transfert de chaleur / matière jusqu'à un ordre de grandeur plus élevés que dans les tubes droits. De plus, les données CAO ont confirmé que leur compacité maximale est beaucoup plus élevée que celle des hélices classiques (bien qu'elle soit inférieure à celle des tubes droits). Ainsi, le taux de transfert volumique autorisé par les HCHPs est jusqu'à 8 fois plus élevé que celui atteint avec des tubes droits. Ceci démontre l'énorme potentiel de ces géométries pour l'intensification des procédés impliquant du transfert de chaleur / matière dans une conduite. Enfin, des corrélations sont développées pour évaluer l'aire interfaciale développée et l'efficacité du transfert de chaleur / matière (exprimée via le nombre de Nusselt ou de Sherwood) dans les tubes hélicoïdaux classiques et fortement incurvés et courbés. Ces nouvelles corrélations permettent d'identifier des conceptions d'hélice optimales pour maximiser le taux de transfert volumique de chaleur / matière (c'est-à-dire minimiser le volume des équipements de transfert de chaleur / matière) avec une efficacité énergétique satisfaisante.

Dans le chapitre IV de cette thèse, une analyse systématique des performances de transfert de chaleur / matière dans les contacteurs à membrane creuse et les échangeurs de chaleur est menée. L'influence des nombres adimensionnels R_H^* et p^* (respectivement le rayon hélicoïdal et le pas hélicoïdal, tous deux non dimensionnés par le diamètre interne du tuyau, d) sur le transfert de chaleur / matière est évaluée par des simulations de type CFD. On considère des contacteurs à membranes et des échangeurs de chaleur hélicoïdaux de longueurs allant de 30 à 6 000 d , des rayons hélicoïdaux non dimensionnels R_H^* compris entre 0,05 et 10 et des pas hélicoïdaux non dimensionnels p^* compris entre

1,25 et 15. Le facteur d'intensification, qui est égal au rapport de transfert de chaleur / matière (en comparant le nombre Nusselt / Sherwood de tuyaux hélicoïdaux et droits) multiplié par le rapport de densité de garnissage des tuyaux hélicoïdaux et droits, est utilisé pour évaluer les performances de chaque géométrie. Une amélioration maximale est obtenue pour les tuyaux hélicoïdaux fortement courbés et relativement élongés. A titre d'exemple, pour un nombre Prandtl / Schmidt de 100 et un Reynolds de 2 000, de telles géométries permettent d'atteindre des valeurs asymptotiques de Nusselt / Sherwood qui sont environ 18 fois plus élevées que celles obtenues dans des tubes droits. Pour un nombre Prandtl / Schmidt de 1 000 (qui correspond aux processus d'absorption de gaz dans les applications à membranes à fibres creuses et les applications d'échangeurs de chaleur impliquant des liquides et des huiles très visqueux) et Reynolds de 2 000, les taux de transfert convectif asymptotique de chaleur / matière sont près de 55 fois supérieurs à ceux obtenus avec des tuyaux droits. Cette étude démontre l'énorme potentiel des ces géométries pour l'intensification des transferts dans les échangeurs de chaleur et de matière.

Dans le chapitre V de cette thèse, différents critères de performance sont proposés afin d'évaluer l'efficacité et le potentiel de différentes géométries utilisées pour intensifier les transferts de chaleur et de matière. En effet, différentes techniques d'amélioration du transfert de chaleur / matière existent comme l'utilisation de tubes hélicoïdaux ou d'inserts à ruban torsadé, et plusieurs critères ont été proposés dans la littérature pour évaluer et comparer leurs performances. Ces critères comparent généralement l'amélioration du transfert de chaleur / matière apportée par une technique donnée à l'augmentation du coefficient de frottement qu'elle induit. Cependant, comme ils ne tiennent pas compte des effets de surface spécifique, ils ne sont pas pertinents pour évaluer le potentiel de nouvelles conceptions en termes d'intensification volumique des échanges, en particulier dans le cas des procédés où un grand nombre de tubes doivent être utilisés simultanément au sein d'une même unité (par exemple échangeurs de chaleur tubulaires, réacteurs catalytiques monolithes, contacteurs membranaires à fibres creuses, échangeurs multifonctionnels, etc.). Dans ce chapitre, différents critères de performance tenant compte des effets de surface spécifique sont proposés, et l'efficacité des tuyaux hélicoïdaux par rapport à ces indices est étudiée. Les résultats révèlent que la plupart des géométries de tubes hélicoïdaux présentent des rendements faibles et moyens en termes de taux de transfert volumétrique. En effet, les géométries hélicoïdales classiques présentent des surfaces spécifiques très faibles du fait de leur petite compacité. Néanmoins, certaines conceptions d'hélices particulières, avec des formes allongées et / ou de petits rayons de courbure, s'avèrent offrir un potentiel énorme pour des performances de transfert de chaleur / matière intensifiées. En effet, ils permettent à la fois de réduire le volume des réacteurs et des échangeurs de chaleur / matière et de diminuer la puissance de pompage nécessaire. A noter que ces géométries n'avaient pas été étudiées jusque-là dans la littérature du fait qu'elles soient difficiles à fabriquer en utilisant les techniques de fabrication classiques. Il convient toutefois de noter qu'aujourd'hui, grâce au développement important des techniques de fabrication

additive et d'impression 3D, la conception de telles géométries est devenue tout à fait envisageable et réalisable. Enfin, en se basant sur des données en provenance de la littérature, les performances des techniques alternatives sont analysées et comparées à celles des tubes hélicoïdaux, mettant en évidence les faiblesses et les forces de chaque stratégie de valorisation. En particulier, il a été montré que parmi les techniques alternative, seule l'utilisation du ruban torsadé permet d'obtenir des performances comparables à celles des hélices hautement incurvées, toutefois cette technique peut vite engendrer des coûts de pompage élevés du fait des pertes de charge importantes qu'elle génère.

Dans le chapitre VI de cette thèse, de nouvelles géométries incurvées sont proposées et étudiées numériquement dans le but d'intensifier davantage les transferts de chaleur et de matière. En effet, les géométries incurvées sont préférées à d'autres techniques passives car elles fonctionnent de manière similaire voire meilleur et cela pour une consommation énergétique et un coût de maintenance inférieurs. En conséquence, les phénomènes de transport dans les tuyaux hélicoïdaux et autres géométries enroulées ont été étudiés dans de nombreuses études numériques et expérimentales. Comme démontré dans les chapitres précédents, les tuyaux hélicoïdaux fortement courbés et / ou allongés offrent des potentialités extraordinaires pour des performances de transfert de chaleur / matière intensifiées car ils génèrent des tourbillons intenses de type Dean et peuvent être densément compactés. Dans ce chapitre, deux nouvelles conceptions complexes en spirale sont proposées et étudiées. : tubes hélicoïdaux ondulés et tubes doublement hélicoïdaux. Les performances de ces géométries ont été évaluées à l'aide de différents critères tenant compte de l'amélioration du transfert de chaleur / matière, des pertes par frottement et des effets de surface spécifique. Les résultats numériques obtenus démontrent que plusieurs des nouvelles géométries proposées et étudiées dans ce chapitre surpassent les tuyaux hélicoïdaux en termes d'optimalité de Pareto, c'est-à-dire que pour une puissance de pompage donnée, ils permettent d'atteindre des performances de transfert encore plus élevées. Toutefois, il convient de noter que ces géométries sont très complexes à fabriquer, ce qui peut limiter leur perspective d'application à l'instant actuel.

Cette thèse a révélé l'énorme potentiel des échangeurs hélicoïdaux pour intensifier le transfert de chaleur et de matière. En particulier, les tuyaux hélicoïdaux très incurvés (HCHP) ont montré d'excellentes performances en ce qui concerne :

- + L'efficacité du transfert de matière/chaleur obtenue (généralement exprimée par le nombre de Sherwood/Nusselt).
- + Les pertes de charge impliquées (généralement caractérisées par le coefficient de frottement) puisque l'énergie de pompage nécessaire pour les compenser constitue un coût de fonctionnement important.
- + La densité de conditionnement ou la compacité, qui représente la plus grande surface spécifique d'échange par unité de volume que ces échangeurs/séparateurs permettent de développer.

Cette thèse ouvre différentes perspectives pour améliorer les performances de transfert des échangeurs de chaleur/matière. Il convient en particulier d'exploiter la nouveauté des HCHP. Le présent travail peut être étendu de cinq manières :

Premièrement, le chapitre VI s'est focalisé sur la possibilité d'utiliser des géométries hélicoïdales complexes (hélices ondulées et doubles hélices) dans les applications d'échangeurs de chaleur/matière où le nombre de Prandtl/Schmidt est faible. Selon différents critères de performance, ces géométries permettent d'aboutir à des performances largement supérieures à celles qui pourraient être obtenues avec des tuyaux hélicoïdaux simples. Il serait donc très intéressant d'étudier ces géométries pour des conditions d'exploitation différentes et un nombre de Prandtl/Schmidt élevé.

Deuxièmement, à la connaissance de l'auteur, aucune étude antérieure ne s'est encore penchée sur l'efficacité du mélange dans les géométries de type HCHP. Les résultats de ce doctorat ouvrent la possibilité d'appliquer ces géométries au micro-mélange, comme par exemple sur un mélangeur en T avec un corps hélicoïdal, qui pourrait être étudié à la fois numériquement et expérimentalement. En effet, avec le développement de la fabrication additive, l'élaboration de géométries hélicoïdales fortement incurvées devient réalisable.

Troisièmement, des mesures expérimentales de l'efficacité du transfert de chaleur/matière dans les HCHP devraient être entreprises pour valider les résultats numériques. En effet, comme expliqué dans cette thèse (chapitre III et chapitre IV), ces données manquent dans la littérature car les HCHP sont difficiles à fabriquer en utilisant des techniques de fabrication traditionnelles, ce qui est maintenant rendu possible grâce à l'impression 3D. Des modèles en matériaux polymères permettraient de mesurer le champ d'écoulement à l'aide de l'imagerie par résonance magnétique, et si un matériau transparent était utilisé, des mesures de PIV (vélocimétrie par image de particules) ou de μ PIV pourraient être effectuées. Si le polymère est suffisamment perméable, des expériences de transfert de matière gazeuse pourraient être entreprises et les nombres de Sherwood correspondants calculés. D'autre part, des modèles imprimés en 3D en métal permettraient de quantifier le transfert de chaleur dans les HCHP et de calculer les nombres de Nusselt correspondants.

Quatrièmement, bien que les tourbillons de Dean intenses dans les HCHP entraînent une amélioration des rendements de transfert de chaleur et de matière par rapport aux tubes droits, ils induisent également des pertes par frottement plus élevées par unité de longueur de tube. Au Chapitre 5, ces critères conflictuels ont été réunis en un seul objectif. Mais la meilleure façon de l'évaluation du potentiel des HCHP reste l'optimisation multi-objectifs et le calcul du front de Pareto qui traduit le compromis optimal entre les avantages fournis par les HCHP et les coûts de fonctionnement supplémentaires qu'ils engendrent.

Différents problèmes d'importance industrielle peuvent être traités par optimisation multi-objectifs : traitement des effluents gazeux (réduction des NO_x) par des réacteurs catalytiques monolithiques, échangeurs de chaleur à circuit imprimé, etc. Les propriétés et les débits des fluides étant fixées, les

corrélations pour le calcul du nombre de Nusselt/Sherwood et du coefficient de frottement (Chapitres II et III) pourront être utilisées comme modèles de substitut dans une optimisation mathématique et permettront de déterminer le flux total de chaleur/matière et la puissance de pompage nécessaire pour une configuration donnée de réacteur/échangeur. Le calcul du front de Pareto permettra de déterminer le compromis réalisable entre la puissance de pompage et le volume (ou la matière) du réacteur/échangeur, c'est-à-dire le volume minimal permettant d'atteindre le flux de chaleur/matière visé pour un coût de pompage donné.

Contents

List of Tables	xix
----------------	-----

List of Figures	xxi
-----------------	-----

Introduction

1	Synthesis and Objectives of the thesis	3
2	Organization of the Thesis	4
3	Publications	6
3.1	Journals	6
3.2	Conferences	6
3.3	Talks	6

Chapter 1

Hydrodynamic-based techniques for improving transfer efficiency in membrane separation processes and heat exchangers

1.1	Filtration techniques and membrane separation	9
1.1.1	Tangential liquid filtration	9
1.1.2	Membrane separation processes	10
1.1.3	Main geometries used	11
1.2	Heat exchanger processes	12
1.3	Concentration/ Temperature polarization	14
1.4	Hydrodynamic solutions to limit concentration/temperature polarization	15
1.4.1	Tangential flow	15
1.4.2	Turbulence promoters	15
1.4.3	Rough walls	17
1.4.4	Pulsate flow	19
1.4.5	Vibrating system in membrane separation	22
1.4.6	Ultrasound	23
1.4.7	Rotary systems	26
1.4.8	Gas sparging	27
1.4.9	Complex shapes	30

Chapter 2

Laminar flow friction factor in highly curved helical pipes: numerical investigation, predictive correlation and experimental validation using a 3D-printed model*

2.1	Introduction	40
2.2	Materials and methods	45
2.2.1	Friction factor and dimensional analysis	45
2.2.2	CFD modeling and simulation	46
2.2.3	3D-printed helical pipe	47
2.2.4	Experimental setup for pressure drop measurements	50
2.3	Results and discussion	50
2.3.1	CFD results	50
2.3.2	Correlation development	52
2.3.3	Comparison with literature correlations	53
2.3.4	Correlation validation using experimental data from literature	56
2.3.5	Correlation validation using data acquired on the 3D-printed highly curved helix	57
2.4	Conclusion	59

Chapter 3

Optimal design of helical heat/mass exchangers under laminar flow: CFD investigation and correlations for maximal transfer efficiency and process intensification performances*

3.1	Introduction	64
3.2	CFD computation of Nusselt (and Sherwood) number in helical pipe flows	69
3.2.1	Nusselt (and Sherwood) number in helical pipe flows	69
3.2.2	CFD modeling and simulation of heat transfer in helical pipes under laminar flow conditions	72
3.2.3	Heat and mass transfer analogy	73
3.3	Optimal packing density of helices	74
3.4	Results and discussion	76
3.4.1	CFD results	76
3.4.2	Correlation for predicting Nusselt (and Sherwood) numbers in helical pipe laminar flows	77
3.4.3	Comparison between the current and literature correlations	80
3.4.4	Correlation and CFD data validation using experimental data from literature	83
3.4.5	Optimal packing density of helices: results and correlation	85
3.4.6	Overall intensification factor and potentiality of highly curved helical pipes designs	87
3.5	Conclusion	89

Chapter 4**Transport phenomena in helical heat and mass exchangers under high Prandtl/Schmidt number conditions***

4.1	Introduction	93
4.2	CFD computation of Nusselt (and Sherwood) number in helical pipe flows	95
4.2.1	Mesh-independence study	95
4.2.2	CFD modeling and governing equations	97
4.2.3	Thermally developing and hydrodynamically developed flow	98
4.3	Results and discussion	100
4.3.1	CFD Results	100
4.3.2	Non-periodic flow	103
4.3.3	Overall intensification factor and potentiality of highly curved helical pipes	104
4.4	Conclusion	106

Chapter 5**Heat / Mass transfer intensification using helically coiled pipes: potentiality and comparison to alternative enhancement techniques***

5.1	Introduction	109
5.2	Transport phenomena in helical pipe flow	111
5.2.1	Helical pipes design, packing density and specific surface area	112
5.2.2	Hydrodynamics and heat/mass transfer in helical pipe flows	115
5.3	Alternative heat/mass transfer enhancement techniques	117
5.4	Results and discussion	120
5.4.1	Heat/Mass transfer enhancement per unit surface	121
5.4.2	Volumetric heat/mass transfer enhancement	123
5.4.3	Cost-effectiveness of heat/mass transfer enhancement per unit surface	125
5.4.4	Cost-effectiveness of volumetric heat/mass transfer enhancement	128
5.4.5	Cost-effectiveness of volumetric heat/mass transfer enhancement in ‘shell-and-tube’ configurations	130
5.5	Conclusion	132

Chapter 6**Toward novel coiled heat/mass exchangers designs**

6.1	Introduction of the Complex helical shapes	135
6.1.1	Wavy helical pipes	136
6.1.2	Double helical pipes	144
6.2	Conclusion	153

Future work and perspectives**Appendix**

List of Tables

1.1	Performance of Membrane Processes with Turbulence Promoters MF: microfiltration; UF: ultrafiltration; RO: reverse osmosis; NF: nanofiltration.	15
1.2	Performance of heat exchanger processes using turbulence promoters from literature compared to classical heat exchangers.	17
1.3	Membrane process performance with pulsed flow. MF: microfiltration. RO: reverse osmosis.	21
1.4	Performance of heat exchanger processes using pulsed flow from literature compared to classical heat exchangers	22
1.5	Performance of membrane processes with vibrating membranes. MF: microfiltration.	23
1.6	Performance obtained by ultrasonic exposure of filtration modules. US: ultrasound; MF: microfiltration; UF: ultrafiltration.	25
1.7	Performance of heat exchanger processes using rotary systems from literature compared to classical heat exchangers	27
1.8	Performance of filtration processes intensified by air injection. MF: microfiltration; UF: ultrafiltration	28
1.9	Performance of heat exchanger processes using Spray technique from literature	30
1.10	Performances of membrane processes of complex form	33
1.11	Numerical and Experimental Studies on Heat Transfer Curved Tubes for Constant wall temperature or Heat Flux	34
2.1	Set of commonly used correlations for predicting the friction factor of fully developed laminar flow in helical pipes. $C_{f,H}^\infty$ and $C_{f,S}^\infty$ correspond to the asymptotic friction factor in helical and straight pipes respectively. $C_{f,S}^\infty$ is equal to $64/Re$ following the Darcy-Weisbach definition which is used in this chapter.	42
2.2	Targeted and obtained geometric parameters of the 3D-printed helical pipe	47
2.3	Optimal set for the parameters of the correlation expressed by Equations 2.7	53
2.4	: Ranges of geometric and operating conditions over which the literature experimental data were acquired and the present correlation was built.	57

3.1	Set of commonly used correlations for predicting Nu_H^∞ and Sh_H^∞ for laminar flow in helical pipes under uniform wall temperature/concentration. Nu_H^∞ and Sh_H^∞ respectively correspond to the asymptotic Nusselt and Sherwood numbers in helical pipes	68
3.2	Optimal sets for the parameters of the correlation expressed by Equations 3.13	79
3.3	Ranges of geometric and operating conditions over which the literature experimental data were acquired and the present correlation was built	84
3.4	Optimal sets for the parameters of the correlation expressed by Equations 3.16	86
4.1	Results for the different grids used for the mesh-independence tests. A pipe of 125 mm arc length, 1mm diameter, 2.5 mm helix radius and 1.25 mm pitch was considered. The inlet velocity was 0.4 m/s	96
5.1	Summary of studies dealing with alternative techniques of heat transfer enhancement under laminar flow conditions	119
6.1	Performances of heat/mass exchangers processes of complex shape	136
6.2	Heat/mass transfer enhancement factor $\eta_{1,0}$ ratio of the optimal helical pipes (OHPs) to the wavy helical pipes (WHPs) $(\eta_{1,0})_{OHPs}/(\eta_{1,0})_{WHPs}$	138
6.3	Performance factor $\eta_{1,1}$ ratio of the optimal helical case (OHPs) to the wavy helical pipes (WHPs) $(\eta_{1,1})_{OHPs}/(\eta_{1,1})_{WHPs}$	139
6.4	The volumetric heat/mass flux $\theta_{1,0}$ ratio of the optimal helical case (OHPs) to the wavy helical pipes (WHPs) $(\theta_{1,0})_{OHPs}/(\theta_{1,0})_{WHPs}$	141
6.5	Performance factor $\theta_{1,1}$ ratio of the optimal helical case (OHPs) to the wavy helical pipes (WHPs) $(\theta_{1,1})_{OHPs}/(\theta_{1,1})_{WHPs}$	142
6.6	The heat/mass transfer enhancement $\eta_{1,0}$ ratio of the optimal helical case (OHPs) to the double helical pipe (DHPs) $(\eta_{1,0})_{OHPs}/(\eta_{1,0})_{DHPs}$	145
6.7	Performance factor $\eta_{1,1}$ ratio of the optimal helical case (OHPs) to the double helical pipe (DHPs) $(\eta_{1,1})_{OHPs}/(\eta_{1,1})_{DHPs}$	148
6.8	The volumetric heat/mass flux $\theta_{1,0}$ ratio of the optimal helical case (OHPs) to the double helical pipes (DHPs) $(\theta_{1,0})_{OHPs}/(\theta_{1,0})_{DHPs}$	150
6.9	Performance factor $\theta_{1,1}$ ratio of the optimal helical case (OHPs) to the double helical pipes (DHPs) $(\theta_{1,1})_{OHPs}/(\theta_{1,1})_{DHPs}$	152

List of Figures

1.1	The Comparison of: (a) Frontal flow filtration. (b) Tangential flow filtration	9
1.2	The filtration spectrum. Source: Osmonics, Inc.	10
1.3	Main membrane separation modules	12
1.4	Classification of heat exchangers on the basis of geometry structure shape	13
1.5	The two types of polarization phenomenon in membrane processes	14
1.6	Swirling alley of Bénard-Von Karman, appearing in the wake of a cylinder transverse to the flow, beyond a minimum speed	16
1.7	Channels equipped with turbulence promoters	16
1.8	Membrane printed with a helical relief	18
1.9	Different roughness geometries used in heat exchanger	19
1.10	Effect of an oscillation of the flow (Left) Direct flow. (Right) Reverse flow	20
1.11	Ultrasonic particle detachment mechanisms	24
1.12	The rotary systems models	26
1.13	The sparging systems models	29
1.14	Schematic representation of Dean cells	31
1.15	Curved channels proposed in the literature	32
1.16	The S-shaped tube	35
1.17	Three-dimensional geometry with alternating curvatures	35
2.1	Schematic representation of Dean cells	40
2.2	Limit of the forbidden region in the (R_H^*, p^*) space (adapted from Przybył and Pierański (2001)) and some representative helix geometries	43
2.3	Contour plot of the dimensionless helix curvature in the (R_H^*, p^*) space	44
2.4	Shape of a wall element (in red) over which C_f is averaged	45
2.5	Typical variation of the friction factor from the entrance of a straight or a helical pipe	46
2.6	3D-printed helical tubes	48
2.7	MRI images of the 3D printed model	49
2.8	Typical variation of the friction factor from the entrance of a straight or a helical pipe	50

2.9	Contour plots of the $C_{f,H}^\infty$ to $C_{f,S}^\infty$ ratio at a Reynolds number. The black dots represent the geometric conditions for which CFD results are acquired. The contours are derived by interpolating these data.	51
2.10	Parity diagram of $C_{f,H}^\infty$: CFD and experimental data versus correlation predictions . . .	54
2.11	Contour plot of the $C_{f,H}^\infty$ to $C_{f,S}^\infty$ ratio: present correlation data (Equations 2.7).	54
2.12	$C_{f,H}^\infty$ versus R_H^* at two different p^* : comparison of different correlations.	55
2.13	$C_{f,H}^\infty$ versus p^* at two different R_H^* : comparison between the present correlation and that of Mishra and Gupta (1979)	55
2.14	$C_{f,H}^\infty$ variation with Re for four different helices	56
2.15	Comparison between the present correlation predictions and the experimental data of De Amicis et al. (2014)	57
2.16	Comparison between the present correlation predictions and the present experimental data	58
3.1	Schematic representation of Dean cells in a helical pipe	64
3.2	Limit of the forbidden region in the (R_H^*, p^*) space (adapted from Przybył and Pierański (2001)) and some representative helix geometries Abushammala et al. (2019a)	65
3.3	Contour plot of the dimensionless helix curvature in the (R_H^*, p^*) space	66
3.4	Typical shape of a wall element (in red) over which h is averaged	69
3.5	Typical variation of the Nusselt (Sherwood) number from the entrance of a straight or a helical pipe	70
3.6	Top view of ideally packed helices of $R_H^* = 2.5$ and $p^* = 1.25$. The black dots represent the axes of the helical or straight tubes.	75
3.7	Contour plots of the Nu_H^∞ to Nu_S^∞ (respectively Sh_H^∞ to Sh_S^∞) ratio. The black dots represent the geometric conditions for which CFD simulations have been performed. The contours are derived by interpolating these data	78
3.8	Parity diagram of Nu_H^∞ : CFD and experimental data versus correlation predictions	80
3.9	Contour plots of the Nu_H^∞ to Nu_S^∞ (respectively Sh_H^∞ to Sh_S^∞) ratio calculated using the present correlation (Eqs. 3.13). The contour plots at $Re = 400$ were generated using the set of parameters valid for $10 \leq Re \leq 400$ (Table 3.2)	81
3.10	Nu_H^∞ (respectively Sh_H^∞) versus R_H^* at two different p^* : comparison of different correlations	81
3.11	Nu_H^∞ (respectively Sh_H^∞) versus p^* at two different R_H^* : comparison between the present correlation and those of Moulin et al. (1996) and Sheeba et al (2019)	82
3.12	Nu_H^∞ (respectively Sh_H^∞) variation with Re for four different helices at Pr (respectively Sc) = 10	83

3.13 Comparison between the present correlation predictions and the experimental data of Sheeba et al. (2019)	84
3.14 Contour plot of a_{min}^* in the (R_H^*, p^*) space. The black dots represent the geometric conditions for which CAD results are acquired and some representative helix geometries	85
3.15 a_{min}^* versus p^* with comparison between the CAD results and the present correlation (Equations 3.16)	87
3.16 Contour plots in the (R_H^*, p^*) space of (a) a_{min}^* and (b) of the $\phi_{(H,max)}$ to $\phi_{(S,max)}$ ratio	87
3.17 Contour plots of the intensification factor, ϵ	89
4.1 Limit of the forbidden region in the (R_H^*, p^*) space (adapted from Przybył and Pierański (2001)) and some representative helix geometries Abushammala et al. (2019a)	93
4.2 Contour plot of the dimensionless helix curvature in the (R_H^*, p^*) space	94
4.3 Contour plot of the friction factor correlation at $Re = 400$	94
4.4 The Export-Import technique of the velocity and temperature (resp. concentration) fields	96
4.5 Grid topology on a cross-sectional plane of Mesh C	97
4.6 Typical variation of the Nusselt (Sherwood) number as a function of the curvilinear distance from the inlet in a helical pipe	99
4.7 Typical variation of the Nusselt (Sherwood) number from the entrance at $Re = 800$ and $Pr (Sc) = 1\ 000$	101
4.8 Contour plots of the Nu_H^∞ to Nu_S^∞ (respectively Sh_H^∞ to Sh_S^∞ ratio). The black dots represent the geometric conditions for which CFD simulations have been performed, in addition the black stars represent the geometries generating the non-periodic flow. The contours are derived by interpolating these data	102
4.9 Contours of the problem variables	104
4.10 Contour plots of the intensification factor, ϵ	105
5.1 Transport phenomena in helical pipe flows	112
5.2 Limit of the forbidden region in the (R_H^*, p^*) space (adapted from Przybył and Pierański (2001)) and some representative helix geometries	112
5.3 Contour plot of the dimensionless helix curvature in the (R_H^*, p^*) space	113
5.4 Top view of ideally packed helixes of $R_H^* = 2.5$ and $p^* = 1.25$. The black dots represent the axes of the helical or straight tubes.	114
5.5 Contour plot of in the (R_H^*, p^*) space	115
5.6 Example of contour plots in the (R_H^*, p^*) space. Note that a different scale is used for each subfigure	117
5.7 Schematic representations of the novel heat exchanger designs	118

5.8	Performances of helical pipes and alternative enhancement techniques based on the $\eta_{1,0}$ criterion. In the figure caption, for the data of Kurnia et al. (2020) , HP and SP respectively refer to the use of a helical or a straight pipe, while TR refers to the twist ratio of the used twisted tape	122
5.9	Contour plots in the (R_H^* , p^*) of the $\theta_{1,0}$ criterion	124
5.10	Performances of helical pipes and alternative enhancement techniques based on the $\theta_{1,0}$ criterion. In the figure caption, for the data of Kurnia et al. (2020) , HP and SP respectively refer to the use of a helical or a straight pipe, while TR refers to the twist ratio of the used twisted tape	125
5.11	Contour plots in the (R_H^* , p^*) of the $\eta_{1,1}$ criterion	126
5.12	Performances of helical pipes and alternative enhancement techniques based on the $\eta_{1,1}$ criterion. In the figure caption, for the data of Kurnia et al. (2020) , HP and SP respectively refer to the use of a helical or a straight pipe, while TR refers to the twist ratio of the used twisted tape	127
5.13	Contour plots in the (R_H^* , p^*) of the $\theta_{1,1}$ criterion	128
5.14	Performances of helical pipes and alternative enhancement techniques based on the $\theta_{1,1}$ criterion. In the figure caption, for the data of Kurnia et al. (2020) , HP and SP respectively refer to the use of a helical or a straight pipe, while TR refers to the twist ratio of the used twisted tape	129
5.15	Contour plot in the (R_H^* , p^*) of the $\chi_{1,1}$ criterion for $Re = 2\,000$ and $Pr/Sc = 10$. .	131
5.16	Performances of helical pipes and alternative enhancement techniques based on the $\chi_{1,1}$ criterion. In the figure caption, for the data of Kurnia et al. (2020) , HP and SP respectively refer to the use of a helical or a straight pipe, while TR refers to the twist ratio of the used twisted tape	132
6.1	Channel structures designed to benefit from Dean vortices and chaotic advection . . .	135
6.2	The five different wavy helical pipes studied in the present section	137
6.3	Heat/mass transfer enhancement factor $\eta_{1,0}$ vs. Reynolds number for wavy helical pipes (WHPs) and optimal helical pipes (OHPs) at $Pr/Sc=10$ and $Pr/Sc=1$	138
6.4	Performance factor $\eta_{1,1}$ (comparing transfer enhancement to pumping cost) vs. Reynolds number for wavy helical pipes (WHPs) and optimal helical pipes (OHPs) at $Pr/Sc=10$ and $Pr/Sc=1$	140
6.5	The volumetric heat/mass flux $\theta_{1,0}$ vs. Reynolds number for the wavy helical pipes (WHPs) and the optimal helical pipes (OHPs) at $Pr/Sc = 10$ and $Pr/Sc=1$	140
6.6	Performance factor $\theta_{1,1}$ vs. Reynolds number for the wavy helical pipes (WHPs) and optimal helical pipes (OHPs) at $Pr/Sc=10$ and $Pr/Sc=1$	143

6.7	Double helical pipe designs considered in this section	144
6.8	The heat/mass transfer enhancement $\eta_{1,0}$ vs. Reynolds number for the double helical pipes (DHPs) and optimal helical pipes (OHPs) at $Pr/Sc=10$ and $Pr/Sc=1$	146
6.9	Performance factor $\eta_{1,1}$ vs. Reynolds number of the double helical pipes (DHPs) and optimal helical pipes (OHPs) at $Pr/Sc=10$ and $Pr/Sc=1$	147
6.10	The volumetric heat/mass flux $\theta_{1,0}$ vs. Reynolds number for the double helical pipes (DHPs) and optimal helical pipes (OHPs) at $Pr/Sc=10$ and $Pr/Sc=1$	149
6.11	Performance factor $\theta_{1,1}$ vs. Reynolds number of the double helical pipes (DHPs) and optimal helical pipes (OHPs) at $Pr/Sc=10$ and $Pr/Sc=1$	151
6.12	The Pareto frontier (blue curve on the left figure) for a multi-objective optimization problem with two objective functions: the enhancement factor and friction factor at $Re=800$ and $Pr/Sc =10$	153
6.13	The Pareto frontier for a multi-objective optimization problem with two objective functions: the enhancement factor $\theta_{1,0}$ and friction factor of the optimal helical pipes, wavy helical pipes and double helical pipes at $Re = 800$ and $Pr/Sc =10$	154
1	T-shaped micro-mixer with a HCHP design	157
2	Micro-mélangeur en forme de T avec un design HCHP	158

Introduction

1 Synthesis and Objectives of the thesis

Membranes are widely used for separation of multiphase and homogeneous mixtures. Membrane contactors are promising for process intensification especially gas-liquid absorption technologies. In parallel, heat exchangers are an efficient process to transfer heat between two fluids and can be found in many industrial applications, such as refrigeration, air conditioning, power stations, chemical plants, petroleum refineries, and sewage treatment. The design and operation of membrane separators and heat exchangers have been of great interest for many scientific researches aiming at improving the separation/transfer efficiency. In this context, CFD (Computational Fluid Dynamics) reveals to be a powerful tool for assisting and supporting engineers in determining the optimal shape of membrane separators and heat exchangers. In this PhD, an extensive CFD study of the performance of helical shape hollow separators and heat exchangers is conducted. The goal is to determine the effects of the helix geometry (pitch, helical radius and pipe diameter) on:

- + The achieved mass /heat transfer efficiency (generally expressed by the Sherwood/Nusselt number).
- + The involved pressure drops (generally characterized via a friction factor) as pumping constitutes a major operating cost (i.e. energy requirement).
- + The packing density or compactness which represents the highest specific area of membrane separators and heat exchangers, i.e. the surface area packed within a unit volume.

Next chapters will first concentrate on developing correlations dedicated to predicting the heat and mass transfer efficiencies in helical pipes. These correlations, will then be used in model-based optimization of helically coiled heat exchangers and hollow fiber membrane contactors in order to determine the optimal helical tubes design, i.e. the one leading to the best trade-off between the transfer efficiency enhancement and the increase of pumping costs.

2 Organization of the Thesis

In Chapter 1, we present the state of the art of the hydrodynamic techniques aimed at limiting concentration/temperature polarization and fouling. After a review of the basic concepts of filtration, membrane separation and heat exchanger, we detail 7 efficient techniques: turbulence promoters, flow pulsation, vibrating systems, ultrasound, rotating systems, aeration and complex shapes. Wall roughness appears unfavorable to separation. In the remainder of this thesis, we present our contribution to one of the techniques, the complex shapes technique. In particular, the flow in helical pipes is investigated, which is known to exhibit Dean vortices, that lead to improved mixing and thus to enhanced mass/heat transfer.

Chapter 2 presents CFD simulations carried out to determine the friction factor in helical pipes, particularly for highly curved geometries. The emphasis is put on the laminar flow regime which is commonly encountered in hollow fiber membranes and micro-structured heat exchanger applications. Various helix designs and a broad range of Reynolds number values are investigated. In order to validate the simulations, pressure drop measurements were performed on a highly curved helix built by 3D-printing. Existing correlations are known to fail for the accurate prediction of the friction factor in highly curved helices. A new correlation is thus proposed. An excellent agreement is obtained between the experimental pressure drop measurements and the proposed correlation predictions.

In Chapter 3, the heat/mass transfer efficiency in helical pipes (particularly in highly curved ones) is computed through additional CFD simulations under laminar flow conditions. The packing density (i.e. interfacial area) is evaluated using a CAD software. Highly curved helical pipes (HCHPs) offer tremendous potentialities for intensified heat/mass transfer performances as they generate intense Dean-type vortices. However, these designs have not been explored so far in the literature, probably because they are difficult to build using traditional manufacturing techniques. Nowadays, thanks to a witnessed progress in 3D-printing, the fabrication of HCHPs has become achievable. Therefore, investigating their performance in terms of heat and mass transfer intensification presents significant interest from both academic and industrial points of view. The results reveal that HCHPs not only allow achieving much higher transfer rates than straight and classical helical pipes, but they can also be densely packed. Therefore, when appropriate designs are selected, impressive process intensification factors are achievable, with up to 8-fold volume reductions. Finally, correlations are developed for evaluating the interfacial area and the heat/mass transfer efficiency in classical and highly curved helical pipes. In Chapter 5, these correlations are used in model-based optimization to determine the optimal designs of helically coiled heat/mass exchangers.

As for Chapter 4, the systematic analysis of heat/mass transfer performances in highly curved hollow membrane contactors and heat exchangers is conducted. A maximal enhancement is achieved for highly curved and elongated helical pipes. As an example, for a Prandtl/Schmidt number of 100 and a Reynolds of 2000, such geometries allow reaching asymptotic Nusselt/Sherwood values which are about 18 times higher than those achieved in straight tubes. For a Prandtl/Schmidt number of 1 000 and Reynolds of 2 000, asymptotic heat/mass convective transfer rates get nearly 55 times higher than those obtained using straight pipes.

In Chapter 5, different performance criteria accounting for specific surface area effects are proposed, and the efficiency of helical pipes with respect to these indexes is investigated. The results reveal that most helical pipe geometries exhibit poor efficiencies in terms of volumetric transfer rates. Nonetheless, some particular helix designs, with elongated shapes and/or small helix radius, are found to offer huge potential for intensified heat/mass transfer performances. Indeed, they simultaneously allow to reduce the volume of reactors and heat/mass exchangers and to decrease the required pumping power. Finally, relying on literature data, the performances of alternative techniques are analyzed and compared to that of helical pipes, highlighting the weaknesses and strengths of each enhancement strategy.

Finally, in Chapter 6 two novel complex coiled designs are proposed and investigated: wavy helical pipes and double helical pipes. The performances of these geometries were evaluated using different criteria accounting for heat/mass transfer enhancement, frictional losses and specific surface area effects. Comparison to helical pipes reveals that these novel designs allow reaching even higher performances in terms of intensified heat/mass transfer.

3 Publications

3.1 Journals

- **Omran Abushammala**, Rainier Hreiz, Cecile Lemaitre, Eric Favre. (2020): “Heat / Mass transfer intensification: can helically coiled pipes compete with alternative enhancement techniques? ”, *Chemical Engineering Science*, **Submitted on 14/09/2020**.
- **Omran Abushammala**, Rainier Hreiz, Cecile Lemaitre, Eric Favre. (2020): “Optimal design of helical heat/mass exchangers under laminar flow: CFD investigation and correlations for maximal transfer efficiency and process intensification performances”, *International Journal of Heat and Mass Transfer*, **153, 119610**.
- **Omran Abushammala**, Rainier Hreiz, Cecile Lemaitre, Eric Favre. (2019): “Laminar flow friction factor in highly curved helical pipes: Numerical investigation, predictive correlation and experimental validation using a 3D-printed model”, *Chemical Engineering Science*, **207, 1030-1039**.

3.2 Conferences

- **Omran Abushammala**, Rainier Hreiz, Cecile Lemaitre, Denis Wypysek, Maik Tepper, Matthias Wessling, Eric Favre. (2020): “Can Helically Coiled Heat/Mass Exchangers Compete with Alternative Heat/Mass Transfer Intensification Techniques?”, 2020 AIChE Annual meeting, **Submitted on 01/04/2020**.
- **Omran Abushammala**, Rainier Hreiz, Cecile Lemaitre, Eric Favre. (2019): “Generating maximal mass transfer in highly curved helical hollow fiber membranes : A CFD study”, 12th European Congress Of Chemical Engineering (ECCE 12), September 15 - 19, 2019 Florence, Italy.
- **Omran Abushammala**, Rainier Hreiz, Cecile Lemaitre, Eric Favre. (2019): “Maximizing mass transfer using highly curved helical pipes: A CFD investigation”, 6th International Conference on Fluid Flow, Heat and Mass Transfer, June 18-19, 2019 Ottawa, Canada **doi:10.11159/ffhmt19.145**.

3.3 Talks

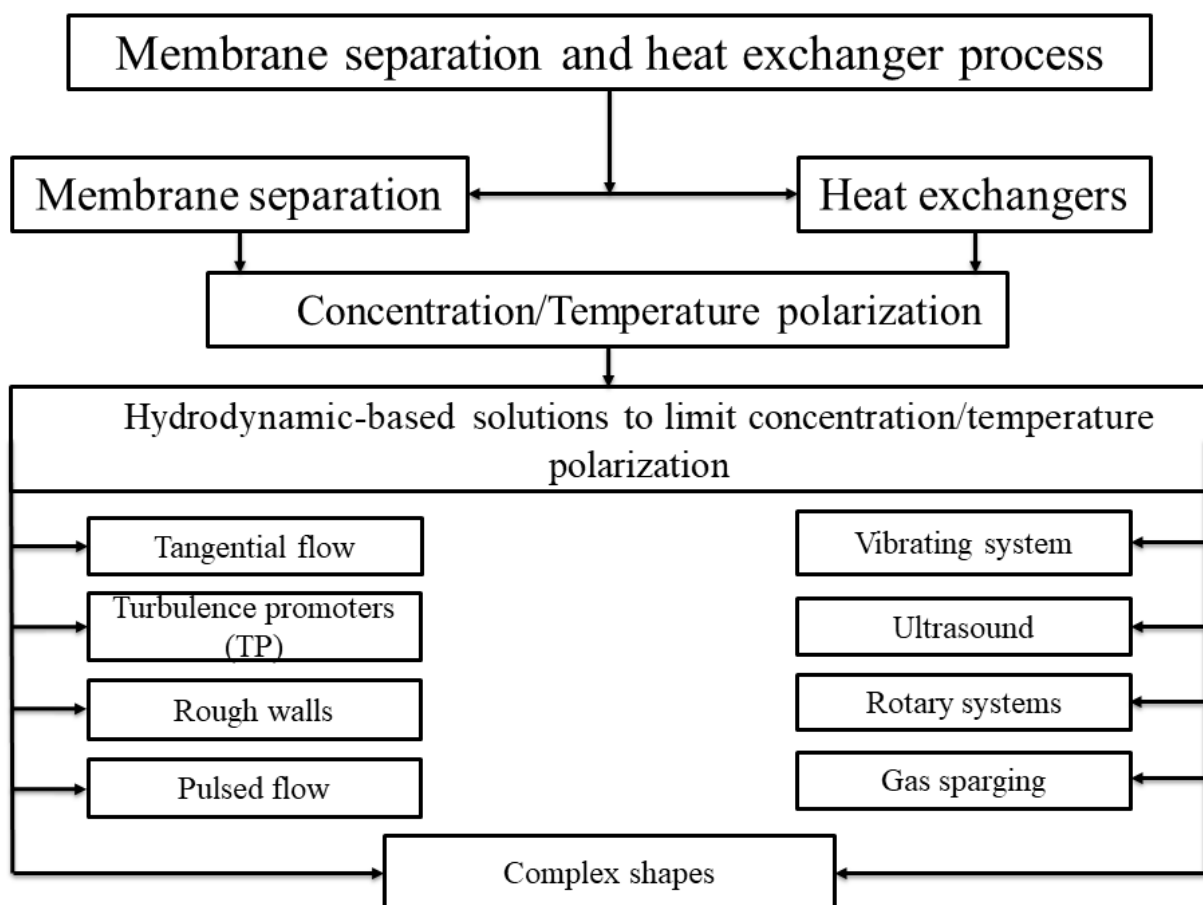
- **Omran Abushammala**, Rainier Hreiz, Cecile Lemaitre, Eric Favre: “Optimal shape design of hollow membrane modules”, December 09, 2019 , **RWTH Aachen University - Germany**.

Chapter 1

Hydrodynamic-based techniques for improving transfer efficiency in membrane separation processes and heat exchangers

Summary

This chapter presents a state of the art of hydrodynamic-based solutions used to intensify separation processes and/or to improve heat transfer techniques. In the first part, the basic concepts of filtration, membrane separation and heat transfer processes are defined, and the main types of separation modules and heat exchangers are presented. Concentration and temperature polarizations are explained to be one of the main limitations for transfer efficiency. Then, a literature survey of seven hydrodynamic-based techniques for counteracting these effects is presented. A first technique is the use of turbulence promoters which are obstacles (parietal or placed in the bulk) that the fluid must circumvent and which produces recirculations favorable for mixing. Another enhancement solution is to vibrate the module wall, which limits the deposition of particles. Ultrasound technique is a very effective method to unclog filters. Gas (often air) may also be injected in the liquid: the passage of plugs (large gas bubbles) efficiently disrupts the liquid flow. Rotational cylindrical or disk systems take advantage of the hydrodynamic instabilities that appear in these geometries and induce recirculations with relatively low energy costs. Finally, the use of complex shapes devices is presented as a passive technique that induces Dean-type vortices or leads to chaotic flow behavior, which results in an extremely efficient mixing at a low energy consumption.



1.1 Filtration techniques and membrane separation

1.1.1 Tangential liquid filtration

Filtration is a unitary operation that consists in separating solids suspended in a fluid using a porous medium. Filtration techniques can be broadly classified into two main categories, frontal (or dead-end) and tangential (or crossflow) filtrations [1]. In frontal filtration, the flow of the suspension is orthogonal to the filtering wall as show in Figure 1.1a; all the carrying fluid passes through the porous wall while the solids are trapped and retained by the filter (apart particles smaller than the characteristic threshold of the filter, which are not stopped) and accumulates in the form of a filter cake [1]. The clear liquid recovered is called filtrate. In tangential filtration, the flow of the suspension is parallel to the filtering wall. Such devices have one inlet and two outlets as show in Figure 1.1b. Part of the liquid, called filtrate or permeate, crosses the filtering wall while the other part, called concentrate or retentate, enriched in particles, is discharged downstream. The separation is not total in this case and it is refered to as clarification or concentration [1]. The concentrate stream is generally larger than the filtrate stream.

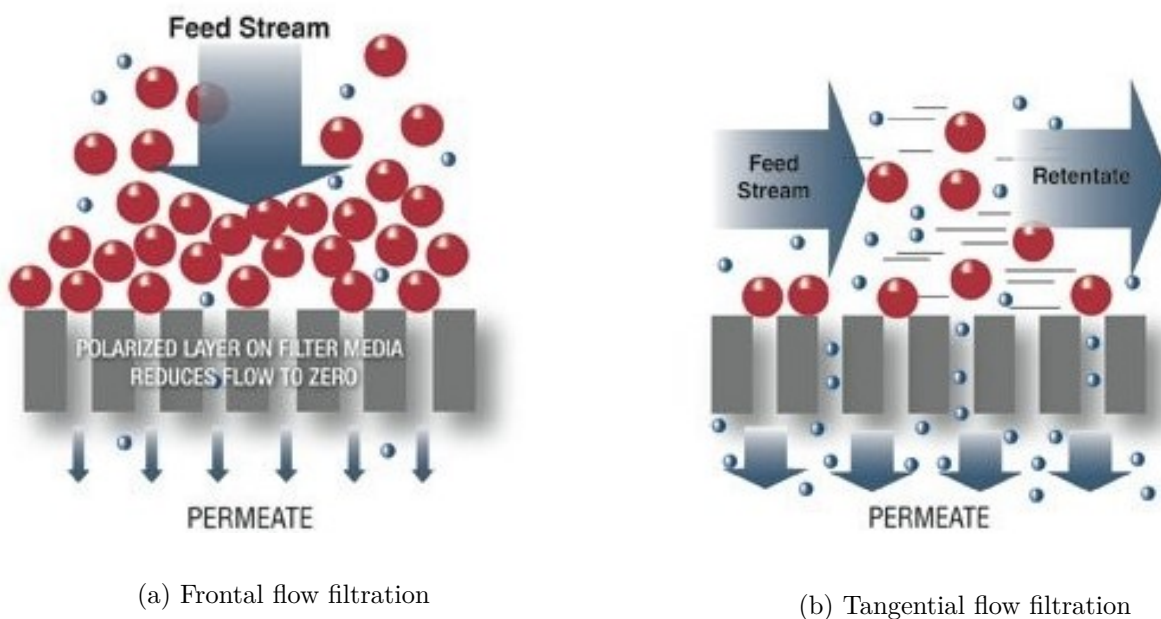


Figure 1.1: The Comparison of: (a) Frontal flow filtration. (b) Tangential flow filtration [2].

Various materials are used as filter media. Fabrics (fiberglass, cotton, wool, paper and polymer) are soft media [3]. There are also rigid materials such as metal, ceramic, coal, ebonite and plastic. When the particles to be filtered are very small, membranes are used as filter media as explained in Figure 1.2.

Tangential filtration represents a first hydrodynamic-based improvement of the filtration process. Indeed, in this process, the main flow generates shear near the filtering wall, which tends to limit the particles accumulation and resuspend the deposited solids. However, high flow velocities are re-

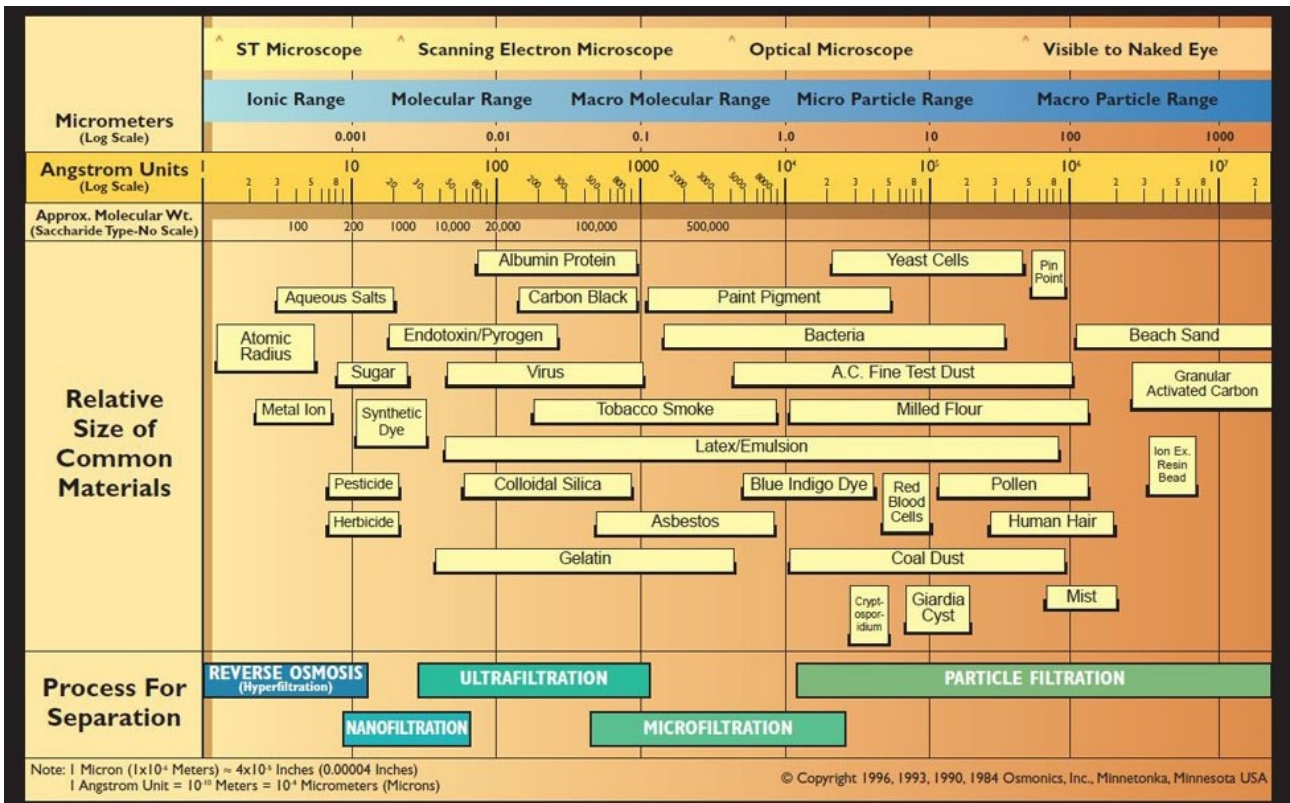


Figure 1.2: The filtration spectrum. Source: Osmonics, Inc.

quired to obtain high shears, which is energy consuming and reduces the slurry residence time. The present PhD study mainly focuses on membrane separation and tangential filtration in the presence of Dean vortices, which constitutes an additional hydrodynamic-based enhancement of these processes efficiency. As will be discussed later, this technique is commonly used for improving the transfer rate in heat exchangers. Given the heat/mass transfer analogy, heat and mass transfer enhancement by Dean vortices will be simultaneously addressed in the following sections.

1.1.2 Membrane separation processes

Membrane contactors are membrane systems mainly used to contact two phases to promote the mass transfer between them. They are considered as one of the most promising intensification technologies for gas-liquid absorption processes in food, chemistry, energy and pharmaceutical industries. Membranes are thin, semi-permeable or permselective objects that allow the retention of solutes or particles contained in a fluid [4]. They can be porous or dense. Porous membranes contain a large number of small cavities called pores, with dimensions large compared to intermolecular distances in solids [5]. The fluid flow through the membrane is generally laminar, obeying Darcy law, or Ergun law for higher speeds [6].

In dense membranes, the medium is continuous. The crossing species dissolve in the membrane and diffuse according to Fick's law [6]. Dense membranes have the major advantage in the sepa-

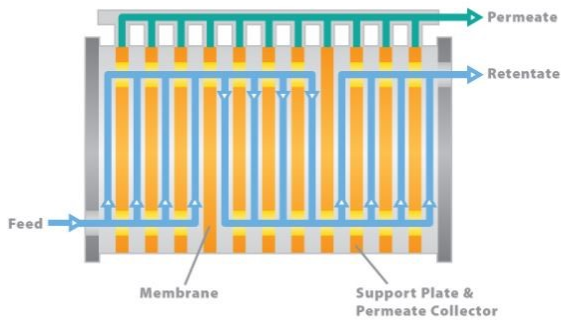
ration of liquid or gaseous homogeneous mixtures. They are selected according to their selectivity and permeability. Because of a difference in affinity, they let through one of the constituents to be separated, but not the others. Membranes are used in separation processes such as microfiltration, ultrafiltration, nanofiltration, reverse osmosis, dialysis and electro dialysis, gas permeation, pervaporation and membrane distillation [5], [7]. Microfiltration is a technique for filtering fine particles, between 0.1 and 10 μm in diameter. These particles may be inert solids, droplets or microorganisms (cells, bacteria). Microfiltration uses frontal filtration (depth filtration) or tangential filtration (flat, spiral, tubular modules). On the other hand, ultrafiltration aims at separating very fine particles or dissolved molecules or macromolecules, of size ranging between 10 and 100 nm [1], [5]. For this purpose, semi-permeable membranes are used in planar, spiral, tubular or hollow fiber modules and sometimes filter-press modules. The pumping pressure used is generally higher than in microfiltration and the transmembrane flow is less important. Nanofiltration is used for molecules smaller than 10 nm (Figure 1.2). Reverse osmosis consists in extracting water from a saline solution by applying enough pressure to the feed to reverse the osmotic flow. Selective membranes are used for this application, allowing water to pass through but not salt. The filter-press, spiral-plane and hollow fiber modules can be used to achieve reverse osmosis [5], [7].

Dialysis processes separate solutes (ionic or nonionic) dissolved in a solvent. The membranes used are permeable to the solute but impermeable to the solvent. This process is used to eliminate metabolite waste from the blood of people with renal failure (hemodialysis). In the case of electro dialysis, the solute to be separated is an ion that is transported through ionic membranes under the action of an electric field [5], [7]. Membranes are also used for gas separation and pervaporation. The separation of a gaseous mixture is called gas permeation. In pervaporation, the mixture to be separated is initially liquid and one of the constituents undergoes evaporation before being transported through the membrane [5], [7]. Membrane distillation is used mainly for the desalination of seawater. In this process, water is transported through a hydrophobic porous membrane. On one side of the membrane, partially vaporized and salty water circulates at high temperature and on the other side circulates fresh water at a lower and imposed temperature. Because of the difference in temperature, a water partial pressure difference is established between the two sides which pushes the water vapor towards the cold side where it condenses [8].

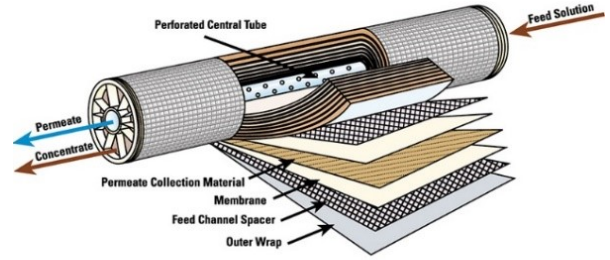
1.1.3 Main geometries used

The classical tangential filtration and membrane separation modules are the planar modules, the spiral modules, the tubular modules and the hollow fiber modules [7], see Figure 1.3.

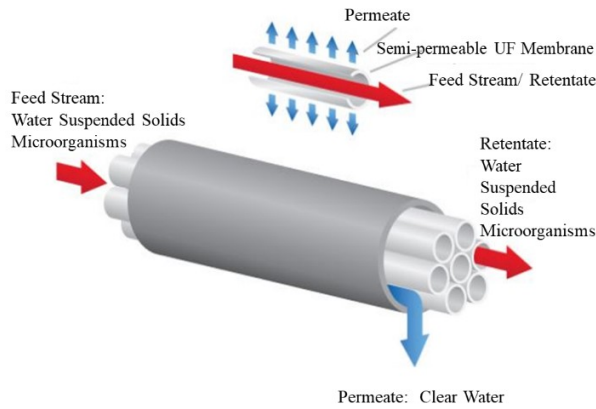
The planar modules are a kind of multi-layered membranes, alternating layers where the supply fluid circulates and layers in which the filtrate (or permeate) circulates, Figure 1.3a. The mixture to be treated enters the feed layers and enriches in particles/solute along its way as liquid flows through the



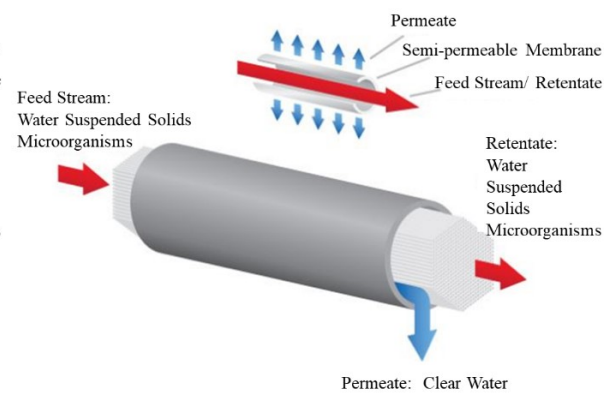
(a) Planar module.



(b) Spiral module.



(c) Tubular module.



(d) Hollow fiber module.

Figure 1.3: Main membrane separation modules [9].

membranes and exits through the permeate layers. Each layer contains internal objects called spacers that maintain a spacing between the membranes. The operation of the spiral modules is similar to that of planar modules, but the membranes are fixed to a collecting cylinder and wrapped around it, Figure 1.3b. The tubular modules consist of cylindrical filters of centimetral diameter, in closed with then cylindrical shell. The suspension circulates inside the tubes and is progressively concentrated in particles while the filtrate passes through the membrane, Figure 1.3c. The hollow fiber modules, which will be considered during this PhD, are composed of a large number (between 50 and 5000) of small pipes (the hollow fibers) disposed parallel in a housing, Figure 1.3d. The liquid to be treated can circulate inside the fibers (and the permeate outside) or outside, in the housing (and permeate inside).

1.2 Heat exchanger processes

A heat exchanger is a device used to transfer heat between two or more fluids. The fluids may be separated by a solid wall to prevent mixing or they may be in direct contact. These technologies can be used at an industrial or domestic scale and cover a large range of applications: heating and cooling

in evaporators, refrigeration and air-conditioning, condensation in power plants, steam generation, waste heat recovery, fluid heating or cooling, radiators for space or terrestrial vehicles, etc. [10], [11]. There are a lot of types of heat exchangers in industrial application such as plate type heat exchanger, shell-and-tube heat exchanger, vertical mantle heat exchanger and a broad classification of heat exchangers based on their geometry structure shape outlined by Bhutta et al. (2012) [12] in the Figure 1.4. The design of these devices is complex, since it requires accurate estimations of the heat

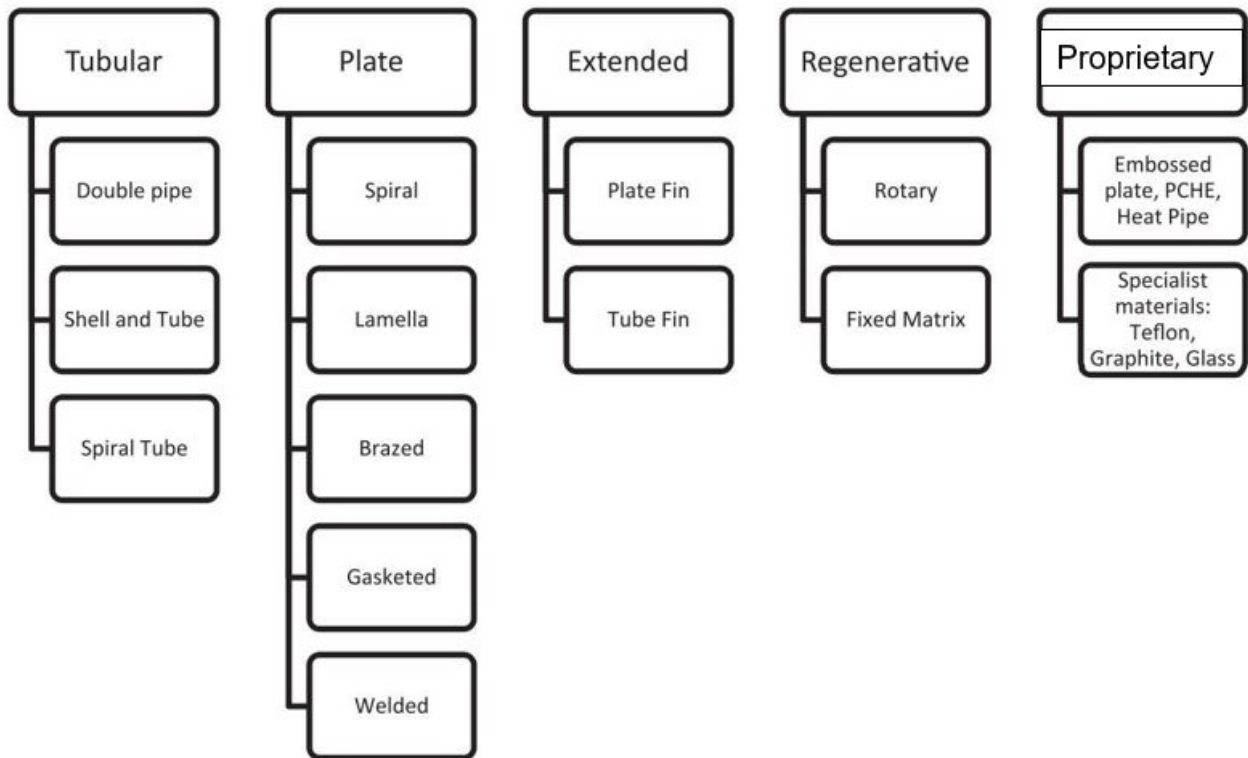


Figure 1.4: Classification of heat exchangers on the basis of geometry structure shape, [12]

transfer rate and pressure drop. Furthermore, engineers need to consider energy, material and cost saving aspects [13]. In fact, the major challenge in designing such facilities is to make the equipment compact and with a high heat transfer rate using minimum power to reduce the costs [11]. This approach can be referred to as Heat transfer Enhancement or Intensification [13]. To help engineers to decide between different methods and technologies, many performance criteria can be used to evaluate the performance of heat exchanger technologies. One of them is the thermal enhancement factor which is used to estimate the performance of different insert such as wire coil, twisted tape, etc [10]. There are active and passive methods to enhance the heat transfer in heat exchanger applications [14]. The active techniques are based on external forces to perform the augmentation [14]. The active technique is effective; however, it is not always easy to perform the compatible design with other component in a system. It also increases the total cost of the system. On the other hand, passive techniques employ special surface geometry. Using the geometry approach is easier, cheaper and does not interfere with other components in the system.

1.3 Concentration/ Temperature polarization

The membrane properties, trans-membrane pressure, liquid flow rate and bulk concentration/temperature affect the membrane efficiency. One of the basic phenomena limiting the separation efficiency in membranes is processes is a physical phenomenon that takes place near the membrane surface referred to as polarization. Depending on the applied driving force of the membrane system, the polarization phenomenon may designate either temperature polarization or concentration polarization, as shown in Figure 1.5 [15]. During separation, an over-concentration of the retained species appears in the

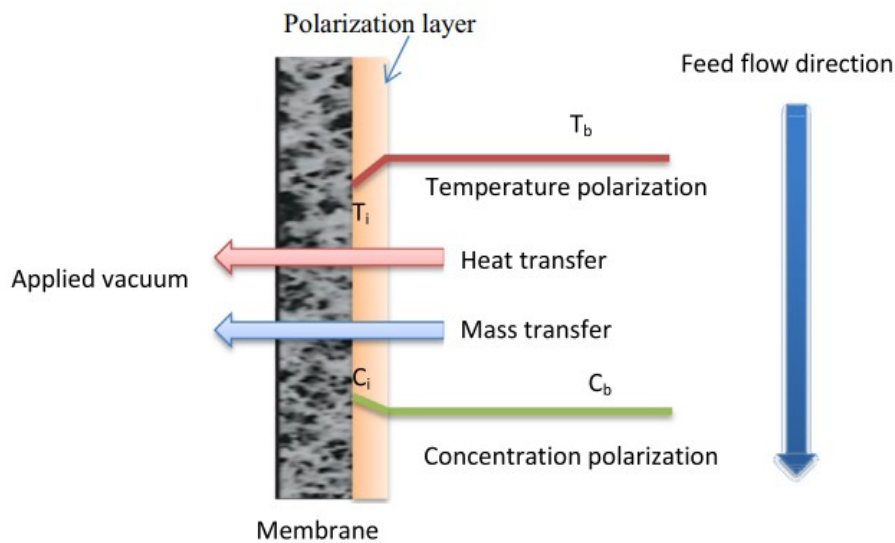


Figure 1.5: The two types of polarization phenomenon in membrane processes [15]

vicinity of the membrane. This phenomenon is referred to as concentration polarization. It causes several problems for membrane transfer. First, the flow of species across the membrane is proportional sometimes to the concentration difference between the two membrane faces, which is reduced by polarization. In addition, molecules that accumulate may lead to fouling. Finally, above a concentration threshold, the mixture becomes rheologically complex and may take the consistency of a gel that opposes the liquid and the species motion [16]. Similarly, when heat transfer is involved (in pure heat or combined mass and heat transfer processes), temperature polarization often occurs. In this phenomenon, temperature is higher (resp. lower) near the exchange surface than in the bulk flow, if the temperature on the other side of the membrane is high (resp. low). As a consequence, heat transfer, which is proportional to the temperature difference across the membrane, is limited. Concentration polarization takes place in both isothermal processes (e.g., reverse osmosis and forward osmosis) and in non-isothermal processes (e.g., membrane distillation) [15].

1.4 Hydrodynamic solutions to limit concentration/temperature polarization

Several bibliographic reviews identify hydrodynamic techniques to reduce concentration/temperature polarization and clogging [17]. These techniques are intended to create additional shear, to cause hydrodynamic instabilities giving rise to recirculations, or to generate the mixture at low flow velocity. This section describes the main technological variants encountered in the literature, the mechanisms at work and the fields of application. The typical performances for each model are presented. However, their performances are difficult to compare because the authors rarely specify the extra energy consumed.

1.4.1 Tangential flow

Tangential filtration, in which the flow of the liquid to be treated is parallel to the filtering wall, can be considered as a hydrodynamic improvement of the frontal filtration. Indeed this flow produces shear, tending to detach the particles from the walls. Nevertheless, it is necessary to use high speeds (typically 1 to 5 m/s) to generate high shear which is expensive and limits the residence time in the filtration module [18].

1.4.2 Turbulence promoters

1.4.2.1 Turbulence promoters in membrane separation

The turbulence promoters (TP) are objects of variable shapes introduced inside the channel where the fluid to be separated circulates. They may be large, glued to the wall or placed in the center of the flow. TP constitute obstacles that the fluid must circumvent, causing recirculations. They make the flow unsteady, with swirling detachments and complex wakes, generating shear and mixing. Therefore, they can significantly increase the permeate flow, Table 1.1. Some configurations of TP, in

Table 1.1: Performance of Membrane Processes with Turbulence Promoters MF: microfiltration; UF: ultrafiltration; RO: reverse osmosis; NF: nanofiltration.

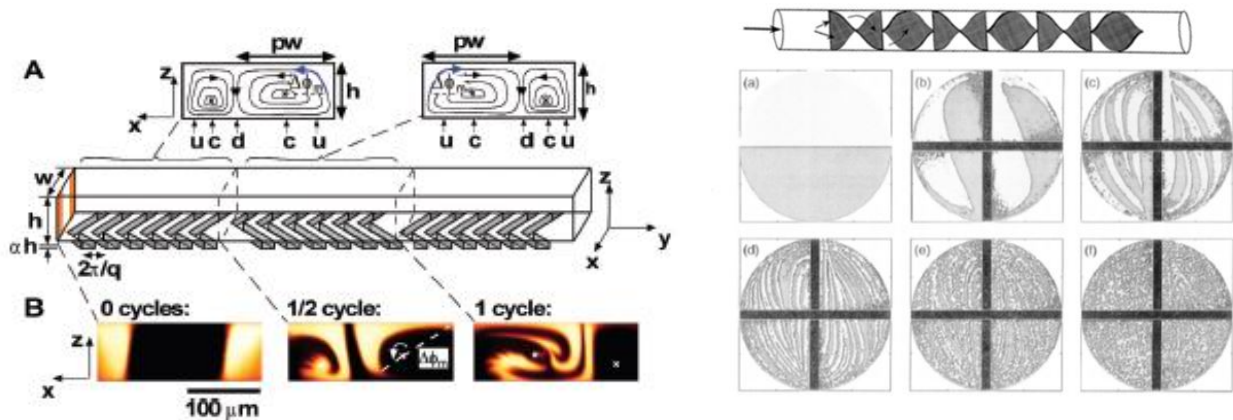
Authors	Process	Geometry	Turbulence promoters	Performance : increased permeate flow
Krstic et al. (2007) [19]	MF oil droplets in water	Tubular	Kenics static mixer	> 500%
Bellhouse et al. (2001) [20]	MF yeast, UF milk, OI NaCl, NF dye	Tubular	Helical screw	900%
Auddy et al. (2005) [21]	NF dye	Plane	Transverse cylinder slightly spaced from the wall	109%

the form of cylinders transverse to the flow, induce a wake instability, known as Bénard-Von Karman instability. Beyond a threshold speed, vortices are released alternately at the top and bottom of the cylinder and advected downstream and contribute to the mixing of the fluid [22], Figure 1.6. Other



Figure 1.6: Swirling alley of Bénard-Von Karman, appearing in the wake of a cylinder transverse to the flow, beyond a minimum speed [23]

configurations of TP cause chaotic mixing, high performance mixing with lower energy consumption. In this type of flow the fluid particles are successively stretched and folded, causing an exponential divergence of the initially neighboring particle trajectories [24]. Chaotic trajectories phenomenon has been observed in a channel whose wall exhibit asymmetrical reliefs of alternating forms [25], Figure 1.7a, and for static mixers [26], Figure 1.7b. Turbulence promoters are used in microfiltration of



(a) Microchannel with a wall printed with an alternating asymmetric chevron relief [25]

(b) Tube equipped with a Kenics static mixer; progressive mixing of two initially segregated fluids [26]

Figure 1.7: Channels equipped with turbulence promoters

suspensions (activated sludge [27], clay [28], yeasts [29], droplets [19]), in ultrafiltration (solution of macromolecules [30], milk [31]), reverse osmosis and nanofiltration [32]. This technique is frequently coupled with other hydrodynamic techniques. Some studies report pulsate flows in the presence of promoters [33]. Vibrations can also be used in addition to promoters [34].

1.4.2.2 Turbulence promoters in heat exchanger

The use of turbulence promoters is one of the passive intensification methods that is efficient to reduce the size of heat exchanger equipment or to enhance the capacity of existing units. The main types of turbulent promoters for heat exchanger applications are the twisted tapes [35], winglets tapes [36] circular rings [37], baffles [38], helical inserts [39] and coil-wires [40]. Table 1.2 shows a selection of the most classical geometries of turbulence promoters, that exhibit high thermal performance and low pressure drop.

Table 1.2: Performance of heat exchanger processes using turbulence promoters from literature compared to classical heat exchangers.

Authors	Working fluid	Turbulence promoters	Heat transfer performance improvement compared to the straight pipe
Bhuiya et al. (2013) [35]	Air, turbulent flow	Perforated twisted tape	450%
Eiamsa-ard et al. (2013) [41]	Air, turbulent flow	Circular-rings and twisted tapes	450%
Bhuiya et al. (2012) [39]	Air, turbulent flow	Triple helical tape insert	450%
Murugesan et al. (2011) [42]	Water, turbulent flow	V-Cuttwisted tape	250%
Chingtuaythong al.(2017) [37]	Air, turbulent flow	V-Shappedrings	450%

1.4.3 Rough walls

1.4.3.1 Rough walls in membrane separation

Roughness is a limiting case of parietal turbulence promoters. The term here denotes protuberances of small thickness, comparable to the thickness of hydrodynamic and mass boundary layers. Filter media, membrane or not, are rough. Roughness is usually undergone but sometimes chosen. In addition, the deposition of particles is not uniform and induces additional roughness, varying during the accumulation. According to Winzeler & Belfort (1993) [43], the presence of roughness generates local instabilities and flow instationnarity contributing to mixing. However, the axial velocities near the wall and the intensity of the vortices created are low. Broussous et al. (2000) [44] used microfiltration membranes printed with a helical relief and obtained a permeate flux value 1.7 times higher than the smooth membrane, Figure 1.8. Regarding the effect of roughness on the intensity of the filtration rate,

opinions also differ. Some observe a rate increase due to roughness [45].

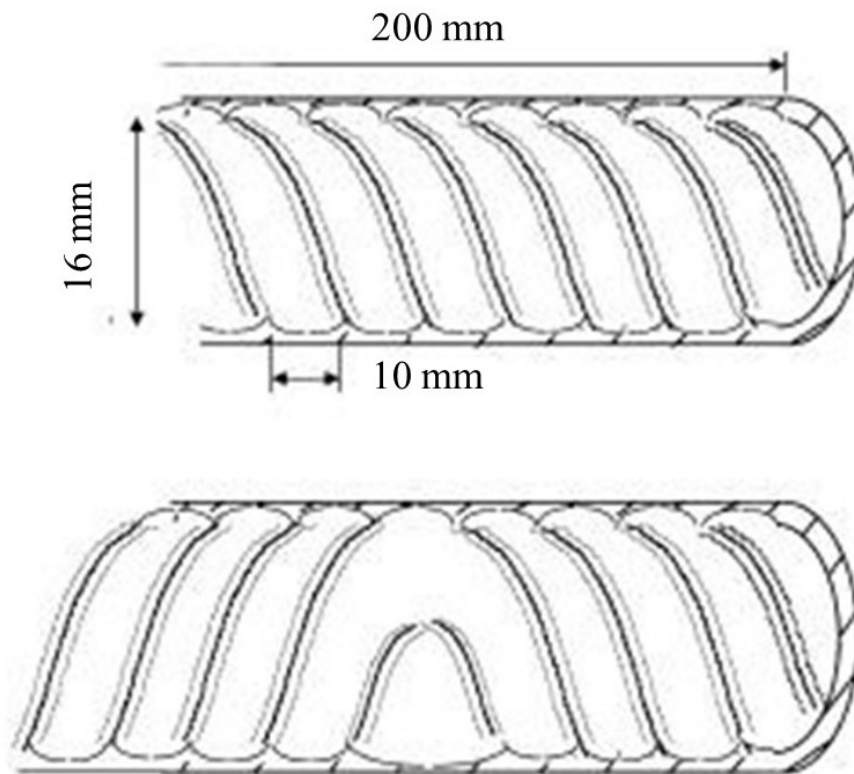


Figure 1.8: Membrane printed with a helical relief [44]

1.4.3.2 Rough walls in heat exchanger

One of the efficient techniques to enhance heat transfer is wall roughness. Numerous roughness geometries have been investigated in the past and their performance on the heat transfer and friction characteristics have been evaluated. Artificial roughness is provided in the form of different geometries such as ribs, dimple shape roughness, wire mesh, baffles, delta winglets etc. Figure 1.9 shows a selection of the roughness configurations used in heat transfer applications in the literature.

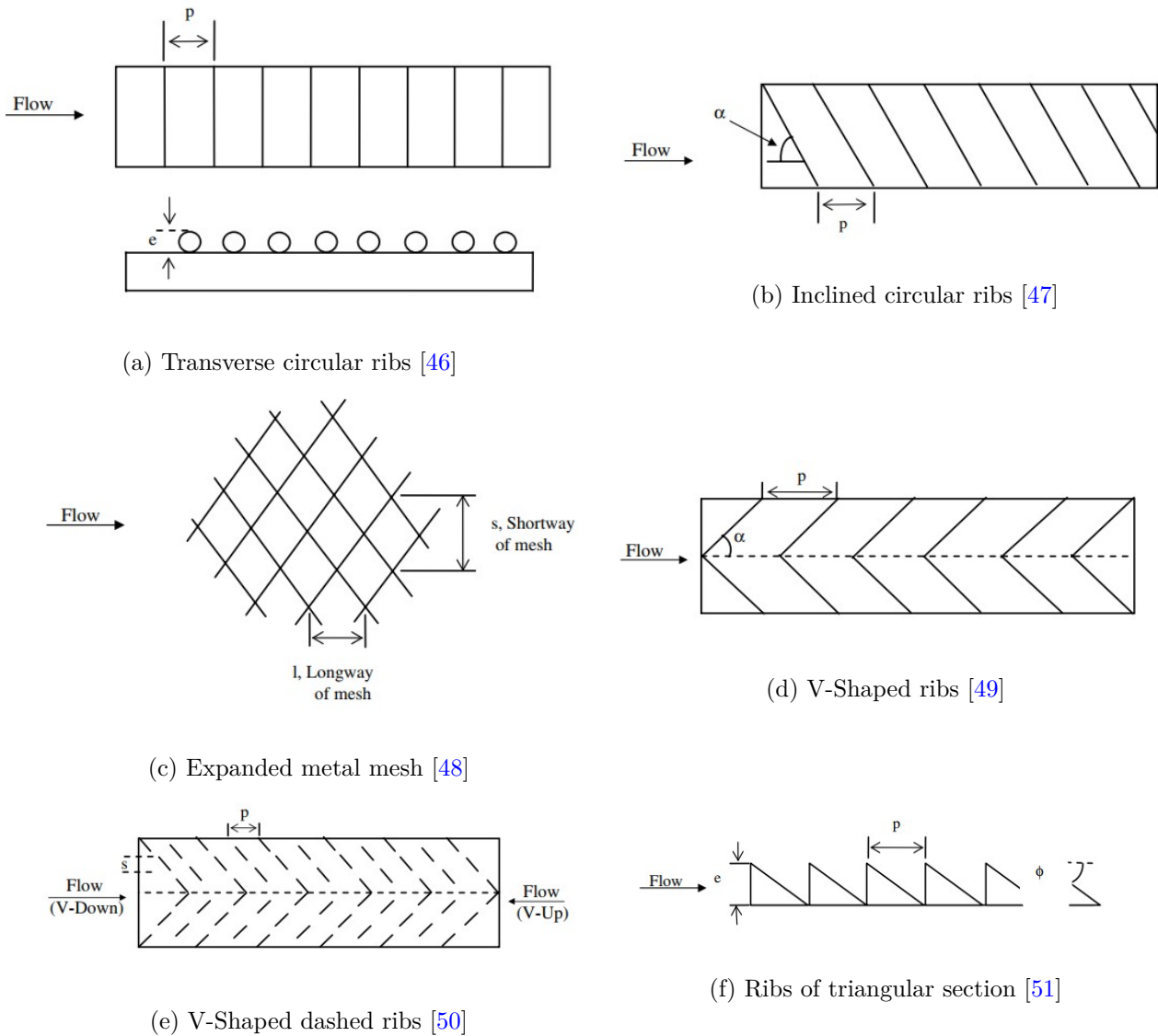


Figure 1.9: Different roughness geometries used in heat exchanger

1.4.4 Pulsate flow

1.4.4.1 Pulsate flow in membrane separation

Another technique to generate an unsteady flow, which is favourable to mixing, is to pulsate the flow within the filtration module. For this, the flow rate or alternatively the pressure at the inlet or one of the filter outlets is periodically varied [17]. The oscillation of the resulting flow produces [52]:

- An increase in the parietal shear stress that limits the accumulation of particles on the membrane.
- Lift forces on particles tending to move them away from the wall, Figure 1.10.
- Mixing intensification decreasing the concentrations of solutes or particles in the filtering wall.
- An oscillation of the interfaces in the case of fluid-fluid two-phase flows, which contributes to unclogging the pores of the filtering wall.

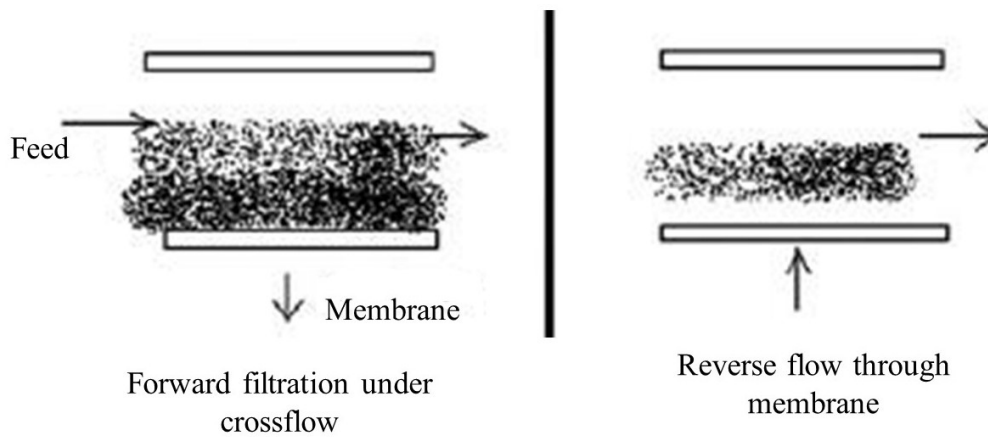


Figure 1.10: Effect of an oscillation of the flow [53] (Left) Direct flow. (Right) Reverse flow

Several studies have varied the feed rate of the filter [54]. In the experimental studies of Arroyo & Fonade (1993) [55] and Maranges & Fonade (1997) [56], part of the mixture was fed into the filter with intermittent jets. Some authors periodically stopped the flow of filtrate while maintaining a constant feed rate [57]. This technique has been used in microfiltration of particles, cells or droplets [34], in ultrafiltration of proteins [58] and desalination by reverse osmosis [59].

Other authors have investigated the impact of a variation of the filtrate outlet rate. When this flow becomes negative or in an equivalent way when the transmembrane pressure becomes negative, it is called backpulsing, backflushing, backwashing or backshocking [60]. During backwashing, filtrate is returned through the membrane, which dislodges particles clogging the wall. Backwashing usually takes less than one second and is repeated periodically at intervals of a few seconds [61]. The simply deposited particles are removed but the adsorbed particles must be peeled off by chemical means [62]. Backwashing was mainly applied to microfiltration of particles, cells or droplets [63], more rarely to ultrafiltration [60], and reverse osmosis [53]. Finally, researchers made a synchronized variation in feed rate and filtrate flow, in order to impose a uniform transmembrane pressure on the entire membrane [64]. Several studies are cited in Table 1.3, with their characteristics and performances.

Table 1.3: Membrane process performance with pulsed flow. MF: microfiltration. RO: reverse osmosis.

Authors	Process	Geometry	Frequency	Performance : increase in average permeate flow
Kennedy et al. (1974) [65]	RO sucrose solution	Tubular	Pulsation of the feed rate at 1Hz	70%
Blanpainet et al. (1999) [66]	MF beer	Tubular	Pulsation of the feed rate at 1Hz	100%
Gomaa & Sabouni (2014) [34]	MF yeast	Plane	Pulsation of the supply flow of 0.25 Hz	100%
Amar et al. (1999) [67]	MF of apple juice	Tubular	Backwashing for 2-5s every 3-5 min	50%
Sondhi & Bhave (2001) [62]	MF of yeasts or droplets	Tubular	Backwashing for 0.5s every 30 sec	100 to 400%
Ma et al. (2000) [68]	MF Escherichia Coli	Tubular	Backpulse for 0.1-0.5 sec every 2-14 sec	160%

1.4.4.2 Pulsate flow in heat exchanger

Pulsate flow is one of the heat transfer enhancement techniques, which tends to increase the heat transfer by disturbing and/or breaking the thermal layer. Some studies analyzed compounds technique involving pulsating flow and asymmetric and symmetric channel [69], grooved channel [70], corrugated channel [71], nanoparticles [72]. Because of the alternate expansion and shrinkage achieved by pulsations, vortices are created [72]. These vortices are generated, grow, expand and are ejected during deceleration phase [69]. In addition, during the acceleration phase, they shrink. By increasing the frequency of the pulsation, the vortex strength is augmented. However, above a certain frequency, heat transfer enhancement decreases due to viscous effects [69]. According to some investigations on inline flow pulsation (cited by [73]), the optimal frequency to increase heat transfer coefficient is twice the natural vibration frequency of the test tube. Table 1.4 mentions the studies which used the pulsed technique to increase heat transfer in heat exchanger applications.

Table 1.4: Performance of heat exchanger processes using pulsed flow from literature compared to classical heat exchangers

Authors	Working fluid	Technique	Heat transfer performance increase
Nandi & Chattopadhyay (2013) [74]	Water, laminar flow	Pulsating flow	100-150%
Selimefendigil & Oztop (2014) [75]	Water with Al_2O_3 nanoparticles, laminar flow	Pulsating flow	120%
Wantha (2016) [73]	Air, laminar flow	Pulsating flow	100-170%
Jin et al. (2007) [70]	Water, laminar flow	Pulsating flow specific tube shape	100-350%
Jafari et al. (2013) [71]	Water, laminar flow	Pulsating flow with corrugated channel	100-120%
Akdag et al. (2014) [72]	Nanofluid, laminar flow	Pulsating flow, nanoparticles	125-310%

1.4.5 Vibrating system in membrane separation

An efficient way to fight concentration polarization is to vibrate the filter membranes. The vibration of the membrane produces a periodic variation of the flow, as it is the case for the Pulsate flows described in paragraph 1.4.4.1. The same mechanisms then work to counter the concentration polarization. Indeed, vibrations produce a shear field that allows operating at lower feed rates and transmembrane pressures [76]. The effect of vibration-induced shear on filtration performance has been reported by

Genkin et al. (2006) [77], Akoum et al. (2002) [78] and Beier et al. (2006) [79]. It induces an efficient mixture as shown for microfluidic systems [80]. Acoustic micromixers, involving high vibration frequencies, have been developed [81]. Unlike rotating systems, vibrating systems can withstand high pressures, up to 40 bar for VESP (Vibratory Shear-Enhanced Processing), necessary for nanofiltration and reverse osmosis [76]. Vibrating membranes are used in biotechnology and pharmacy [82] for the filtration of fermentation broths intended to separate yeasts or bovine serum albumin (BSA). They are also used in the food industry [83], largely for the separation of milk components. They are finally found in the field of water treatment [84] where they are used for desalination, removal of dissolved organic matter, filtration of algae [85]. Typical performances of the vibrating membrane processes are given in Table 1.5.

Table 1.5: Performance of membrane processes with vibrating membranes. MF: microfiltration.

Authors	Process	Geometry	Direction of vibration	Frequency	Performance : increased permeate flow
Slater et al. (2015) [85]	MF of an algae suspension	VSEP	Oscillations of the membrane	54.6Hz	390% compared to VESP used in static mode
Gomaa et al. (2011) [86]	MF yeast	Plane	Parallel to the membrane	6-18 Hz	200% compared to static case
Krantz et al. (1997) [87]	Absorption of O_2 by water	Tubular	Parallel to the tube	<25Hz	165% compared to static case
Genkin et al. (2006) [77]	MF yeast	Submerged hollow fibers	Parallel and transverse combined	10Hz	100% compared to the axial vibration alone

1.4.6 Ultrasound

1.4.6.1 Ultrasound in membrane separation

Ultrasounds are acoustic waves, which are localized pressure oscillations that propagate in waveform, at high frequencies, greater than 20 kHz. Ultrasound is a limiting case of the vibrating membrane technique. They are generated by high frequency vibrating transducers. Ultrasound is often used to clean membranes when the process is stopped, [88], but they can also be used during filtration to limit concentration polarization [89]. Ultrasound can be generated outside the filtration module, for example in ultrasonic baths, but in this case additional energy must be provided to compensate for the attenuation of the waves when passing through the walls of the module, [89]. For this reason, some authors have generated ultrasound inside the filtration modules, near the membranes [90]. Ultrasonic

waves have several effects: cavitation, microjets, acoustic micro-flow and acoustic flow [91]. The main effect is cavitation, the appearance of bubbles (empty or filled with gas or steam) under the effect of a local and transient pressure drop. It takes place for sufficiently energetic ultrasonic waves of frequencies ranging from 20 to 1000 kHz. The size of the cavitation bubbles is between 1 and 200 microns. The implosion of the bubbles generates hot spots with local temperatures of the order of 5000 K and pressures close to 150 MPa and produces shock waves [92]. The collapse of a cavitation bubble near a wall is asymmetric and causes an asymmetric influx of liquid to fill the void, in the form of a high velocity jet, about 100 m / s, directed against the wall, Figure 1.11a. These microjets make it possible to detach very efficiently the particles deposited on the filtering wall. On the other hand, they can prove to be aggressive for the filtering medium. In addition, before imploding, the cavitation bubbles see their diameter oscillate at the same frequency as the pressure waves, which induces a flow of radial liquid alternately incoming and outgoing around the bubble, Figure 1.11b. This phenomenon is called acoustic micro-flow and causes a detachment of the particles. Finally, ultrasound causes turbulence, called acoustic flow, which plays a role in the removal of floating particles. Lower ultrasonic frequencies

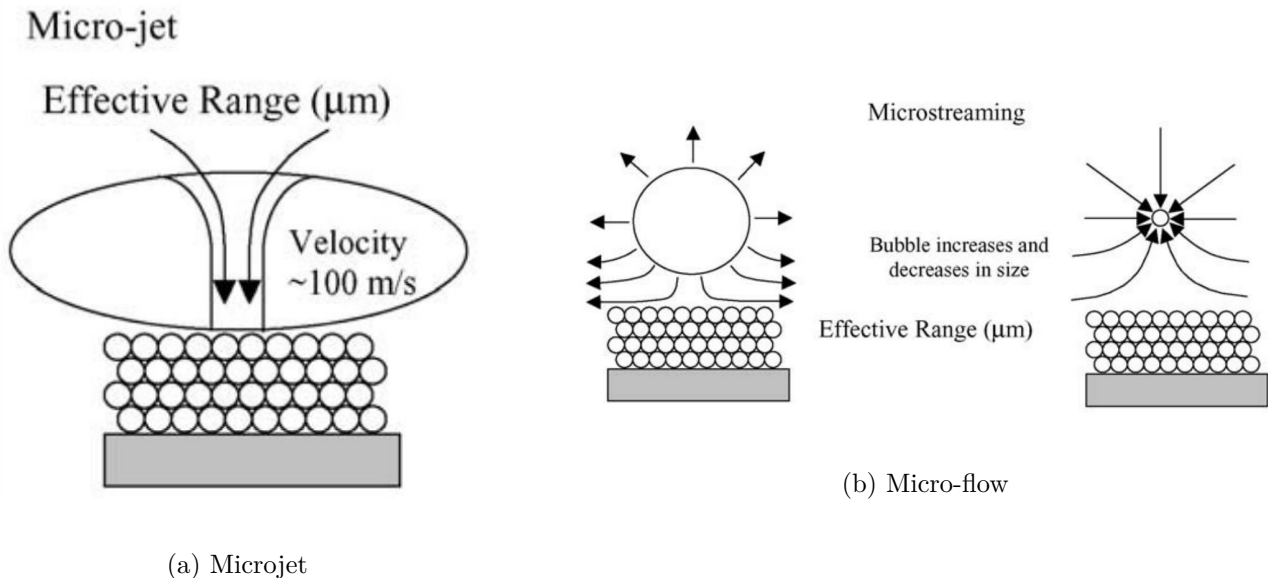


Figure 1.11: Ultrasonic particle detachment mechanisms [93]

(slightly above 20 kHz) are more efficient than higher frequencies [94]. If there are more cavitation bubbles at high frequencies, they are smaller and less energetic. Their collapse releases less energy and is less efficient in detaching particles. Ultrasonic assisted filtration has been used in microfiltration to filter yeasts [95], in ultrafiltration (dextran [96], peptone [97] and polymers in solution [98]), in reverse osmosis [88] and in membrane distillation [99]. Table 1.6 gives examples of performances obtained thanks to ultrasound to fight against clogging and polarization.

Table 1.6: Performance obtained by ultrasonic exposure of filtration modules. US: ultrasound; MF: microfiltration; UF: ultrafiltration.

Authors	Process	Geometry	Frequency	Performance : increased permeate flow
Chai et al. (1998) [100]	UF of a dextran solution	Flat membrane Bath at US	45 kHz	300%
Muthukumaran et al. (2005) [101]	UF of whey	Flat membrane Bath at US	50 kHz	70%
Kyllönen et al. (2006) [93]	UF and MF industrial effluents	Flat membrane US transmitter inside the filtration module	27-200 kHz	400%

1.4.6.2 Ultrasound and vibration systems in heat exchanger

One of the techniques to enhance heat transfer is to use a vibration system while the fluid is subject to natural convection or forced convection [102]. The vibration technique can be divided according to the vibration source:

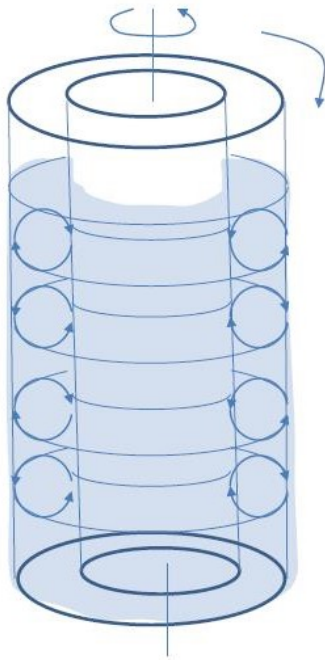
- Mechanical vibration: periodical movement of a membrane -or the heated surface- induce turbulences in the fluid.
- Acoustic vibration: acoustic waves are generated and travel through the fluid.

These two categories share the same physical mechanism: vibration creates an oscillating relative velocity vector between the heated surface and the fluid, leading to heat transfer enhancement [102]. Regarding mechanical vibration, the “synthetic jet” technology is the most spread one. It relies on the forced flow of a fluid through a tiny orifice on the apparatus wall. This forced flow is generated by a diaphragm, which alternately suck and eject the fluid through the orifice (also called sometimes “cavity”) [103]. This technology has been analysed numerically [104] and experimentally with the use of a speaker acting as the moving diaphragm [105]. The characteristics of the orifice has a great influence on heat transfer enhancement (the hydraulic diameter as well as its shape). In fact, it seems that a square orifice gives the best heat transfer enhancement [105]. On the contrary, the cavity depth has a negligible effect on the heat transfer [105]. Regarding acoustic vibration, heat transfer is enhanced due to the violent motion of the bubbles created by cavitation [103]. Some studies also suggest that heat transfer enhancement may also be due to the creation of a stirring motion in the water at a microscale [106]. Others argue that the formation of “jet-flow” bundle (created by the collapsing asymmetry of cavitation bubbles) may enhance fluid mixing and destroy thermal layer [107].

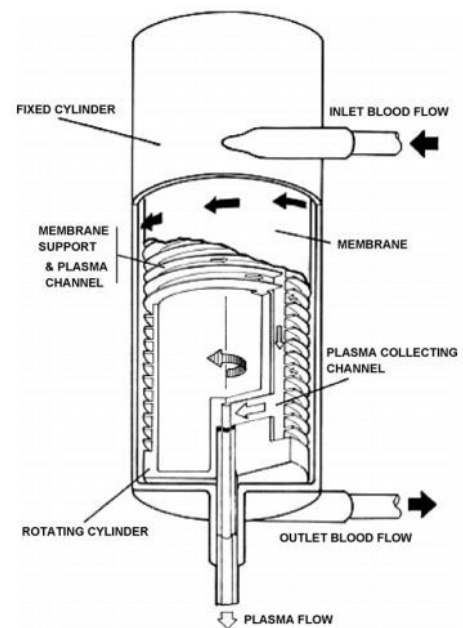
1.4.7 Rotary systems

1.4.7.1 Rotary systems in membrane separation

One of the main types of rotary systems can be found is rotating cylinder systems [76]. The rotating cylinders produce modified Taylor-Couette flows. Taylor-Couette flow [108] is the flow in the annular space between two concentric rotating cylinders, Figure 1.12. For a given external cylinder rotation speed ω_2 , there is a minimum rotation speed of the inner cylinder ω_{1c} beyond which recirculations appear, called Taylor vortices. These vortices are the result of a hydrodynamic instability. Depending on the rotational speed of the outer cylinder, they can be closed, torus-shaped, or open spirally wound around the inner cylinder [109]. It is when the outer cylinder is fixed, $\omega_2 = 0$, that one can generate Taylor vortices at lowest cost because the speed ω_{1c} at which rolls appear is then the lowest. In this case, the vortices are toroidal [109]. The toroidal recirculations generate shear and mixing. This is why a filtration device has been created, taking advantage of Taylor vortices. In this application, the inner cylinder is composed of a porous or dense membrane. The suspension is injected at the top of the annular space and travels down to the outlet, at the bottom. During the descent, liquid passes through the filter wall and the suspension (or solution) becomes more concentrated. In some cases, the outer cylinder is also porous. When the inner wall rotates fast enough, Taylor vortices appear. They circulate the particles and tend to homogenize their concentration in the suspension and to limit their deposition at the filtering wall. Rotary cylinder filters have been used to filter droplets [110],



(a) Taylor rolls



(b) Cylindrical rotary filter

Figure 1.12: The rotary systems models [76]

cells [111], or particles [112]. They are found in ultrafiltration of protein solutions [113] and reverse osmosis water treatment, [114]. However, their wider application is the filtration of blood [115]. They are limited in size, which limits their industrial use [76].

1.4.7.2 Rotary systems in heat exchanger

The rotary systems are expected to create tangential velocity or swirling flow, which enhance heat transfer. In addition, thanks to the tangential and radial modifications on the fluid velocity, they increase turbulence near the walls of the heat exchangers. Table 1.7 exposes the studies which use the rotary system as a heat transfer enhancement technique.

Table 1.7: Performance of heat exchanger processes using rotary systems from literature compared to classical heat exchangers

Authors	Working fluid	Technique	Heat transfer performance increase
Gardiner & Sabersky (1978) [116]	Water, laminar and turbulent flow	Rotating cylinder	100-400%
Fénot et al. (2013) [117]	Air, turbulent flow	Rotating cylinder	100-130%
Shirejini et al. (2016) [118]	Nanofluid, laminar flow	Rotating cylinder	107-132%
Duangthongsuk & Wongwises (2013) [119]	Water, turbulent flow	Rotating turbine	100-170%

1.4.8 Gas sparging

1.4.8.1 Gas sparging in membrane separation

Gas may be injected to aerate processes as in membrane bioreactors employed for water treatment (Membrane Bioreactors MBR) [120]. Gas injection can be used during filter cleaning phases [121]. It can also take place during filtration or membrane separation, for purely hydrodynamic reasons, without participating in the reactions [122]. The first studies date back to the late 1980s with Imasaka et al. (1988) [123], who performed methane injections in a microfiltration module and found an intensification of flux for low energy consumption [124]. In subsequent studies and applications, air was mainly used. The bubbling technique has thus been applied to the micro and ultrafiltration of water [130], solutions of macromolecules such as dextran, proteins (lysozyme, human and bovine serum albumin, Immunoglobulin G) [131], or suspensions of cells or microparticles (yeasts, clays, silicone particles, droplets) [132]. Very recently, it was applied to membrane distillation [129] and reverse osmosis desalination [133]. The various experiments have concluded that the permeation flow increases significantly. A selection of results is given in Table 1.8. Several two-phase flow regimes may

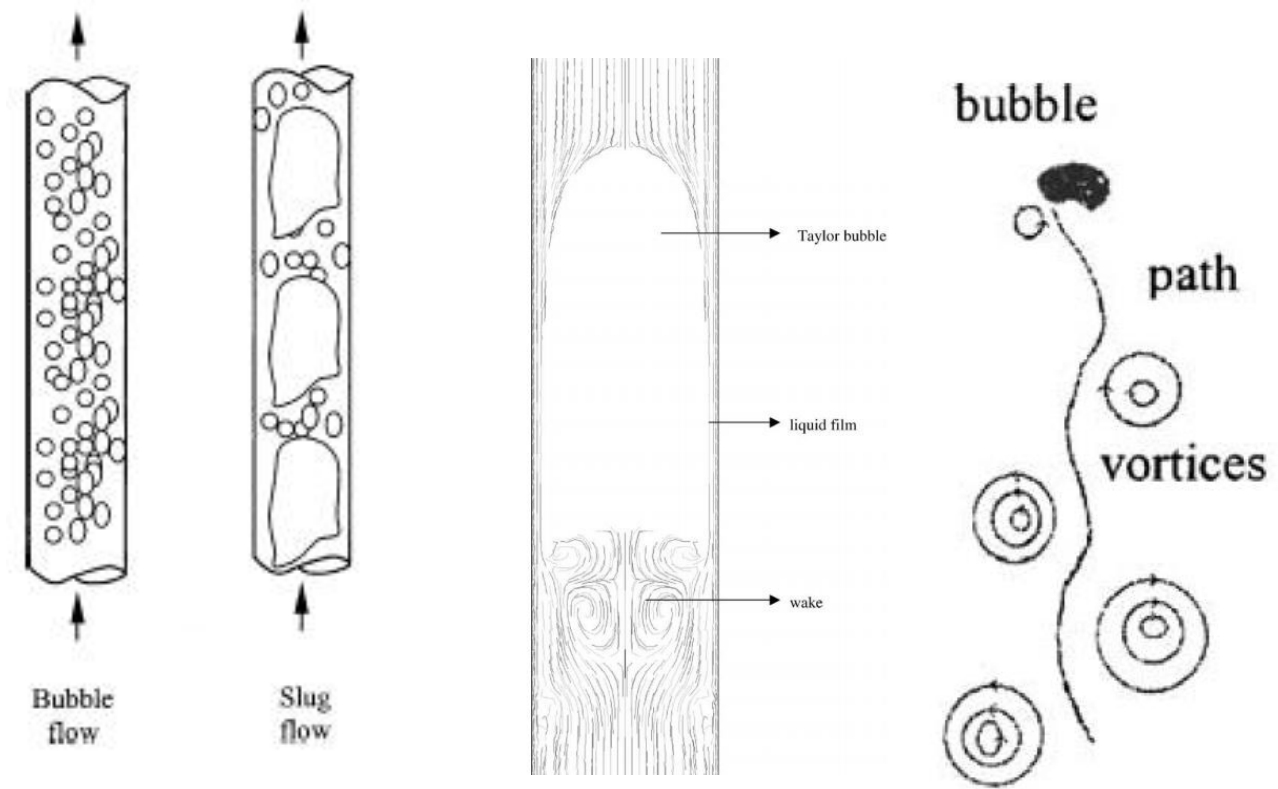
Table 1.8: Performance of filtration processes intensified by air injection. MF: microfiltration; UF: ultrafiltration

Authors	Process	Geometry	Performance : increased permeate flow
Cui et al. (1996) [125]	UF of a dextran solution	Vertical tubular membrane	320%
Mercier et al. (2000) [126]	MF of a suspension of yeasts	Membrane plane	300%
Cabassud et al. (1997) [127]	MF of a clay suspension	Hollow fibers	200%
Cheng et al. (1999) [128]	UF of a dextran solution	Inclined tubular membrane	200%
Chunrui et al. (2011) [129]	Membrane distillation	Hollow fibers	80%

exist in a vertical pipe, depending on the relative velocities of gas and liquid: bubble, plug, broth, annular, [134]. The desired regimes for bubbling are the bubble regime (bubbles smaller than the diameter of the pipe) and even more the plug regime (large bubbles invading the entire width of the pipe), Figure 1.13a. In most cases, the gas flow rates are considerably lower than the liquid flow rates, and the bubbles are in the form of plugs. The efficiency of bubbling depends on the nature of the species to be separated (particles). Bubbles have several effects:

- They induce on their way secondary flows and a wake that disturbs the mass boundary layer and generates mixing near the membrane, [135], Figure 1.13b and 1.13c.
- The plugs strongly reduce the section crossed by the liquid, which produces acceleration and induces significant mixing shear [136].
- The plugs penetrate partially into the liquid boundary layer and produce a displacement of accumulated species [137].
- The plug flow causes pressure surges, which have the same consequences as a flow pulsation [135].

The effect of the filtration module orientation with respect to the vertical on the efficiency of the gas injection was tested [139]. Other things being equal, a vertical orientation of the tube (vertical flow of the liquid) is more efficient than a horizontal orientation (horizontal flow of the liquid). In addition, when the orientation of the tube is vertical, downward flow of the liquid gives better results than upwards flow. An inclination of 50° to the horizontal would give the best results. To reduce the phenomenon of polarization near membranes, some authors have considered introducing solid particles into the solutions in order to produce additional shear [140]. However, this solution is likely to cause clogging and erosion of the membrane and requires an additional step of separation of the



(a) Two-phase flow regimes sought for aeration: left bubble regime and right plug regime [135]

(b) Streamlines of liquid flow around a plug [138]

(c) Wake behind a bubble [135]

Figure 1.13: The sparging systems models

solid downstream. Gas injection does not create the same problem because it is easier to separate a gas from a liquid.

1.4.8.2 Sparging in heat exchanger

In this technique, a spray, that is to say liquid droplets generated by a spray dryer (or nozzle), is projected on a heated surface [141]. The droplets spread over the surface and evaporate (phase change also referred as “nucleate boiling” [142]) or form a thin liquid film [141]. The main mechanisms of this technique are nucleate boiling (surface and secondary nuclei), convective heat transfer and direct evaporation [141]. To characterize the heat transferred from the drops, some of the authors refer to the Critical Heat Flux (CHF), which can be considered an efficiency parameter [141], [143]. When the specific heat flux (heat flux divided by the exchange surface) exceeds a critical value, the CHF, nucleate boiling ceases to exist [142]. Above this value, the augmentation of heat transfer is only due to the agitation provided by the impingement of droplet onto the liquid film [142]. Table 1.9 shows the Critical Heat Flux (CHF) obtained in the literature studies.

Table 1.9: Performance of heat exchanger processes using Spray technique from literature

Authors	Working fluid	Technique	Best CHF value (W/cm^2)
Chen et al. (2002) [141]	Water	Spray	945.7
Chen et al. (2004) [142]	Water	Spray	708.1
Estes & Mudawar (1995) [143]	Refrigerant	Spray	160
Li et al. (2006) [144]	Refrigerant	Spray	63
Mudawar & Estes (1996) [145]	Refrigerant	Spray	109
Cheng et al. (2010) [146]	Distilled water	Spray	250
Wang et al. (2010) [147]	Water, laminar flow	Spray	95

1.4.9 Complex shapes

Curved geometry is one of the passive mass/heat transfer enhancement methods that fits several heat transfer applications such as energy, chemical and food industries, environment engineering, etc. Due to their compact structure and to the high heat transfer coefficient they produce, curved tubes have been used as one of the passive heat transfer enhancement techniques and are widely used in various industrial applications.

1.4.9.1 Dean vortices

Dean flow [148] develops in curved pipes or channels. In this geometry, recirculations appear, transverse to the average flow, Figure 1.14. These recirculations, called Dean Vortices [149]. In toroidal pipes and bends, a pair of symmetric counter-rotating vortices called Dean cells appears superimposed to the axial flow, Figure 1.14a. In the case of helical pipes, Dean-type cells also develop, but their symmetry is broken due to torsion effects (Figure 1.14b). The secondary flow generated by Dean vortices leads to additional mixing and thus to enhanced transfer. This is why curved geometries are widely used in industrial processes and other applications, in particular for:

- Heat transfer enhancement. Helically coiled heat exchangers are commonly encountered in anaerobic digesters [150], refrigeration systems [151], power plants and nuclear reactors [152] among many other applications.
- Mass transfer enhancement in catalytic reactors [153], dense [154] and porous [155] membrane contactors, etc.
- Fouling and clogging reduction in filtration membranes [156].

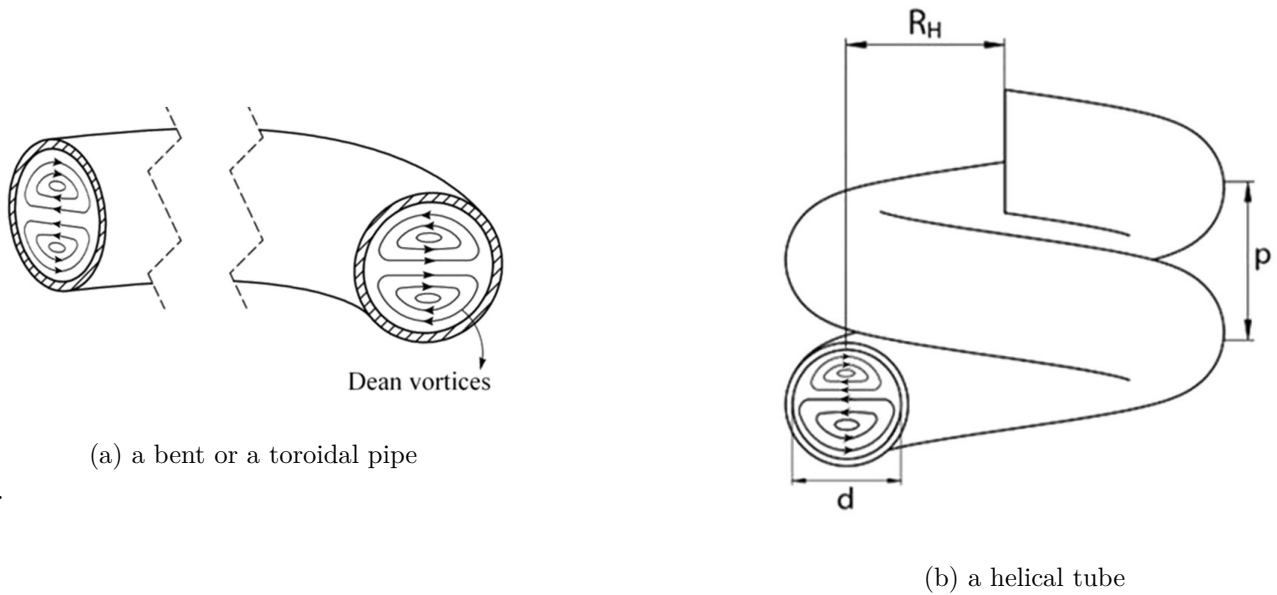


Figure 1.14: Schematic representation of Dean cells

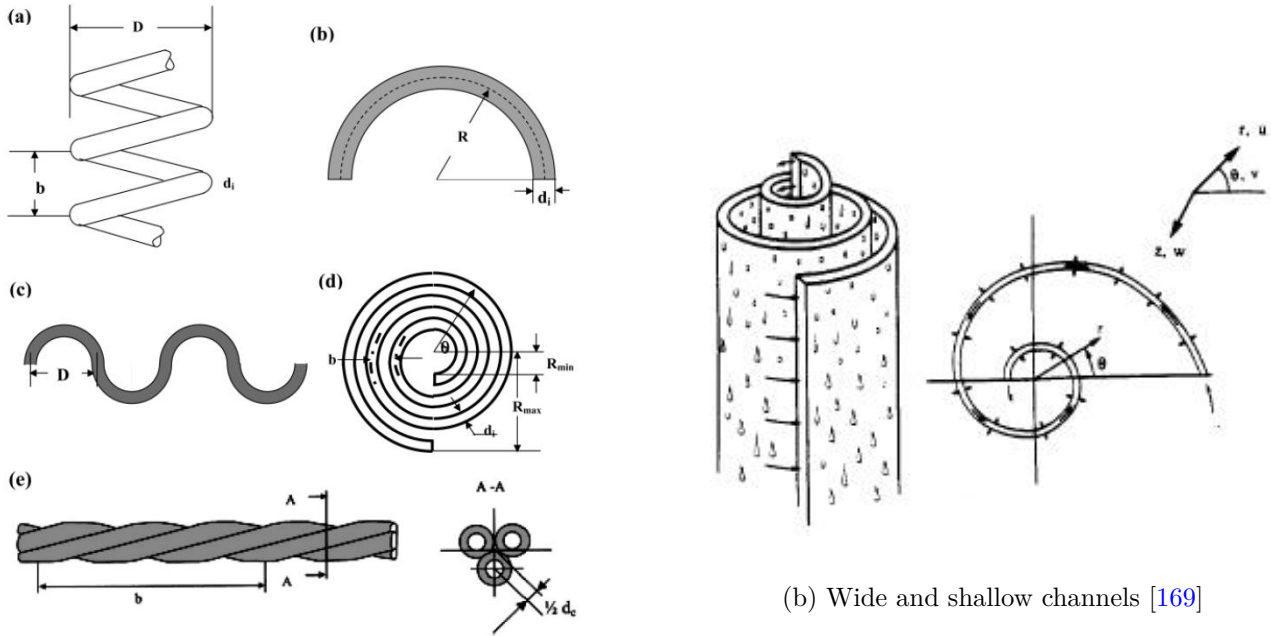
- Improvement of mixing efficiency and homogenization [157].

Several studies [158] have shown that heat and mass transfer rates are improved when the intensity of the secondary flow increases. Furthermore, at high Dean numbers, heat transfer coefficients in the thermally fully developed region are higher in a coiled tube than in a straight tube by a factor which varies as $\sqrt{De_{RH}}$ [158].

1.4.9.2 Dean flow in membrane separation

Dean flow has been used in membrane processes since the 1960s to increase transfer in blood oxygenators [159]. It is also found in reverse osmosis processes [160]. Several curved channel geometries have been considered in the literature, Figure 1.15a. In the case of channels of large width compared to their thickness, Dean Vortices appear beyond a minimum flow velocity, under the effect of instability. In the case of curved tubes, Dean Vortices appear as soon as the flow velocity is non-zero, even if they are of low intensity at low speed. The simplest geometry is the tube (or channel) describing a portion of a circle [160], a bend [161] or a U [162], Figure 1.15a (b). Tubes with circular or square section [163] were used. These geometries have allowed theoretical studies and experiments at the laboratory scale, but they do not allow developing large areas of filtration. Some studies can also be found on semicircular section tubes, coiled and plated on a flat membrane [164], Figure 1.15a (d). However, the most studied geometry is the helical tube [116], Figure 1.15a (a). Bolinder & Sunden (1995) [165] was interested in a helical tube of square section. It should be noted that semi-industrial versions exist in the form of woven hollow fibers [166] or twisted fibers [167], Figure 1.15a (e). Moulin et al. (1996) [168] investigated numerically and experimentally the effects of Dean vortices on mass transfer in the case of an oxygenation operation under laminar flow conditions. Their results revealed

that mass transfer in the helical geometries is improved by a factor 2 to 4 compared to the case of a straight tube. Finally, the flow in spiral channels, of small thickness compared to their width, (geometry similar to that of spiral modules described in section 1.1.3, but without spacers) has been modeled [169], Figure 1.15b. These complex shapes have been little used on an industrial scale because



(a) Curved tubes [170]

(b) Wide and shallow channels [169]

Figure 1.15: Curved channels proposed in the literature

they are difficult to manufacture. 3D printing, however, opens very interesting perspectives. They also raise a problem of space. The separation modules must indeed be compact, and it is more difficult to assemble many complex-shaped fibers than rectilinear fibers. Examples of performance of complex geometries are given in Table 1.10.

1.4.9.3 Dean flow in heat exchanger

Yang and Ebadion (1995) [171] simulated the heat transfer in a helical pipe under fully developed laminar flow conditions. According to their results, obtained at high Prandtl number, the Nusselt number significantly decreases when the helix torsion is increased (i.e. the pitch is decreased). On the other hand, for low Prandtl numbers, the Nusselt number only slightly declines as the torsion increases. Xin and Ebadion (1997) [172] assessed the impacts of the Prandtl number and geometric parameters on the local and average heat transfer efficiency in helical pipes. Five helical channels with various helical diameter, pitch and tube diameter were investigated as well as three working fluids, in addition, they noticed that No obvious effects of the coil pitch or torsion were observed in the scope of his investigation. Datta et al. (2017) [173] studied numerically heat transfer phenomena in the laminar flow through a helical pipe of circular cross-section. The study was performed for three

Table 1.10: Performances of membrane processes of complex form

Authors	Process	Geometry	Performance : increased permeate flow
Ghogomu et al. (2001) [149]	UF colloidal bentonite	Helical fiber S-fiber Twisted fibers	50% compared to the straight case
Moll et al. (2007) [156]	UF of bentonite	Woven fibers	100% compared to the straight case for the same energy supplied
Winzeler & Belfort (1993) [164]	UF of whey	Coiled half-pipe glued on flat membrane	471%

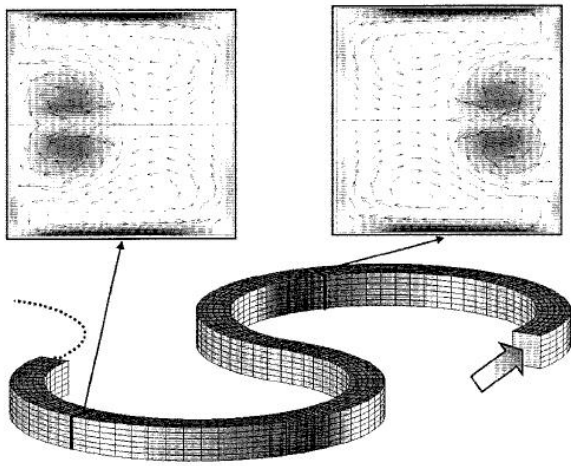
Prandtl numbers, $Pr = 8.5, 7.5$ and 4 , and over a wide range of helix torsion. Their results were in good agreement with experimental data. More numerical and theoretical studies ([174]; [175]) and also experimental studies ([176]) were conducted. For all these studies, either constant wall temperature or constant wall heat flux boundary conditions were enforced. Table 1.11 details some numerical and experimental studies from literature.

1.4.9.4 Alternate direction geometries and chaotic mixing

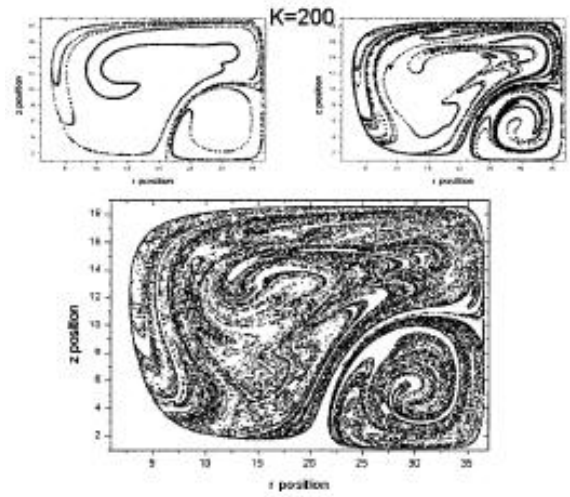
The search for flows even more efficient than the flow of Dean led the researchers to study curved geometries with changes of direction. The S-shaped geometry, a plane geometry with periodic inversion of curvature, Figure 1.16, induces chaotic mixing [186]. It is used on a semi-industrial scale with corrugated hollow fibers obtained by thermoforming [187], [188]. Other geometries with three-dimensional alternating curvatures have been proposed [189], Figure 1.17. They also implement chaotic mixing. This type of geometry can be coupled to a pulsation of the flow [190].

Table 1.11: Numerical and Experimental Studies on Heat Transfer Curved Tubes for Constant wall temperature or Heat Flux

Authors	Conditions	Studies tech- niques	Validity range
Kubair & Kuloor (1966) [177]	Constant wall temperature	Experimental	$80 < Re < 6000$ $20 < Pr < 100$
Schmidt et al. (1967) [176]	Constant wall temperature	Experimental	$1 < De_{RH} < 10$
Dravid et al. (1971) [178]	Constant wall temperature	Experimental	$5 < Pr < 175$ $50 < De_{RH} < 2000$
Yildiz et al. (1997) [179]	Constant wall temperature	Experimental	$Pr = 0.7$ $1265 < De_{RH} < 2850$
Rainieri et al. (2012) [180]	Constant wall temperature	Experimental	$125 < Pr < 280$ $12 < De_{RH} < 280$
Liu & Masliyah (1993) [181]	Constant wall temperature	Numerical	$0.1 < Pr < 500$ $20 < De_{RH} < 5000$
Kirpov (1957) [182]	Constant heat flux	Experimental	$10000 < Re < 45000$
Seban & McLaughlin (1963) [183]	Constant heat flux	Experimental	$2.9 < Pr < 5.7$ $6000 < Re < 65600$
Xin & Ebadion (1997) [172]	Constant heat flux	Experimental	$5000 < Re < 100000$
Moawed (2011) [184]	Constant heat flux	Experimental	$660 < Re < 2300$
Kalb & Seader (1972) [185]	Constant heat flux	Numerical	$0.005 < Pr < 0.05$ $20 < De_{RH} < 1200$

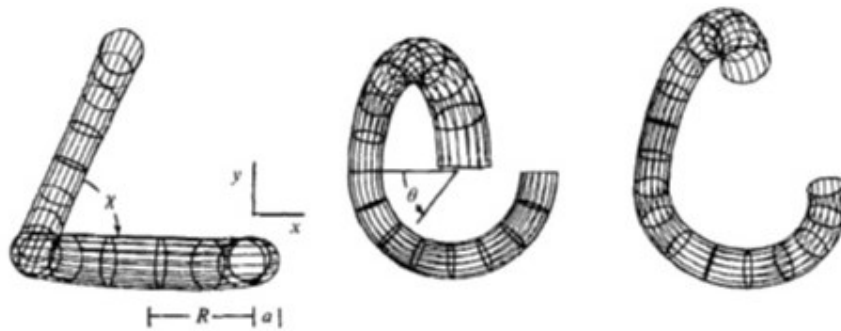


(a) Meandering channel build up from two circular segments with corresponding secondary flow patterns [186]



(b) Interface shapes obtained from particle tracking for $De_{RH}=200$ [186]

Figure 1.16: The S-shaped tube [186]



(a)



(b)

Figure 1.17: Three-dimensional geometry with alternating curvatures [189]

Chapter 2

Laminar flow friction factor in highly curved helical pipes: numerical investigation, predictive correlation and experimental validation using a 3D-printed model*

*This chapter constitutes an extended version of an article that has been published in Chemical Engineering Science.

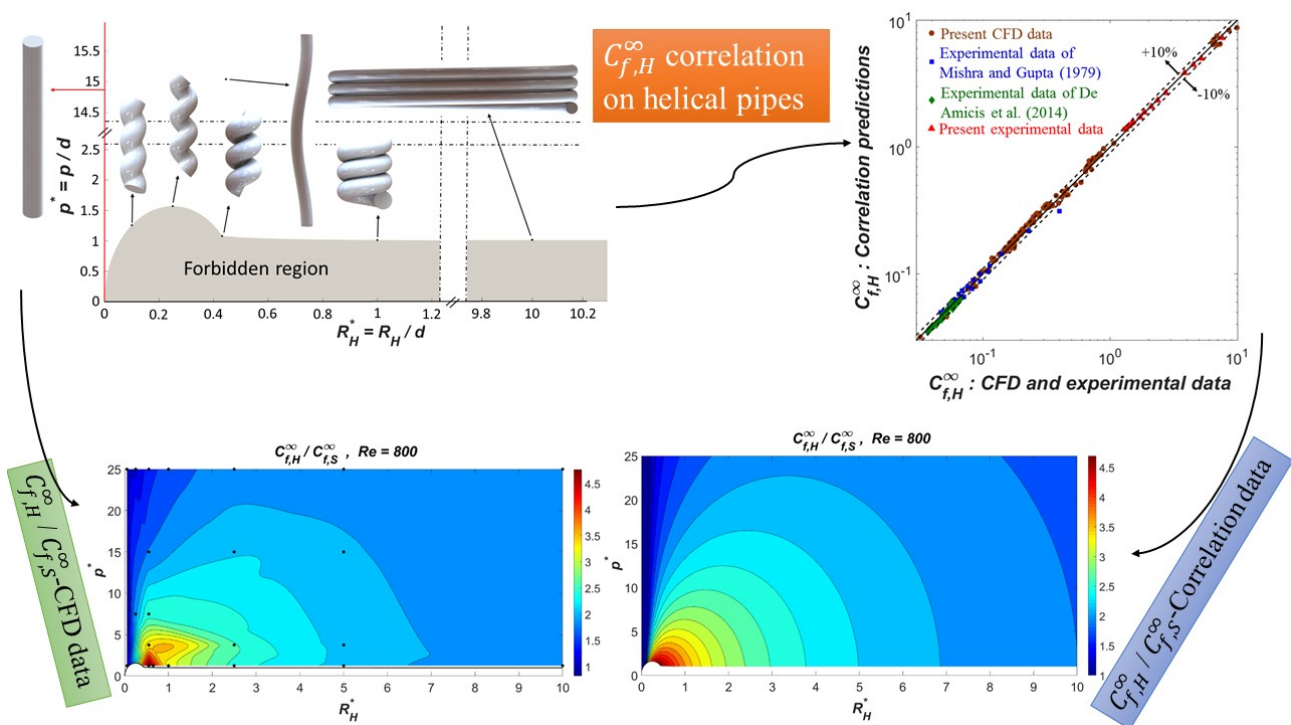
[191] **Omran Abushammala**, Rainier Hreiz, Cecile Lemaitre, Eric Favre. (2019): “Laminar flow friction factor in highly curved helical pipes: Numerical investigation, predictive correlation and experimental validation using a 3D-printed model”, *Chemical Engineering Science*, **207**, 1030-1039.

Background

The first chapter presented the two types of methods used to improve the transfer rate in heat and mass exchangers: active and passive techniques. Active techniques are based on external forces such as pulsed flow, vibration system, etc. to perform the augmentation. They are efficient; however, they are not always easy to implement with the other components in a system. They also increase the total cost of the system manufacturing and maintenance. On the other hand, passive techniques involve special surface geometry. They are easier to operate and generally cheaper than active techniques, and do not interfere with other components in the system. Enhancing heat/mass transfer in heat/mass exchangers is the primary objective, but at the same time, pumping costs should be taken into account (pressure drop or friction factor). Curved geometries are preferred to other enhancement techniques because they perform similarly or even better with lower energy consumption and maintenance cost. Curved pipes performance is due to the Dean-type vortices they generate. However, these secondary flows also induce higher pressure drops compared to straight tubes and so, generate larger specific energy requirements. Literature studies have only addressed heat/mass transfer and pressure drop in moderately curved pipes. The present PhD focuses on highly curved helical pipes, that is to say helical pipes of small helical radius and pitch. As a first approach, CFD simulations were conducted using the commercial code ANSYS Fluent 16. The flow field in different helical pipes was determined by solving the continuity and Navier-Stokes equations in the case of a Newtonian, incompressible, isothermal and steady flow. In order to validate the simulations results, experiments were conducted. A highly curved helical pipe was fabricated using a 3D-printing machine, which was a challenge due to the complexity of the shape. The pressure drop was measured for different flow rates and compared successfully with simulation results. Finally, based on CFD data fitting, a mathematical model for predicting the pressure drop (friction factor) in curved pipes was derived.

Summary

Highly curved helical pipes offer attracting potentialities for intensified mass and/or heat transfer performances as they generate intense Dean-type vortices. However, these secondary flows also induce higher pressure drop compared to straight tubes, and so, generate larger specific energy requirements. Therefore, the evaluation of friction factor in this type of geometries is of major interest in order to rigorously assess, for a given design, the trade-off between the increase of transfer rate (i.e. unit volume reduction of heat and mass exchangers) and the associated specific energy requirement. Unfortunately, in the literature, such data are lacking for highly curved helices, probably due to the difficulty to manufacture these geometries through traditional manufacturing techniques. In this chapter, CFD simulations are carried out for determining the friction factor in helical pipes, particularly highly curved ones. Emphasis is put on the laminar flow regime which is commonly encountered in hollow fiber membranes and micro-structured heat exchanger applications. Various helix designs and a broad range of Reynolds number values are investigated. For an experimental validation of the numerical results, a highly curved helix was built by 3D-printing. Existing correlations are shown to fail for the accurate prediction of the friction factor in highly curved helices. A new correlation is thus proposed. The experimental pressure drop measurements acquired on the 3D-printed model and the proposed correlation predictions are in excellent agreement, the relative error being less than 8% for all the conditions investigated. Moreover, the new correlation is shown to be efficient and predictive as it correctly estimates literature data obtained with geometric and operating conditions beyond those investigated in the chapter (and upon which the correlation was built).



Graphical abstract of Chapter 2

2.1 Introduction

Hydrodynamics in curved pipes is characterized by the occurrence of secondary flows, i.e. recirculations of relatively low magnitude in the cross-stream direction, perpendicularly to the primary flow. In toroidal pipes and bends, they consist of a symmetric pair of counter-rotating vortices known as Dean cells (Figure 2.1a), after Dean (1927, 1928) [192], [193]. In these pioneering papers, Dean derived an analytical solution for the laminar flow hydrodynamics in toroidal pipes which curvature radius is much larger than the pipe diameter. The so-called Dean number, De , is generally used to quantify the intensity of these secondary flows:

$$De = Re \sqrt{\frac{d}{2R}} = \frac{\rho d U}{\mu} \sqrt{\frac{d}{2R}} \quad (2.1)$$

where Re represents the Reynolds number, ρ the fluid density, μ its dynamic viscosity, U the mean velocity of the primary flow, d the internal diameter of the pipe and R the radius of the torus/bend. This dimensionless number is often used as the sole representative parameter in correlations concerning the flow characteristics and the heat and mass transfer efficiencies in curved pipes; indeed, the magnitude of these transport phenomena is strongly correlated to the intensity of Dean vortices.

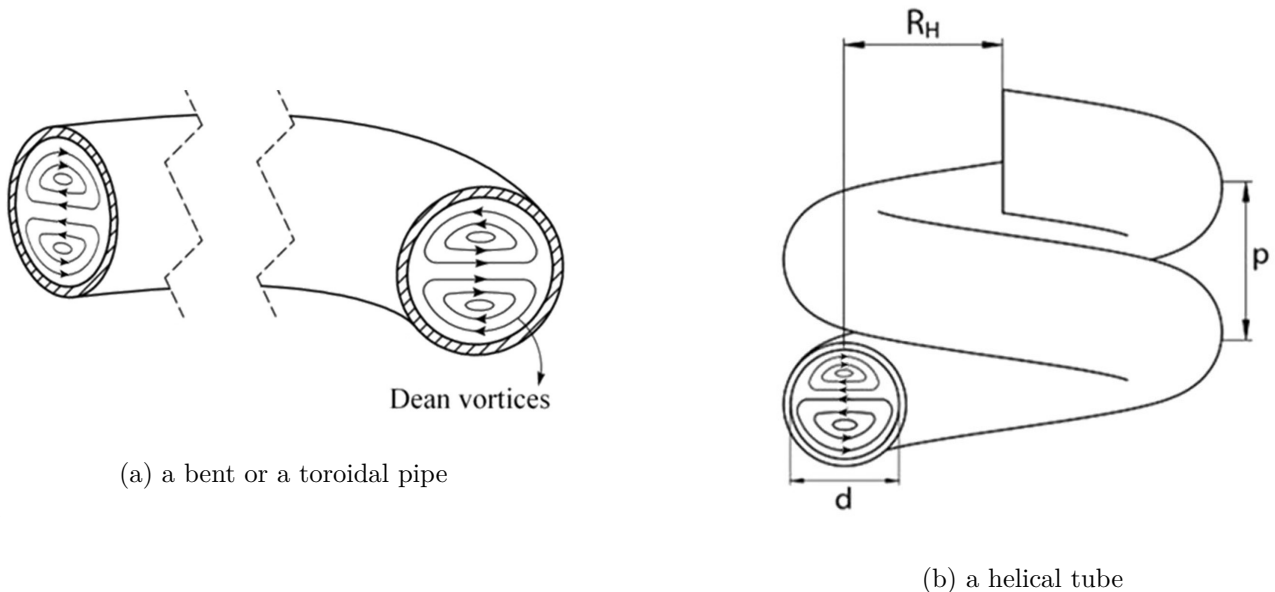


Figure 2.1: Schematic representation of Dean cells

In the case of helical pipes, Dean-type cells still develop, however, their symmetry is broken because of torsion effects. This geometry is widely used in industrial processes and applications where the presence of secondary flows allows reaching much better performance than straight pipes, e.g.:

- Heat transfer enhancement. Helically coiled heat exchangers are commonly encountered in anaerobic digesters [150], refrigeration systems [151], power plants and nuclear reactors [152] among many other applications.

- Mass transfer enhancement in catalytic reactors [153], dense [154] and porous [155] membrane contactors, etc.
- Fouling and clogging reduction in filtration membranes [156].
- Improvement of mixing efficiency and homogenization [157].

Many studies focusing on flow and/or transport phenomena in helical pipes relied upon the Dean number as the sole dimensionless parameter accounting for both flow and geometry effects (see Table 2.1 for example). Most of these authors extended the Dean number definition to helical geometries simply by replacing the pipe curvature radius with the helix radius, R_H , (Figure 2.1b), in the original form (Eq.2.2):

$$De_{R_H} = \frac{\rho d U}{\mu} \sqrt{\frac{d}{2R_H}} = Re \sqrt{\frac{d}{2R_H}} \quad (2.2)$$

However, doing so, the effects of the helix pitch are completely ignored, which may lead to important errors in several situations. Effectively, as discussed later in this chapter, the flow characteristics may substantially vary with the helix pitch, especially in the case of pipes with a small helix radius. On the other hand, some authors adopted a different expression for the Dean number in helical pipes as follows:

$$De_{\gamma} = \frac{\rho d U}{\mu} \sqrt{\frac{d}{2\gamma}} = Re \sqrt{\frac{d\kappa}{2}} = Re \sqrt{\frac{d}{2R_H [1 + (\frac{p}{2\pi R_H})^2]}} \quad (2.3)$$

where γ , κ and p are respectively the radius of curvature, the curvature (i.e. the inverse of γ) and the pitch of the helix. Unlike Eq.2.2, this expression for the Dean number is consistent with the original definition, Eq. 2.1. Indeed, in the case of a torus/bend, the radius, R , and the radius of curvature, γ , are identical. Comparing Equations 2.2 and 2.3, it can be noticed that they lead to significantly different results in the case of geometries with a high pitch to helix radius ratio, as γ becomes much higher than R_H . To the authors' best knowledge, among the studies dealing with friction factor in helical pipes (Table 2.1), only Mishra and Gupta (1979) [194] have based their correlation on the Dean number expression given in Equation 2.3.

Table 2.1: Set of commonly used correlations for predicting the friction factor of fully developed laminar flow in helical pipes. $C_{f,H}^\infty$ and $C_{f,S}^\infty$ correspond to the asymptotic friction factor in helical and straight pipes respectively. $C_{f,S}^\infty$ is equal to $64/Re$ following the Darcy-Weisbach definition which is used in this chapter.

Reference	Correlation	Correlation's validity range according to its authors	Geometry of the pipe(s) with which experiments were conducted
White (1929) [195]	$C_{f,H}^\infty = C_{f,S}^\infty \left\{ 1 - \left[1 - \left(\frac{11.6}{De_{RH}} \right)^{0.45} \right]^{2.2} \right\}^{-1}$	$11.6 \leq De_{RH} \leq 2000$	$7.6 \leq R_H^* \leq 1024$ The range of p^* was not reported.
Mori & Nakayama (1965) [196]	$C_{f,H}^\infty = C_{f,S}^\infty \frac{0.108 De_{RH}^{0.5}}{1 - 3.253 De_{RH}^{0.5}}$	Entire laminar regime when $R_H^* >> 1$	$R_H^* = 80$. The value of p^* was not reported.
Schmidt (1967) [197]	$C_{f,H}^\infty = C_{f,S}^\infty = \left\{ 1 + 0.14 \left(\frac{1}{2R_H^*} \right)^{0.97} Re \left[1 - 0.644 \left(1/2R_H^* \right)^{0.312} \right] \right\}$	Laminar regime with $Re \geq 100$	$2.5 \leq R_H^* \leq 42$ $3 \leq p^* \leq 137$
Srinivasan et al. (1968) [198] (cited by Ali (2001) [199])	$C_{f,H}^\infty = \begin{cases} 128/Re & \text{for } De_{RH} \leq 30 \\ 20.9 De_{RH}^{-0.6} & \text{for } 30 \leq De_{RH} \leq 300 \\ 7.2 De_{RH}^{-0.5} & \text{for } De_{RH} \geq 300 \end{cases}$	Entire laminar regime	$3.7 \leq R_H^* \leq 50.5$ The range of p^* is not reported in [199]
Mishra & Gupta (1979) [194]	$C_{f,H}^\infty = C_{f,S}^\infty \left[1 + 0.033 (\log_{10} De_{RH})^4 \right]$	$1 \leq De_{RH} \leq 3000$	$3.33 \leq R_H^* \leq 167$ $13.8 \leq p^* \leq 172$
Hart et al. [200]	$C_{f,H}^\infty = C_{f,S}^\infty \left[1 + \frac{0.09 De_{RH}^{1.5}}{70 + De_{RH}} \right]$	Entire laminar regime	Not clearly mentioned but seemingly: $p^* = 5.8$, $R_H^* = 14.4$

In order to clarify the reasons why the Dean number definition given in Eq. 2.3 is much more convenient than that of Eq. 2.2, Figures 2.2 and 2.3 should be considered. Figure 2.2 presents the limits of the so-called forbidden region, i.e. the zone in which it is not possible to design helical shapes because the consecutive turns of the helix would intersect/overlap one with/on another. The equation of this frontier has been determined by Przybył and Pierański (2001) [201]. It represents the set of geometric parameters describing closely packed helices, i.e. which pitch cannot be further decreased. Helix designs at some points are also represented at Figure 2.2. They illustrate the fact that the helical pipe geometry tends toward that of a straight tube at three asymptotic limits: (1) when the dimensionless pitch $p^* = p/d$ tends to infinity. (2) when the dimensionless helix radius $R_H^* = R_H/d$ tends to infinity. (3) when the dimensionless helix radius R_H^* tends to zero.

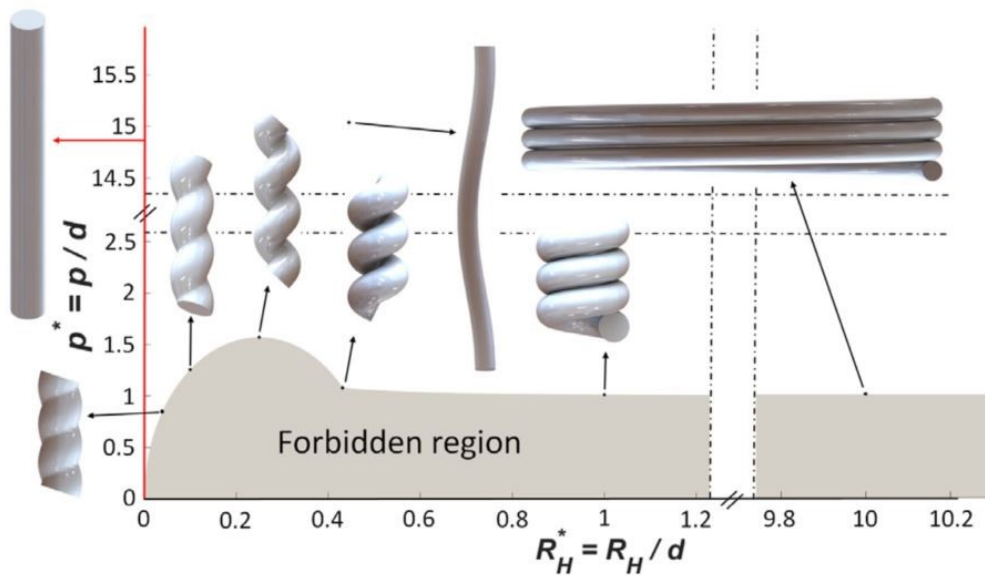


Figure 2.2: Limit of the forbidden region in the (R_H^*, p^*) space (adapted from Przybył and Pierański (2001) [201]) and some representative helix geometries

Figure 2.3 shows the contour plot of the dimensionless helix curvature, $\kappa^* = \kappa \cdot d$, in the (R_H^*, p^*) space. It illustrates the fact that κ^* tends to zero at the abovementioned asymptotic limits, as the helix turns into a straight pipe. Thus, the Dean number as defined by Eq.2.3 vanishes at these limits, which is consistent with the absence of Dean vortices and centrifugal effects in straight pipe flows. On the contrary, the Dean number as defined by Eq.2.2 does not vanish at infinite helix pitches since it does not depend on the pitch value. More importantly, it tends to infinity when the helix radius approaches zero, which corresponds to Dean cells of infinite intensity. Therefore, as proved later in this paper, correlations based on this latter definition lead to systematic errors at low helix radiuses or relatively high helical pitches.

Moreover, Figure 2.3 reveals that the highest curvatures are associated to helices of low pitch and relatively low helical radius. These geometries will be referred to as ‘highly curved helical pipes’ further on in this chapter. They are expected to exhibit the highest centrifugal effects, i.e. the most intense

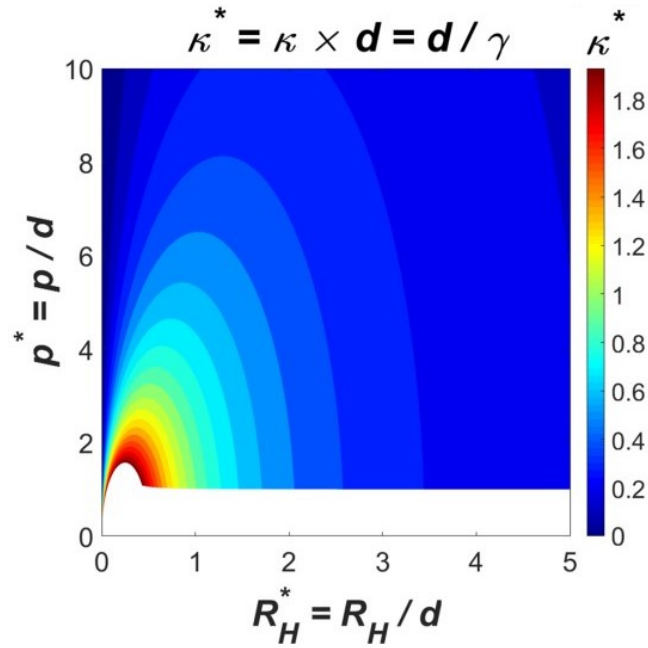


Figure 2.3: Contour plot of the dimensionless helix curvature in the (R_H^*, p^*) space

Dean vortices. Indeed, a CFD (computational fluid dynamics) study (which is detailed in Chapter 3) has confirmed that the mass and/or heat transfer efficiencies in highly curved helical pipes can be an order of magnitude higher than in straight pipes, which makes these designs potentially interesting for heat exchangers and hollow fiber membranes applications [202]. Moreover, their elongated shape allows them to be densely packed (the packing density of helical pipes is addressed in Chapter 3). Thus, highly curved helices enable a great improvement of the overall transfer rates, and thus, allow a great unit volume reduction of heat/mass transfer equipment [202]. It is worthy to underline that classic ‘non-highly’ curved helices may lead to lower volumetric transfer rates than straight tubes as the transfer efficiency improvement can be counterbalanced by the important decrease of the packing density [203]. Nevertheless, to the authors’ knowledge, no other study has investigated yet the hydrodynamics or transport phenomena in highly curved helices. As can be noticed from Table 2.1 for example, literature has focused on helices with a high R_H to d ratio (i.e. R_H^*), probably because these geometries are easier to manufacture using conventional manufacturing techniques. However, nowadays, with the development of additive manufacturing, the elaboration of highly curved helical geometries has become easily achievable. It is noteworthy that 3D printing offers a great potential for improving heat exchangers and membranes designs [204]; [205]. The current study focuses on laminar flow friction factor in highly curved helical pipes: laminar flow is encountered in many applications of practical interest, in particular small-scale devices, e.g. microfluidics, micro-structured heat exchangers and hollow fiber membranes. Although intense Dean vortices in highly curved helices lead to improved heat and mass transfer efficiencies compared to straight pipes, they also induce higher pressure drops and hence greater pumping costs. Therefore, friction factor data in highly curved helices are required so as to be able to compare the provided benefits with the additional operating costs, and therefore,

to assess the usefulness of such designs. In this chapter, a series of CFD simulations are carried out to evaluate the friction factor in helical pipes, particularly highly curved ones. Different operating conditions, described by the Reynolds number, and various helix designs are examined. It is shown that available correlations fail in estimating the friction factor in highly curved helices with a sufficient accuracy. Therefore, a new correlation predicting the friction factor over a wide range of helical pipe geometries and operating conditions is proposed. In order to validate the numerical results, a highly curved helical pipe was 3D-printed and pressure drops measurements are performed over it. The experimental data were in very good agreement with the proposed correlation results. Additionally, the correlation is shown to be robust, efficient and predictive since it correctly estimates experimental data from literature which were obtained under geometric and operating conditions beyond those investigated in the present chapter (and upon which the correlation was built).

2.2 Materials and methods

2.2.1 Friction factor and dimensional analysis

In helical and curved pipes, the wall shear stress and so the local friction factor are not uniform over the pipe wall. In most engineering applications, only the friction coefficient averaged over the pipe circumference is of practical interest (it will be simply referred to as friction factor in the remaining part of this chapter):

$$C_f = \lim_{S \rightarrow 0} \left[\frac{8}{\rho U^2} \frac{1}{S} \int \int t_w dS \right] \quad (2.4)$$

where C_f is the averaged local friction factor (defined after Darcy-Weisbach) at a given longitudinal position, t_w the averaged local wall shear stress and S the surface of a wall annular element sliced over the helix surface (Figure 2.4), and over which t_w and C_f are averaged. Figure 2.5 illustrates a

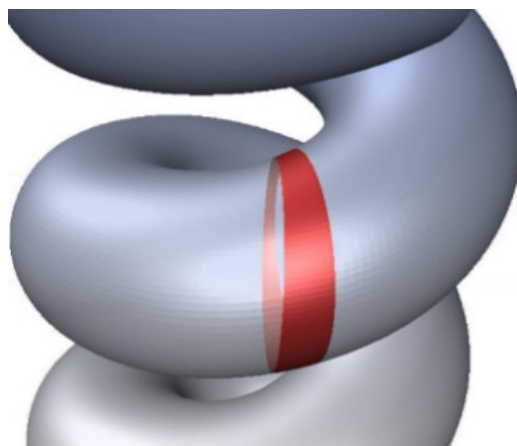


Figure 2.4: Shape of a wall element (in red) over which C_f is averaged

qualitative variation of C_f along a helical or a straight tube, the abscissa axis being the - curvilinear - position along the pipe centerline. The friction factor is the highest at the pipe entrance and decreases

over a relatively short distance called ‘hydrodynamic entrance length’ before reaching an asymptotic value, C_f^∞ . Even though C_f^∞ is lower than the friction factor at the pipe entrance, whenever the pipe is sufficiently long, it gives the largest contribution to the mechanical energy dissipation, the so-called ‘major head losses’. The additional head losses due to the higher friction coefficient at the entrance length are called ‘minor losses’. The effects of minor losses and the hydrodynamic entrance length are generally negligible in the case of pipes of small diameter and/or sufficient length, which is generally the case in the applications targeted in this study, namely heat exchangers and hollow fiber membranes. Therefore, only major losses are addressed in this chapter. Due to the occurrence

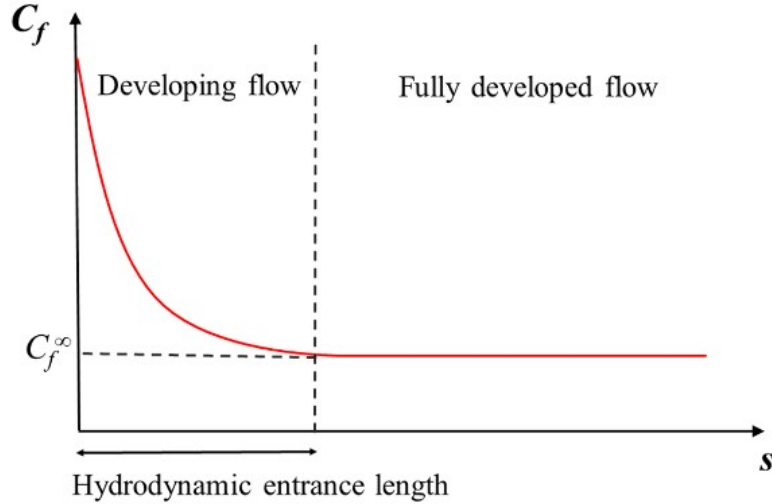


Figure 2.5: Typical variation of the friction factor from the entrance of a straight or a helical pipe

of secondary flows, for a same Reynolds number value, the asymptotic friction factor in helical pipes, $C_{f,H}^\infty$, is higher than that in straight ones, $C_{f,S}^\infty$ (which equals $64/Re$ in the case of a laminar flow). Assuming an incompressible flow under laminar conditions, $C_{f,H}^\infty$ value depends on the pipe internal diameter, d , the helical radius of the helix, R_H , its pitch, p , the fluid density, ρ , its dynamic viscosity, μ , and the mean velocity of the primary flow, U . Therefore, according to the Buckingham π theorem, the following three independent dimensionless parameters are required to correlate $C_{f,H}^\infty$ data: (1) The dimensionless helix pitch, $p^* = p/d$. (2) The dimensionless helix radius, $R_H^* = R_H/d$. These first two parameters characterize the helix shape. (3) The Reynolds number, $Re = \frac{\rho U d}{\mu}$, which accounts for the operating conditions.

2.2.2 CFD modeling and simulation

Flow simulations were conducted for various helical pipe designs and operating conditions. The geometries were drawn using Autodesk Inventor Professional 2018 software, considering a sufficient tube length to attain the fully developed flow region. The 3D numerical domain was meshed using ANSYS Meshing. The grid consisted of hexahedral cells only, with a boundary layer mesh in the near-wall zone for a more accurate calculation of the steep gradients prevailing in this zone. Based on

preliminary simulations, the cells' size and density were chosen so as to ensure a mesh-independent solution. CFD simulations were conducted using the commercial code ANSYS Fluent 16. The flow field in the pipe was determined by solving the continuity and Navier-Stokes equations in the case of a Newtonian, incompressible, isothermal and steady flow:

$$\text{div}(\vec{v}) = 0 \quad (2.5)$$

$$\rho \vec{\text{div}}(\vec{v} \otimes \vec{v}) = -\vec{\nabla}P + \mu \vec{\Delta} \vec{v}$$

where \vec{v} is the velocity vector. As boundary conditions, a uniform velocity profile was set at the pipe inlet: as the flow rate is imposed, the gravity force has no effect on the velocity field and therefore this body force term was not included in the Navier-Stokes equations. It is noteworthy that the velocity profile at the inlet only affects the flow in the entrance length region and does not have any effect on the value of $C_{f,H}^\infty$. At the pipe outlet, a uniform pressure condition was used and the no-slip condition was set at the pipe walls. The advective terms in Eqs.2.5 were discretized using the QUICK scheme while the diffusive ones were central-differenced. Pressure interpolation was carried out using a second order scheme. The equations were solved using a coupled iterative solver until convergence. More than 150 simulations were carried out in the following range of operating conditions and aspect ratios: (a) $1.25 \leq p^* \leq 25$. (b) $0.05 \leq R_H^* \leq 10$. (c) $10 \leq Re \leq 2000$. In each simulation, the local friction factor was calculated at different longitudinal positions across the pipe length using Eq. 2.4 (considering a sufficiently small wall element as that depicted on Figure 2.4), and its asymptotic value, $C_{f,H}^\infty$, was determined. These CFD results were used to correlate $C_{f,H}^\infty$ as a function of the helix design and flow conditions. They are provided in **Appendix A.1**.

2.2.3 3D-printed helical pipe

In order to validate the numerical results, a highly curved helical pipe was built with nylon material using a fused-filament 3D printer (Stream 30 Dual MK2). The geometric parameters of the helix that were targeted are summarized in the first column of Table 2.2. A first helical pipe having a wall

Table 2.2: Targeted and obtained geometric parameters of the 3D-printed helical pipe

	Targeted dimensions	Obtained dimensions
Pipe inner diameter, d (mm)	1.6	1.25 ± 0.1
Helix radius, R_H (mm)	0.88	0.80 ± 0.1
Helix pitch, p (mm)	6	5.80 ± 0.1

thickness around 0.8 mm and a total height of 156 mm was 3D-printed (Figure 2.6a). Printing was carried out in the vertical direction, z . However, once the pipe has reached a certain height, the back and forth movement of the printing platform (in the x -direction) causes the pipe free end to vibrate: hence, the printing quality decreases and the pipe cross-section becomes no longer properly circular

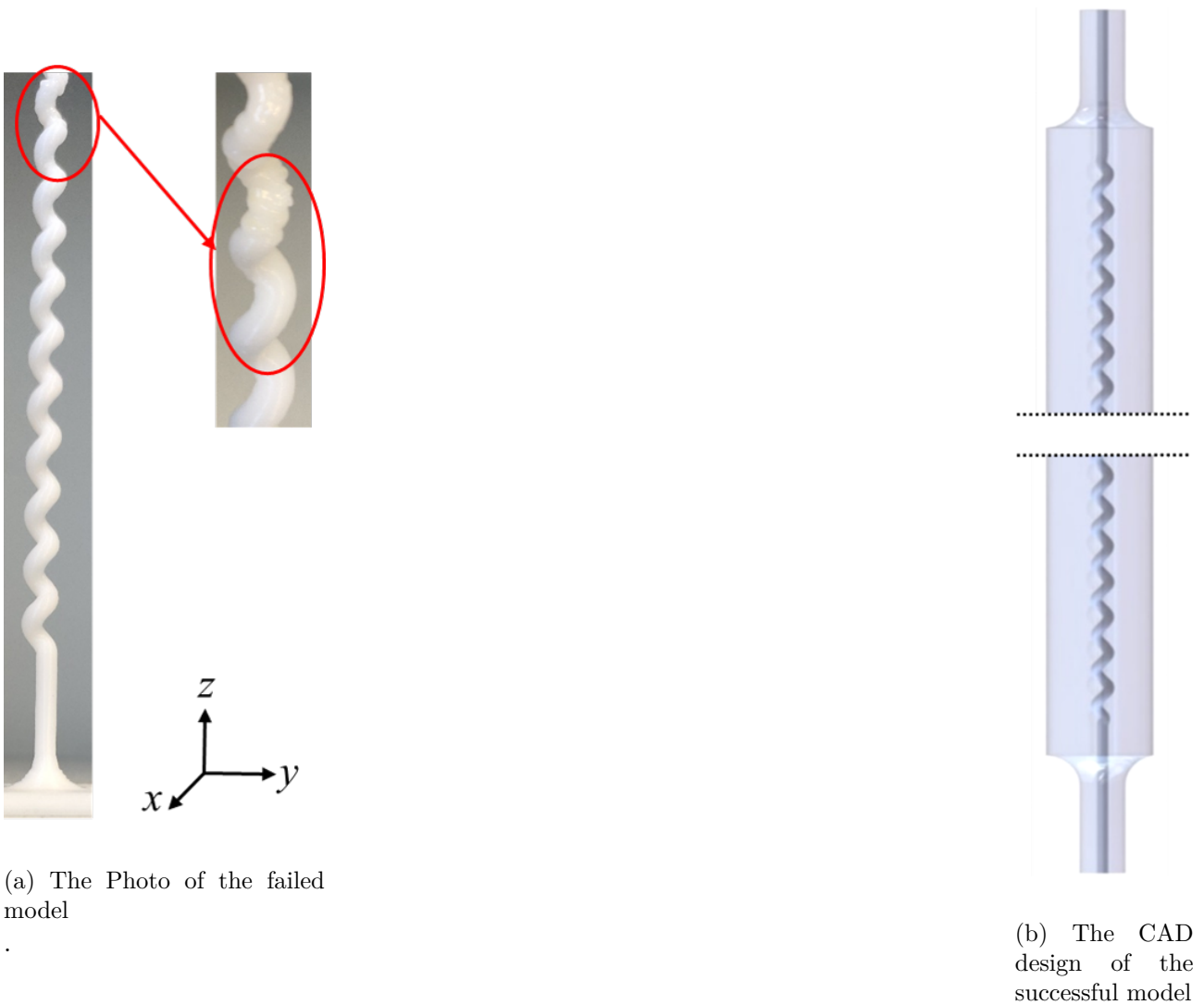


Figure 2.6: 3D-printed helical tubes

(Figure 2.6b). Therefore, a new design was tested (Figure 2.6b). It consists in surrounding the helical tube with a cylindrical block having an external diameter of 15 mm. Indeed, weighting down the structure enhances its stability and reduces its oscillations during the printing process. This design is 200 mm high, which is the maximum height authorized by the 3D printer. It consists of a 156 mm high helical pipe connected at its ends to two straight pipes of 22 mm length each. The straight tubes are required to connect the pipe ends to a pressure transducer for pressure drop measurements. The model represented in Figure 2.6b could be successfully 3D-printed without any detectable vibration to the naked eye. In order to check the printing quality, the pipe interior has been visualized using magnetic resonance imaging (MRI), a non-intrusive imaging technique commonly used in medical investigations. The MRI apparatus of the LEMTA MRI platform, a Bruker spectrometer (Bruker Avance III 600 Wide Bore) producing a static magnetic field of 14.1 T (600 MHz proton resonance frequency) equipped with a micro-imaging probe (MicWB40) was used. The pipe was filled with water and plugged at both ends and then introduced into the spectrometer. The model was visualized at different sections with different scanning angles. The MRI images, including the images presented in

Figure 2.7, showed that the helical tube cross-section was properly circular and uniform all over the pipe length. However, they revealed that the tube internal diameter is slightly smaller than the one initially targeted (Table 2.2).

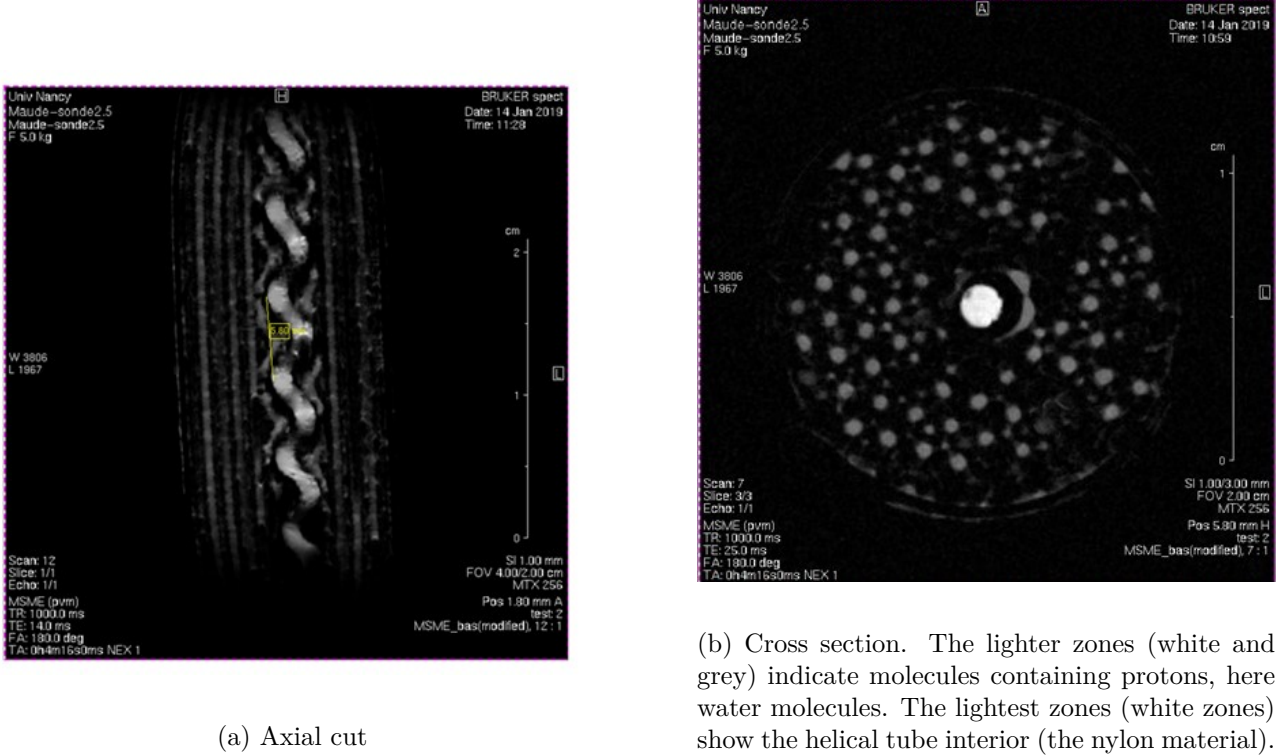


Figure 2.7: MRI images of the 3D printed model

This difference is mainly due to the limited precision of the 3D-printer (especially in the x and y directions) and to the relatively large diameter of the nozzle used, which is about 0.4 mm. The geometric parameters of the obtained helical pipe are summarized in the second column of Table 2.2: they correspond to a R_H^* of about 0.64 and a p^* around 4.64. The total curvilinear length of the tube is about 206 mm, and is calculated as follows:

$$L = n \left[(2\pi R_H)^2 + p^2 \right]^{1/2} \quad (2.6)$$

where n is the number of helix turns which is equal to the total height of the helical pipe divided by its pitch. N.B: As detailed in **Appendix A.2**, further tests using an advanced 3D-printing machine allowed a successful manufacturing of highly curved helices without the need to surround the pipe with any heavy cylindrical block.

2.2.4 Experimental setup for pressure drop measurements

The experimental setup for pressure drop measurements is represented in Figure 2.8. The 3D-printed model was placed horizontally and fed with an aqueous glycerol solution using a high precision micro annular gear pump (MZR-7205, HNP mikrosysteme, Schwerin, Germany. Operating flow rate range: 0.048 - 288 ml/min). A differential pressure sensor (Kobold PAD-d, Kobold instruments, Pittsburgh, USA. Operating range from 19 mbar to 1.9 bar, with a precision of about 2 mbar) connected to both ends of the pipe (Figure 2.6b) allows measuring the total pressure drop across the system. Three aqueous solutions with different glycerol concentrations were used as working fluids. Their dynamic viscosity was measured and their Newtonian behavior checked using a strain-imposed rheometer (AREF, TA Instrument, New Castle, USA) equipped with a parallel plates geometry of 50 mm diameter. To ensure reliable viscosity measurements, only solutions of viscosity higher than 20 times the viscosity of water were used.

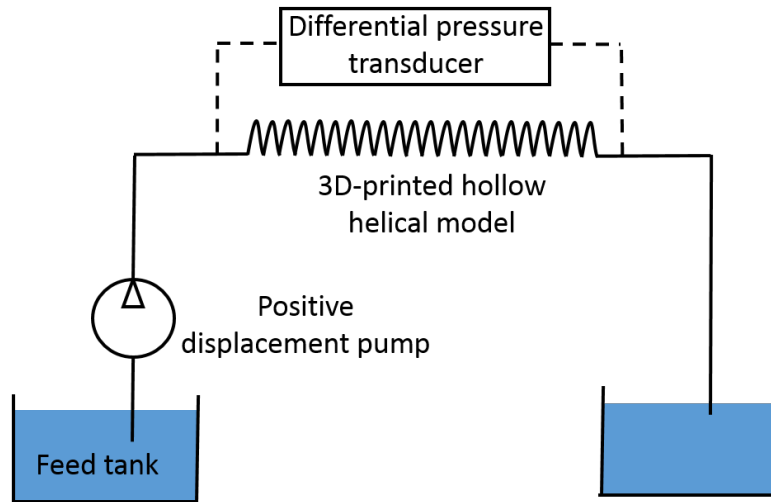


Figure 2.8: Typical variation of the friction factor from the entrance of a straight or a helical pipe

2.3 Results and discussion

2.3.1 CFD results

Figure 2.9 shows contour plots of the $C_{f,H}^\infty$ to $C_{f,S}^\infty$ ratio that were obtained using a triangulation-based cubic interpolation of the CFD results. The geometric parameters for which simulations were performed are represented by black dots. It is worthy to note that, at these points, the values of $C_{f,H}^\infty$ (divided by $C_{f,S}^\infty$) that are displayed on the contour plots are exactly the same than those provided by CFD. On the other hand, the results predicted between these points are generated by interpolation. Therefore, they may be expected to not be very accurate since they are quite sensitive to the interpolation scheme used. Indeed, as can be noticed from Figure 2.9, the contour plots exhibit some relatively irregular variations, and at some positions, the predicted $C_{f,H}^\infty$ to $C_{f,S}^\infty$ values are even

slightly lower than unity. Nonetheless, these contour plots provide considerable valuable information:

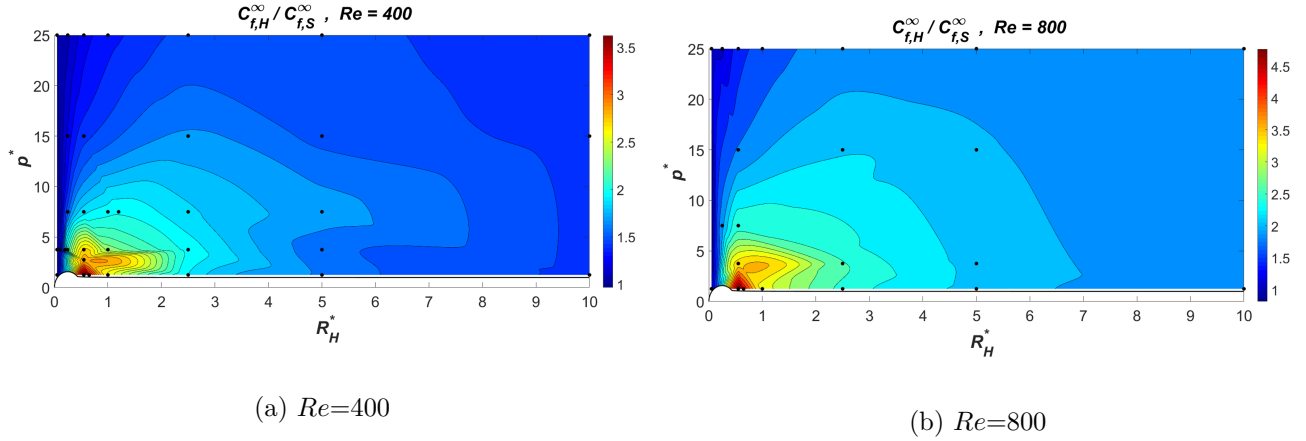


Figure 2.9: Contour plots of the $C_{f,H}^{\infty}$ to $C_{f,S}^{\infty}$ ratio at a Reynolds number. The black dots represent the geometric conditions for which CFD results are acquired. The contours are derived by interpolating these data.

- Comparison to Figure 2.3 confirms that the more curved is the pipe, the higher the magnitude of $C_{f,H}^{\infty}$. Indeed, highly curved helices engender the most intense Dean-type vortices and hence the highest friction factors.
- For a given dimensionless pitch, p^* , there exists a dimensionless helix radius, R_H^* , at which the friction coefficient is maximal. The $C_{f,H}^{\infty}$ to $C_{f,S}^{\infty}$ ratio decreases for higher or lower helical radiuses and tends toward unity when R_H^* tends to zero or to infinity as the helix geometry approaches that of a straight pipe.
- For a given R_H^* , the $C_{f,H}^{\infty}$ to $C_{f,S}^{\infty}$ ratio decreases when p^* increases (although interpolated data indicate the opposite at some positions). Indeed, as can be noticed from Figure 2.3 and Eq. 2.3, the pipe curvature (and hence centrifugal effects) diminishes when p^* is increased. In fact, the $C_{f,H}^{\infty}$ to $C_{f,S}^{\infty}$ ratio should tend towards unity at infinite p^* as the helix design approaches a straight pipe.
- Although $C_{f,H}^{\infty}$ decreases when p^* is increased, as can be seen from Figures 2.9, this effect is only significant in the case of highly curved helices. Indeed, for relatively high R_H^* , the curvature is not much sensitive to the value of p^* (Figure 2.3). As only helical pipes with rather large R_H^* were investigated in the literature, most authors concluded that the pitch value has no significant effect on $C_{f,H}^{\infty}$ (Table 2.1). Thus, it is obvious that their correlations, which are based on De_{R_H} (Eq. 2.2), cannot accurately predict the friction coefficient in highly curved helical pipes. Only the one derived by Mishra and Gupta (1979) [194] may lead to acceptable results since it considers pitch effects through the use of De_{γ} (Eq.2.3).
- When Re is increased, centrifugal effects get more intense, thus the flow and so $C_{f,H}^{\infty}$ become

more sensitive to the helix geometry. Hence, while the maximum value of the $C_{f,H}^\infty$ to $C_{f,HS}^\infty$ ratio is about 3.5 under $Re = 400$, it exceeds 4.5 for $Re = 800$. However, the geometric parameters for which $C_{f,H}^\infty$ is maximal do not seem to be significantly affected by the Reynolds value.

2.3.2 Correlation development

Although the $C_{f,H}^\infty$ field in the (R_H^*, p^*) space (Figure 2.9) presents a single maximum (no local optima) for a given Re , finding a mathematical model that correctly fits the CFD data was very challenging and tedious. In fact, the $C_{f,H}^\infty$ field exhibits steep variations in the highly curved helices region, with highly non-uniform and anisotropic gradients, which magnitudes are very sensitive to the helix geometry. Accordingly, the development of the regression model for $C_{f,H}^\infty$ has been conducted by trial-and-error. The following expression has been found to provide the best fit of the CFD data:

$$\begin{aligned}
 C_{f,H}^\infty &= \frac{64}{Re} + A \cdot B \cdot \exp(-C) \\
 A &= p_1 \cdot D \left(\frac{D}{Re}\right)^{p_2} \\
 B &= \left(R_H^* + \frac{1}{R_H^*}\right)^{p_3} \\
 C &= p_4 \cdot D \cdot p^* \cdot R_H^{*-p_5} \\
 D &= \left[R_H^{*p_6} \left(1 + \left(\frac{p^*}{2\pi R_H^*}\right)^2\right) \right]^{-p_7}
 \end{aligned} \tag{2.7}$$

The present expression includes 7 positive regression parameters denoted p_i (i being an integer ranging from 1 to 7) which values are determined using an optimization procedure, as explained later, in order to minimize the differences between the correlation outputs and the CFD data. The term $64/Re$ corresponds to the asymptotic friction factor in a straight tube, $C_{f,S}^\infty$, with the Darcy-Weisbach definition. A and B being positive terms, for any given Re , the present correlation guarantees that the predicted $C_{f,H}^\infty$ value remains greater (or equal) than $C_{f,S}^\infty$. The term $64/Re$ corresponds to the asymptotic friction factor in a straight tube, $C_{f,S}^\infty$, with the Darcy-Weisbach definition. A and B being positive terms, for any given Re , the present correlation guarantees that the predicted $C_{f,H}^\infty$ value remains greater (or equal) than $C_{f,S}^\infty$. Coefficient D is analogous to κ^* , with the difference that p_6 and p_7 are treated as optimization variables instead of assigning their values to 1 and 2 respectively. Parameters p_6 and p_7 being strictly positive, term D vanishes when R_H^* tends to zero or infinity or when p^* tends to infinity, i.e. when the helical pipe geometry tends toward that of a straight one. The structure of term A expresses the fact that the magnitude of $C_{f,H}^\infty$ increases in zones of high curvatures and decreases with increasing Re (as the optimal value of p_2 was found to be strictly positive). The term D appears with a strictly positive power, $1 + p_2$, in the expression of A . Accordingly, term A vanishes at the asymptotic limits for which the helical pipe reduces to a straight one. Thus, the structure of the developed correlation guarantees that the predicted $C_{f,H}^\infty$ becomes

equal to $C_{f,S}^\infty$ at these limits. Term B allows adjusting the model behavior at large and low R_H^* values, and its incorporation into the mathematical expression significantly improved the correlation accuracy. Term C being positive, $\exp(-C)$ represents a decreasing exponential. Since D appears with a positive power in the expression of C , $\exp(-C)$ allows reproducing the steep variations of $C_{f,H}^\infty$ in the regions of high helix curvature, and the flattening of the $C_{f,H}^\infty$ contour plot in zones of low helix curvature, namely at high R_H^* and p^* values.

Table 2.3: Optimal set for the parameters of the correlation expressed by Equations 2.7

Validity range	p_1	p_2	p_3	p_4	p_5	p_6	p_7
$10 \leq Re \leq 400$	1.98	4.07×10^{-1}	8.49×10^{-1}	8.71×10^{-2}	8.91×10^{-1}	2.31	3.67×10^{-1}
$400 \leq Re \leq 2000$	2.88	3.82×10^{-1}	9.16×10^{-3}	2.48×10^{-3}	2.62	1.1	3.23×10^{-1}

The mathematical expression presented in Equations 2.7 used to correlate the CFD data. It should be recalled that, as mentioned in Section 2.2.2, these results were obtained in the following range of dimensionless parameters: $1.25 \leq p^* \leq 25$, $0.05 \leq R_H^* \leq 10$, $10 \leq Re \leq 2000$. For a better accuracy, two correlations were derived: the first one using the data where Re ranges from 10 to 400, and the second one for Re ranging from 400 and 2000. The optimization problem was formulated as a minimization of the maximum relative difference between the model predictions and the numerical data. The optimal set of the parameters p_i , which is reported in Table 2.3, was determined using a genetic algorithm and the results were further refined using a local optimizer, GRG2. Figure 2.10 compares the correlation predictions and CFD results (represented by brown disks). It shows that the proposed correlation correctly fits the $C_{f,H}^\infty$ data as most points are within an error margin of 10%. Indeed, the maximum relative difference between the numerical results and the correlation predictions is respectively 13.8% for Re below and 400 and 13.2% for Re above 400. Figure 2.11b shows the contour plot of the $C_{f,H}^\infty$ to $C_{f,S}^\infty$ ratio calculated using the present correlation for a Re of 800. Comparison to Figure 2.9b shows a good agreement, with the difference that the model data are much smoother since they are not affected by interpolation approximations. As can be noticed from Figure 2.11, $C_{f,H}^\infty$ exhibits the largest values as well as the highest gradients in the highly curved helixes region. The $C_{f,H}^\infty$ to $C_{f,S}^\infty$ ratio tends toward unity at very low values of R_H^* . Indeed, the formulation of the mathematical expression (Eqs. 2.7) ensures that $C_{f,H}^\infty$ becomes equal to $C_{f,S}^\infty$ at the three asymptotic limits at which the helix geometry tends toward that of a straight pipe.

2.3.3 Comparison with literature correlations

In order to assess the potentiality of the new correlation, its performance are compared to that of literature correlations in Figures 2.12, 2.13 and 2.14. Figure 2.12 depicts the variations of $C_{f,H}^\infty$ as a function of R_H^* for two values of p^* . Given that literature correlations were derived by regressing experimental measurements acquired on helixes with large R_H^* (Table 2.1), they are expected to be

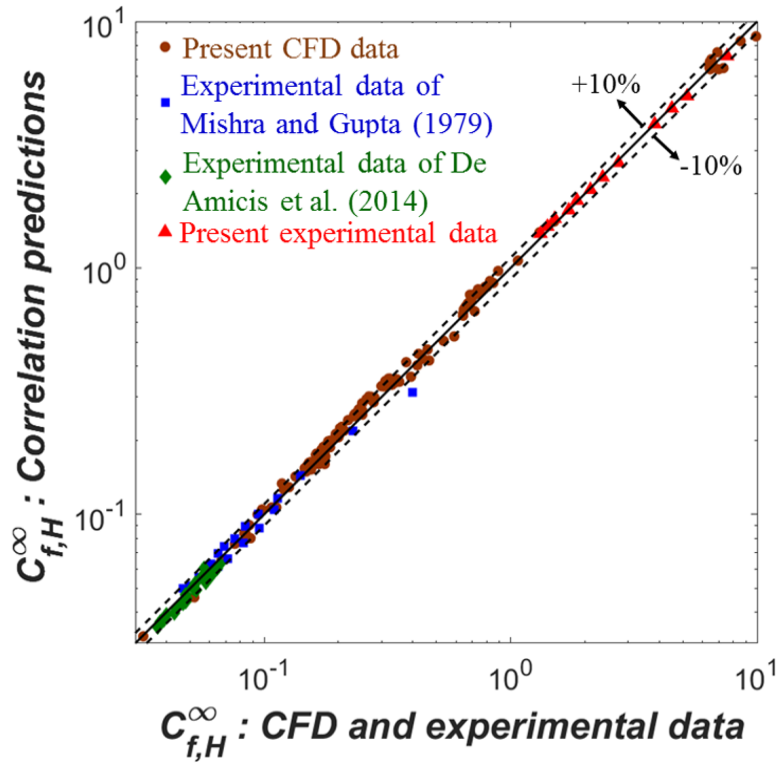


Figure 2.10: Parity diagram of $C_{f,H}^{\infty}$: CFD and experimental data versus correlation predictions

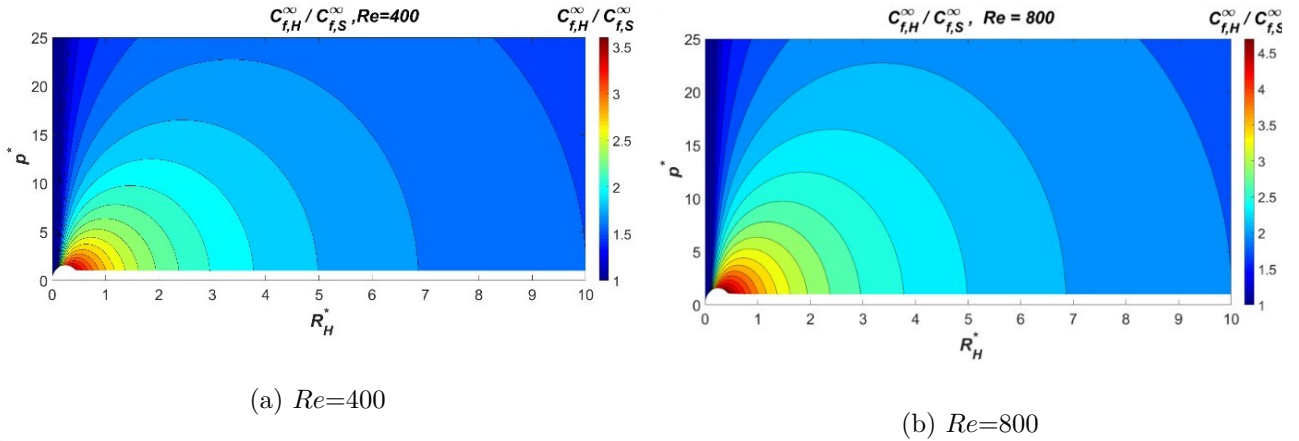


Figure 2.11: Contour plot of the $C_{f,H}^{\infty}$ to $C_{f,S}^{\infty}$ ratio: present correlation data (Equations 2.7).

accurate for non-highly curved helices. As can be noticed, at relatively large R_H^* values, the results provided by all of the plotted correlations are in good agreement with the current CFD data. This constitutes a first validation of the present CFD simulations.

However, Figure 2.12 also shows that literature correlations do not correctly estimate $C_{f,H}^{\infty}$ in the case of highly curved helices. Indeed, the correlation of Hart et al. (1988) [200] and all the correlations based on De_{R_H} (Equation 2.2) (see Table 2.1) do predict an infinite friction factor when R_H^* tends towards zero.

On the other hand, the correlations of Schmidt (1967) [197] and Mishra and Gupta (1979) [194] reproduce correctly the shape of the curves showing $C_{f,H}^{\infty}$ versus R_H^* . However, the correlation of Schmidt (1967) [197] does not account for any pitch effect. Therefore, it leads to systematic errors in

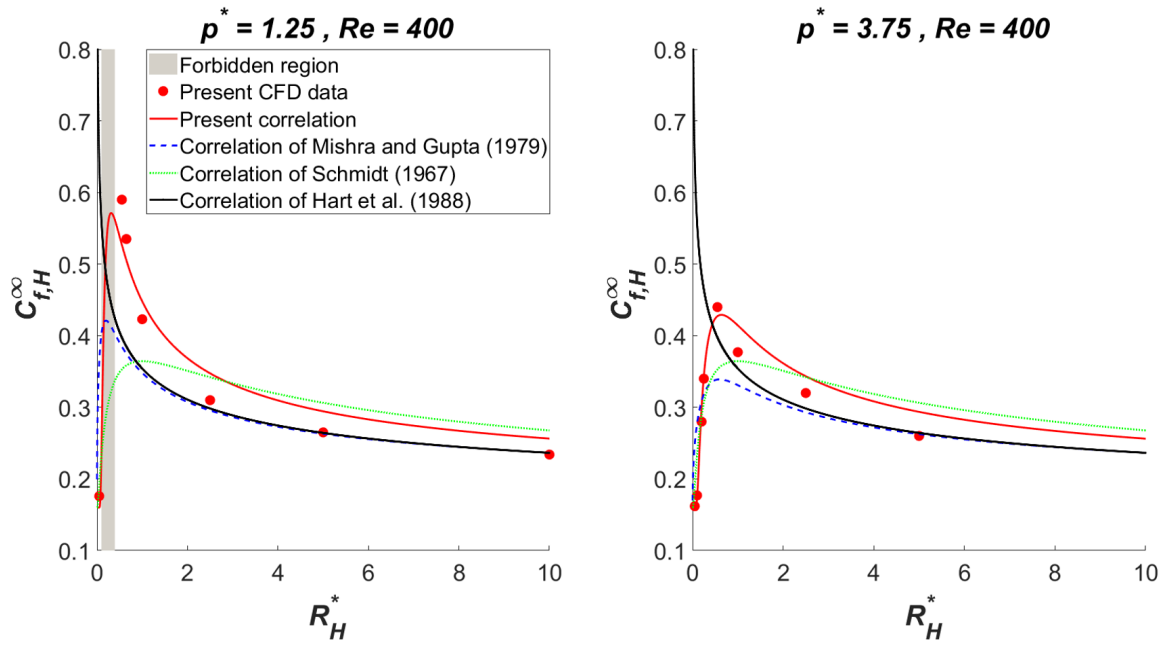


Figure 2.12: $C_{f,H}^{\infty}$ versus R_H^* at two different p^* : comparison of different correlations.

the highly curved helixes zone where the friction factor is very sensitive to the pitch (Figures 2.9, 2.11 and 2.12). The correlation of Mishra and Gupta (1979) [194] proved to be the most accurate among literature models. In some cases as illustrated in Figure 2.12, it does even provide slightly better predictions than the current correlation. However, its major weak point is that it generally largely underestimates the friction factor in highly curved helixes as can be noticed from Figures 2.12, 2.13 and 2.14.

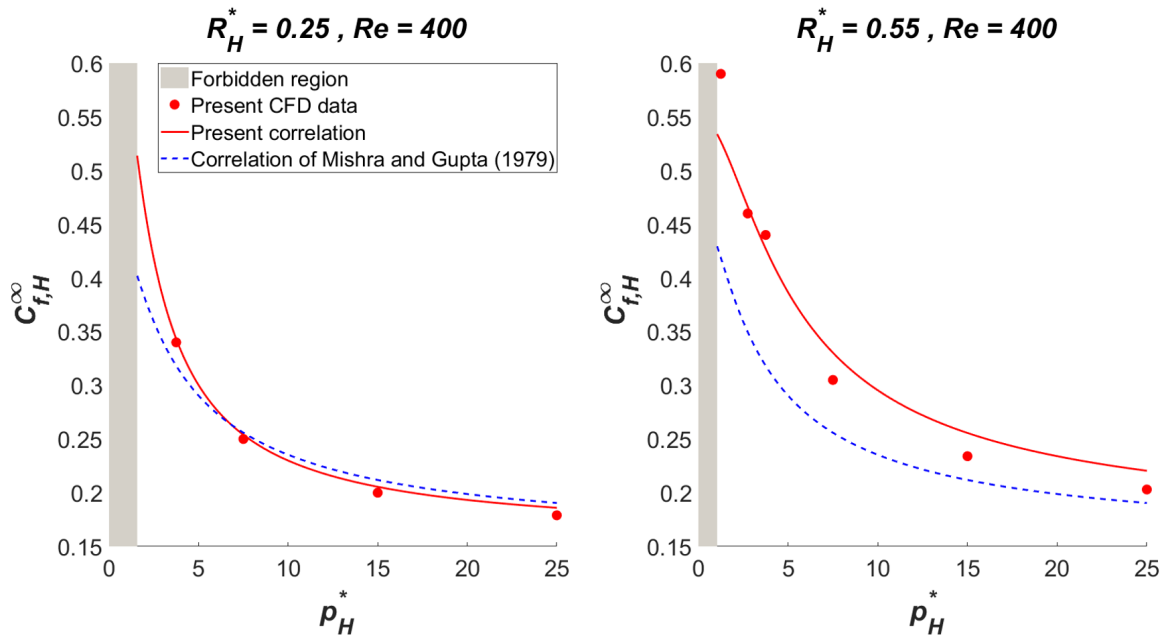


Figure 2.13: $C_{f,H}^{\infty}$ versus p_H^* at two different R_H^* : comparison between the present correlation and that of Mishra and Gupta (1979) [194]

Finally, the variations of $C_{f,H}^{\infty}$ with the Reynolds number are plotted on Figure 2.14 for four highly

curved helices. This figure illustrates the fact that the present model (Eqs. 2.7) correctly captures the Re effects, and is generally more accurate than that of Mishra and Gupta (1979) [194]. A discontinuity in the curves obtained with the present correlation can be noticed. It is due to the use of different parameter values depending on whether Re is below or above 400 (Table 2.3).

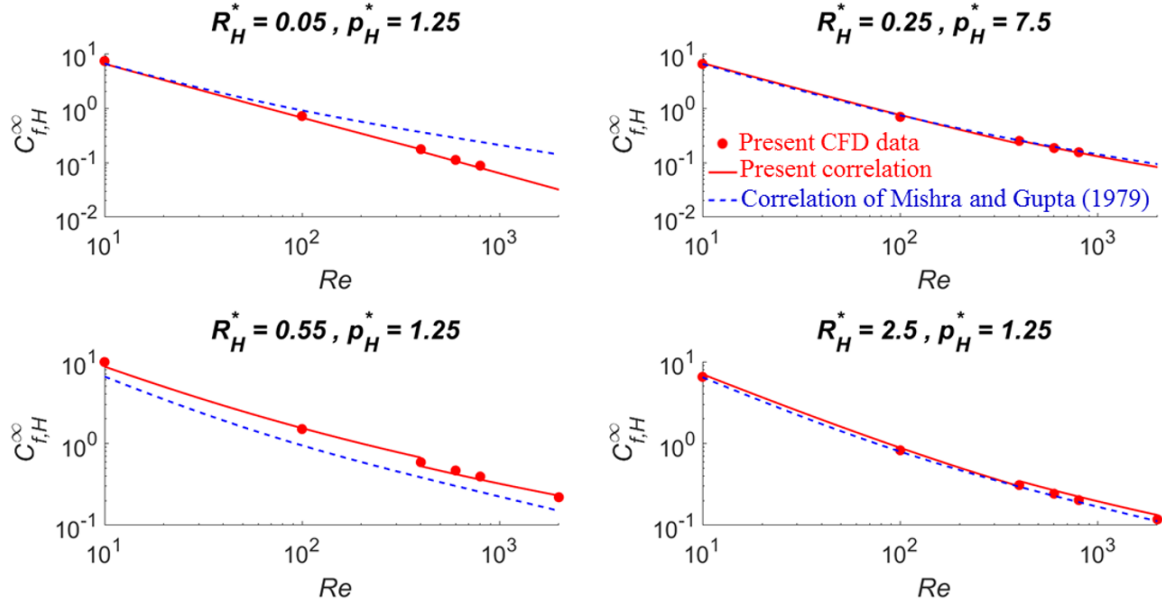


Figure 2.14: $C_{f,H}^{\infty}$ variation with Re for four different helices

2.3.4 Correlation validation using experimental data from literature

In addition to CFD data, for a more trustworthy validation, the correlation results were compared to the experimental data of Mishra and Gupta (1979) [194] and De Amicis et al. (2014) [206]. Table 2.4 summarizes the geometric and operating conditions over which these measurements were obtained. It is noteworthy that, although most of these experiments were performed for a Re higher than 2300, they do all correspond to a laminar flow regime. Indeed, in the case of helical pipes, centrifugal forces do generally have a stabilizing effect on the flow which delays the transition to turbulence. Hence, the flow can remain laminar for Reynolds values much higher than in straight pipes ([206]; [207]).

The last column in Table 2.4 recalls the range of geometric and operating conditions over which the current CFD data were performed, and hence, upon which the present correlation was built. It can be noticed that all of the literature experimental results were acquired for conditions beyond the validity range of the present correlation. Nevertheless, as shown in Figures 2.10 and 2.15, all of De Amicis et al. (2014) [206] results are predicted within a margin error of 10%, and most of Mishra and Gupta (1979) [194] data are predicted with a relative error less than 8%. Only a single point falls beyond this limit and is predicted with an error of about 28%. It corresponds to a measurement acquired by Mishra and Gupta (1979) [194] under a Re of 266, which represents the lowest Re investigated in their study (Table 2.4). Such a low Re leads to a low pressure drop especially since the helix considered is

not highly curved; hence, this measurement is expected to be much affected by experimental errors.

Table 2.4: : Ranges of geometric and operating conditions over which the literature experimental data were acquired and the present correlation was built.

	Mishra and Gupta (1979) [194]:helical 1	Mishra and Gupta (1979) [194]: helical 2	De Amicis et al. (2014) [206]	Range of parameters investigated using CFD
R_H^*	3.4	20.2	39.9	[0.05 – 10]
p^*	27.5	18.9	63.8	[1.25 – 25]
Re	[266 – 5500]	[1100 – 2550]	[1790 – 4160]	[10 – 2000]

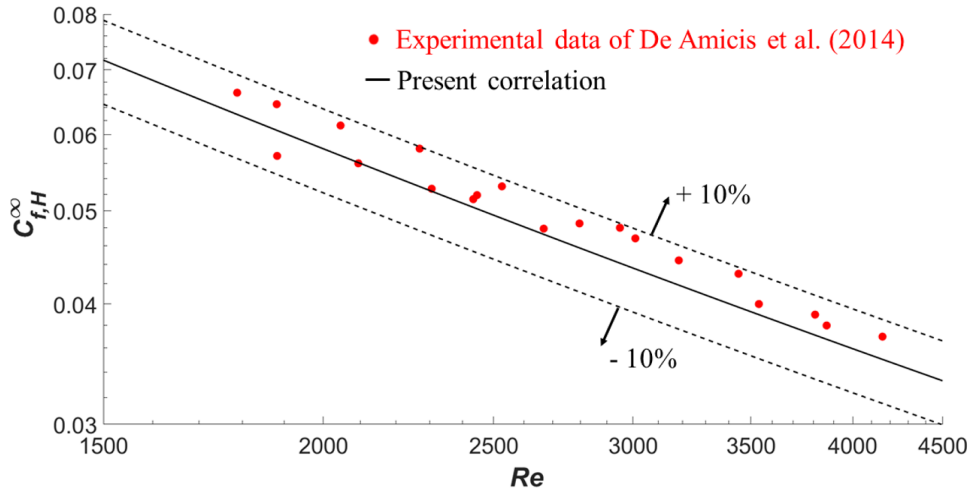


Figure 2.15: Comparison between the present correlation predictions and the experimental data of De Amicis et al. (2014) [206]

The results presented in this section demonstrate the predictive capacities of the present correlation, as it successfully estimated experimental data which were acquired beyond its supposed range of validity. This advantageous feature is probably due to the structure of the present model (Eqs. 2.7): in particular, it guarantees correct results at the asymptotic limits where the helical pipe geometry tends toward that of a straight one, i.e. it ensures results to be correctly bounded. Therefore, the present correlation is believed to lead to realistic and accurate friction factor values even beyond the range of geometric and operating conditions investigated using CFD.

2.3.5 Correlation validation using data acquired on the 3D-printed highly curved helix

The performed pressure measurements correspond to the total pressure drop across the 3D-printed model, i.e. through the helical pipe (which R_H^* is about 0.64 and p^* around 4.64, see Section 2.2.3) and the two straight pipes connections. Assuming that the friction factor in the straight tubes equals $64/Re$, the pressure drop across the helical pipe, Δp_H , could be calculated (calculation details are provided in **Appendix A.3**). Given the important length and the small diameter of the helical pipe, minor head losses can be neglected. Thus, $C_{f,H}^{\infty}$ is calculated following Darcy-Weisbach:

$$C_{f,H}^{\infty} = \frac{\Delta p_H d}{\frac{1}{2} \rho L U^2} \quad (2.8)$$

where L is the total curvilinear length of the helical pipe. Figures 2.10 and 2.16 compare the experimental friction factor to the correlation (Equations 2.7) predictions. All the experimental data are predicted within a relative error margin less than 8%, which demonstrates the accuracy of the proposed correlation in the case of highly curved helical pipes. This correlation is the first one to accurately predict the pressure drop in highly curved helical pipes. Moreover, as shown in this chapter, it proved to be efficient over a broad range of geometric and operating conditions. The precise estimation of the specific energy requirement of a whole set of heat and mass exchangers designs, over a broad range of operating conditions (under the assumption of a laminar flow regime) is thus now achievable. This offers the possibility to systematically explore which heat or mass exchanger geometry offers the best combination of increased transfer performances together with a minimal specific energy requirement. Process intensification studies typically correspond to such an objective and the results reported in this chapter should be helpful for optimal exchangers design studies.

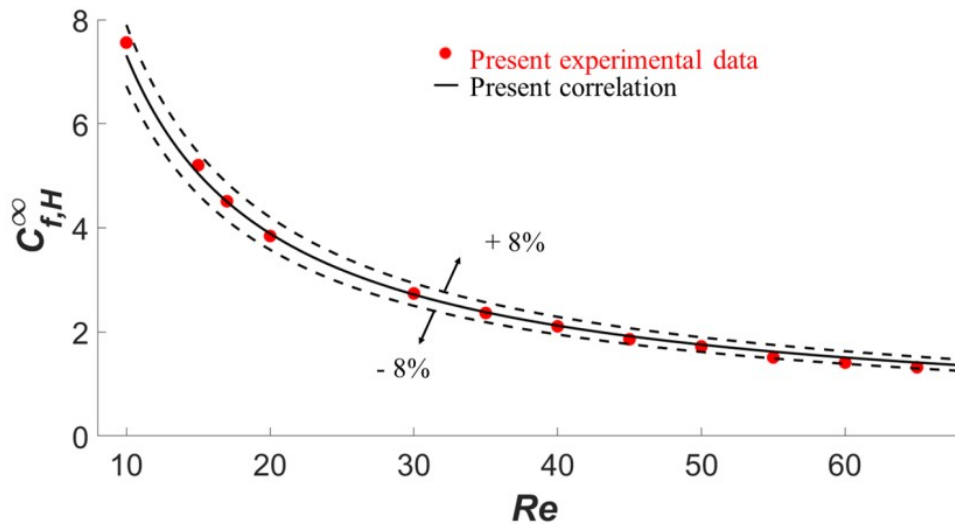


Figure 2.16: Comparison between the present correlation predictions and the present experimental data

2.4 Conclusion

This chapter focused on the laminar flow friction factor in helical pipes, especially highly curved geometries. CFD simulations were conducted to determine the friction factor for various helix designs under different Reynolds numbers. On the basis of these numerical results, a general correlation for calculating the friction factor in helical pipes was developed. The correlation proved to be robust, efficient and predictive as its results were in excellent agreement with literature experimental data as well as with measurements performed on a 3D-printed highly curved helical tube. Chapter 3 will concentrate on developing correlations predicting the heat and mass transfer efficiencies in helical pipes. These correlations, along with the one developed in this chapter, will then be used in model-based optimization of helically coiled heat exchangers and hollow fiber membrane contactors in order to determine the optimal helical tubes design, i.e. the one leading to the most lucrative trade-off between the transfer efficiency enhancement and the increase of pumping costs.

Acknowledgment

The author gratefully thanks Mrs. Maude Ferrari for the MRI measurements and Mr. Philippe Marchal for the rheological experiments.

Chapter 3

Optimal design of helical heat/mass exchangers under laminar flow: CFD investigation and correlations for maximal transfer efficiency and process intensification performances*

*This chapter constitutes an extended version of an article that has been published in International Journal of Heat and Mass Transfer.

[208] **Omran Abushammala**, Rainier Hreiz, Cecile Lemaitre, Eric Favre. (2020): “Optimal design of helical heat/mass exchangers under laminar flow: CFD investigation and correlations for maximal transfer efficiency and process intensification performances”, *International Journal of Heat and Mass Transfer*, **153**, 119610.

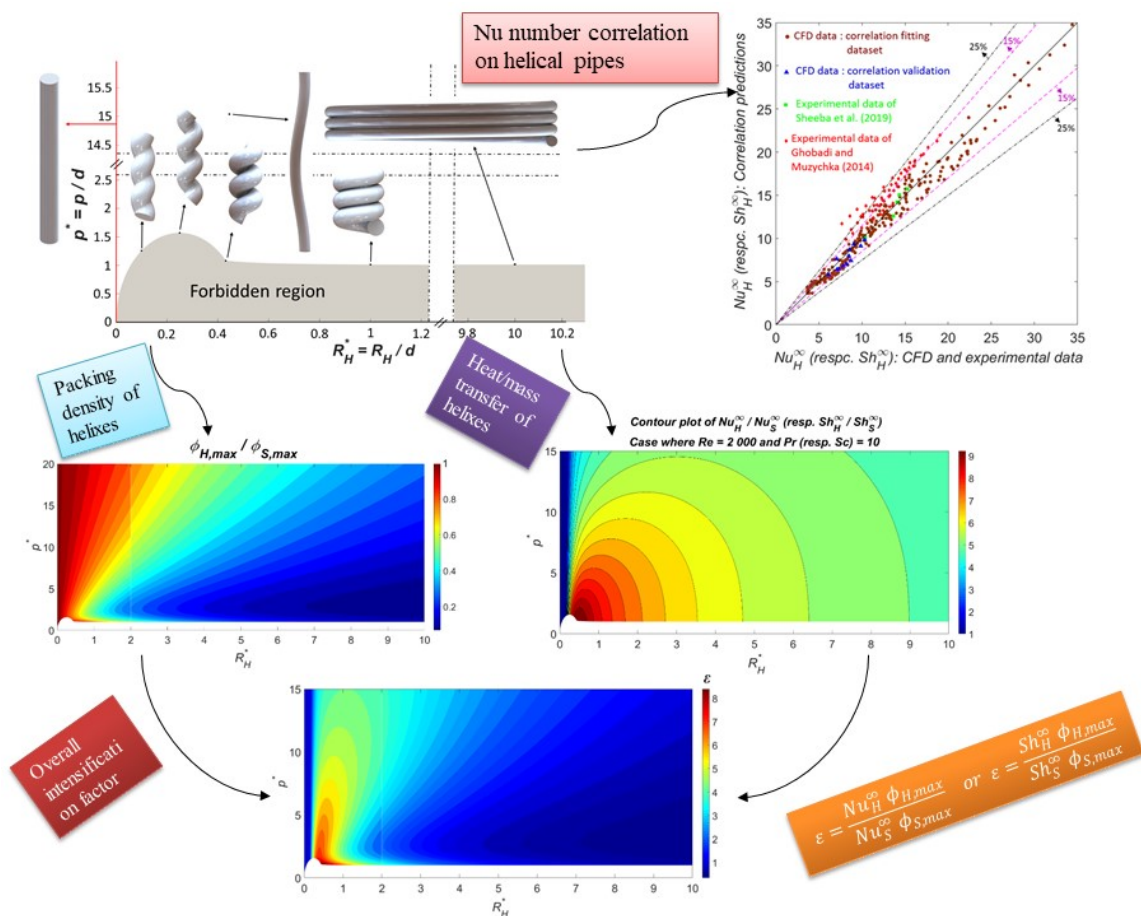
Background

The design and operation of membrane separators and heat exchangers have been of great interest for many scientific researches aiming at improving the separation/transfer efficiency. In this context, CFD (computational fluid dynamics) reveals to be a powerful tool for assisting and supporting engineers for determining the optimal shape of membrane and heat exchanger modules. Two strategies may be applied in order to push process intensification: maximize heat/mass transfer coefficients and maximize the specific membrane/heat exchanger surface area (i.e. packing density) of the module. Dean vortices generation is one of the most efficient methods but requires helical shape pipes, which cannot be as densely packed as straight tubes. This is why a combined packing density and heat/mass transfer study is conducted in this chapter in order to evaluate the optimal performances of helical membrane and heat exchanger modules. In particular, the performance of highly curved helical pipes (HCHPs) is investigated. The heat/mass transfer enhancement factor ϵ is introduced, which is equal to Nu_H^∞/Nu_S^∞ (respectively Sh_H^∞/Sh_S^∞) – the ratio between the heat (respectively mass) transfer coefficients in helical and straight tubes – multiplied by $\phi_{(H,max)}/\phi_{(S,max)}$ – the ratio between the specific surface area of helical and straight pipes. This factor represents the volumetric transfer rate enhancement that helical pipes allow achieving when used in packed modules, i.e. it corresponds to the maximum unit volume reduction (of reactors, heat exchangers or membrane contactors) that such designs allow to reach. CFD simulations were performed to investigate heat/mass transfer in helical pipes, in particular highly curved ones, which have not been studied in the former literature. CFD simulations covered extreme helical geometries under laminar flow conditions. On the other hand, a CAD (computer-aided design) software was used to determine helices packing density depending on their geometry. CFD results revealed that HCHPs allow achieving heat/mass transfer rates up to an order of magnitude higher than straight tubes. Moreover, CAD data confirmed that their packing density is much higher than that of classical helices (although it is lower than that of straight tubes). Hence, the volumetric transfer rate allowed by HCHPs is found to be up to 8 times higher than that reached with straight tubes, which demonstrate the huge potential of these geometries for process intensification.

Finally, correlations are developed for evaluating the interfacial area and the heat/mass transfer efficiency (Nu_H^∞/Sh_H^∞) in classical and highly curved helical pipes. These new correlations allow identifying optimal helix designs for maximizing the volumetric heat/mass transfer rate (i.e. minimizing the volume of heat/mass transfer equipment) with a satisfying energy efficiency.

Summary

Highly curved helical pipes (HCHPs) offer tremendous potentialities for intensified heat/mass transfer performances as they generate intense Dean-type vortices. However, these designs have not been explored so far in the literature, probably because they are difficult to build using traditional manufacturing techniques. Nowadays, thanks to a witnessed progress in 3D-printing, the fabrication of HCHPs has become achievable. Therefore, investigating their performance in terms of heat and mass transfer intensification presents significant interest from both academic and industrial points of view. In this chapter, CFD simulations are carried out to determine the heat/mass transfer efficiency in helical pipes (particularly highly curved ones) under laminar flow conditions. The packing density (i.e. interfacial area) of these geometries is evaluated using a CAD software. The results reveal that HCHPs not only allow achieving much higher transfer rates than straight and classical helical pipes, but they can also be densely packed. Therefore, when appropriate designs are selected, impressive process intensification factors are achievable, with up to 8-fold volume reductions. Finally, correlations are developed for evaluating the interfacial area and the heat/mass transfer efficiency in classical and highly curved helical pipes. In future works, these correlations will be used in model-based optimization for determining the optimal designs of helically coiled heat/mass exchangers.



Graphical abstract of Chapter 3

3.1 Introduction

Economic issues and continuously strengthening environmental regulations force the industry to develop increasingly compact reactors and heat and mass transfer equipment. Such units allow improving the processes efficiency while reducing their overall energy requirements, costs, environmental impacts, weight and footprint. More specifically, minimizing volume and/or weight is of primary importance in applications where space is limited, e.g. decentralized energy production, domestic applications, space and offshore processes. Various strategies to enhance heat and mass transfer efficiencies have been proposed and employed [209]; [155]. They include the use of rotating devices [210], pulsating flow [211], twisted tape inserts [212], vortex generators [213] or helical pipes, etc. Compared to other alternatives, helical pipes present the advantage of not involving any internals or moving parts. Therefore, they are less subject to failure, breakdown, fouling and clogging, and thus, require lower maintenance costs.

Compared to straight tubes, due to centrifugal effects, the flow in curved and helical pipes develops secondary flow structures called Dean cells (Figure 3.1). They consist in a pair of counter-rotating vortices in the cross-stream direction, perpendicularly to the primary flow. These vortices allow a great improvement of the transfer efficiency. Indeed, if we consider fully developed laminar flow conditions, in the case of straight tubes, fluid particles move along straight streamlines parallel to the walls. Therefore, lateral mixing, i.e. radial heat/mass transfer, occurs under the sole effect of conduction/diffusion, which leads to poor transfer efficiencies when the pipe diameter is not too small. On the other hand, in helical pipes, Dean cells provide efficient advective transport of the fluid particles between the pipe walls and its centerline, leading to increased transfer performance. Accordingly, these geometries have been suggested and/or employed in several applications and industrial processes: (1) Heat transfer enhancement for nuclear plants [214] and many other applications [215]; [216]. (2) Increased Mass transfer enhancement in catalytic reactors [153], dense [154] and porous [155] membrane contactors, etc. (3) Improvement of mixing efficiency [157].

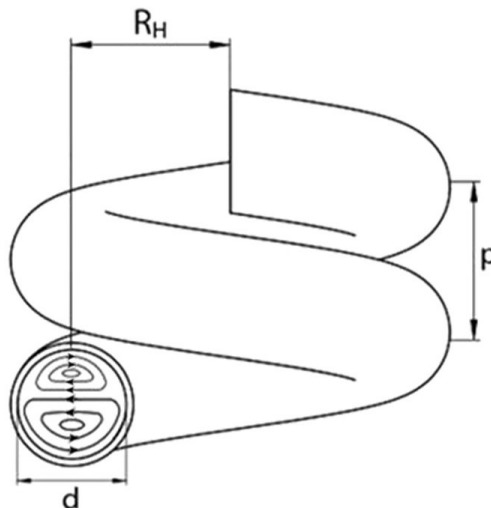


Figure 3.1: Schematic representation of Dean cells in a helical pipe

The shape of a helical pipe is described by two geometric parameters, the dimensionless pitch, $p^* = p/d$, and the dimensionless helix radius, $R_H^* = R_H/d$, where d is the pipe diameter, p the helix pitch and R_H the helix radius. Figure 3.2 illustrates some representative helical tube geometries and the limits of the so-called forbidden region. The equation of this frontier has been determined by Przybył and Pierański (2001) [201]: it corresponds to the limit beyond which it is not possible to further decrease the helix pitch because the consecutive turns of the helix would overlap one with another. In other terms, the forbidden region corresponds to the set of p^* and R_H^* for which it is no more possible to design helical shapes. Figure 3.3 is a contour plot of the dimensionless helix curvature, $\kappa^* = \kappa d = d/\gamma$, in the (R_H^*, p^*) space, where κ is the pipe curvature and γ its curvature radius. The mathematical expression of κ is as follows:

$$\kappa = \frac{1}{R_H \left[1 + \left(\frac{p}{2\pi R_H} \right)^2 \right]} \quad (3.1)$$

Figure 3.3 illustrates the fact that the helix curvature tends toward zero at three asymptotic limits: (1) when the dimensionless pitch, $p^* = p/d$, tends to infinity. (2) when the dimensionless helix radius $R_H^* = R_H/d$ tends to zero. (3) when R_H^* tends to infinity. Indeed, as shown in Figure 3.2, at the first two limits, the helix geometry tends toward that of a straight tube, while at the third limit, the helical tube straightens and becomes locally similar to a straight pipe. Most importantly, Figure

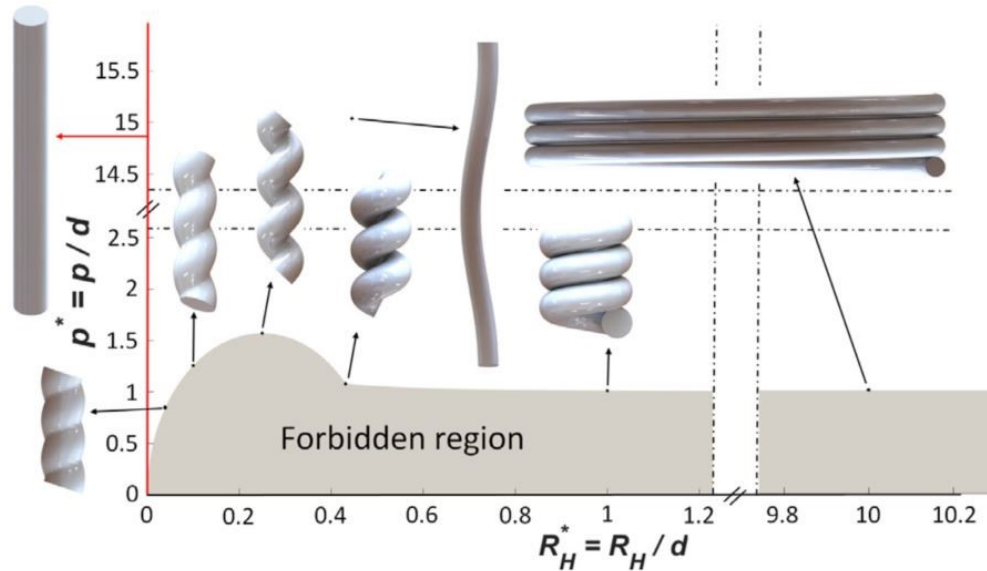


Figure 3.2: Limit of the forbidden region in the (R_H^*, p^*) space (adapted from Przybył and Pierański (2001) [201]) and some representative helix geometries Abushammala et al. (2019a) [191]

3.3 reveals that the highest pipe curvatures are associated to helices of low pitch and relatively low helical radius. These geometries will be referred to as Highly Curved Helical Pipes (HCHPs) further on in this chapter. Given their low radius of curvature, they exhibit the highest centrifugal effects. Thus, HCHPs are expected to produce the most intense Dean vortices, which should lead to the

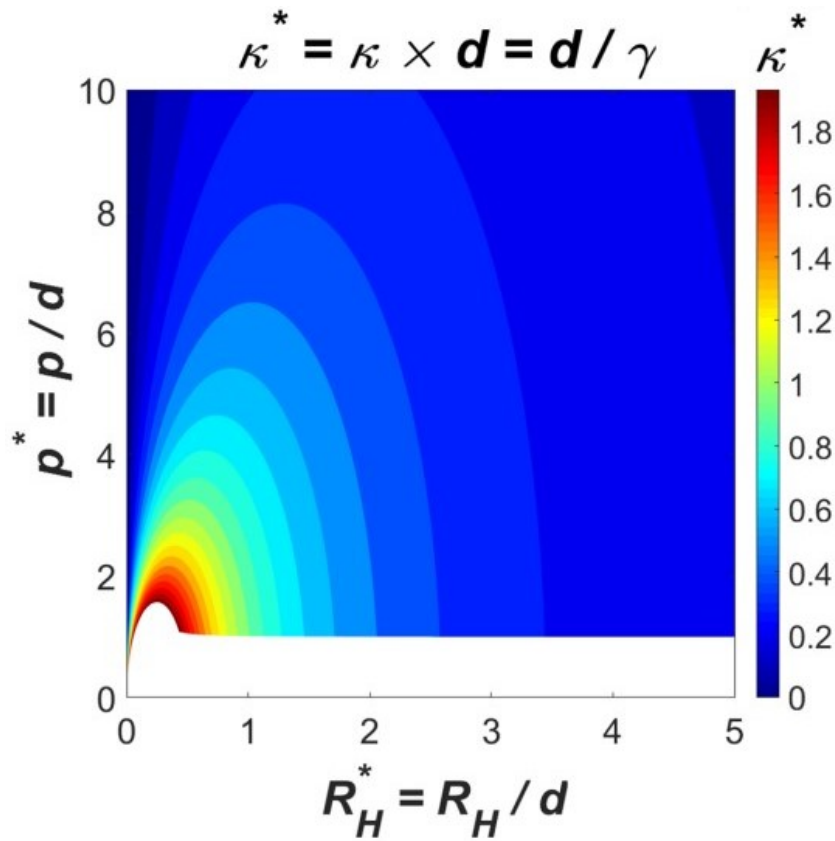


Figure 3.3: Contour plot of the dimensionless helix curvature in the (R_H^*, p^*) space

best heat/mass transfer performance. Nonetheless, to the authors' best knowledge, no previous study has focused yet on the transfer efficiency in such geometries. As can be noticed from Table 3.1 for example, only 'classical' helical geometries have been considered thus far in literature. This is probably because HCHPs are difficult to fabricate using traditional manufacturing techniques. Studies dealing with classical helical pipes have shown that these geometries allow a significant enhancement of the heat/mass transfer. Indeed, Nusselt and Sherwood numbers up to 7 times greater than in straight tubes were reported in literature [168]; [207]; [217]. However, it is noteworthy that helical pipes cannot be as densely packed as straight ones. Therefore, the transfer efficiency improvement they allow is - at least partially - counterbalanced by their lower packing density. For example, Kaufhold et al. (2012) [203] reported that if R_H^* is not sufficiently small, classical helices lead to lower performance than straight tubes in terms of volumetric mass transfer rates (i.e. mass flux per unit volume).

Interestingly, HCHPs are not only expected to lead to better transfer rates than classical helices, but also, their elongated shape (Figure 3.2) allow them to be densely packed. Hence they should allow a significant intensification of the overall transfer rate, i.e. a meaningful unit volume reduction of reactors, heat exchangers and membrane contactors. Nowadays, with the development of 3D-printing technologies, manufacturing HCHPs has become achievable [191]. Therefore, investigating their performance in terms of heat and mass transfer efficiency offers significant interest from both academic and industrial points of view.

This chapter focuses on transport phenomena in helical pipes, particularly highly curved ones (HCHPs), under fully developed laminar flow conditions. The laminar flow regime is encountered in many applications of practical interest, in particular small-scale devices, e.g. microfluidics, micro-structured heat exchangers and reactors, micro-mixers and hollow fiber membranes. CFD (computational fluid dynamics) simulations are reported hereafter in order to determine the Nusselt number in helical pipes, and by analogy, the Sherwood number. Different operating conditions, described by the Reynolds number, and various helix designs are examined. Prandtl numbers (and by analogy, Schmidt numbers) ranging from 1 to 10 are considered. This range of fluid properties covers many existing processes. Additionally, for evaluating the volumetric transfer rates allowed, helices packing density as a function of the helices geometry has been determined using a CAD (computer-aided design) software.

CFD results revealed that among helical pipes, highly curved ones allow achieving the maximal Nusselt and Sherwood numbers, which can be nearly an order of magnitude higher than in straight ones. Moreover, numerical data confirmed that HCHPs can be densely packed. The volumetric transfer rates they allow is up to 8 times higher than that reached with straight tubes. On the other hand, given their low packing densities, classical helical pipes may lead to lower overall performance than straight ones. It is also shown that available correlations fail in estimating the heat/mass transfer rates in HCHPs and the helices packing density with a sufficient accuracy. Therefore, two new correlations are proposed in this chapter. The first one allows predicting the Nusselt and Sherwood numbers over a wide range of helical pipe geometries and operating condition, and the second allows determining the optimal packing density as a function of the helix geometry. This set of correlations, along with that proposed by Abushammala et al. (2019a) [191] (see Equations 2.7, Chapter 2) for calculating the friction coefficient in helical pipes, can be used in model-based optimization of helically coiled heat exchangers / membrane contactors. This procedure allows determining the optimal helix geometry, i.e. the one leading to the most lucrative trade-off between the process intensification (unit volume reduction of heat/mass exchangers) and energy efficiency (extra pressure drop).

Table 3.1: Set of commonly used correlations for predicting Nu_H^∞ and Sh_H^∞ for laminar flow in helical pipes under uniform wall temperature/concentration. Nu_H^∞ and Sh_H^∞ respectively correspond to the asymptotic Nusselt and Sherwood numbers in helical pipes

Reference	Correlation	Correlation's validity range according to its authors	Geometric parameters of the helical pipes investigated
Schmidt (1967) [197]	$Nu_H^\infty = 3.65 + 0.08 \left[1 + 0.8 \left(\frac{1}{2R_H^*} \right)^{0.9} \right] Pr^{\frac{1}{3}} Re^m$ $m = 0.5 + 0.2903 \left(\frac{1}{2R_H^*} \right)^{0.194}$	Laminar regime with $Re \geq 100$ Large range of Pr (air, water and oil were used as test fluids)	$2.5 \leq R_H^* \leq 42$ $3 \leq p^* \leq 137$
Dravid et al. (1971) [178]	$Nu_H^\infty = (0.76 + 0.65 De_{RH}^{0.5}) Pr^{0.175}$	$50 \leq De_{RH} \leq 2000$ $5 \leq Pr \leq 175$	$10 \leq R_H^* \leq 50$ The range of p^* is not reported
Kalb & Seader (1974) [218]	$Nu_H^\infty = 0.836 De_{RH}^{0.5} Pr^{0.10}$	$80 \leq De_{RH}$ $0.7 \leq Pr \leq 5$	$5 \leq R_H^* \leq 50$ The range of p^* is not reported
Manlapaz & Churchill (1981) [174]	$Nu_H^\infty = \left[(3.657 + \frac{4.343}{z_1})^3 + 1.158 \left(\frac{De_{RH}}{z_2} \right)^3 / 2 \right]^{1/3}$ $z_1 = \left(1 + \frac{957}{De_{RH}^2 Pr} \right); z_2 = 1 + \frac{0.477}{Pr}$	Entire laminar regime	$2.5 \leq R_H^*$ The range of p^* is not reported
Moulin et al. (1996) [168]	$Sh_H^\infty = 0.14 De_{\gamma}^{0.75} Sc^{0.33}$	$150 \leq Re \leq 2000$	$11.5 \leq R_H^* \leq 12.4$ $9.9 \leq p^* \leq 15.4$
Yildiz et al. (1997) [179]	$Nu_H^\infty = 0.0551 De_{RH}^{0.864} Pr^{0.40}$	$1265 \leq De_{RH} \leq 2000$ $5 \leq Pr \leq 175$	$120 \leq p^* \leq 360$ $R_H^* = 7.5$
Xin & Ebadion (1997) [172]	$Nu_H^\infty = (0.318 De_{RH}^{0.643} + 2.153) Pr^{0.177}$	$20 \leq De_{RH} \leq 2000$ $0.7 \leq Pr \leq 175$	$22.6 \leq R_H^* \leq 75$ The range of p^* is not reported
Ghobadi and Muzychka (2014) [219]	$Nu_H^\infty = [3.66^4 + (0.91375 De_{RH}^{0.5} Pr^{-0.1})^4]^{1/4}$	$40 \leq De_{RH} \leq 700$ $5 \leq Pr \leq 15$	$6.1 \leq R_H^* \leq 24.2$ The range of p^* is not reported
Sheeba et al. (2019) [220]	$Nu_H^\infty = 3.6063 De_{RH}^{0.2216} Pr^{0.0540} \left(\frac{p^*}{2\pi R_H^*} \right)^{0.0472}$	$200 \leq De_{RH} \leq 700$	$R_H^* = 29.7$ $2 \leq p^* \leq 18.2$

3.2 CFD computation of Nusselt (and Sherwood) number in helical pipe flows

3.2.1 Nusselt (and Sherwood) number in helical pipe flows

In helical and curved pipes undergoing heat transfer between the fluid flow and the wall, the convective heat transfer is not uniform over the wall. However, in most engineering applications, only the heat transfer coefficient averaged over the pipe circumference (i.e. in the azimuth direction) is of practical interest. It will be simply referred to as convective heat transfer coefficient, h , in the remaining part of this chapter. Considering a cross-section of the tube, the fluid mixing-cup temperature (i.e. mass flow rate weighted temperature), $T_{f,MC}$, at this position is calculated as follows:

$$T_{f,MC} = \frac{\iint_S \rho T \vec{u} \cdot \vec{n} \, dS}{\iint_S \rho \vec{u} \cdot \vec{n} \, dS} = \frac{\iint_S \rho T \vec{u} \cdot \vec{n} \, dS}{\dot{m}} \quad (3.2)$$

where S is the surface of the circular flow section (Figure 3.4) and \vec{n} its unit normal vector. ρ denotes the fluid density, T the local fluid temperature, \vec{u} its velocity and \dot{m} its total mass flow rate. The convective heat transfer coefficient at this position is defined and can be calculated as follows:

$$h = \lim_{S_w \rightarrow 0} \frac{\phi}{S_w (T_w - T_{f,MC})} \quad (3.3)$$

where S_w is an annular surface on the wall (Figure 3.4) inclosing the flow section, S . T_w is the average temperature of this wall element, or simply the wall temperature when an isothermal wall is considered as in this chapter. ϕ denotes the heat flux transferred between the wall element and the flow. The Nusselt number, Nu , which can be regarded as a dimensionless expression of h , is defined as follows in both helical and straight pipes:

$$Nu = \frac{hd}{\lambda} \quad (3.4)$$

where d is the pipe internal diameter and λ the fluid thermal conductivity. Figure 3.5 illustrates a



Figure 3.4: Typical shape of a wall element (in red) over which h is averaged

qualitative variation of Nu (and thus of h) along a helical or a straight tube, the abscissa axis being the - curvilinear - position along the pipe centerline. The Nusselt number is the highest at the pipe entrance and decreases over a distance called ‘thermal entrance length’ before reaching an asymptotic value, Nu^∞ . For a laminar flow in a straight pipe under uniform wall temperature conditions, the length of the thermal entrance region, L_{th} , can be estimated as follows [221]:

$$L_{th} = \text{Maximum}(0.0565Re \ d ; \ 0.037Re \ Pr \ d) \quad (3.5)$$

$Re = Ud/\nu$ is the Reynolds number, where U is the mean velocity of the primary flow and ν the fluid kinematic viscosity, $Pr = \nu/\alpha$ is the Prandtl number where α is the fluid thermal diffusivity. The first term on the right hand side of Eq. 3.5 represents the length required for the flow to fully develop, i.e. for the velocity field and the local friction factor to become axially invariant, while the second term corresponds to the distance required for the flow to become thermally developed. Equation 3.5 reveals

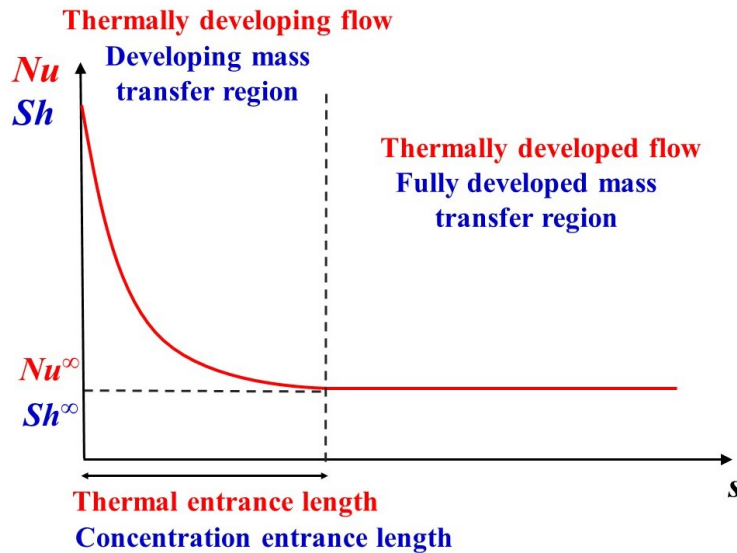


Figure 3.5: Typical variation of the Nusselt (Sherwood) number from the entrance of a straight or a helical pipe

that the thermal entrance length may become very important for large values of Pr . However, in the current study, only Pr numbers ranging from 1 to 10 are considered. With such fluids, entrance effects are usually negligible in the case of pipes of small diameter and/or sufficient length, which is generally the case in the applications targeted in this study, namely heat exchangers (and catalytic reactors and hollow fiber membranes in the case of mass transfer). This is particularly true when dealing with helical geometries. Indeed, under similar operating conditions, the entrance length in helical pipes is generally shorter than in straight ones [222]. Therefore, the asymptotic Nusselt number, Nu^∞ , is sufficient for characterizing the effective heat transfer in helical shape exchangers as long as the fluid Prandtl number is not too high. Accordingly, in this paper, determination of Nu^∞ in helical pipes via CFD simulations will be emphasized. Thus, although the flow and heat transfer characteristics over

the entire pipe are simulated, only Nu^∞ results are reported; entrance effects data are considered beyond the scope of this chapter and will not be reported here.

With a laminar flow regime and an isothermal wall, under ideal conditions (see Section 3.2.2), the asymptotic Nusselt number in straight pipes, Nu_S^∞ , equals 3.657 [223]. On the other hand, contrary to Nu_S^∞ , the asymptotic Nusselt number in helical pipes, Nu_H^∞ , is not constant, but depends on both Reynolds and Prandtl numbers as well as on the pipe geometry. Assuming an incompressible flow with uniform fluid properties, the heat transfer coefficient under thermally developed flow conditions would depend on the helical pipe geometric parameters (d , R_H and p), the fluid properties (ρ , ν , λ and α) and the mean velocity of the primary flow, U . Therefore, according to the Buckingham π theorem, Nu_H^∞ is a functional relation of the following four independent dimensionless parameters: (1) The dimensionless helix pitch, $p^* = p/d$. (2) The dimensionless helix radius, $R_H^* = R_H/d$. These first two parameters characterize the helix shape. (3) The Reynolds number, $Re = Ud/\nu$, which accounts for the operating conditions. (4) The Prandtl number, Pr , which accounts for the fluid properties. As a result of the heat transfer enhancement by the Dean vortices, Nu_H^∞ is always greater than 3.657. Table 3.1 shows a summary of commonly used correlations for evaluating Nu_H^∞ under laminar flow conditions.

Finally, it is worthy to note that the heat transfer analysis carried out in this section can be transposed and applied to mass transfer phenomena. In fact, it has been long recognized that heat and mass transfer processes present similar behaviours. Indeed, in many practical situations, the equations describing mass and heat transfer are mathematically analogous (see Sections 3.2.2 and 3.2.3 for details). Accordingly, heat transfer results can be converted to mass transfer results and vice versa.

Hence, in the framework of the present study, the heat/mass analogy stipulates that if the same geometric (R_H^* and p^*) and operating conditions (Re) are considered, then:

$$Sh_H^\infty = Nu_H^\infty \quad (\text{and } Sh = Nu) \quad \text{if } Sc = Pr \quad (3.6)$$

where Sh is the Sherwood number (the mass transfer analogue to Nu) and Sh_H^∞ its asymptotic value in helical pipes. Sh is defined as follows:

$$Sh = \frac{kd}{D} \quad (3.7)$$

where k is the convective mass transfer coefficient between the wall and the fluid and D the mass diffusivity of the involved species. Under laminar flow conditions and uniform wall concentration, Sh_H^∞ equals 3.657 in virtue of the heat/mass transfer analogy. $Sc = \nu/D$ is the Schmidt number, the mass transfer analogue of Pr . It represents the ratio of momentum diffusivity (kinematic viscosity) to mass diffusivity. Based on the above discussion about Nu_H^∞ and the heat/mass transfer analogy, it

can be argued that Sh_H^∞ depends on the following four dimensionless numbers: R_H^* , p^* , Re and Sc .

3.2.2 CFD modeling and simulation of heat transfer in helical pipes under laminar flow conditions

CFD simulations were carried out for various helical pipe designs and operating conditions. The geometries were drawn using Autodesk Inventor Professional 2018 software. A sufficient tube length was used in order to attain the thermally developed flow region. The 3D numerical domain was meshed using the ANSYS Meshing software. The grid consisted of hexahedral cells only, with a boundary layer mesh in the near-wall region for an accurate calculation of the steep gradients prevailing in this zone. Based on preliminary simulations, the cells size and density were chosen so as to ensure a mesh-independent solution for all the cases studied. CFD simulations were conducted using the commercial code ANSYS Fluent 16. The flow field in the pipe was determined by solving the continuity and Navier-Stokes equations assuming a Newtonian, incompressible, and steady flow and uniform fluid properties (density and viscosity):

$$\text{div}(\vec{\mathbf{u}}) = 0 \quad (3.8)$$

$$\mathbf{d}\vec{\mathbf{iv}}(\vec{\mathbf{u}} \otimes \vec{\mathbf{u}}) = -\frac{1}{\rho} \vec{\nabla} P + \vec{\mathbf{u}} \Delta \nu$$

As boundary conditions, a uniform velocity profile was set at the pipe inlet: as the flow rate is imposed and since a uniform fluid density is considered, the gravity force has no effect on the velocity field and therefore this body force term was not included in the Navier-Stokes equations. At the pipe outlet, a uniform pressure condition was used and the no-slip condition was set at the pipe wall. The temperature field was determined by solving the energy balance equation:

$$\text{div}(\vec{\mathbf{u}}T) = \alpha \Delta T \quad (3.9)$$

As boundary conditions, a uniform fluid temperature is enforced at the inlet, an isothermal wall is considered and the zero temperature gradient is imposed at the pipe outlet. It is noteworthy that the velocity and temperature profiles at the inlet affect the flow and heat transfer phenomena in the entrance region only. Therefore, as this chapter focuses on heat transfer in the thermally developed zone (i.e. Nu_H^∞), the velocity and temperature distributions at the inlet were simply considered as uniform.

The CFD model (i.e. Equations 3.8 and 3.9 and their boundary conditions) assumes: (1) Steady-state flow and heat transfer phenomena. (2) An incompressible Newtonian fluid with uniform properties. (3) The absence of phase transition phenomena. (4) A purely forced convection. Indeed, natural convection effects are neglected since the fluid density is supposed uniform. This assumption is relevant

as long as the Reynolds number is not extremely low and the Grashof number (quantifying buoyancy effects) not extremely high, which is generally the case in heat exchangers. (5) Radiative phenomena are ignored. (6) Heat generation by viscous dissipation is neglected in Equation 3.9. This hypothesis is relevant apart in few particular situations where highly viscous fluids are used under high strain rate conditions. It is worthy to note that, if in addition the axial heat conduction effects are neglected, these assumptions lead to the theoretical result of $Nu_S^\infty = 3.657$ in the case of straight pipes [223]. The hydrodynamics and heat equations were iteratively solved until convergence. The advective terms were discretized using the QUICK scheme while the diffusive ones were central-differenced. Pressure interpolation was carried out using a second order scheme. A total of nearly 280 CFD simulations was carried out. More than 25 helix designs (particularly highly curved ones) were investigated within the following range of geometric conditions: $1.25 \leq p^* \leq 15$ and $0.05 \leq R_H^* \leq 10$. Eight Reynolds number values, ranging from 10 to 2 000, were examined. Three Prandtl numbers were considered in the simulations: 1, 5 and 10. Fluids used in many industrial applications fall within this range of Pr , e.g. most gases, water, refrigerants, many light organic liquids, molten salts and some oils under very high temperature conditions. For each simulation, the local Nu was calculated at different longitudinal positions across the pipe length using Equations 3.3 and 3.4 (and considering a sufficiently small wall element as that depicted on Figure 3.4), and its asymptotic value, Nu_H^∞ , was determined. These CFD results were used to correlate Nu_H^∞ as a function of the helix design (p^* and R_H^*), the fluid properties (Pr) and the flow conditions (Re). They are provided in **appendix A4**

3.2.3 Heat and mass transfer analogy

The procedure described in Section 3.2.2 allows determining the Nusselt number characterizing the heat transfer between the fluid and the pipe wall for Pr ranging from 1 to 10. Under some conditions discussed thereafter, the obtained results may be transposed to describe mass transfer between the fluid and the wall (e.g. mass transfer in membranes, adsorption or heterogeneous reaction processes). Obviously, this is possible for Schmidt numbers in the range of 1 to 10, which is the case in most gas-gas systems. In binary mixtures with uniform density, the diffusive mass flux of a component A , \mathbf{n}_A (in $kg \ m^{-2}s^{-1}$), is given by Fick's law:

$$\mathbf{n}_A = -D\vec{\nabla}\rho_A + \rho_A\vec{v} \quad (3.10)$$

where ρ_A is the mass concentration of A and D its mass diffusivity. \vec{v} is the velocity resulting from the diffusive motion of A and the other species within the mixture. The second term on the right-hand side of Eq.3.10 is generally referred to as the 'bulk motion contribution'. It represents the advective mass flux resulting from the diffusion of the different species which induces a local motion of the mixture. When this term is negligible, Fick's law becomes analogue to Fourier's law of heat conduction. This

is the case under equimolar counter diffusion of species of similar molecular weights or under dilute mixture conditions. Such conditions are encountered in many important gas-gas applications such as tritium removal, recovery of volatile organic compounds and adsorption processes in isotropic mixtures, etc. Most importantly, the bulk motion contribution can be generally neglected in forced convection situations when the Reynolds number is not very low and the flow field three-dimensional (as in the presence of Dean vortices). This significantly broadens the range of conditions for which the heat/mass transfer analogy can be applied in helical geometries. When the bulk motion contribution is negligible, in the absence of any homogeneous chemical reaction, if uniform fluid properties are considered, the steady-state the mass transfer equation becomes analogue to Eq. 3.9 and is given by:

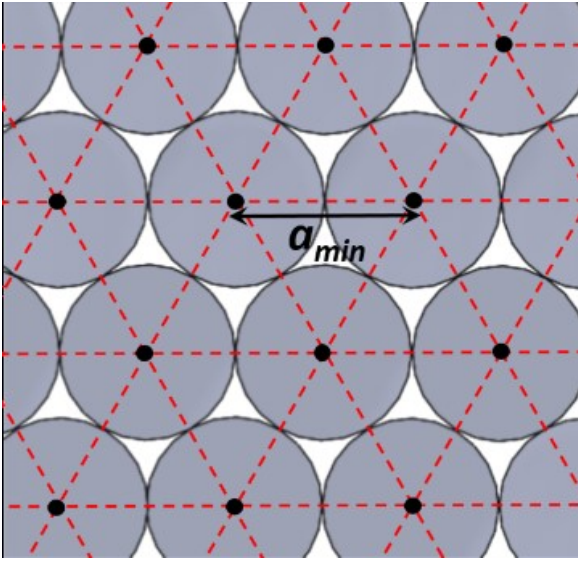
$$\text{div}(\vec{\mathbf{u}}C_A) = D\Delta C_A \quad (3.11)$$

where C_A is the molar concentration of component A . Another restriction to the validity of the heat/mass transfer analogy concerns the boundary condition at the wall. Indeed, in heat transfer simulations (Section 3.2.2), the no-slip condition applies at the pipe wall, while in mass transfer processes, the mass flux at the wall obviously results in a non-zero wall-normal velocity. However, in many situations, this velocity component has negligible effects on the flow field, and thus, the heat/mass transfer analogy remains valid. This is the case in equimolar counter diffusion of species of similar molecular weights or under dilute mixture conditions, even in the presence of a heterogeneous reaction or adsorption phenomena at the wall. In any case, in situations where the heat/mass transfer analogy is not strictly valid, although the results reported in this chapter do not allow a precise evaluation of the Sherwood number, they still provide a first insight about the optimal shape of helical tubes in mass transfer devices.

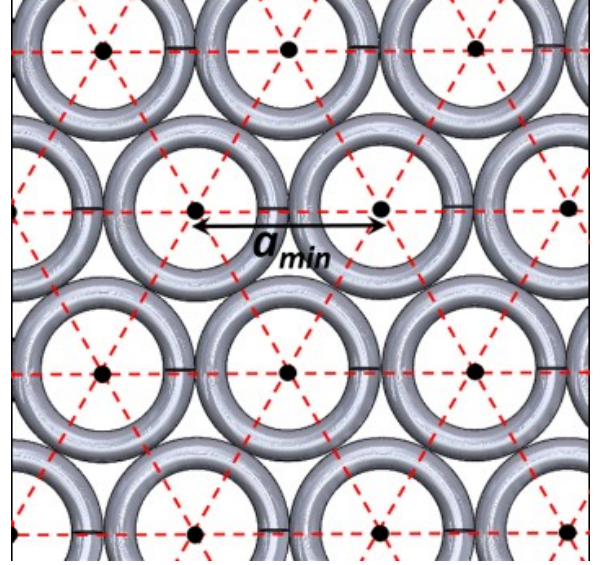
3.3 Optimal packing density of helixes

Helical pipes allow higher transfer efficiencies per unit surface than straight ones. However, they cannot be as densely packed as straight tubes. Thus, the transfer efficiency improvement they provide can be - at least partially - counterbalanced by their lower packing density. Therefore, in order to determine the overall volumetric transfer rate (i.e. heat/mass flux per unit volume) that helical pipes allow achieving, it is necessary to calculate their optimal packing density. To the authors' best knowledge, no analytical solution for this problem has been published thus far in literature. Only Kaufhold et al. (2012) [203] have reported a correlation for estimating helixes packing density, however, as discussed in Section 3.4.5, their model is highly inaccurate. The ideal arrangement for non-overlapping straight tubes or cylinders is an - equilateral - triangular packing (also known as dense hexagonal lattice) (Figure 3.6a) where the distance between the axes of two neighboring cylinders equals their diameter. This configuration allows the straight tubes to best cover the available volume: it can be analytically

shown that, $\phi_{(S,max)}$, the volume fraction they fill, equals $\pi/[4 \sin(\pi/3)] \approx 90.7\%$.



(a) ideally packed cylinders



(b) The triangular (or dense hexagonal) lattice is illustrated by dashed lines

Figure 3.6: Top view of ideally packed helixes of $R_H^* = 2.5$ and $p^* = 1.25$. The black dots represent the axes of the helical or straight tubes.

The CAD commercial software Autodesk Inventor Professional 2018 was used for determining the ideal packing of identical helixes under a triangular arrangement. a_{min} will denote the minimum achievable distance between two neighboring non-overlapping helixes (Figure 3.6b) and $\phi_{(H,max)}$ the volume fraction occupied by these closely packed helixes. a_{min} was determined for more than 240 helix designs in the following range of geometric conditions: $1 \leq p^* \leq 20$ and $0.05 \leq R_H^* \leq 10$. Given the periodicity of the lattice, only three helixes disposed on an equilateral triangular pattern were drawn using the CAD software. Their diameter, d , was arbitrarily taken as 1 mm. The distance separating these helixes was iteratively decreased until determining a_{min} with an absolute tolerance of 0.01 mm. As the lowest possible value for a_{min} is the pipe diameter (situation that occurs in the case of straight pipes), i.e. 1 mm in the present case, thus, the maximum relative error on the computed a_{min} values is about 1%.

These results allowed calculating, $a_{min}^* = a_{min}/d$, the dimensionless minimum distance separating the closely packed helixes. Indeed, dimensionless analysis shows that a_{min}^* is a functional relation of p^* and R_H^* . The CAD results were used to correlate a_{min}^* as a function of these two geometric parameters. They are provided in **appendix A5**.

For a given helix design, once the a_{min}^* value is known, $\phi_{(H,max)}$ can be easily calculated. Indeed, let's consider a triangular prism of height equal to p , the pitch of the helix, and which base is the equilateral triangle that connects the axes of the three closely packed helixes. This volume encloses $1/6th$ of each of the three helices, which corresponds to the volume of half a helix. Thus, $\phi_{(H,max)}$

equals to the half volume of a helix over the volume of the prism element:

$$\phi_{(H,max)} = \frac{\frac{1}{2}V_{Helix}}{V_{prism}} = \frac{\frac{1}{2}\frac{\pi d^2}{4}\sqrt{p^2 + (2\pi R_H)^2}}{\frac{1}{2}a_{min}^2 \sin(\frac{\pi}{3})p} = \frac{\pi\sqrt{1 + (2\pi R_H^*/p^*)^2}}{4a_{min}^* \sin(\frac{\pi}{3})} \quad (3.12)$$

3.4 Results and discussion

3.4.1 CFD results

In the following sections, the CFD results will be mainly presented in terms of Nusselt number and heat transfer enhancement. However, as discussed in Section 3.2.3, based on the heat/mass transfer analogy, these same results can be interpreted in terms of Sherwood number and mass transfer enhancement. As mentioned earlier, for each CFD simulation performed, the circumference-averaged Nu was calculated at different positions along the helical pipe length so as to determine its asymptotic value, Nu_H^∞ . This value, divided by the Nusselt number in a straight pipe, $Nu_S^\infty = 3.657$, represents the heat transfer enhancement allowed by a given helical pipe.

Figure 3.7 shows contour plots of the Nu_H^∞ to Nu_S^∞ ratio in the (R_H^*, p^*) space. These contours were obtained using a triangulation-based cubic interpolation of the CFD results. The geometric parameters for which simulations were performed are represented by black dots. It is worthy to note that, at these points, the values of Nu_H^∞ (divided by Nu_S^∞) that are displayed on the contour plots are exactly the same than those provided by CFD. On the other hand, the results predicted between these points are generated by interpolation. Therefore, they may be expected to not be very accurate since they are quite sensitive to the interpolation scheme used. Indeed, as can be noticed from Figure 3.7, the contour plots exhibit some relatively irregular variations. Nonetheless, these contours allow deriving several major conclusions:

1. HCHPs allow a great improvement of the heat transfer efficiency compared to straight tubes. Indeed, given their high curvatures (Figure 3.3), the flow in HCHPs undergoes strong centrifugal effects leading to intense Dean-type vortices that greatly improve the heat transfer rates.
2. As Re increases, centrifugal forces become more intense, which further enhances the heat transfer efficiency. Hence, in the case where $Pr = 1$, for $Re = 400$, the maximal Nu_H^∞ achieved in HCHPs is about 3.5 times higher than in straight tubes (Figure 3.7a), and its gets nearly 8 times greater than Nu_S^∞ for $Re = 2\,000$ (Figure 3.7c).
3. Nu_H^∞ increases when Pr is increased. For example, under a Re of 2 000, the maximal Nu_H^∞ is about 8 times higher than in straight tubes for $Pr = 1$ (Figure 3.7c), and becomes more than 9 times greater than Nu_S^∞ for $Pr = 10$ (Figure 3.7d).
4. The geometric parameters for which Nu_H^∞ is maximal are not significantly affected by the Reynolds

and Prandtl numbers values. However, when Re and/or Pr are increased, the value of Nu_H^∞ becomes more sensitive to the helix geometry.

5. For any given dimensionless pitch, p^* , there exists an optimal dimensionless helix radius, R_H^* , at which Nu_H^∞ is maximal. The Nu_H^∞ to Nu_S^∞ ratio sharply decreases toward unity when R_H^* tends to zero as the helix geometry approaches that of a straight pipe. This ratio also decreases to unity when R_H^* tends to infinity as the helical pipe straightens (its curvature tends to zero as can be seen from Figure 3.3) and becomes locally similar to a straight tube. However, these effects are not always clearly noticeable from the contour plots of Figure 3.7 since simulations were performed in the range of $0.05 \leq R_H^* \leq 10$ only.
6. For any given R_H^* , the Nu_H^∞ to Nu_S^∞ ratio decreases when p^* increases and tends towards unity at infinite p^* as the helix design approaches a straight pipe, although this effect is not always noticeable in Figure 3.7 as no simulations were performed for p^* values higher than 15.
7. Although Nu_H^∞ generally decreases when p^* is increased, as can be seen from Figure 3.7, this effect is only significant in the case of HCHPs. Indeed, for relatively high R_H^* values, the curvature is not much sensitive to the value of p^* (Figure 3.3). As only helical pipes with rather large R_H^* were investigated in the literature, most authors concluded that the helix pitch has no significant effect on Nu_H^∞ as can be noticed from the correlations reported in Table 3.1. Thus, it is obvious that these correlations cannot accurately predict the Nusselt number in HCHPs as detailed in Section 3.4.3.

3.4.2 Correlation for predicting Nusselt (and Sherwood) numbers in helical pipe laminar flows

The CFD results revealed that, for given Re and Pr numbers, the Nu_H^∞ field in the (R_H^*, p^*) space (Figure 3.7) presents a single maximum (no local optima). And apart the particular case of straight pipes, for any helix geometry, Nu_H^∞ increases with increasing Re and Pr . Despite such a relatively regular behavior, finding a mathematical model that correctly fits the CFD data was extremely challenging and tedious. Indeed, Nu_H^∞ exhibits highly nonlinear variations, especially with respect to the geometric parameters. In fact, the Nu_H^∞ field undergoes steep variations in the HCHPs region, with highly non-uniform and anisotropic gradients, which magnitudes are very sensitive to the helix geometry. Moreover, the mathematical formulation should ensure that the model predicts that $Nu_H^\infty = Nu_S^\infty = 3.657$ at all of the three asymptotic limits where the pipe curvature vanishes and the helix geometry tends toward that of a straight tube, i.e. when R_H^* tends to zero or infinity and when p^* tends to infinity. Otherwise, the derived correlation cannot be reliably used in any model-based optimization for determining the optimal pipe design in heat/mass transfer devices. The development

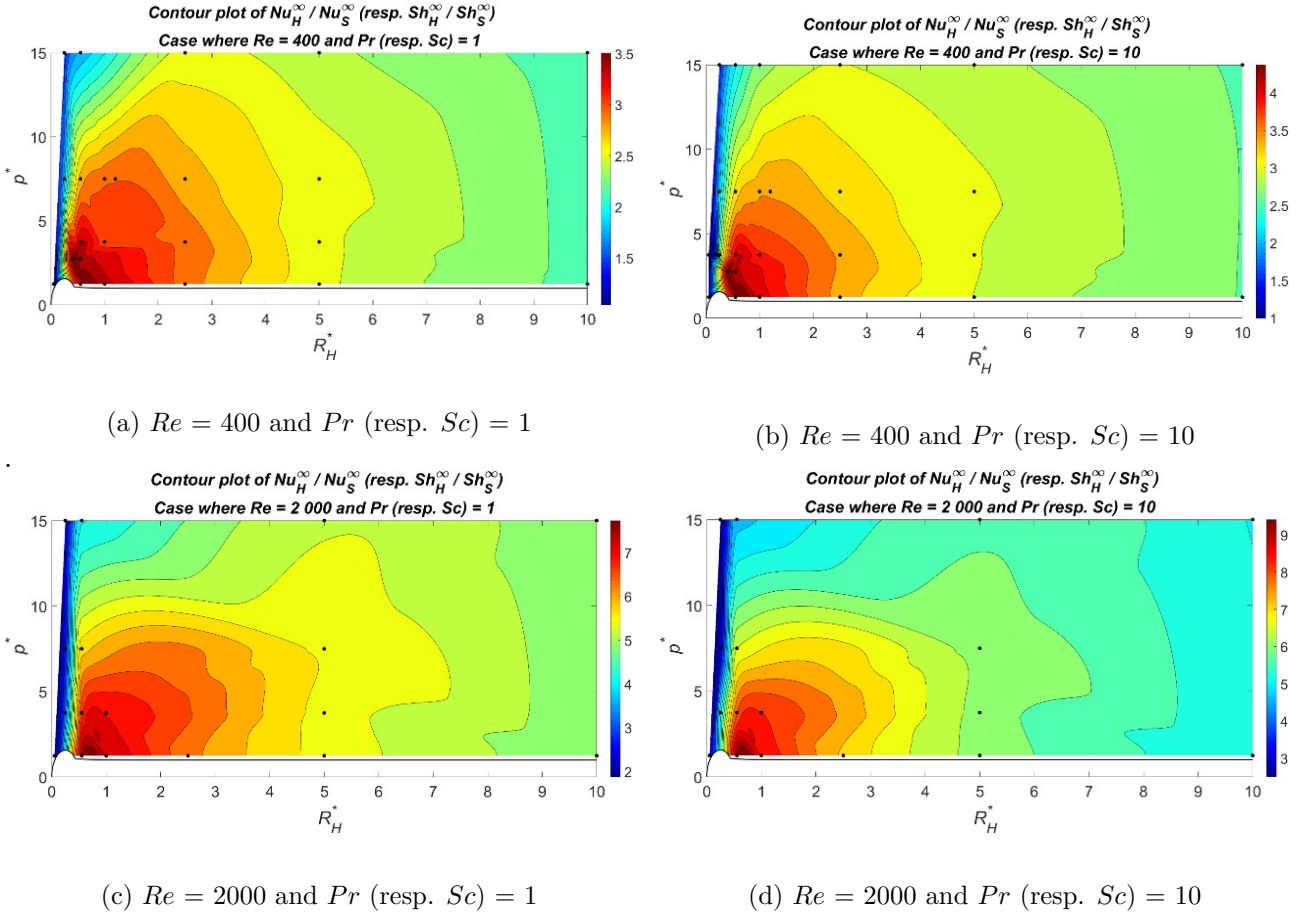


Figure 3.7: Contour plots of the Nu_H^∞ to Nu_S^∞ (respectively Sh_H^∞ to Sh_S^∞) ratio. The black dots represent the geometric conditions for which CFD simulations have been performed. The contours are derived by interpolating these data

of the regression model for fitting the Nu_H^∞ data has been conducted by trial-and-error. The following complex expression has been found to provide the best fit of the CFD results:

$$\begin{aligned}
 Nu_H^\infty &= 3.657 + p_1 A^{p_2} Re^B Pr^{p_7} \exp(-C) \\
 A &= \left[R_H^* \left(1 + \left(\frac{p^*}{2\pi R_H^* p_3} \right)^{p_4} \right) \right]^{-1} \\
 B &= p_5 Pr^{p_6} \\
 C &= p_8 R_H^{*p_9} Pr^{p_{10}}
 \end{aligned} \tag{3.13}$$

The present model includes 10 regression parameters denoted p_i (i being an integer ranging from 1 to 10) which values were determined using an optimization procedure. The term 3.657 corresponds to the asymptotic Nusselt number in a straight tube, Nu_S^∞ . The second right-hand side term in the mathematical model is formulated so as to be always positive, hence, the present correlation guarantees that the predicted Nu_H^∞ value remains greater (or equal) than Nu_S^∞ .

The term denoted A is analogous to the helix dimensionless curvature κ^* (see Eq. 3.1), with the difference that p_3 and p_4 are treated as optimization variables instead of assigning their values to 1

and 2 respectively. The term A vanishes when R_H^* tends to zero or infinity or when p^* tends to infinity, i.e. when the helical pipe geometry tends toward that of a straight one. Thus, the model correctly predicts that $Nu_H^\infty = Nu_S^\infty = 3.657$ at these three limits. The mathematical expression presented in Equations 3.13 was used to correlate the CFD data. It should be recalled that, as mentioned in Section 3.2.2, these results were obtained in the following range of dimensionless parameters: $1.25 \leq p^* \leq 15$, $0.05 \leq R_H^* \leq 10$, $10 \leq Re \leq 2\,000$ and $1 \leq Pr \leq 10$. The optimization problem was formulated as a minimization of the maximum relative difference between the model predictions and the numerical data. For a better accuracy, two sets of parameter values were calculated, the first one for Re ranging from 10 to 400, and the second one for Re between 400 and 2 000. The optimal sets of parameters p_i are reported in Table 3.2. They were determined using a genetic algorithm and the results were further refined using a local optimizer, GRG2.

Table 3.2: Optimal sets for the parameters of the correlation expressed by Equations 3.13

Validity range	p_1	p_2	p_3	p_4	p_5	p_6	p_7	p_8	p_9	p_{10}
$10 \leq Re \leq 400$	3.73×10^{-2}	3.81×10^{-1}	9.50×10^{-1}	2.64	9.38×10^{-1}	-7.09×10^{-2}	5.71×10^{-1}	6.43×10^{-2}	-1.15	3.84×10^{-1}
$400 \leq Re \leq 2000$	3.03×10^{-2}	2.82×10^{-1}	7.19×10^{-1}	2.62	5.7×10^{-1}	-9.01×10^{-2}	4.35×10^{-1}	1.01×10^{-2}	-3.13	-1.32×10^{-1}

Figure 3.8 compares the correlation predictions and the present CFD results (represented by brown disks). It shows that the proposed correlation correctly fits the Nu_H^∞ data as most points are within an error margin of 15%. Indeed, the maximum relative difference between the numerical results and the correlation predictions is respectively 16.9% for Re below and 400 and 14.8% for Re above 400. To check the robustness of the correlation, additional CFD simulations were performed for p^* up to 60 and R_H^* up to 20. Although the correlation was built upon CFD results acquired for $p^* \leq 15$ and $R_H^* \leq 10$, it successfully predicts these additional Nu_H^∞ data (represented by blue triangles in Figure 3.8) within an error margin below 15%. This predictive capacity of the present correlation is due to its mathematical formulation (Eqs. 3.13) which as discussed previously, guarantees correct results at the asymptotic limits where the helical pipe geometry tends toward that of a straight one, i.e. ensures results to be correctly bounded. Therefore, the present correlation is believed to lead to realistic and valid Nu_H^∞ values even beyond the range of geometric conditions investigated in this chapter.

Figure 3.9 shows the contour plots of the Nu_H^∞ to Nu_S^∞ ratio that are calculated using the present correlation for Re values of 400 and 2 000 and Pr values of 1 and 10. A good agreement with Figure 3.7 is observed, although the model data are much smoother since they are not affected by interpolation approximations. The maximal values of Nu_H^∞ and the geometric parameters for which they occur are correctly estimated by the model, and the Nu_H^∞ variations with respect to the helix geometry,

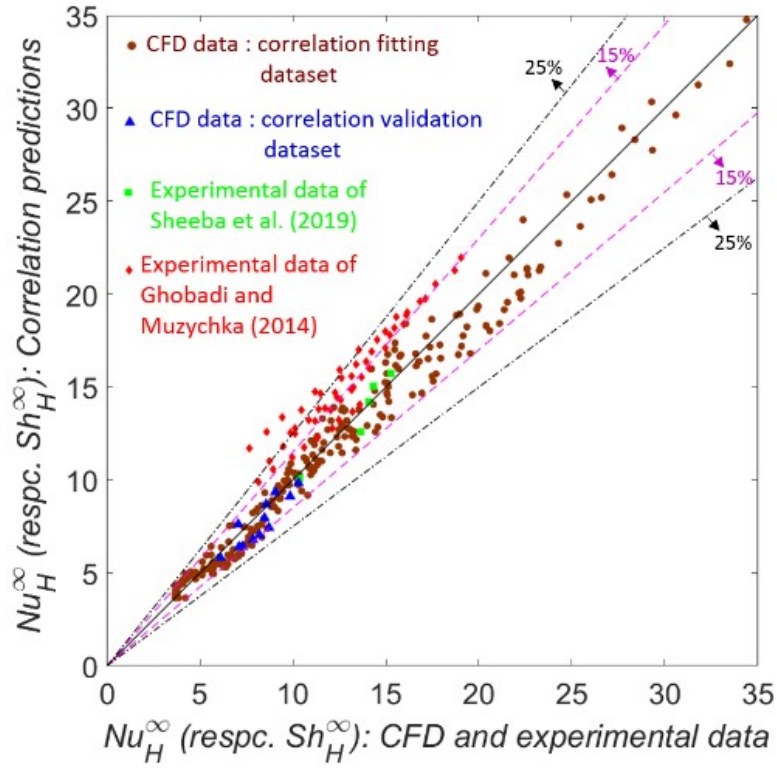


Figure 3.8: Parity diagram of Nu_H^∞ : CFD and experimental data versus correlation predictions

operating conditions and fluid properties are successfully predicted.

3.4.3 Comparison between the current and literature correlations

In order to further assess the potentiality of the new correlation, its predictions are compared to that of literature correlations in Figures 3.10, 3.11 and 3.12. It is noteworthy that most available correlations (see Table 3.1) account for both flow and geometry effects via a single dimensionless parameter, the Dean number, which is defined as follows:

$$De_{RH} = \frac{\rho d U}{\mu} \sqrt{\frac{d}{2R_H}} = Re \sqrt{\frac{1}{2R_H^*}} \quad (3.14)$$

However, this formulation leads to systematic errors in the HCHPs region. First, as shown in Figure 3.10 for the correlations of Dravid et al. (1971) [178] and Kalb and Seader (1974) [218], when R_H^* tends to zero, models based on De_{RH} predict an infinite Nusselt number instead of 3.657. Moreover, these correlations ignore the effects of the helix pitch on the achieved Nu_H^∞ . Indeed, as reported in Table 3.1, so far, literature studies has only dealt with ‘classical helixes geometries’, i.e. helical designs with a relatively high R_H^* . For such geometries, the helix pitch has little effect on Nu_H^∞ values as can be noticed from Figures 3.7 and 3.9, which explains why this parameter has not been considered in most previous correlations. Nonetheless, since these correlations were derived by regressing experimental measurements acquired on non-highly curved helixes, they are expected to accurately predict Nu_H^∞ in such geometries. Therefore, the good agreement between the current correlation and the former ones

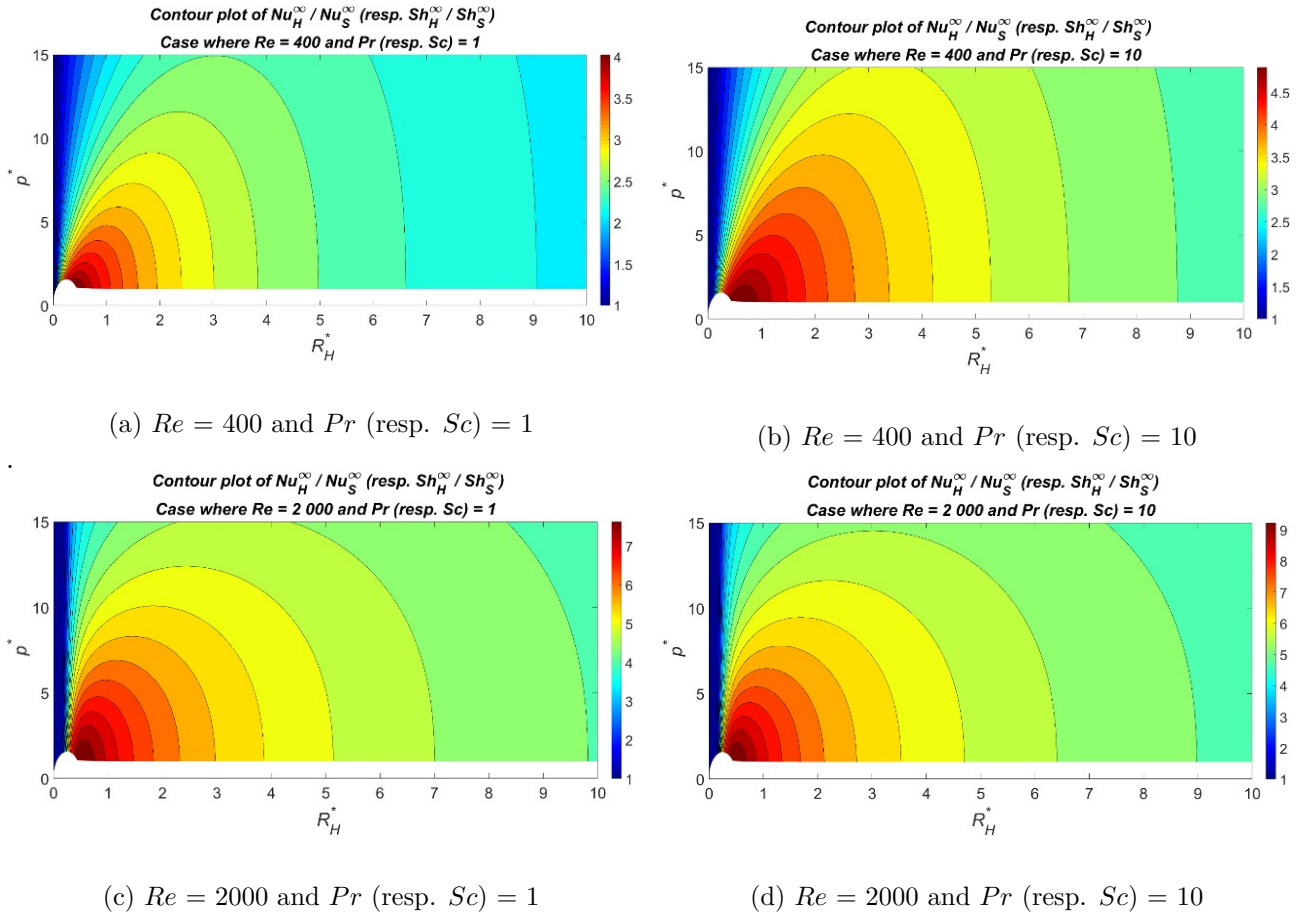


Figure 3.9: Contour plots of the Nu_H^∞ to Nu_S^∞ (respectively Sh_S^∞ to Sh_H^∞) ratio calculated using the present correlation (Eqs. 3.13). The contour plots at $Re = 400$ were generated using the set of parameters valid for $10 \leq Re \leq 400$ (Table 3.2)

at large R_H^* values (Figure 3.9) validates the current CFD simulations and correlation for the case of classical helixes.

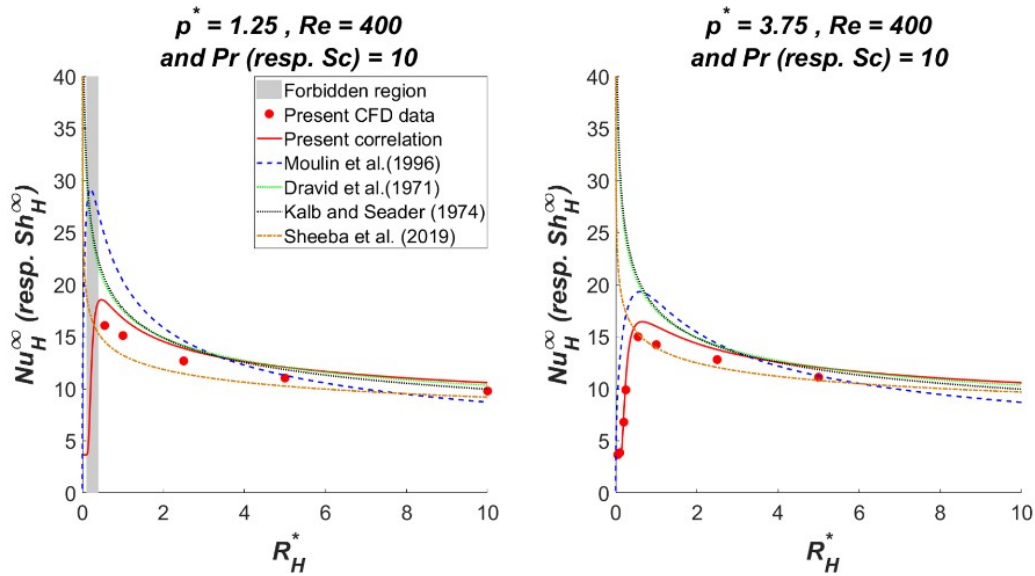


Figure 3.10: Nu_H^∞ (respectively Sh_H^∞) versus R_H^* at two different p^* : comparison of different correlations

The correlation provided by Sheeba et al. (2019) [220] (Table 3.1) accounts for the helix pitch effects on the achieved Nu_H^∞ . However, it presents two major weaknesses. First, it leads to an infinite Nusselt number when R_H^* tends to zero (Figure 3.10), and second, it predicts a slight increase of Nu_H^∞ when the helix pitch is increased (Figure 3.11) contrary to what is obtained by CFD and observed experimentally in other studies (e.g. [224]).

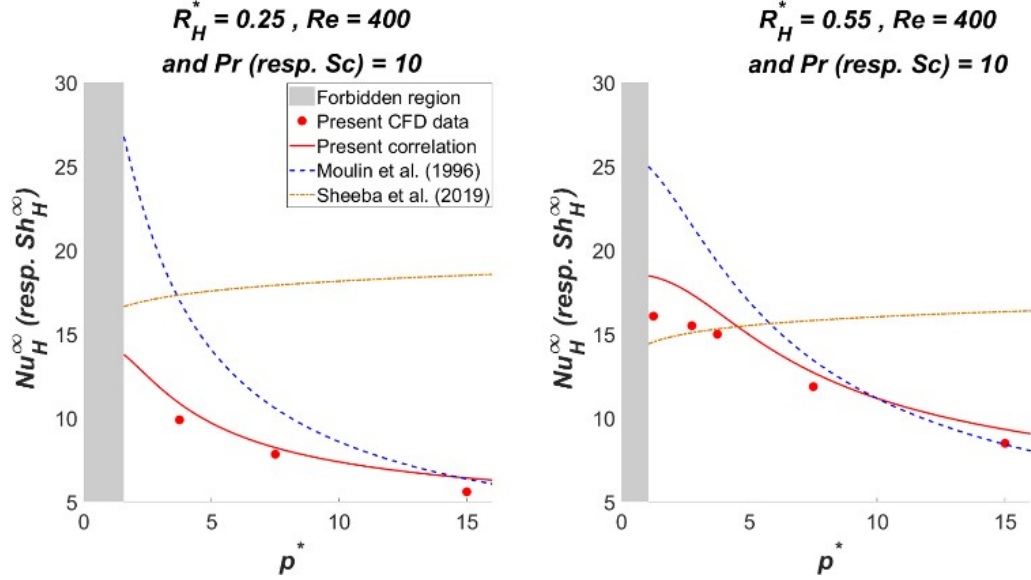


Figure 3.11: Nu_H^∞ (respectively Sh_H^∞) versus p^* at two different R_H^* : comparison between the present correlation and those of Moulin et al. (1996) [168] and Sheeba et al (2019) [220]

The correlation of Moulin et al. (1996) [168] (Table 3.1), built upon mass transfer experimental data, accounts for the helix geometry and operating conditions effects via a Dean number defined as follows:

$$De_\gamma = \frac{\rho d U}{\mu} \sqrt{\frac{d}{2\gamma}} = Re \sqrt{\frac{\kappa^*}{2}} = Re \sqrt{\frac{1}{2R_H^* [1 + (\frac{p^*}{2\pi R_H^*})^2]}} \quad (3.15)$$

where κ^* is the dimensionless helix curvature. This definition of the Dean number is more appropriate than that presented in Eq. 3.14. In particular, De_γ vanishes at the three asymptotic limits for which the helix geometry approaches a straight pipe. This is why the correlation of Moulin et al. (1996) [168] correctly reproduces the shape of the curves showing Nu_H^∞ versus R_H^* (Figure 3.10) and captures the decrease of Nu_H^∞ when p^* is increased (Figure 3.11). However, it also suffers from several drawbacks. Indeed, it leads to Nu_H^∞ equal zero instead of 3.657 at the limits at which the helix curvature vanishes, i.e. when R_H^* tends to zero (Figure 3.10) or infinity and when p^* tends to infinity. More importantly, it largely overestimates the Nu_H^∞ value in HCHPs when Re is increased. As shown in Figure 3.12, the present model correctly captures the Re effects and is way more accurate than the correlation of Moulin et al. (1996) [168]. Note that the discontinuity in the actual correlation curves is due to the use of two different sets of parameter values depending on whether Re is higher or lower

than 400 (Table 3.2).

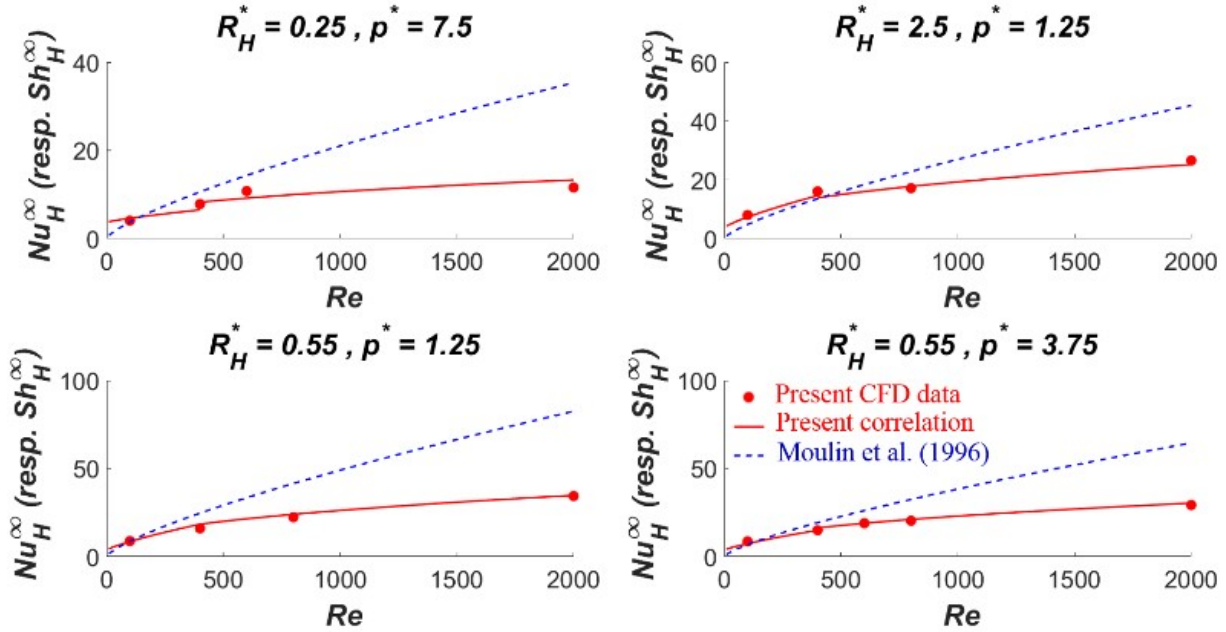


Figure 3.12: Nu_H^∞ (respectively Sh_H^∞) variation with Re for four different helices at Pr (respectively Sc) = 10

3.4.4 Correlation and CFD data validation using experimental data from literature

In addition to CFD results, for a more trustworthy validation, the correlation results were compared to the experimental data of Ghobadi and Muzychka (2014) [219] and Sheeba et al. (2019) [220]. Table 3.3 summarizes the geometric and operating conditions over which these measurements were obtained. It is noteworthy that even the experiments performed for a Re higher than 2 300 correspond to a laminar flow regime. Indeed, transition to turbulence is delayed in helical pipe flows due to the stabilizing effects of centrifugal forces ([206]; [14]).

The last column in Table 3.3 recalls the range of conditions over which the present CFD data were performed, and hence, upon which the current correlation was built. It can be noticed that most of the experimental results were acquired for conditions beyond the validity range of the present correlation. Nevertheless, as shown in Figure 3.8 and Figure 3.13, an excellent agreement is obtained between the correlation and Sheeba et al. (2019) [220] results (represented by green squares on Figure 3.8) which were all predicted within an error margin of 9%. Figure 3.13 shows that the correlation correctly captures the effects of the Reynolds number. A good agreement is obtained with the data of Ghobadi and Muzychka (2014) [219] (represented by red diamonds in Figure 3.8) as most of their experimental results are predicted with a relative error less than 25%.

Differences between the correlation and the experimental results are due to several reasons, mainly the assumption of uniform fluid properties in CFD simulations, the accuracy of the current correlation

Table 3.3: Ranges of geometric and operating conditions over which the literature experimental data were acquired and the present correlation was built

	Sheeba et al. (2019) [220]	Ghobadi and Muzychka (2014) [219]: helical pipe 1	Ghobadi and Muzychka (2014) [219]: helical pipe 2	Ghobadi and Muzychka (2014) [219]: helical pipe 3	Range of parameters investigated using CFD and upon which the present correlation was built
R_H^*	29.8	6.1	12.1	24.2	[0.05 – 10]
p^*	6.1	nearly 1	nearly 1	nearly 1	[1.25 – 15]
Pr	[3 – 5]	[5 – 8.5]	[5 – 8.5]	[5 – 8.5]	[1 – 10]
Re	[940 – 3200]	[440 – 2510]	[960 – 2530]	[700 – 2020]	[10 – 2000]

and experimental errors. However, as can be noticed from Figure 3.8, the data of Ghobadi and Muzychka (2014) [219] are systematically overestimated by the current model. This is probably due to the experimental procedure they followed. Indeed, Ghobadi and Muzychka (2014) [219] placed their helical coil within a non-agitated water bath which temperature was maintained at 40°C. For calculating the convective heat transfer coefficient and the Nusselt number, they assumed the wall temperature of their helical pipe to be equal to 40°C. However, in the absence of an efficient agitation, the wall temperature can significantly deviate from that of the water bath, especially because the heat transfer coefficient in the internal flow is large. This leads to an underestimation of the experimentally measured Nu_H^∞ and probably explains the systematic deviation between their measurements and the actual correlation predictions.

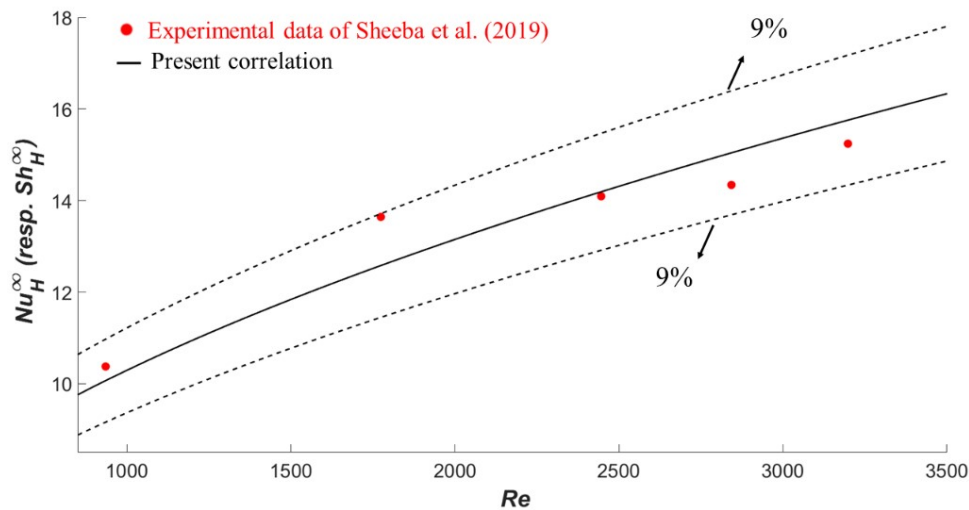


Figure 3.13: Comparison between the present correlation predictions and the experimental data of Sheeba et al. (2019) [220]

3.4.5 Optimal packing density of helices: results and correlation

As noted in Section 3.3, the dimensionless distance between closely packed helices, a_{min}^* , was determined using a CAD software for different helices geometries. Figure 3.14 shows the contour plot of the interpolated results. The lowest possible value for a_{min}^* is 1, and is achieved with straight tubes, i.e. when R_H^* is zero or when p^* tends to infinity. a_{min}^* obviously increases when R_H^* is increased as can be noticed from Figure 3.6 for example. When p^* is increased, the spacing between the helices turns enlarges. Hence, the helices can be brought closer and imbricate, which leads to a decrease of a_{min}^* (as can be noticed from Figure 3.15).

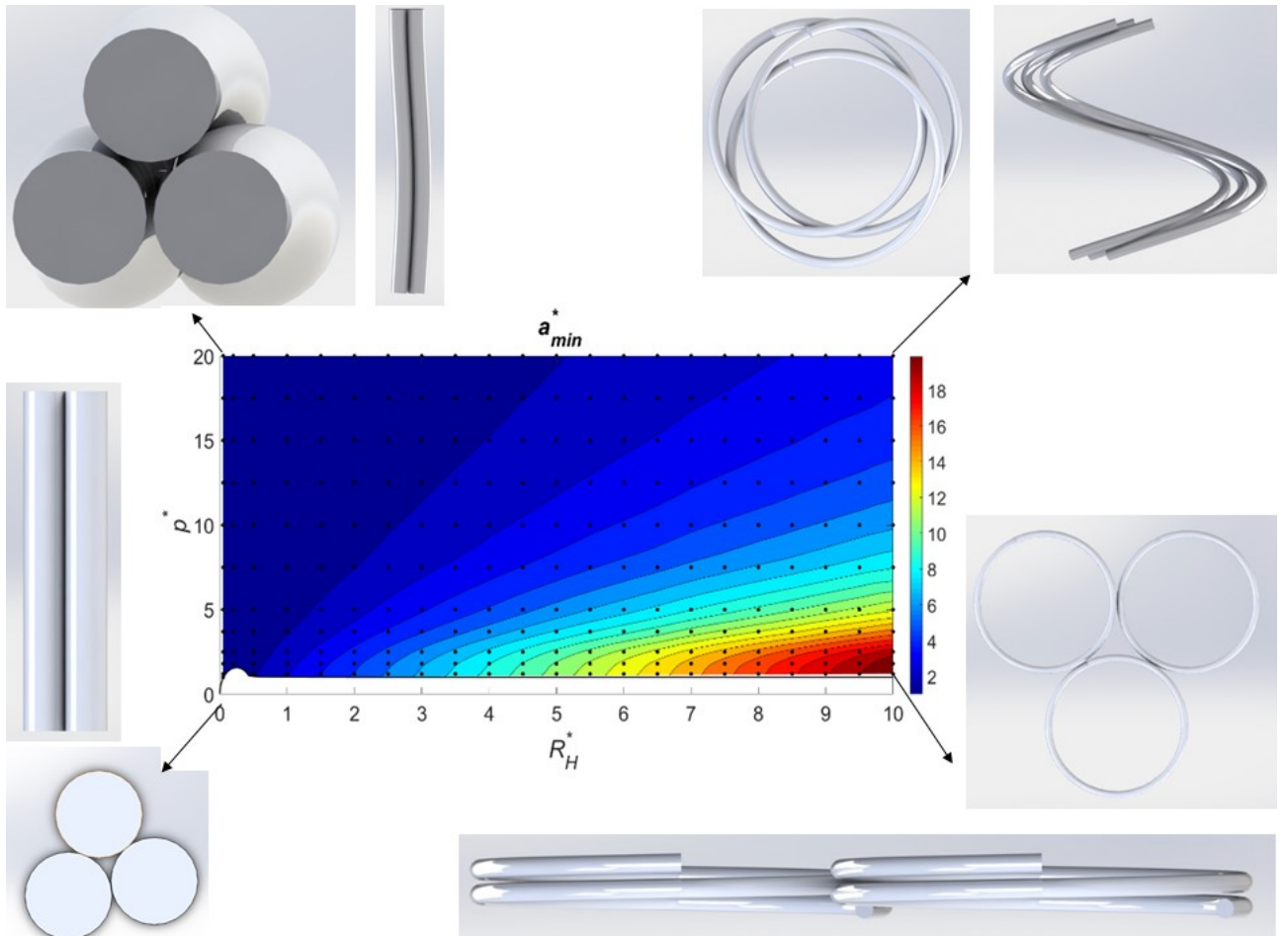


Figure 3.14: Contour plot of a_{min}^* in the (R_H^*, p^*) space. The black dots represent the geometric conditions for which CAD results are acquired and some representative helix geometries

To the authors' knowledge, the only available correlation for determining a_{min}^* or the helices packing density is that reported in Kaufhold et al. (2012) [203]. However, the effects of the helix pitch are not taken into account in this correlation. Thus, it obviously lacks accuracy since a_{min}^* can be very sensitive to p^* value as can be noticed from Figure 3.14. Therefore, a regression model for a_{min}^* is proposed in this chapter. The following mathematical expression, constructed by trial-and-error, was found to provide the best fit of the CAD data:

$$\begin{aligned}
a_{min}^* &= 1 + A \tanh(Bp^{*C}) \\
A &= p_1 R_H^* + p_2 \\
B &= p_3 R_H^{*p_4} \\
C &= p_5 \ln(R_H^*) + p_6
\end{aligned} \tag{3.16}$$

The present expression includes 6 regression parameters denoted p_i (i being an integer ranging from 1 to 6) which values were determined using an optimization procedure in order to minimize the maximum relative difference between the correlation outputs and the CAD data. The hyperbolic tangent term is formulated so as to vanish when R_H^* tends to zero or when p^* tends to infinity. Accordingly, the correlation correctly predicts that a_{min}^* equals one at these limits. The mathematical expression presented in Equations 3.16 was used to correlate the CAD data which were obtained in the following range of dimensionless parameters: $1 \leq p^* \leq 20$ and $0.05 \leq R_H^* \leq 10$. The optimization problem was solved using a genetic algorithm and the results were further refined using a local optimizer, GRG2. For a better accuracy, two correlations were derived, depending on whether R_H^* is lower or higher than 2 respectively. The optimal sets of the parameters p_i are reported in Table 3.4. An excellent agreement

Table 3.4: Optimal sets for the parameters of the correlation expressed by Equations 3.16

Validity range	p_1	p_2	p_3	p_4	p_5	p_6
$0 \leq R_H^* \leq 2$	1.88	-5.54×10^{-2}	3.50	5.65×10^{-1}	-1.65×10^{-2}	-1.50
$2 \leq R_H^* \leq 10$	2.04	-3.65×10^{-1}	4.44	0	1.35×10^{-1}	-1.52

between the model and the CAD results is obtained (Figure 3.15) as their maximal relative difference is 2.80% for R_H^* below 2 and 4.30% for R_H^* above 2 respectively. To check the robustness of the correlation, additional a_{min}^* computations (provided as **Appendix A.5**) were performed for p^* up to 1 000 and R_H^* up to 500. The model was able to predict all of these data with within a maximum error margin of 4.5% which demonstrates its predictive capacity. The contour plot of a_{min}^* was calculated using the present model (Equations 3.16) and is given in Figure 3.16a. The current correlation along with Equation 3.12 were used to determine the helixes optimal packing density, $\phi_{(H,max)}$, in the (R_H^*, p^*) space. The contour plot of the $\phi_{(H,max)}$ to $\phi_{(S,max)}$ ratio is given in Figure 3.16b. $\phi_{(S,max)}$ is the optimal packing density of straight tubes which approximately equals 90.7%.

Figure 3.16b shows that the $\phi_{(H,max)}$ to $\phi_{(S,max)}$ ratio is always lower than unity as helixes cannot be as efficiently packed as straight tubes. However, it can be noticed that highly curved helixes allow considerably higher packing densities than classical ones, and thus, they provide much larger specific surface areas for heat/mass transfer. As HCHPs also lead to higher transfer efficiencies, they are by far more advantageous than classical ones in term of process intensification. Figure 3.16b also

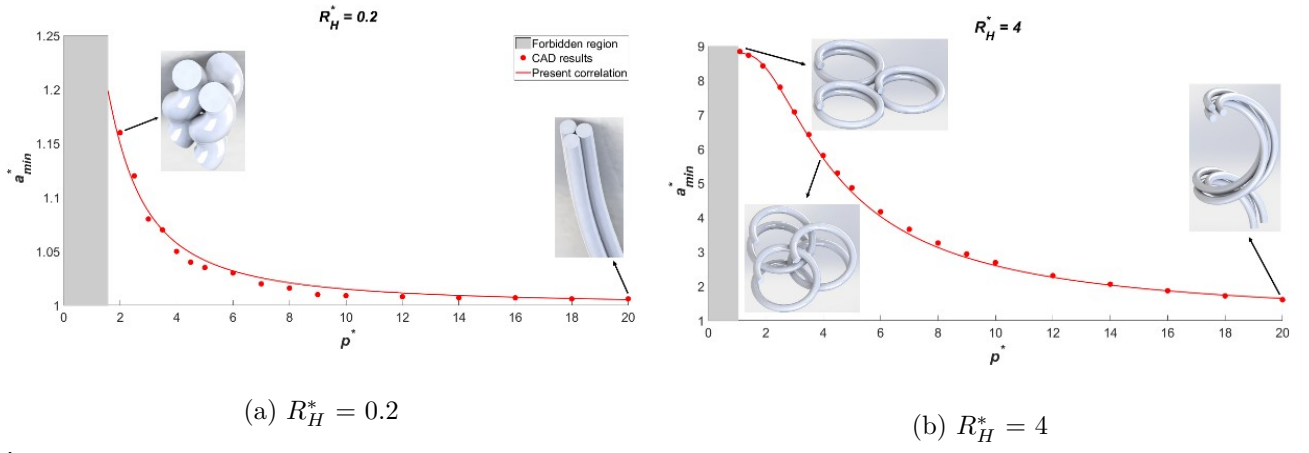


Figure 3.15: a_{min}^* versus p^* with comparison between the CAD results and the present correlation (Equations 3.16)

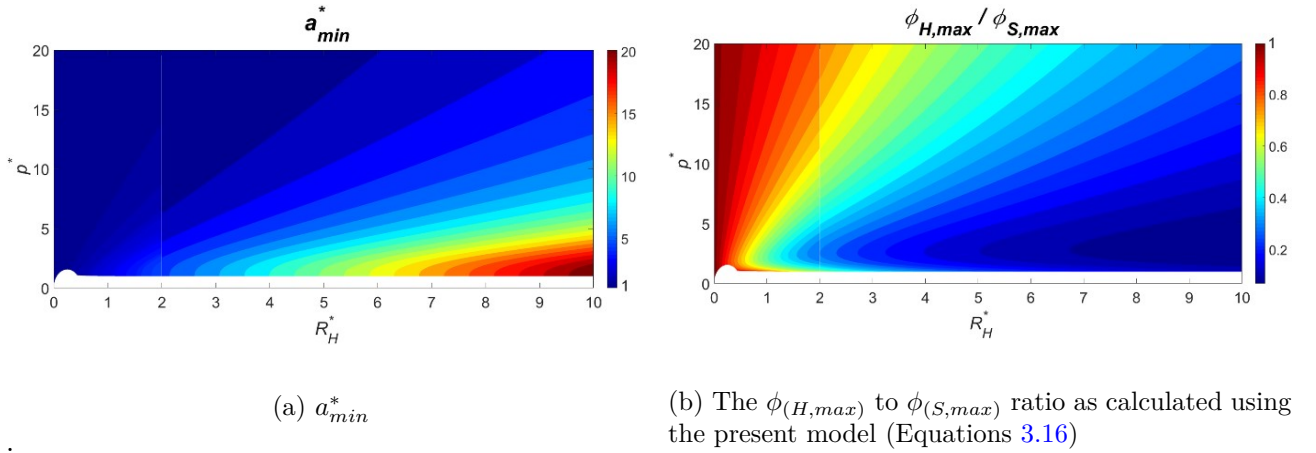


Figure 3.16: Contour plots in the (R_H^*, p^*) space of (a) a_{min}^* and (b) of the $\phi_{(H,max)}$ to $\phi_{(S,max)}$ ratio

reveals that apart for very low R_H^* , when p^* is increased, $\phi_{(H,max)}$ first decreases to a minimum before starting to increase. This is explained by the fact that increasing the helix pitch engenders additional void between the helix turns on the one hand, and on the other hand, the larger space between the helix turns allows the different helices to be brought closer together. However, at very low pitches, this additional spacing enables the helices to slightly approach only but not to imbricate. Therefore, the overall volume fraction filled by the helices decreases. Once a sufficient p^* is reached, further increasing the helix pitch allow the helices to better imbricate (Figure 3.15) which increases their optimal packing density.

3.4.6 Overall intensification factor and potentiality of highly curved helical pipes designs

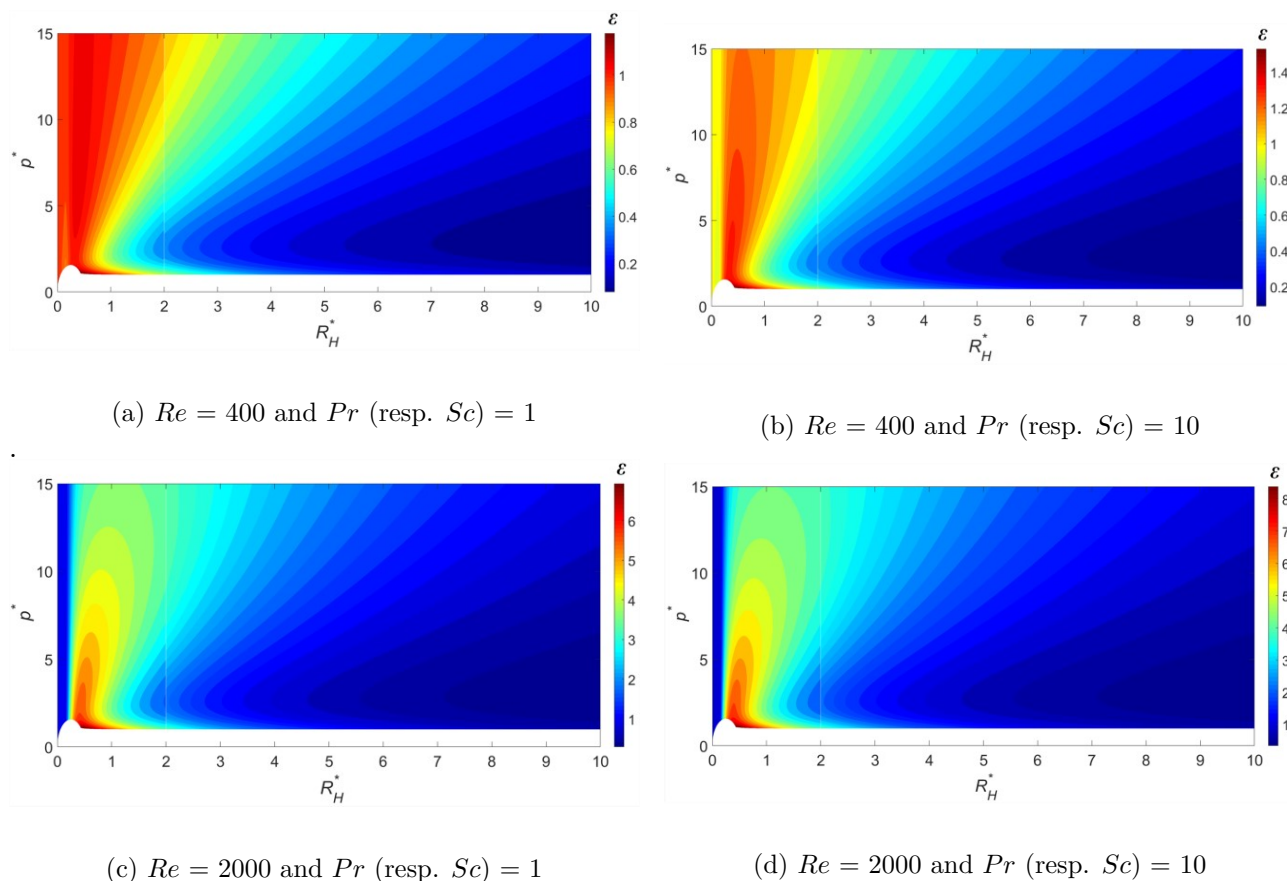
As shown in the previous sections, HCHPs lead to great transfer efficiencies but cannot be as densely packed as straight tubes. These two aspects should be combined together for quantifying the volumetric transfer rate enhancement that these designs allow achieving when used in packed modules, i.e. for assessing the enabled unit volume reduction of reactors, heat exchangers or membrane contactors.

Accordingly, the following intensification factor, ϵ , is proposed:

$$\epsilon = \frac{Nu_H^\infty \phi_{H,max}}{Nu_S^\infty \phi_{S,max}} \quad \text{or} \quad \epsilon = \frac{Sh_H^\infty \phi_{H,max}}{Sh_S^\infty \phi_{S,max}} \quad (3.17)$$

For a same tube diameter, it can be analytically shown that the $\phi_{H,max}$ to $\phi_{S,max}$ ratio equals the ratio of the specific surface area of helical and straight pipes. For a same fluid, the Nu_H^∞ to Nu_S^∞ (resp. Sh_H^∞ to Sh_S^∞) ratio is equal to the ratio of the heat (resp. mass) transfer coefficients in helical and straight tubes respectively. Thus, ϵ physically represents the ratio of the heat/mass flux achieved in helical pipes to that achieved in straight ones. For example, an $\epsilon = 2$ indicates that the use of HCHPs allows obtaining similar transfer performance than straight tubes while reducing the volume of the heat/mass transfer device by nearly a factor 2. This is true whenever the heat/mass transfer resistance in the internal fluid side is the one that limits the overall transfer rate. This situation is commonly encountered in heat exchangers. It also occurs in many mass transfer devices, e.g. fluid degassing in membrane contactors under vacuum operation and fluid dispensing systems based on vaporization (e.g. pure liquid on the shell side of a contactor).

Figure 3.17 shows the contour plot of ϵ in the (R_H^*, p^*) plane for different fluid properties and operating conditions. Note that different scales are used for each subfigure. Figures 3.17a and 3.17b reveal that, at very low Re, HCHPs allow a moderate improvement of the transfer rates only, while classical helices perform even worse than straight tubes. The reason is that, at low Re, centrifugal effects are moderate and thus generate Dean vortices of low intensity. Therefore, the provided heat/mass transfer enhancement remains limited and barely compensates the effects of the decrease of the packing density. The intensification factor improves with increasing Re and Pr (resp. Sc) numbers. For $Re = 2\,000$ for example, HCHPs achieve volumetric transfer rates nearly 6.5 times higher than straight tubes for Pr (resp. Sc) = 1 (Figure 3.17c), and the intensification factor exceeds 8 for Pr (resp. Sc) = 10 (Figure 3.17d). These results demonstrate the huge potential of HCHPs for process intensification.

Figure 3.17: Contour plots of the intensification factor, ϵ

3.5 Conclusion

This chapter focused on the heat/mass transfer enhancement in helical pipes, especially highly curved ones, under laminar flow conditions. Novel designs, offering huge potentialities for intensified mass and/or heat transfer performance have been identified: on the one hand, they generate intense Dean-type vortices, and on the other hand, they can be densely packed. The results demonstrate that highly curved helices allow intensifying the volumetric transfer rate up to a factor 8, which should enable a massive unit volume reduction of reactors, heat exchangers and membrane contactors, as soon as the mass or heat transfer resistance is mostly located in the internal fluid (bore) side. This situation is likely to occur in gas-liquid heat exchangers, catalytic reactors with large reaction rates, fluid degassing in membrane contactors under vacuum operation, or fluid dispensing systems based on vaporization (e.g. pure liquid on the shell side of a contactor).

Chapter 4

Transport phenomena in helical heat and mass exchangers under high Prandtl/Schmidt number conditions*

*This chapter constitutes an extended version of an full paper that has been published in 6th International Conference on Fluid Flow, Heat and Mass Transfer- Ottawa- Canada, **FFHMT'19**.

[202] **Omran Abushammala**, Rainier Hreiz, Cecile Lemaitre, Eric Favre. (2019): “Maximizing mass transfer using highly curved helical pipes: A CFD investigation”, *6th International Conference on Fluid Flow, Heat and Mass Transfer*, June 18-19, 2019 Ottawa, Canada -**doi:10.11159/ffhmt19.145**.

Summary

In this chapter, a systematic analysis of heat/mass transfer performances in highly curved hollow membrane contactors and heat exchangers is conducted. The influence of the nondimensional numbers R_H^* and p^* (respectively the helical radius and helical pitch, both nondimensionalized by the pipe diameter, d) on heat/mass transfer is evaluated through CFD simulations. Helical membranes contactors and heat exchangers of lengths ranging from 30 to 6 000 d , nondimensional helical radiuses R_H^* between 0.05 and 10, and nondimensional helical pitches p^* between 1.25 and 15 are considered. The enhancement factor ϵ , which is equal to the heat/mass transfer ratio (comparing the Nusselt/Sherwood number of helical and straight pipes) multiplied by the packing density ratio of helical and straight pipes, is used to evaluate the performance of each geometry. A maximal enhancement is achieved for highly curved and elongated helical pipes. As an example, for a Prandtl/Schmidt number of 100 and a Reynolds of 2 000, such geometries allow reaching asymptotic Nusselt/Sherwood values which are about 18 times as high as those achieved in straight tubes. For a Prandtl/Schmidt number of 1 000 and Reynolds of 2 000, asymptotic heat/mass convective transfer rates get nearly 55 times higher than those obtained using straight pipes.

4.1 Introduction

Curved geometries are frequently encountered in industrial processes because of the presence of Dean vortices which produce better performances than the straight pipes. In particular, these geometries are used for: (1) Helically coiled heat exchangers, for example in anaerobic digesters [150], refrigeration systems [151], power plants, and nuclear reactors [152] among many other applications; (2) Mass transfer enhancement in catalytic reactors [153], dense [154] and porous [155] membrane contactors, etc; (3) Fouling and clogging reduction in membrane filtration [156]; (4) Improvement of mixing efficiency and homogenization [157]. The pipe curvature induces a centrifugal force that generates Dean vortices, two longitudinal counter-rotating recirculations. Dean vortices disrupt the thermal/mass boundary layer, thus limiting concentration and temperature polarization, and enhance the overall heat/mass transfer performance, with an amplified Nusselt and Sherwood numbers. This chapter is a complement to Chapter 3, since it addresses heat/mass transfer in highly curved helical pipes, i.e. helical geometries with small helical radius and pitch, at high Prandtl numbers (and by analogy, high Schmidt numbers) ranging from 100 to 1 000.

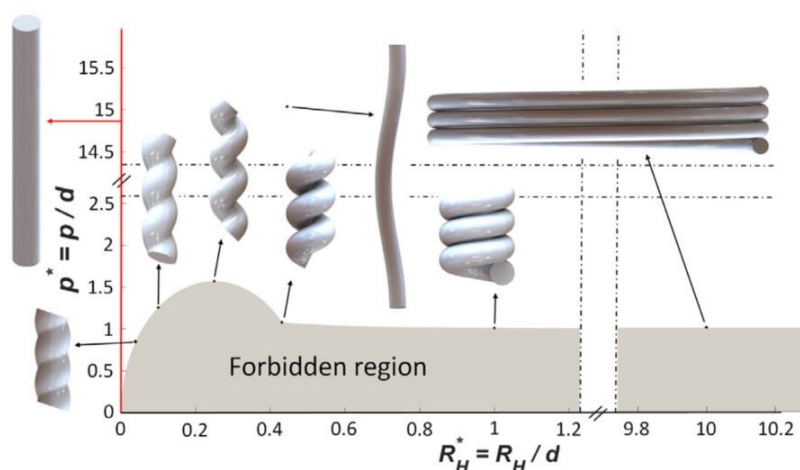


Figure 4.1: Limit of the forbidden region in the (R_H^*, p^*) space (adapted from Przybył and Pierański (2001) [201]) and some representative helix geometries Abushammala et al. (2019a) [191]

Figure 4.1 shows in the plane (R_H^*, p^*) different helical shapes and the forbidden region in which it is not possible to design a helical pipe due to overlapping walls. It appears that the helical shape tends toward that of a straight pipe at three asymptotic limits: (i) for a dimensionless pitch p^* tending to infinity; (ii) for a dimensionless helix radius R_H^* tending to infinity; (iii) for a dimensionless helix radius R_H^* tending to zero.

In Figure 4.2 are presented the contours of the dimensionless helix curvature, κ^* , in the (R_H^*, p^*) plane. The dimensionless helix curvature is defined as $\kappa^* = \kappa d = d/\gamma$, γ being the helix radius of curvature. As can be observed in Figure 4.2, the helix curvature tends to zero (the radius of curvature tends to infinity) for the three asymptotic limits reported earlier. Furthermore, the smallest curvature

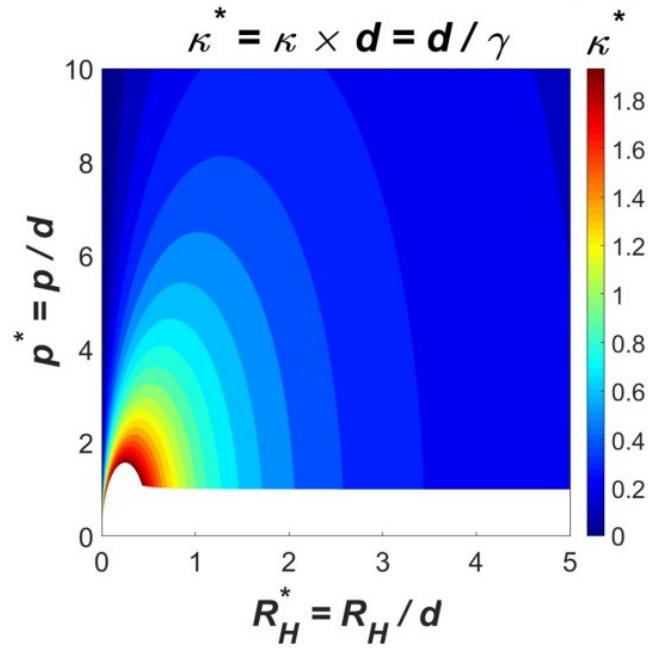


Figure 4.2: Contour plot of the dimensionless helix curvature in the (R_H^*, p^*) space

radii are associated with geometries of low pitches and relatively low helical radii, the so-called ‘highly curved helical pipes (HCHPs)’.

In order to be optimal, helical heat (resp. mass) exchangers should display the best balance between three parameters: the heat/mass transfer expressed by the Nusselt (resp. Sherwood) number, the pressure drop characterized via the friction factor and the packing density. In Chapter 2, the pressure drop in HCHPs was investigated [191] and a correlation for the ratio $C_{f,H}/C_{f,S}$ ($C_{f,H}$ and $C_{f,S} = 64/Re$ being the fully developed friction factor in helical pipes and straight pipes respectively) was derived. An example of $C_{f,H}/C_{f,S}$ contours in the (R_H^*, p^*) plane for a Reynolds number $Re=400$, is reproduced in Figure 4.3, showing maximal friction factor values in zones of maximal dimensionless curvature κ^* .

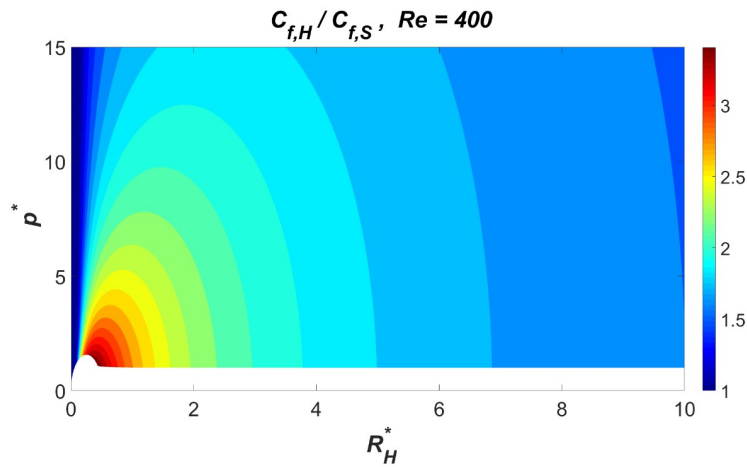


Figure 4.3: Contour plot of the friction factor correlation at $Re = 400$ [191]

As shown in Chapter 3, even for relatively low Prandtl or Schmidt numbers ranging from 1 to 10,

HCHPs allows significant heat/mass transfer enhancement, and these transfer performances improves with increasing Prandtl and Schmidt numbers. Thus, HCHPs are expected to be even more attractive for applications involving fluids with high Sc and Pr as convective transfer rates should be further improved, while the friction remains the same (as it depends on the helix geometry and Reynolds number only). This chapter addresses the heat/mass transfer efficiency in helical pipes under relatively high Pr and Sc values, 100 and 1 000. Computational fluid dynamics (CFD) simulations are performed to determine the Nusselt (resp. Sherwood) numbers in different pipe geometries for Reynolds numbers ranging from 100 to 2 000. Only laminar flow conditions are considered since this flow regime is frequent in hollow fibre membranes, micro-structured heat exchangers and microfluidics applications, etc., due to the small scales of the employed devices [202].

4.2 CFD computation of Nusselt (and Sherwood) number in helical pipe flows

The CFD simulations presented in this chapter were conducted following the procedure already presented in Chapter 3. However, when Pr or Sc values are increased, the thermal/mass boundary layer becomes thinner, i.e. thermal and concentration gradients in the near wall region become higher. Accordingly, it is necessary to use an extremely fine mesh, especially in the near wall zone, to correctly capture these steep variations. Therefore, the following section presents the mesh-sensitivity tests conducted to ensure that the numerical solutions obtained are reliable and little affected by numerical diffusion and errors issues.

4.2.1 Mesh-independence study

The simulations were conducted for helical pipes with $1.25 \leq p^* \leq 15$ and $0.05 \leq R_H^* \leq 10$, two Prandtl (Schmidt) values were considered, 100 and 1 000, and four Reynold values 100, 400, 800 and 2 000. Autodesk Inventor Professional 2018 software was used to design the geometries. It is noteworthy that Prandtl numbers in the range of 100 to 1 000 are representative of numerous highly viscous fluids such as oils, while Schmidt numbers in this range typically represent diffusion in liquid mediums. As mentioned earlier, when dealing with fluids of high Prandtl or Schmidt numbers, an extremely fine mesh is necessary to obtain a reliable solution. However, with such fluids, the entrance length necessary to achieve the fully developed Nu or Sh becomes extremely important at high Re , as can be noticed from Equation 4.1 [221] which allow estimating the thermal entrance length in straight pipes:

$$L_{th} = \text{Maximum}(0.0565Re \ d ; \ 0.037Re \ Pr \ d) \quad (4.1)$$

Given the important tube length and high mesh density to be considered, even with high per-

formance computers, it is not possible to perform single-run simulations allowing to obtain the fully developed Nu and Sh numbers at high Pr (resp. Sc) conditions. Therefore, simulations were performed in a ‘multi-block’ fashion as represented in Figure 4.4.

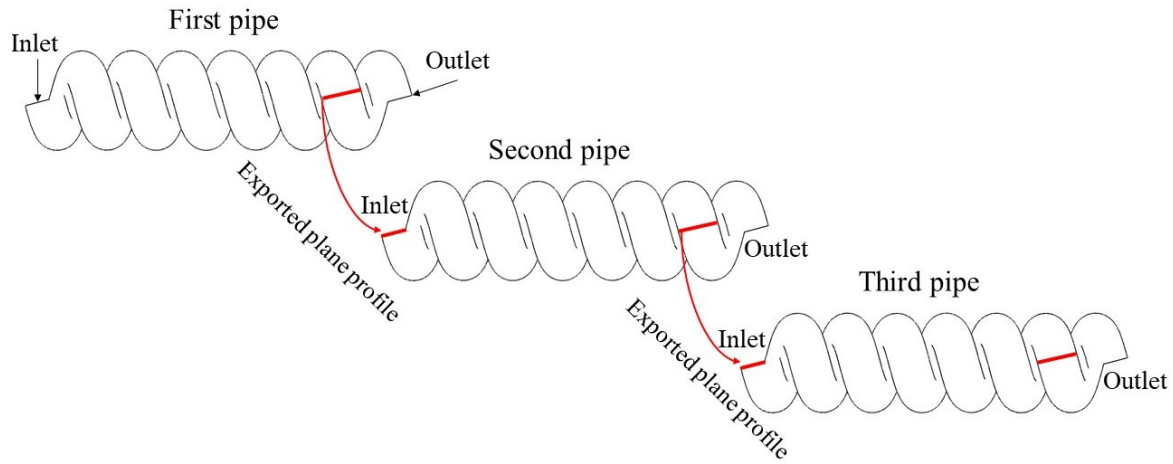


Figure 4.4: The Export-Import technique of the velocity and temperature (resp. concentration) fields

Indeed, simulations were performed on a first pipe segment, and the results obtained at this pipe outlet (or more precisely, at a small distance from the outlet to avoid exit effects) were exported and used then as inlet boundary condition for a second pipe segment. The procedure was repeated until a sufficient total pipe length was simulated to obtain the fully developed Nusselt/Sherwood number.

The mesh used is composed of hexahedral cells only, with a fine boundary layer mesh in the near-wall zone so as to accurately calculate the steep gradients in this zone. A mesh-independence study was conducted, comparing the results obtained with 4 different meshes A , B , C of different resolutions. Each mesh was used for the same reference Fluent simulation. A mean entrance Nusselt (Sherwood) was then calculated as the average of the local Sherwood between the pipe inlet and until the plane at which the Nusselt reaches Nu_H^∞ , the fully developed value. Meshes A , B and C provided very similar results as can be noticed from Table 4.1. Accordingly, the coarsest of these 3 meshes, mesh C , was thus selected and used for all following simulations. Mesh C , shown in Figure 4.5, includes 32 inflation layers with a first layer thickness 10^{-03} mm and edge sizing divisions numbers 80 and sweep division number 20 points per mm.

Table 4.1: Results for the different grids used for the mesh-independence tests. A pipe of 125 mm arc length, 1mm diameter, 2.5 mm helix radius and 1.25 mm pitch was considered. The inlet velocity was 0.4 m/s

Mesh	Number of cells	Mean entrance Nusselt (Sherwood) number	Percentage difference % with mesh A
Model A	23.8 Million	24.50	
Model B	12.6 Million	24.59	0.3% difference with mesh A
Model C	8.80 Million	24.70	0.8% difference with mesh A
Model D	4.60 Million	25.50	3.9% difference with mesh A

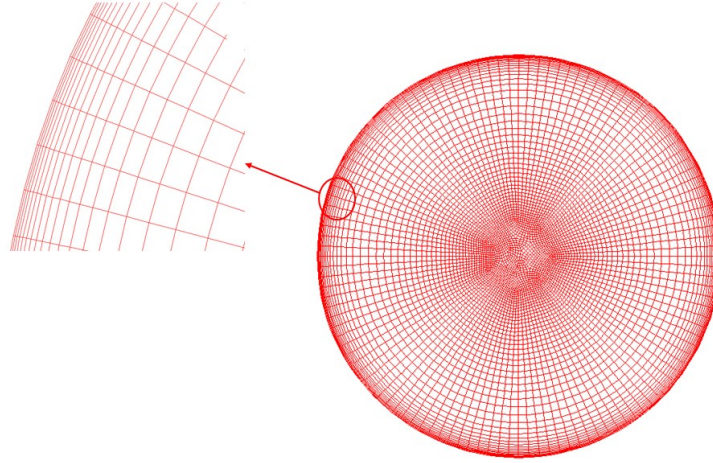


Figure 4.5: Grid topology on a cross-sectional plane of Mesh C

4.2.2 CFD modeling and governing equations

ANSYS Fluent 16 was used for the CFD simulations. The continuity and Navier-Stokes equations were solved for a Newtonian fluid of uniform properties (density and viscosity) flowing in steady state conditions:

$$\text{div}(\vec{\mathbf{u}}) = 0 \quad (4.2)$$

$$\mathbf{d}\vec{\text{iv}}(\vec{\mathbf{u}} \otimes \vec{\mathbf{u}}) = -\frac{1}{\rho} \vec{\nabla} P + \vec{\mathbf{u}} \Delta \nu$$

Concerning the boundary conditions, a uniform velocity profile was set at the pipe inlet (i.e. the inlet of the first pipe segment). As the flow rate is imposed and since a uniform fluid density is considered, the gravity force has no effect on the velocity field and therefore this body force term was not included in the Navier-Stokes equations. At the pipe outlet, a uniform pressure condition is enforced and the no-slip condition on the wall.

The temperature field was determined by solving the steady energy balance equation:

$$\text{div}(\vec{\mathbf{u}}T) = \alpha \Delta T \quad (4.3)$$

The temperature is set uniform at the inlet, the pipe wall is isothermal and a zero-temperature gradient is imposed at the pipe outlet.

In Equations 4.2 and 4.3 and their boundary conditions, it is assumed: (1) Steady flow and heat transfer phenomena. (2) An incompressible Newtonian fluid of uniform properties. (3) No phase transition phenomena. (4) Purely forced convection. In particular, natural convection is ignored since the fluid density is supposed uniform. This assumption is relevant as long as the Reynolds number is

not extremely low and the Grashof number (quantifying buoyancy effects) not extremely high, which is generally the case in heat exchangers. (5) Radiative phenomena are neglected. (6) Heat generation by viscous dissipation is assumed negligible in Equation 4.3. In Equations 4.2 and 4.3, the advective terms were discretized using the Quadratic Upwind Interpolation of Convective Kinematics (QUICK) scheme while the diffusive ones were central-differenced. The momentum and energy equations were resolved using the Semi Implicit Method for Pressure-Linked Equations Consistent (COUPLED) algorithm. A second order scheme was applied for pressure interpolation. Convergence was considered satisfying when residuals decreased at least 10 orders of magnitude.

More than 132 CFD simulations were performed. More than 25 highly curved helical geometries were simulated with the following parameter ranges: $1.25 \leq p^* \leq 15$ and $0.05 \leq R_H^* \leq 10$. Four Reynolds number values from 100 to 2 000, were considered. Two Prandtl/Schmidt numbers were considered in the simulations: 100 and 1 000. For each simulation, the developed Nusselt number Nu_H^∞ (respectively Sherwood number Sh_H^∞) was calculated.

4.2.3 Thermally developing and hydrodynamically developed flow

The entrance length is the distance a flow travels after entering a pipe before the flow becomes fully developed. Entrance length refers to the length of the entry region, the zone following the pipe entrance where effects originating from the interior wall of the pipe propagate into the flow as an expanding boundary layer. Several studies [225]; [226] estimated the calculations of entrance length and the factors affecting it. Saffari et al. (2014) [222] showed numerically and experimentally that in both helical pipe single-phase and two-phase flows, the hydrodynamic and thermal entrance lengths increase with increasing Reynolds number and pipe diameter. Most importantly, their results revealed that entrance lengths decrease when the helix curvature increases (i.e. when coil diameter decreases).

Many authors developed correlations to predict entrance lengths based on numerical [227] or experimental [228] data. The correlation of Austin and Seader (1974) [228] expresses the hydrodynamic entrance length in helical pipes in terms of δ , the helix angle necessary for reaching the fully developed region (expressed in degrees):

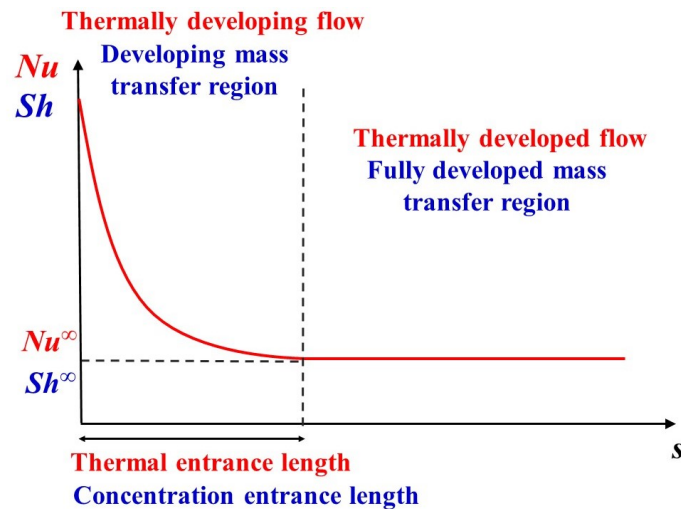
$$\delta = 49 \left(De_{R_H} \frac{1}{2R_H^*} \right)^{1/3} \quad (4.4)$$

where De_{R_H} is the Dean number defined by equation (Eq. 3.14)

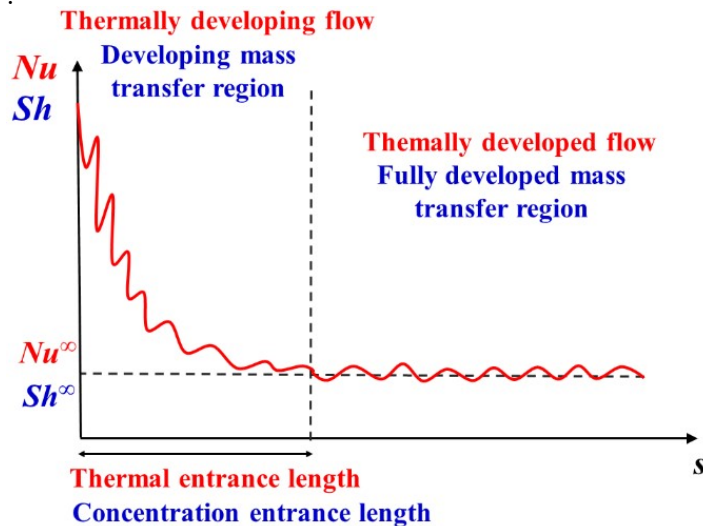
Equation 4.4 is valid for $190 \leq De_{R_H} \leq 950$. δ was found to vary between 90 and 200 degrees in most of the cases studied which indicates very short hydrodynamic entrance lengths (i.e. developed flow conditions reached within a single helix turn). Experimental results obtained later by Agrawal et al. (1978) [229] and Moulin et al. (2001) [160] were in good agreement with the predictions of Equation 4.4. On the other hand, the theoretical results by Yao and Berger (1975) [230], based on the boundary

layer theory, were significantly different from the data of Austin and Seader (1974) [228]. Concerning the thermal entrance length in curved and helical pipes, numerical [231] [232] and experimental [233] studies reported that it is 20 to 50 percent shorter in helical than in straight pipes.

In Chapter 3, only Pr numbers ranging from 1 to 10 are considered. With such fluids, entrance effects are usually negligible in the case of pipes of small diameter and/or sufficient length, which is generally the case in the applications targeted in this study, namely heat exchangers (and catalytic reactors and hollow fiber membranes in the case of mass transfer). This is particularly true when dealing with helical geometries.



(a) classical behavior under axially invariant flow conditions



(b) under non-periodic or chaotic flow conditions

Figure 4.6: Typical variation of the Nusselt (Sherwood) number as a function of the curvilinear distance from the inlet in a helical pipe

In this chapter, the high Pr numbers 100 and 1 000 are studied with several Reynolds numbers on the helical curved pipes. Figure 4.6a illustrates a qualitative variation of Nu (and thus of h) along a

highly curved and a classical helical pipe, the abscissa axis being the - curvilinear - position along the pipe centerline. The Nusselt number is the highest at the pipe entrance and decreases over a distance called ‘thermal entrance length’ before reaching an asymptotic value, Nu_H^∞ . The thermal entrance length reaches several meters in some situations, particularly at high Reynolds numbers. Therefore, as noted previously, it was necessary to conduct the simulations in a multi-block fashion in order to attain the thermally developed flow zone. However, under high Reynolds number conditions in some particular helix designs (details are reported later in this chapter), the Nusselt (resp. Sherwood) number did not exhibit a monotonic decrease along the pipe length, but displayed some oscillations as represented in Figure 4.6b. Similar results were reported in the case of zigzag geometries [234] and were due to non-periodic flow behavior, i.e. to the fact that under certain geometric and operating conditions, the flow becomes no more axially invariant. It is noteworthy that under these conditions, oscillations also appear in the C_f curve as well as in the Nu and (resp. Sh) curves at low Pr (resp. Sc) values. However, their magnitude remains very low and therefore, they were not noticed and reported in the previous chapters. On the other hand, at high Pr (resp. Sc), these oscillations become noticeable as their magnitude gets much higher.

Figures 4.7a and 4.7b show the variations of Nu (resp. Sh) along the pipe length in two helical and a straight tube respectively. One can notice that under high Pr conditions, the thermal entrance length becomes very important, and is generally higher than the pipe lengths commonly encountered in heat and mass exchangers. Therefore, the performances in terms of heat/mass transfer enhancement of a given geometry depend on the pipe length used, which makes the comparison of different designs a very complex task.

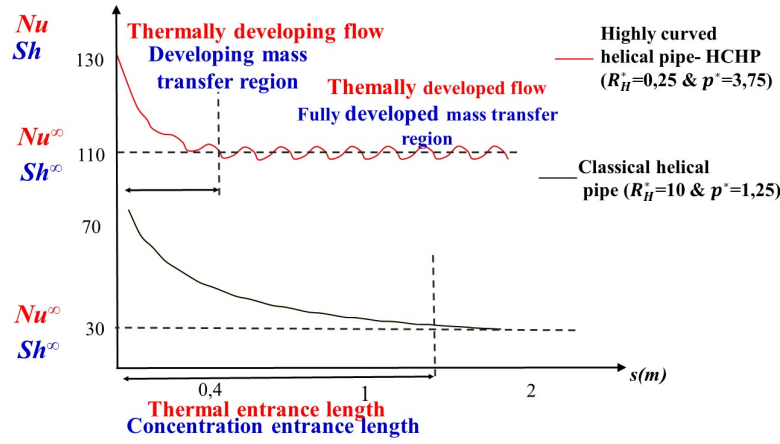
On the other hand, Figures 4.7 reveal that geometries exhibiting the highest asymptotic Nusselt numbers, Nu^∞ , do also lead generally to higher Nusselt values in the thermally developing zone (but exhibit shorter thermal entrance lengths). Therefore, for simplification purposes, in the remaining part of this chapter, comparison between the performances of different designs will be carried out based on the asymptotic Nusselt values they allow achieving. Indeed, designs with the highest Nu^∞ also lead to higher transfer rates in the thermal entrance zone, and thus, can be considered to be the most efficient in terms of heat transfer enhancement at high Pr values.

4.3 Results and discussion

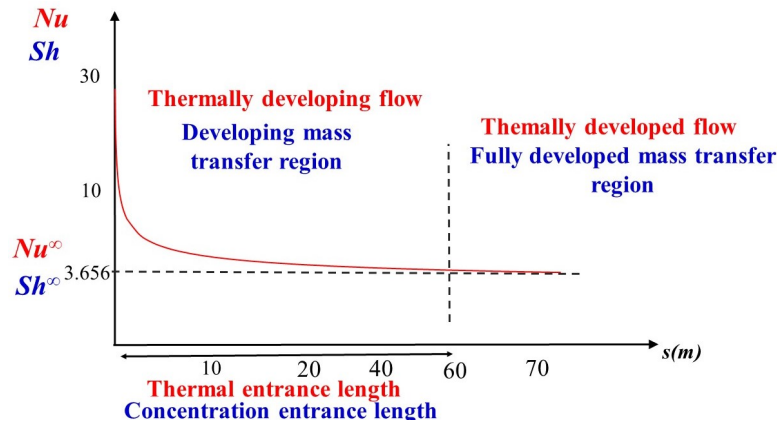
4.3.1 CFD Results

In this section, the CFD results will be presented in terms of Nusselt number and heat transfer enhancement. However, as discussed in Section 3.2.3, based on the heat/mass transfer analogy, these same results can be interpreted in terms of Sherwood number and mass transfer enhancement.

As mentioned earlier in Chapter 3, for each CFD simulation performed, the circumferential-



(a) a HCHP and a classical helical pipe (current CFD data)



(b) a straight pipe (solution of the L ev eque equation [175])

Figure 4.7: Typical variation of the Nusselt (Sherwood) number from the entrance at $Re = 800$ and $Pr (Sc) = 1\ 000$

averaged Nusselt Nu_H was calculated at different positions along the helical pipe in order to determine its asymptotic value, Nu_H^∞ . This value, divided by the Nusselt number in a straight pipe, $Nu_S^\infty = 3.657$, represents the heat transfer enhancement allowed by a given helical pipe.

Figure 4.8 shows contour plots of the Nu_H^∞ to Nu_S^∞ ratio in the (R_H^*, p^*) space that were obtained from a triangulation-based cubic interpolation of the CFD results. The black dots and stars represent the cases that were simulated, and respectively correspond to the situations where the flow is axially invariant (Figure 4.8a) or non-periodic (Figure 4.8b). It is stressed here, that at these points the values of Nu_H^∞ to Nu_S^∞ that are displayed on the contour are equal to those provided by CFD. The values predicted between these points are generated by interpolation and they may be inaccurate since they are quite sensitive to the used interpolation scheme. This is why the contours exhibit some irregularities.

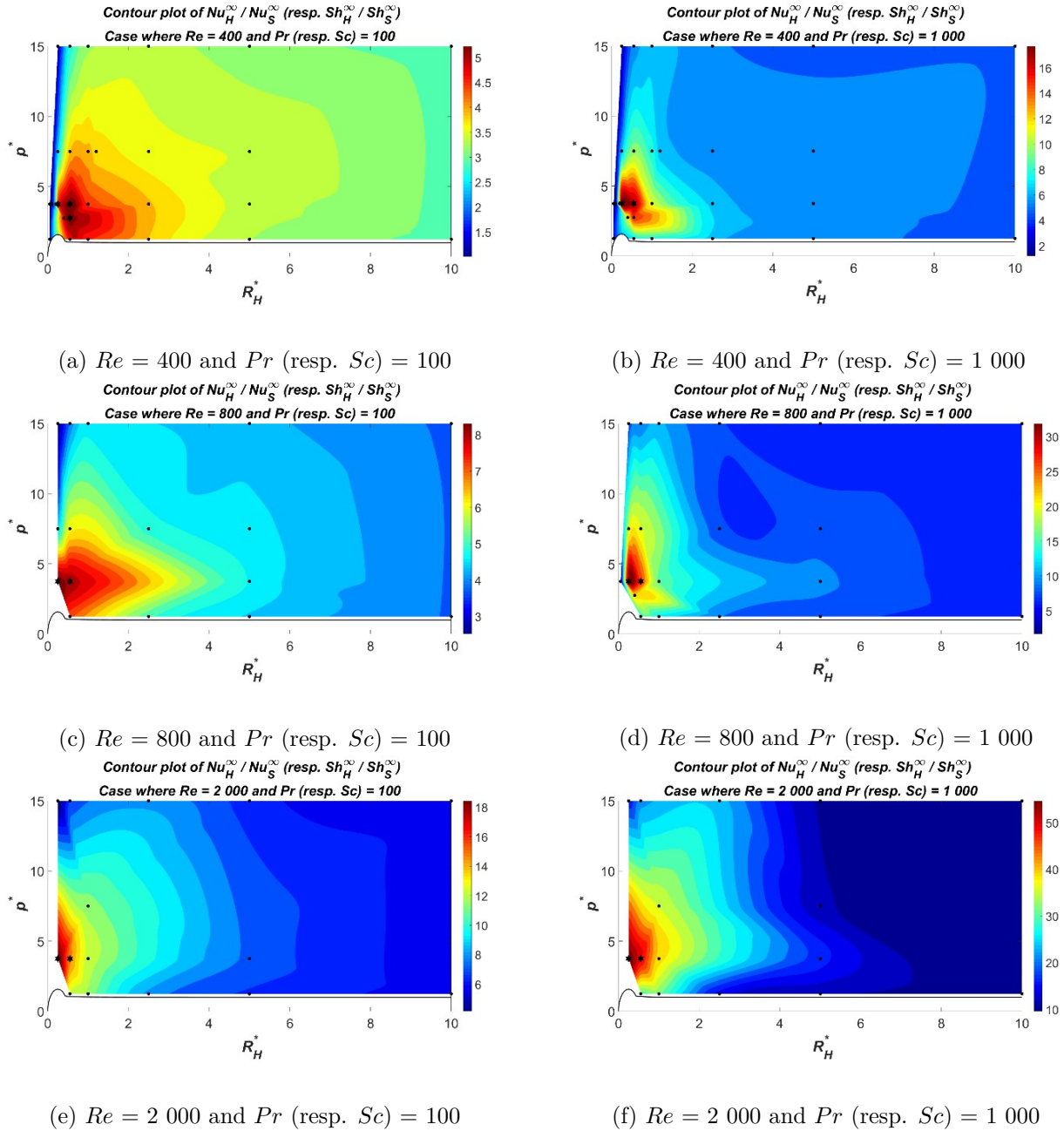


Figure 4.8: Contour plots of the Nu_H^∞ to Nu_S^∞ (respectively Sh_H^∞ to Sh_S^∞ ratio). The black dots represent the geometric conditions for which CFD simulations have been performed, in addition the black stars represent the geometries generating the non-periodic flow. The contours are derived by interpolating these data

Nonetheless, the following conclusions can be drawn:

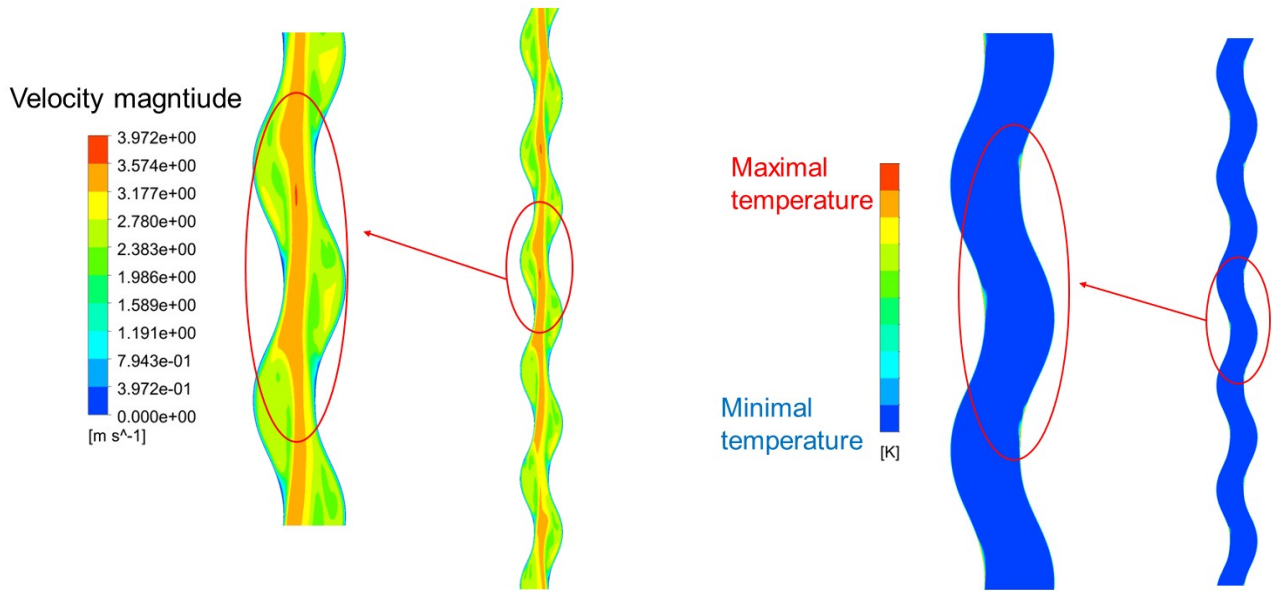
1. As in the case of low Pr values, highly curved helixes still exhibit much higher transfer rates than classical helical pipes. However, the best performances are no longer achieved by the most curved geometries, but by designs having a moderate dimensionless pitch, p^* , of about 3.75 and a low dimensionless radius, R_H^* , around 0.2 to 0.6. Indeed, these particular designs lead to non-periodic flow behaviours when the Reynolds number is sufficiently high. Thus, it seems that, at high Pr values, best heat transfer enhancement rates are obtained under oscillating flow behaviour rather than under intense Dean vortices.

2. When Re increases, the centrifugal forces are intensified, which further enhances the heat transfer efficiency. Hence, in the case $Pr = 100$, for $Re = 400$, the maximal Nu_H^∞ achieved in HCHPs is about 5 times higher than in straight tubes (Figure 4.8a), and its gets nearly 18 times greater than Nu_H^∞ for $Re = 2\,000$ (Figure 4.8e).
3. Nu_H^∞ increases for growing Pr . For example, with $Re = 2\,000$, the maximal Nu_H^∞ is about 18 times as high as in straight tubes for $Pr = 100$ (Figure 4.8c), and becomes more than 55 times greater than Nu_S^∞ for $Pr = 1\,000$ (Figure 4.8d).

4.3.2 Non-periodic flow

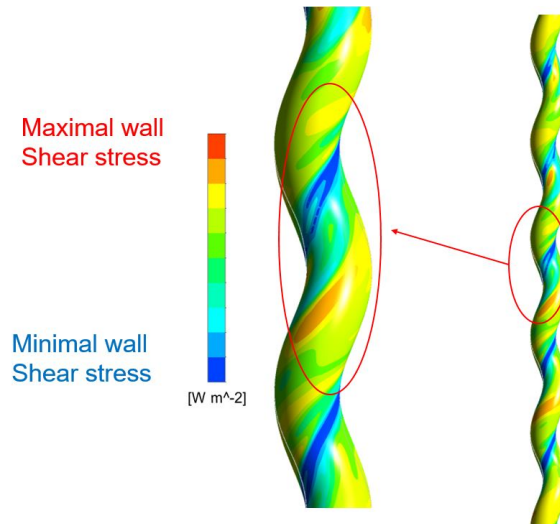
It has been reported in literature [234] that, under some operating conditions, the flow in periodic geometries such as zigzag channels may become non-periodic and exhibits axial variations. This same phenomenon was observed here in highly curved and elongated helical pipes (having a p^* around 3.75 and a low dimensionless radius, R_H^* , in the range of 0.2 to 0.6) when the Reynolds number exceeds 800.

Figure 4.9 represents contour plots of the velocity and temperature fields in a fully developed helical pipe flow where axial invariance is broken. As can be noticed from Figure 4.9a, the flow forms a high-velocity plume that exhibits spatial oscillations (it is noteworthy that the flow remains steady). Maximal convective transfer rates occur in zones where the high-speed jet impacts the pipe walls as can be seen from Figures 4.9a, 4.9b and 4.9c. At high Prandtl numbers, heat transfer is limited by a very thin thermal boundary layer. Thus, the high-speed jet that impacts the walls and shreds this layer reveals to be more beneficial than intense Dean vortices flow for heat transfer enhancement at high Prandtl numbers. By impacting the walls and shredding this layer, the high-speed jet flow allows reaching much higher transfer rates than in the classical helical pipes.



(a) Velocity magnitude field plotted in an axial plane

(b) Temperature field in an axial plane



(c) Shear stress field across the walls

Figure 4.9: Contours of the problem variables

4.3.3 Overall intensification factor and potentiality of highly curved helical pipes

As explained in sections 3.4.5 and 3.4.6, two strategies may be applied in order to push process intensification: (i) to maximize the heat (resp. mass) transfer coefficients and (ii) to maximize the specific heat exchanger/membrane surface area, by increasing the packing density of the module. The enhancement factor, ϵ (addressed in the next chapter as $\theta_{1,0}$), constitutes a combined evaluation of these two strategies and is defined as follows (see Chapter 3):

$$\epsilon = \frac{Nu_H^\infty \phi_{H,max}}{Nu_S^\infty \phi_{S,max}} \quad \text{or} \quad \epsilon = \frac{Sh_H^\infty \phi_{H,max}}{Sh_S^\infty \phi_{S,max}} \quad (4.5)$$

For a same tube diameter, it can be shown analytically that the ratio $\phi_{H,max}$ to $\phi_{S,max}$ (the packing

density ratio of the helical pipes to the packing density of the straight pipes) equals the ratio between the specific surface area of a module filled with the helical pipes and the surface of a module filled with straight pipes. The ratio Nu_H to Nu_S (resp. Sh_H to Sh_S) is equal to the ratio between the heat (resp. mass) transfer coefficients in helical and straight tubes respectively.

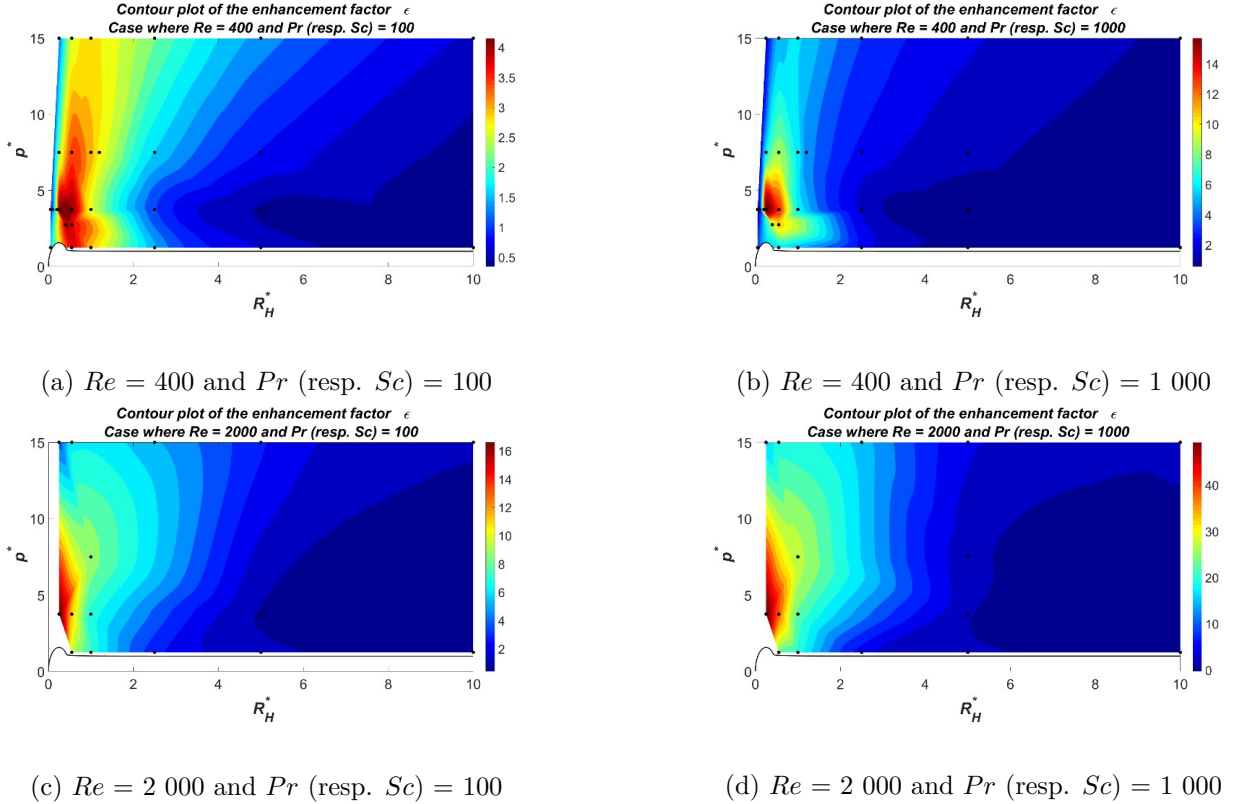


Figure 4.10: Contour plots of the intensification factor, ϵ

Figure 4.10 shows the contour plot of ϵ in the (R_H^*, p^*) plane for different fluid properties and operating conditions. It should be noted that different scales are used for each subfigure. It appears that:

1. Figure 4.10a, presenting the contour of ϵ for Reynold number 400 and Pr (resp. Sc) = 100, shows that the highly curved helical geometries yield an enhancement factor ϵ up to 4.5 times higher than the straight tube, which confirms the efficiency of these geometries. In addition, when $Pr = 1\ 000$ (resp. $Sc = 1\ 000$) (Figure 4.10b), the intensification factor gets about 14 times as high as for straight tubes.
2. The intensification factor improves with increasing Re and Pr (resp. Sc) numbers. For $Re = 2\ 000$ for example, HCHPs achieve volumetric transfer rates nearly 16 times higher than straight tubes for $Pr = 100$ (resp. $Sc = 100$) (Figure 4.10c), while the intensification factor exceeds 50 for $Pr = 1\ 000$ (resp. $Sc = 1\ 000$) (Figure 4.10a). These results demonstrate the huge potential of HCHPs for process intensification under high Pr (resp. Sc) conditions.

4.4 Conclusion

In this chapter, the heat (resp. mass) transfer across the wall of highly curved helical pipes was investigated numerically at high Pr (resp. Sc), by computing the asymptotic Nusselt (resp. Sherwood) number Nu_H^∞ . The results demonstrate that particular helix designs, leading to a non-periodic flow behaviour, allow achieving the best transfer rates. Moreover, these geometries can be densely packed and therefore, they offer tremendous potentialities for heat/mass transfer enhancement. For example, under a Reynolds number of 2 000, for a Pr (resp. Sc) of about 1 000 (which corresponds to gas absorption processes in membrane application and heat exchanger applications involving very viscous liquids and oils), the achieved heat (resp. mass) transfer intensification rate is about 50 times higher than in classic membrane contactors and heat exchangers.

Chapter 5

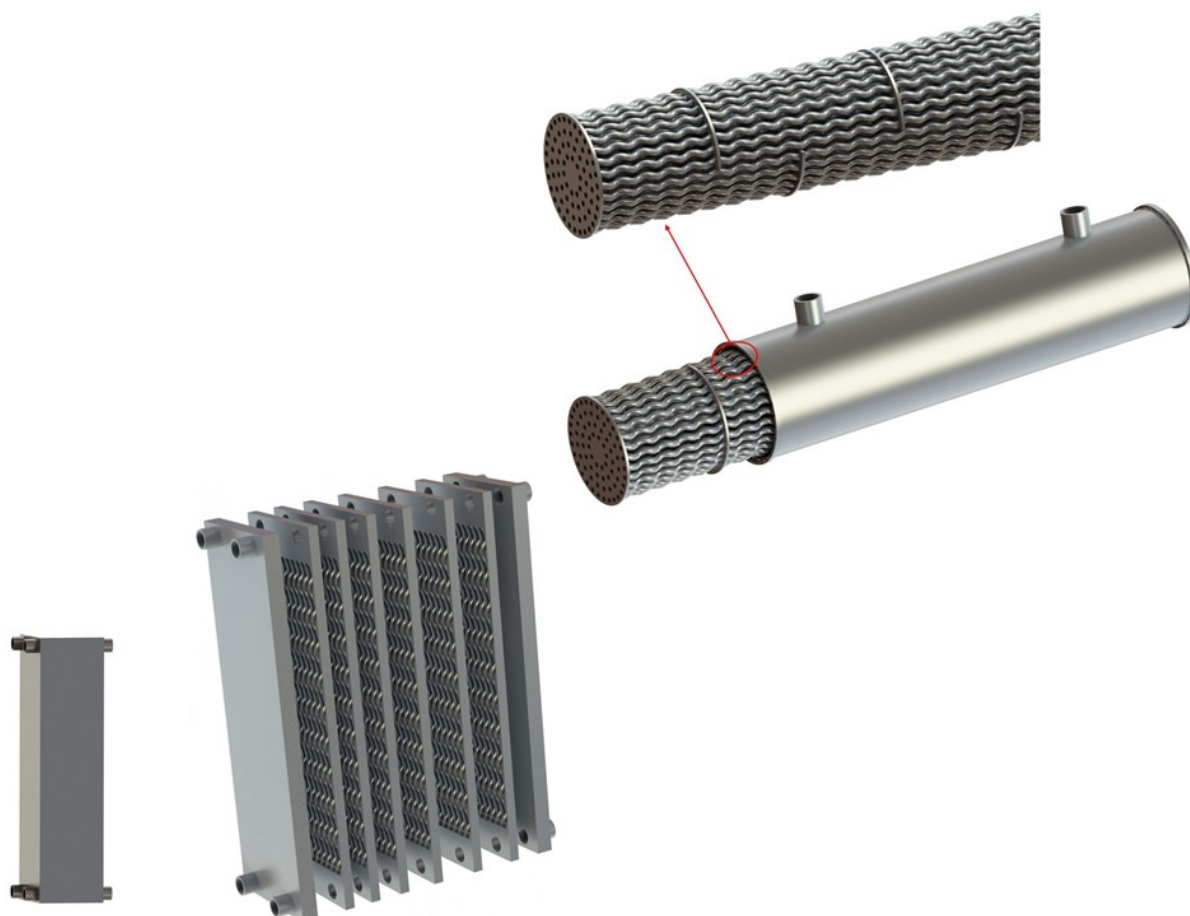
Heat / Mass transfer intensification using helically coiled pipes: potentiality and comparison to alternative enhancement techniques*

*This chapter constitutes an extended version of an article that has been submitted on **14-09-2020**.

Omran Abushammala, Rainier Hreiz, Cecile Lemaitre, Eric Favre. (2020): “Heat / Mass transfer intensification: can helically coiled pipes compete with alternative enhancement techniques?”, Submitted on **13-05-2020**.

Summary

Various techniques for heat/mass transfer enhancement exist such as the use of helical pipes or twisted tape inserts, and several criteria have been proposed for evaluating and comparing their performances. These criteria generally compare the heat/mass transfer enhancement provided by a given technique to the friction factor increase that it induces. However, as they do not account for specific surface area effects, they are not relevant for assessing the potentiality of novel designs in terms of process intensification, particularly in the case of processes where a large number of flow tubes need to be packed together (e.g. shell-and tube heat exchangers, monolith catalytic reactors, hollow fiber dense membrane contactors). In this chapter, different performance criteria accounting for specific surface area effects are proposed, and the efficiency of helical pipes with respect to these indexes is investigated. The results reveal that most helical pipe geometries exhibit poor efficiencies in terms of volumetric transfer rates. Nonetheless, some particular helix designs, with elongated shapes and/or small helix radii, are shown to offer huge potentiality for intensified heat/mass transfer performances. Indeed, they simultaneously allow to reduce the volume of reactors and heat/mass exchangers and to decrease the required pumping power. Finally, relying on literature data, the performances of alternative techniques are analyzed and compared to that of helical pipes, highlighting the weaknesses and strengths of each enhancement strategy.



Graphical abstract of Chapter 5

5.1 Introduction

Active research on heat/mass transfer enhancement is driven by the purpose of reducing both equipment size and energy requirement, i.e. saving material mass and minimizing operating costs. In particular, compact and lightweight units are of primary interest in applications with mobile operation and/or where space is limited, e.g. transport systems, decentralized energy production, domestic applications, space and offshore processes. In addition, as they contain less fluid, compact systems significantly reduce the risk of thermal runaway as well as the consequences of a process failure (e.g. leakage) if hazardous fluids are used. Moreover, in the case of chemical reactors or multifunctional heat exchangers, enhanced heat and mass transfer rates allow achieving better yields and selectivities. Various techniques have been investigated in the literature in order to enhance heat/mass transfer between a flowing fluid and the surrounding pipe walls [43, 209, 235]. They include the use of internals (e.g. twisted tapes, swirl devices, vortex generators), artificial wall roughness, pulsatile flow and/or the use of curved pipe geometries (e.g. helical or coiled designs) which generate Dean-type secondary flows or lead to chaotic advection. Compared to the base case of smooth straight pipes without any inserts and under steady flow conditions (which will be simply referred as ‘the base case’ further on in this chapter), these techniques allow enhancing the convective transfer rate, however, they induce higher frictional losses per unit length. Therefore, in this context, the main challenge when improving existing techniques or designing novel geometries is to simultaneously address these conflicting criteria, i.e. significantly improving the heat/mass transfer while maintaining the pressure drop as low as possible. Several performance criteria, combining these two conflicting objectives, have been proposed in the literature to evaluate and compare the effectiveness of enhancement strategies. They are generally expressed as follows (for heat and mass transfer situations respectively):

$$\eta_{1,n} = \frac{Nu/Nu_S}{(C_f/C_{f,S})^n} \quad \text{or} \quad \eta_{1,n} = \frac{Sh/Sh_S}{(C_f/C_{f,S})^n} \quad (5.1)$$

Nu , Sh and C_f without subscript receptively designate the effective Nusselt number, Sherwood number and friction factor, obtained when the enhancement technique is applied, whereas the subscript S refers to the base case of a smooth straight pipe. Exponent n is a positive weighting factor: a value of 1 indicates that similar importance is accorded to both objectives, while a value lower than unity indicates that a higher priority is given to heat/mass transfer enhancement to the detriment of the friction factor increase. η designates the performance evaluation criterion, and subscripts 1 and n respectively refer to the powers of the Nu (or Sh) and C_f ratios.

A frequently used performance index is $\eta_{1,1}$ [236] which is expressed as follows:

$$\eta_{1,1} = \frac{Nu/Nu_S}{C_f/C_{f,S}} \quad \text{or} \quad \eta_{1,1} = \frac{Sh/Sh_S}{C_f/C_{f,S}} \quad (5.2)$$

It compares the heat/mass transfer enhancement allowed by a given method or design to the relative friction factor increase that it induces. As it attributes similar weights to both factors, $\eta_{1,1}$ can be interpreted as an assessment of the energy-efficiency of the considered enhancement technique. However, the most widely used performance indicator is $\eta_{1,1/3}$, initially introduced by Webb and Eckert (1972) [237], and which is defined as follows:

$$\eta_{1,1/3} = \frac{Nu/Nu_S}{(C_f/C_{f,S})^{1/3}} \quad \text{or} \quad \eta_{1,1/3} = \frac{Sh/Sh_S}{(C_f/C_{f,S})^{1/3}} \quad (5.3)$$

$\eta_{1,1/3}$ aims at comparing the transfer performance of an enhancement technique/design to that of the base case, under equal pipe length and pumping power conditions, whence the power (1/3) over the friction factors ratio. However, in the context of process intensification, the use of the $\eta_{1,1/3}$ index is not always relevant. Indeed, to transfer a given heat/mass flux, enhanced heat/mass exchangers require shorter pipe lengths than the base case. Therefore, since by definition $\eta_{1,1/3}$ assumes equal pipe lengths in both situations, this performance index will not be used in this chapter for evaluating and comparing the effectiveness of different augmentation strategies.

A third performance index following the general form presented in Equation 5.1 is $\eta_{1,0}$, which simply corresponds to the Nusselt/Sherwood numbers ratio. This evaluation criterion is appropriate in situations where pumping costs are not an issue, for example when the working fluids are available at sufficient pressure. As can be noticed, evaluation criteria based on the general expression given in Equation 5.1 assess the transfer efficiency via the Nu or Sh numbers, i.e. in terms of transfer rate per pipe unit area. Therefore, they are not relevant for characterizing the potential of novel designs in terms of process intensification, i.e. in terms of allowed unit volume reduction. To make things clearer, the example of heat/mass transfer enhancement via the use of helical pipes can be considered. Compared to the base case, these designs are known to lead to a significant improvement of the convective transfer rate for a moderate increase of the pressure drop only. Consequently, helical pipes constitute an efficient enhancement technique according to criteria based on the definition given in Equation 5.1. Nonetheless, in many heat/mass transfer applications (e.g. hollow fiber membrane contactors, monolith catalytic reactors, shell-and-tube and printed-circuit heat exchangers), a large number of flow tubes is needed. However, helical pipes cannot be as densely packed as straight ones, i.e. cannot occupy the available space as efficiently as straight tubes. Thus, they present a lower specific surface area which can counterbalance the convective transfer enhancement they provide. For example, Kaufhold et al. (2012) [203] reported that when the helix radius is not sufficiently small, helical pipes lead to inferior performance than straight tubes in terms of volumetric transfer rates, i.e. heat/mass flux per unit volume. Thus, since they do not account for packing density effects, evaluation indexes based on the general form given in Equation 5.1 do not allow assessing the intensification potentiality of novel pipe designs for applications where a large number of tubes are to be packed.

So, the question arises as to whether helically coiled tubes are advantageous in terms of process intensification for heat/mass transfer applications. Can they compete with alternative heat/mass transfer intensification techniques? In an attempt to answer these questions, improved evaluation criteria, accounting for specific surface area effects, are presented in this chapter. Based on previously developed correlations for determining the heat/mass transfer coefficient, friction factor and packing density, the performances of helical pipes under laminar flow operation are analyzed. Comparison is carried out with available literature studies that investigated the effectiveness of different inserts, pulsatile flow conditions and novel pipe designs. The results reveal that most helical pipe geometries exhibit poor efficiencies in terms of volumetric transfer rates. Nonetheless, some particular helix designs, with elongated shapes and/or small helix radiuses, are shown to offer huge potentiality for intensified mass and/or heat transfer performances. These geometries, which can be manufactured by 3D-printing, should allow conceiving cost-effective compact units as they simultaneously enable to decrease the required pumping power and considerably reduce the volume of reactors, heat exchangers and membrane contactors.

5.2 Transport phenomena in helical pipe flow

Given their high surface-to-volume ratio, fine tubes are desirable for process intensification and are commonly used in many applications such as hollow fiber membranes, monolith catalytic reactors, micro- and milli-structured heat exchangers. However, turbulent flows which are ordinarily used to improve transfer rates at macro scales are impractical to achieve in miniaturized devices where viscous forces dominate. Therefore, fine tubes are generally operated under laminar flow conditions where lateral mixing, i.e. radial heat/mass transfer, occurs under the sole effect of conduction/diffusion, which leads to lower convective transfer rates than turbulent flows. Accordingly, to sustain the full potential of miniaturization, heat/mass transfer enhancement under laminar flow regimes becomes necessary. One possibility to achieve this goal is through the use of helical pipes instead of straight ones. Indeed, the hydrodynamics in helical - and curved - tubes is characterized by the occurrence of a secondary flow consisting of a pair of counter-rotating vortices in the cross-stream direction (i.e. perpendicularly to the primary flow), known as Dean cells (Figure 5.1a). These structures provide an efficient advective transport of fluid particles between the pipe walls and its centerline (Figure 5.1b), leading to increased transfer performance compared to the straight pipes case.

Therefore, helical pipes offer attractive potentialities for process intensification and heat/mass transfer enhancement. However, as discussed in the following paragraphs, their performances are very sensitive to their design, flow conditions and to the used working fluid.

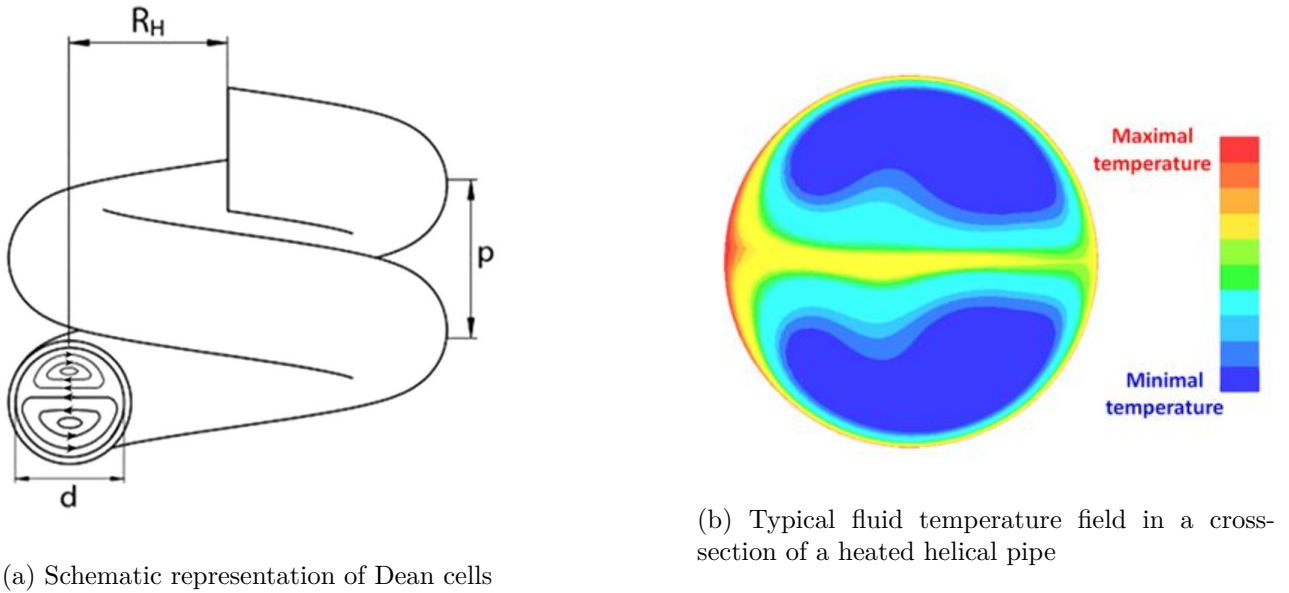


Figure 5.1: Transport phenomena in helical pipe flows

5.2.1 Helical pipes design, packing density and specific surface area

The shape of a helical pipe is described by two geometric parameters, its dimensionless pitch, $p^* = p/d$, and dimensionless helix radius, $R_H^* = R_H/d$, where d is the pipe diameter, p the helix pitch and R_H the helix radius (Figure 5.1a). Figure 5.2 illustrates some representative helix designs and the limit of the so-called forbidden region. The equation of this frontier has been determined by Przybył and Pierański (2001) [201]: it corresponds to the limit under which it is not possible to further decrease the helix pitch because consecutive turns of the helix would overlap one with another. Thus, the forbidden region corresponds to the set of p^* and R_H^* values for which it is not possible to design helical shapes. Figure 5.3 is a contour plot of the dimensionless helix curvature, $\kappa^* = \kappa d = d/\gamma$, in the (R_H^*, p^*)

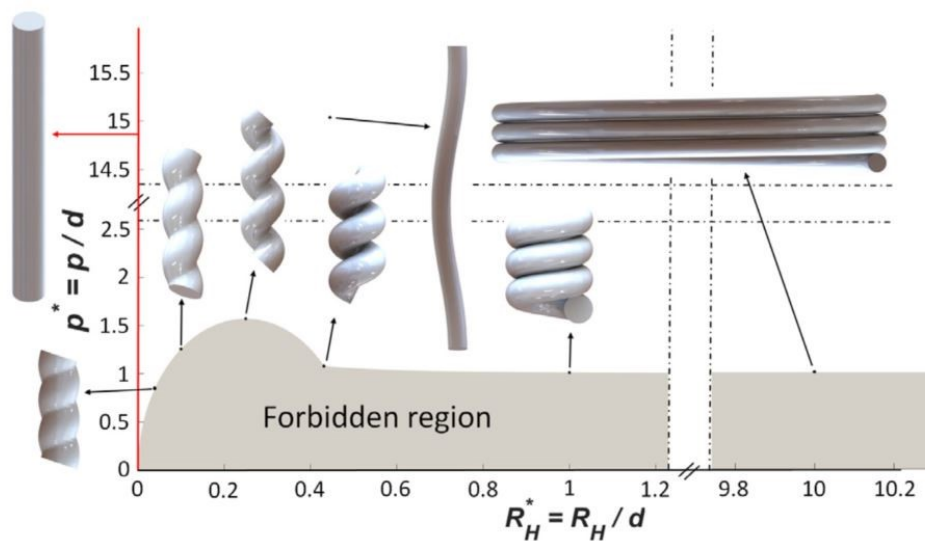


Figure 5.2: Limit of the forbidden region in the (R_H^*, p^*) space (adapted from Przybył and Pierański (2001) [201]) and some representative helix geometries [191]

space, where κ is the helix curvature and γ its curvature radius. The mathematical expression of κ is as follows:

$$\kappa = \frac{1}{R_H \left[1 + \left(\frac{p}{2\pi R_H} \right)^2 \right]} \quad (5.4)$$

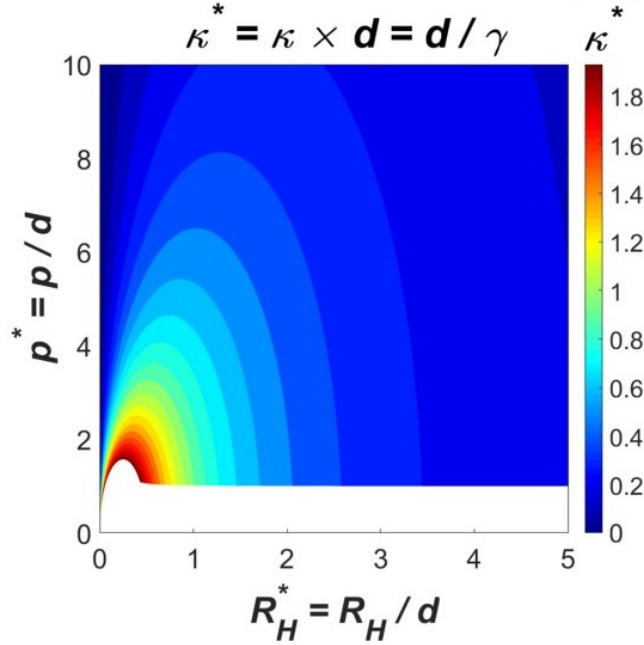
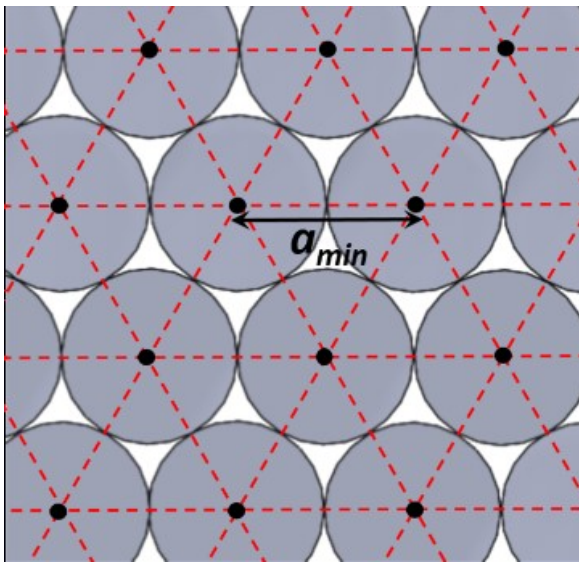


Figure 5.3: Contour plot of the dimensionless helix curvature in the (R_H^*, p^*) space

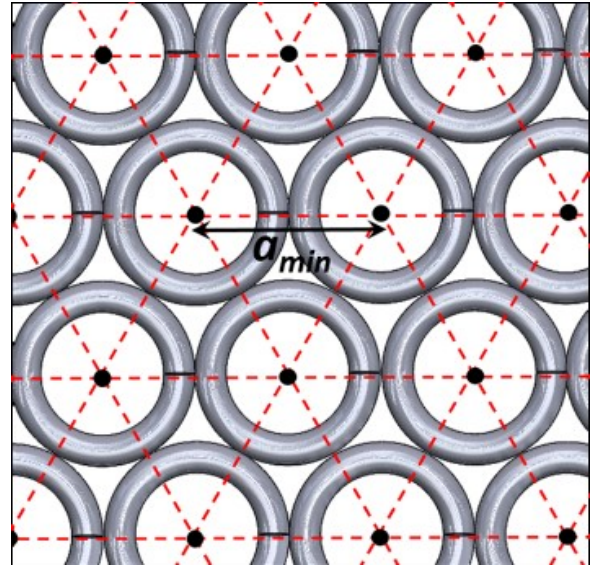
As can be noticed from Figures 5.2 and 5.3, helical pipes curvature vanishes when R_H^* tends to zero or when p^* goes to infinity, as the helix shape tends toward that of a cylinder. Thus, at these limits, helical pipes present the same packing density and transfer performances as straight tubes. Furthermore, as R_H^* tends to infinity, helices curvature vanishes and their shape locally straightens. Thus, at this limit, helical pipes perform as straight tubes from both hydrodynamics and heat/mass transfer point of views, but obviously, they present much lower packing densities than straight pipes. Most importantly, Figure 5.3 reveals that the highest curvatures (i.e. lowest radiuses of curvature) are achieved by helices of low pitch and relatively low helical radius. These geometries have been referred to as Highly Curved Helical Pipes, HCHPs, and it is only recently that their performances in terms of hydrodynamics and heat/mass transfer enhancement were investigated [191, 208]. This is probably due to the fact that HCHPs are difficult to manufacture using traditional manufacturing techniques. However, nowadays, thanks to a witnessed progress in 3D-printing, the fabrication of such designs has become achievable. Given their low radius of curvature, HCHPs exhibit high centrifugal effects and produce intense Dean vortices. Thus, as discussed in Section 5.2.2, they lead to much higher heat/mass transfer rates than ‘classical’ helical pipes or straight tubes. As argued earlier, although curved and helical pipe geometries lead to better transfer efficiencies than straight tubes, they cannot be as densely packed, i.e. they present a lower specific surface area. This factor should be necessarily taken into account when quantifying the potential of any new design in terms of process intensification.

In fact, it should be checked that the convective heat/mass transfer enhancement it provides is not entirely counterbalanced by its lower specific surface area.

Using a CAD software, Abushammala et al. (2020) [208] determined, a_{min} , the minimal achievable distance between non-overlapping helices disposed in a triangular arrangement (Figure 5.4a). The study was conducted for different helix geometries and the results allowed calculating, $a_{min}^* = a_{min}/d$, the dimensionless distance separating closely packed helices, and a correlation (reported in Equation 3.16 from chapter 3) was developed for determining a_{min}^* depending on the helix design, i.e. its p^* and R_H^* values. The provided correlation is valid for $p^* \leq 20$ and $R_H^* \leq 10$, although it has been shown to produce reliable results also beyond this range of geometric parameters. It should be noted that a_{min}^* equals unity (i.e. $a_{min} = d$) in the case of straight pipes as can be noticed from Figure 5.4b.



(a) ideally packed cylinders



(b) The triangular (or dense hexagonal) lattice is illustrated by dashed lines

Figure 5.4: Top view of ideally packed helices of $R_H^* = 2.5$ and $p^* = 1.25$. The black dots represent the axes of the helical or straight tubes.

Figure 5.5a displays the contour plot of a_{min}^* in the (R_H^*, p^*) space, which was calculated using the correlation of Abushammala et al. (2020) [208]. The discontinuity appearing in the contour is due to the fact that different mathematical expressions were used to correlate a_{min}^* , depending on whether R_H^* is lower or higher than 2. As shown by Figure 5.4a, the lowest possible value for a_{min}^* is 1, and it is achieved when R_H^* is zero or when p^* goes to infinity, i.e. when the helix design approaches that of cylinder (Figure 5.2). a_{min}^* obviously increases when R_H^* is increased. When p^* increases, the spacing between two consecutive helix turns enlarges. Hence, the different helices can be brought closer and imbricate, which leads to a decrease of a_{min}^* .

For any helix design, once a_{min}^* is known, its maximum packing density, $\phi_{H,max}$, (which is achieved when the helices are separated by a distance a_{min}^*) can be easily calculated [208] and compared to $\phi_{S,max}$, the maximum packing density of cylinders, which equals $\pi/[4\sin(\pi/3)] \approx 90.7\%$. The maximal

specific surface area (i.e. exchange surface per unit volume) of the set of packed helical pipes, $\sigma_{H,max}$, can be determined relatively to $\sigma_{S,max}$ (the specific surface area of densely packed straight tubes), using the following equation:

$$\frac{\sigma_{H,max}^* \times d_H}{\sigma_{S,max}^* \times d_S} = \frac{\sigma_{H,max}}{\sigma_{S,max}} = \frac{\phi_{H,max} \times s_H}{\phi_{S,max} \times s_S} = \frac{\phi_{H,max} \times 4/d_H}{\phi_{S,max} \times 4/d_S} \quad (5.5)$$

where d denotes the pipe diameter, s the surface-to-volume ratio of a single helical or straight pipe, $\phi_{H,max}$ the maximal packing density, σ_{max} the maximal specific surface area and σ_{max}^* its dimensionless form. Subscripts H and S respectively refer to helical and straight pipes. Thus, considering helical and straight pipes having a same diameter, the ratio of their specific surface area equals their packing density ratio. It is noteworthy that Equation 5.5 also applies to pipe designs other than helical, as long as they present a uniform and circular cross-section.

Figure 5.5b, adapted from [208], displays the contour plot of the $\sigma_{H,max}^*$ to $\sigma_{S,max}^*$ ratio, which is always lower than unity as helices cannot be as efficiently packed as straight tubes. Figure 5.5b reveals that only HCHPs and elongated helical designs (i.e. having a large R_H^* to p^* ratio) present satisfactory specific surface areas (i.e. $\sigma_{H,max}^*$ to $\sigma_{S,max}^*$ ratio close to one). Therefore, HCHPs, which also allow a significant convective transfer enhancement (Section 5.2.2), may be expected to offer huge potentialities for intensified heat/mass transfer performance. On the other hand, ‘classical’ helices exhibit very poor packing densities as they cannot efficiently occupy an available space. Therefore, as shown later, these geometries lead to lower performance than straight tubes in terms of volumetric transfer rates.

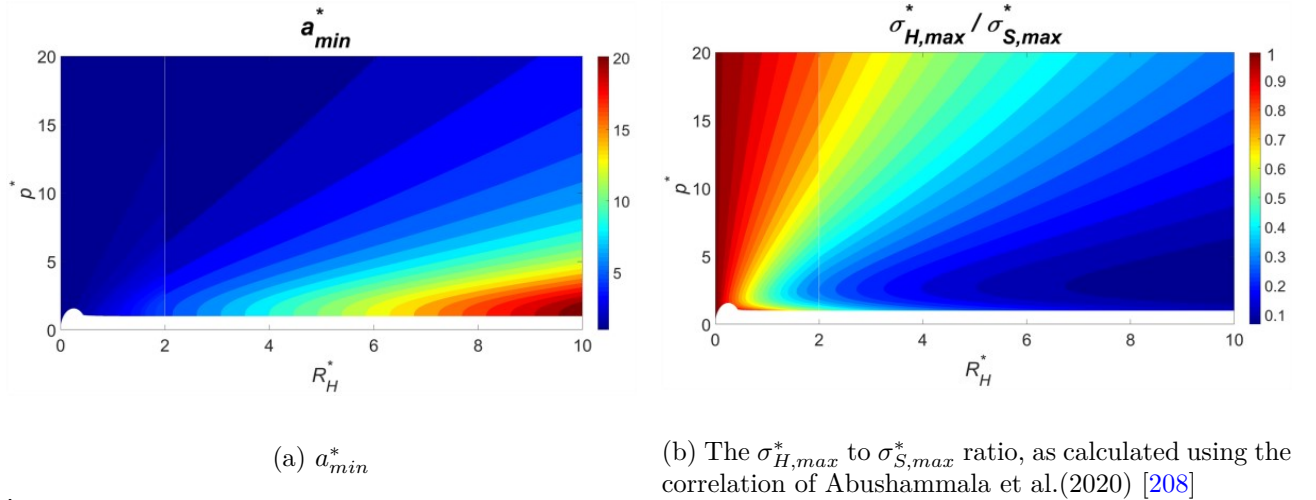


Figure 5.5: Contour plot of in the (R_H^*, p^*) space

5.2.2 Hydrodynamics and heat/mass transfer in helical pipe flows

Although heat/mass transfer enhancement using helical pipes has been widely investigated, as reported in [208], literature studies have only dealt with ‘classical helices’ with large R_H^* values, prob-

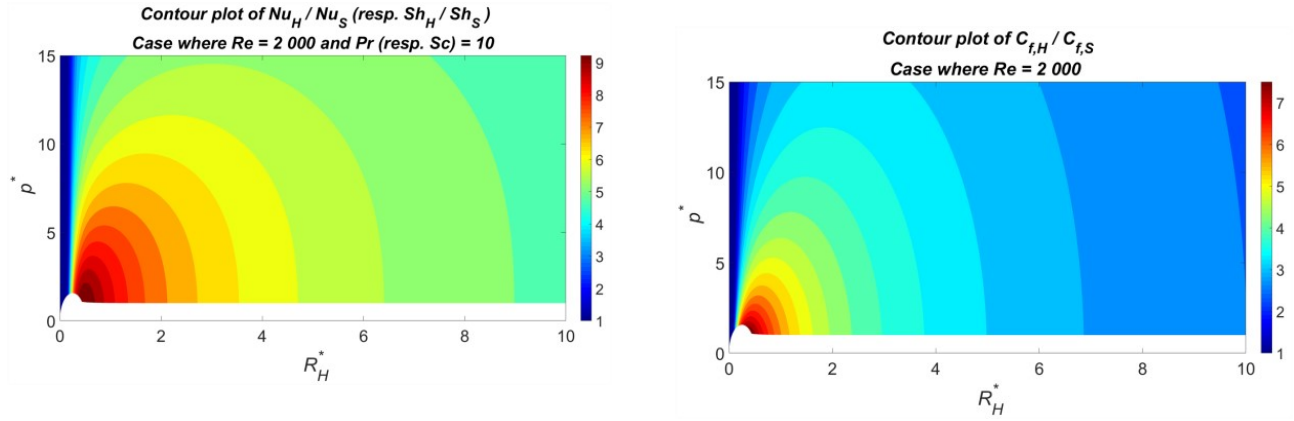
ably because these geometries are easy to fabricate using traditional manufacturing techniques. It is only recently that the heat transfer performance of HCHPs was addressed by Abushammala et al. (2019;2020) [202, 208] using CFD (computational fluid dynamics). Their study has been conducted under the assumptions of uniform wall temperature and negligible heat generation by viscous dissipation. As discussed in their chapter, owing to the heat/mass transfer analogy, their results may be transposed and applied to mass transfer situations in the case of a dilute mixture under uniform wall concentration and in the absence of any homogenous chemical reaction.

Furthermore, Abushammala et al. (2020) [208] developed a correlation to predict the fully developed circumference-averaged Nusselt number (respectively Sherwood number) in both highly curved and classical helices. The proposed correlation (which is reported in chapter 3 (Equation 3.13)) is valid for $R_H^* \leq 10$, $p^* \leq 15$, Reynolds numbers, Re , ranging from 10 to 2 000, and Prandtl numbers, Pr , (respectively Schmidt numbers, Sc) between 1 and 10. With such relatively low values of Pr/Sc , entrance effects may be neglected in the case of pipes of small diameter and/or sufficient length, which is generally the case in the applications targeted in this study, namely micro-structured heat exchangers and monolith catalytic reactors. Accordingly, in these situations, the asymptotic Nusselt/Sherwood numbers that can be calculated using the correlation of Abushammala et al. (2020) [208], allow representing the effective convective heat/mass transfer rate in the pipe, and therefore, they will be simply denoted Nu and Sh further on in this chapter. Figure 5.6a displays the contour plot, calculated using the correlation of Abushammala et al. (2020) [208], of the Nu_H to Nu_S (respectively Sh_H to Sh_S) ratio for Re equal 2 000 and a Pr (respectively Sc) of 10, where the subscripts H and S respectively refer to helical and straight pipes. Note that Nu , Sh and Re are all defined upon the pipe diameter as characteristic length scale. This contour plot illustrates the heat/mass transfer enhancement that helical pipes allow in comparison to the base case. Note that Nu_S equals 3.65 since a laminar flow with an isothermal wall boundary condition is considered (while Nu_S would be equal to 4.36 under a uniform heat flux condition).

As shown by Figure 5.6a, helical pipes lead to a significant improvement of the transfer efficiency, in particular highly curved ones which, thanks to the intense Deans vortices they develop, allow reaching heat/mass transfer rates nearly 9 times higher than straight pipes. However, these strong recirculations also induce higher mechanical energy dissipation per unit pipe length. Therefore, it is necessary to account for this friction factor increase in order to evaluate the cost-effectiveness of HCHP geometries.

Abushammala et al. (2019) [191] proposed a correlation for predicting the friction factor in both highly curved and classical helices, under laminar flow conditions. The proposed correlation (which is reported in chapter 2 (Equation 2.7)) is valid for $R_H^* \leq 10$, $p^* \leq 20$ and Re ranging from 10 to 2 000. Figure 5.6b displays the contour plot, calculated using this correlation, of the $C_{f,H}$ to $C_{f,S}$ ratio (where C_f designates the friction factor) in the case where Re equals 2 000. It can be noticed that

helical pipes may lead to a significant friction factor increase, in particular highly curved ones, where the C_f may exceed by more than 7 times that of straight pipes. Therefore, in order to be able to assess the potentiality of HCHPs and other designs for process intensification of heat/mass exchangers, it is necessary to develop performance criteria simultaneously accounting for the heat/mass transfer enhancement, friction factor increase and packing density effects.



(a) The Nu_H to Nu_S (respectively Sh_H to Sh_S) ratio, as calculated using the correlations of Abushammala et al.(2020) [208]

(b) The $C_{f,H}$ to $C_{f,S}$ ratio, as calculated using the correlations of Abushammala et al.(2019) [191]

Figure 5.6: Example of contour plots in the (R_H^*, p^*) space. Note that a different scale is used for each subfigure

5.3 Alternative heat/mass transfer enhancement techniques

The present chapter aims at evaluating the potentiality of helical pipes for heat/mass transfer intensification under laminar flow conditions, and comparing it to alternative enhancement strategies. This section reviews literature studies (summarized in Table 5.1) dealing with alternative heat transfer enhancement techniques, in which both heat transfer and friction factor data were reported (to be able to assess the cost-effectiveness of the method used). To allow a reliable comparison, only studies with a Prandtl number comprised between 1 and 10 and Reynolds numbers below 2 000 are considered, which corresponds to the range of validity of the correlations presented in Section 5.2.2. Among the papers presenting novel pipe geometries, only those reporting the full geometric details of their designs have been considered. The maximum specific surface area of these designs has been determined using the CAD software Autodesk Inventor Professional 2018 assuming a triangular lattice arrangement (following the procedure presented in [208]), and the results are reported in Table 5.1.

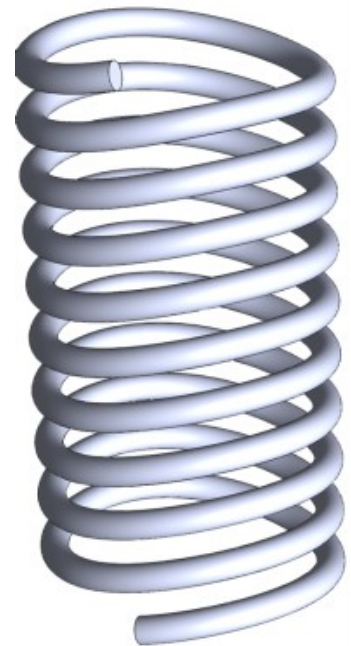
Based on CFD simulations, Wang et al. (2020) [238] identified a novel coiled pipe design with a trilobal cross-section (which was called ‘helically coiled-twisted trilobal tube’, Figure 5.7a) allowing a significant heat transfer enhancement. They also carried out an experimental investigation to validate their numerical data. Compared to a classical helical pipe with a circular cross-section, the novel

design was shown to further improve the Nusselt number at the inner tube side by 19% to 31%, while increasing the friction factor by 24% to 38%. However, because of its relatively large helix radius and moderate pitch, this novel geometry exhibits a low packing density. Thus, as reported in Table 5.1, the calculation of its maximal specific surface area shows that it is less than 25% of that developed by densely packed straight tubes of same - outer - diameter. This drawback limits the potential of this novel design for process intensification purposes as discussed in Section 5.4.

Tohidi et al. (2015) [239] investigated numerically the thermo-hydraulic performance of a helically coiled heat exchanger that induces a chaotic flow behavior. The novel design follows a helically coiled configuration, however its helix turns consist of alternating right-handed and left-handed helix segments (Figure 5.7b). Their numerical results revealed that, compared to a classical helical pipe, the novel geometry allows enhancing heat transfer by 4% to 26% for a friction factor increase of 5% to 8% only. Although Tohidi et al. (2015) [239] claimed that their novel design exhibits a higher packing density than alternative chaotic heat exchangers, because of its relatively large helix radius and low helix pitch, its maximum specific surface area remains very low and is about 5 times smaller than that developed by densely packed straight tubes having the same pipe diameter (Table 5.1).



(a) Proposed by Wang et al. (2020) [238]



(b) Proposed by Tohidi et al. (2015) [239]

Figure 5.7: Schematic representations of the novel heat exchanger designs

Table 5.1: Summary of studies dealing with alternative techniques of heat transfer enhancement under laminar flow conditions

Reference	Heat enhancement technique	Investigation technique	Wall thermal boundary condition	Pr	$\frac{\sigma_{S,max}^*}{\sigma_{S,max}}$
Wang et al. (2020) [238]	Twisted helical pipe with trilobal cross-section which was referred to as 'helically coiled-twisted trilobal tube' (Figure 5.7a)	Only their experimental result with $Re = 2\,000$ is considered in this chapter (their remaining data correspond to turbulent flows)	Uniform wall temperature	7	0.234
Kurnia et al. (2020) [240]	Different twisted tapes fitted within a straight or a helical pipe	CFD	Uniform wall temperature	7	1 for the straight tube; 0.212 for the helical pipe
Khosravi-Bizhaem et al. (2019) [211]	Four helical pipes were investigated under pulsating flow conditions	Experimental. For clarity purposes, only their results under a pulsating frequency of 4 Hz (which led to the best performance) are considered in this chapter.	Uniform heat flux	5.5	0.110, 0.105, 0.071 and 0.053 respectively for the four helical pipes
Tohidi et al. (2015) [239]	Chaotic helically coiled geometry (Figure 5.7b)	CFD	Uniform heat flux	7	0.212
Guo et al. (2011) [241]	Two different twisted tapes fitted within straight pipes	CFD	Uniform heat flux	7	1
Wongcharee and Eiamsa-Ard (2011) [242]	Two different twisted tapes fitted within straight pipes	Experimental study	Uniform heat flux	7	1

Khosravi-Bizhaem et al. (2019) [211] experimentally investigated the effects of pulsatile flow conditions on heat transfer enhancement in helical pipes. Four helix designs were used, all exhibiting a large helical radius and a small pitch, and thus, a very low specific surface area as reported in Table 5.1. Compared to steady-state operation, pulsatile flow conditions were shown to enable a significant improvement of the convective transfer rate, up to 39%, while the pressure drop was increased by 3% to 7% only. It is noteworthy that Khosravi-Bizhaem et al. (2019) [211] mainly focused on turbulent flow conditions, although some of their data fall within the laminar flow regime (only these results are considered in the present chapter). However, the accuracy of the manometer they used was not sufficient for precise measurements of the relatively low pressure drops occurring in the laminar flow experiments. Hence, many of their time-averaged pressure drop measurements under pulsatile conditions were even significantly lower than those predicted by correlations dealing with steady-state operation [191, 194, 200]. Therefore, their friction factor data should be considered with caution especially that, as shown later in Section 5.3, they seem to be largely underestimated as they lead to unrealistic cost-effectiveness performances.

Guo et al. (2011) [241], Wongcharee and Eiamsa-Ard (2011) [242] and Kurnia et al. (2020) [240] have focused on heat transfer enhancement by twisted tapes fitted within straight tubes. All these studies agree that properly designed inserts allow impressive enhancement rates, although they generally lead to a significant pressure drop increase. Kurnia et al. (2020) [240] also considered the situation where the twisted tapes are disposed within a helical pipe. This configuration enabled better enhancement rates than when the twisted tapes are fitted within a straight pipe, but it also led to higher pumping requirements.

5.4 Results and discussion

As mentioned in Section 5.1, performance evaluation criteria proposed thus far in literature do not account for specific surface area effects. Thus, in the case of heat/mass exchangers or reactors where a large number of flow tubes need to be used, these criteria are not relevant for characterizing the potential of novel designs or enhancement strategies in terms of process intensification, i.e. in terms of allowed unit volume reduction. Therefore, new performance evaluation indexes, following the general form given in Equation 5.6, are proposed in this chapter (for heat and mass transfer situations respectively):

$$\theta_{1,n} = \frac{(\sigma_{max}^* Nu)/(\sigma_{S,max}^* Nu_S)}{(C_f/C_{f,S})^n} \quad \text{or} \quad \theta_{1,n} = \frac{(\sigma_{max}^* Sh)/(\sigma_{S,max}^* Sh_S)}{(C_f/C_{f,S})^n} \quad (5.6)$$

where θ is the intensification performance factor. n is a positive weighting factor expressing the relative weight accorded to pumping costs compared to the volumetric heat/mass transfer enhancement. Subscript S refers to the base case of a smooth straight pipe under steady state operation. The numerator

of Eq. 5.6 represents the heat/mass transfer enhancement per unit volume that a given enhancement strategy allows achieving compared to the base case. In the subsequent paragraphs, the potentiality of helical pipes is evaluated using different performance indexes following the general forms presented in Equations 5.1 and 5.6. For each considered criterion, some particular helix designs are shown to enable good to excellent performances. Elongated helices and highly curved ones reveal to be particularly relevant for process intensification purposes, showing comparable or better performances than alternative enhancement techniques and designs.

5.4.1 Heat/Mass transfer enhancement per unit surface

A first criterion for evaluating the performances of helical pipes or alternative techniques is $\eta_{1,0}$ (following the general form given in Eq. 5.1), which simply corresponds to the Nu to Nu_S (respectively Sh to Sh_S) ratio, i.e. to the heat/mass transfer augmentation allowed by the considered technique in comparison to the base case. This criterion is relevant in situations where pumping costs are not an issue, for example when the working fluids are available at sufficient pressure. Since it does not account for specific surface area effects, the use of $\eta_{1,0}$ is relevant in situations where only a single flow tube is to be used and where space is not a major concern. For example, a $\eta_{1,0} = 2$ indicates that the enhancement strategy allows achieving a similar heat/mass flux than that obtained with the base case, while reducing the surface of the heat/mass transfer device (and so the purchased material mass) by a factor up to 2 (in particular when the heat/mass transfer resistance is mostly located at the inner side of the tube, and in the presence of a heterogeneous chemical reaction, if it is diffusion-controlled). Or alternatively, for a same exchange surface, a $\eta_{1,0} = 2$ means that the enhancement technique allow achieving a heat/mass flux that is up to twice that obtained with the base case.

As displayed in Figure 5.6a, among helical pipes, highly curved ones enable the best transfer efficiencies. However, the allowed enhancement rate depends on both Re and Pr (respectively Sc) values. In order to characterize the flow effects, the Reynolds number was varied from 10 to 2 000 using length steps of 10. At each Re value, using the correlation of Abushammala et al.(2020) [208], $\eta_{1,0}$ was calculated for all helices with $R_H^* \leq 10$ and $p^* \leq 15$, using length steps of 0.05 for varying both R_H^* and p^* . Then, at each Re , the maximal $\eta_{1,0}$ value that could be achieved by helical pipes was determined, and the geometric parameters of the helix allowing to achieve this optimal performance were identified. In order to characterize the fluid properties effects, this same procedure was performed for three Pr (respectively Sc) values, 1, 7 and 10. The calculation results are plotted in Figure 5.8. Plots on the upper graph display the maximal $\eta_{1,0}$ that can be achieved by helical pipes, depending on Re and Pr values. The discontinuity in the curves at $Re = 400$ is due to the fact that the correlation of Abushammala et al.(2020) [208] relies on different mathematical expressions respectively when Re is higher or lower than 400. The middle and lower graphs in Figure 5.8 display the geometric parameters of the helices achieving the maximal $\eta_{1,0}$ depending on Re and Pr (respectively Sc) conditions. As

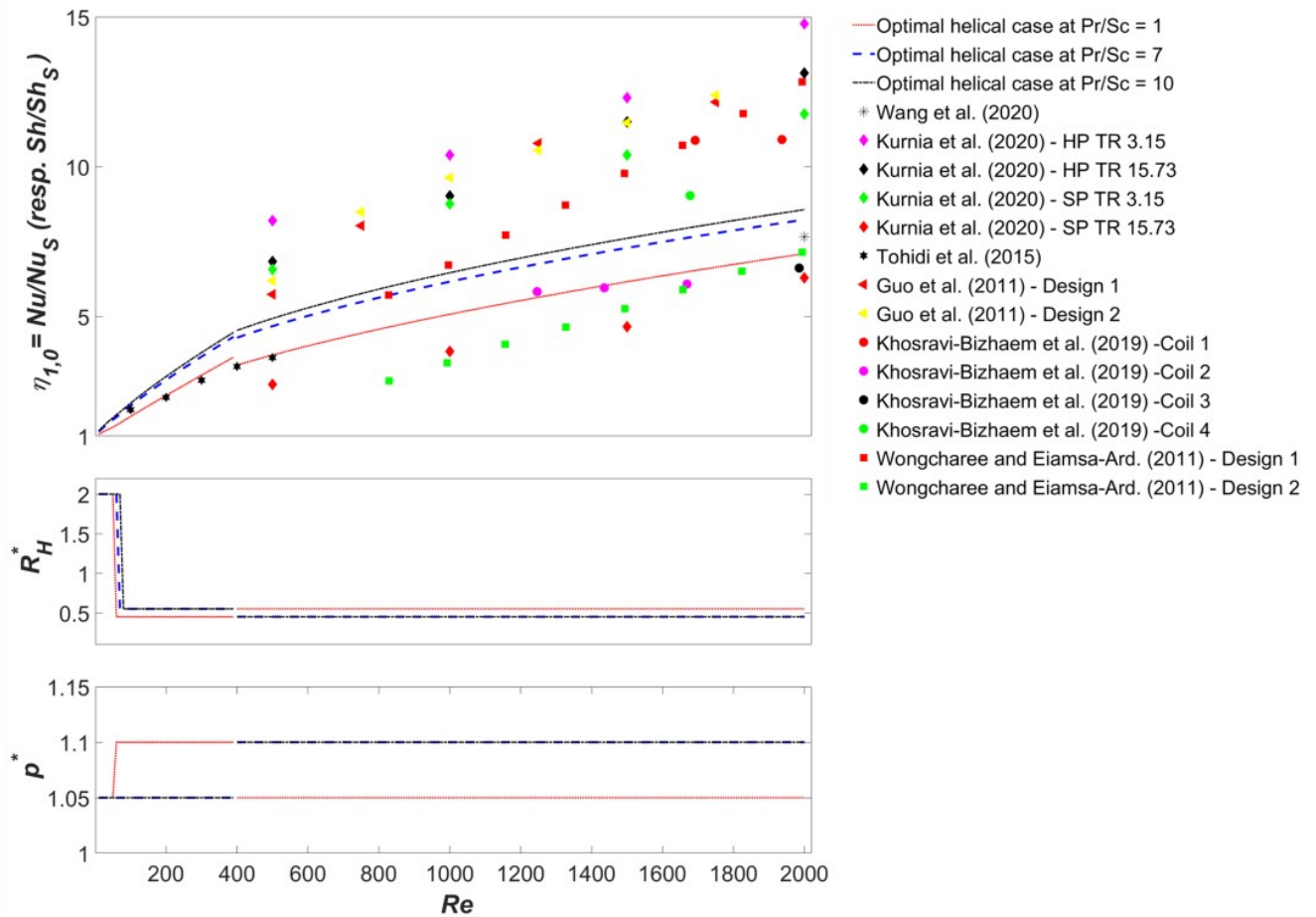


Figure 5.8: Performances of helical pipes and alternative enhancement techniques based on the $\eta_{1,0}$ criterion. In the figure caption, for the data of Kurnia et al. (2020) [240], HP and SP respectively refer to the use of a helical or a straight pipe, while TR refers to the twist ratio of the used twisted tape

revealed by Figure 5.8, helical pipes allow a considerable improvement of heat/mass transfer with an enhancement rate exceeding 9 at $Re = 2\,000$ and Pr (respectively Sc) = 10. Optimal helix performances are always achieved by HCHPs having a R_H^* between 0.4 and 2 and a p^* of about 1.1. When Re increases, centrifugal effects become higher and lead to more intense Dean vortices. Therefore, enhancement capacities of helical pipes improve with increasing Re .

For comparison purposes, literature data (refer to Table 5.1 and Section 5.3 for details) are also plotted in Figure 5.8. It can be noticed that HCHPs allow better performance than the designs proposed by Wang et al. (2020) [238] and Tohidi et al. (2015) [239] (their data were acquired using water at $Pr = 7$, see Table 5.1) which are based on a modified ‘classical’ helical geometry. However, if the design modifications proposed by these authors were applied to HCHPs, it is possible that they would have yielded much better performances. Pulsatile helical pipe flows, investigated by Khosravi-Bizhaem et al. (2019) [211], allow obtaining better performance than HCHPs in some situations, depending on the ‘classical’ helical pipe geometry studied. Given that these authors reported significant enhancement compared to steady state operation, the application of pulsatile flow to HCHPs is worthy of investigation as it could allow a substantial further improvement of their efficiency.

The data of Guo et al. (2011) [241], Wongcharee and Eiamsa-Ard (2011) [242] and Kurnia et al. (2020) [240] correspond to the use of twisted tapes. They reveal that, while inadequately designed internals lead to relatively poor performances, correctly conceived twisted tapes allow achieving impressive enhancement factors, much better than those obtained with HCHPs. The twisted tape with a twist ratio of 3.15 that has been investigated by Kurnia et al.(2020) [240], when fitted within a helical pipe, displays the best efficiency among the augmentation techniques addressed in this chapter. For $Re = 2\,000$ and $Pr = 7$, it allows enhancing the convective transfer rate by nearly 15-fold.

5.4.2 Volumetric heat/mass transfer enhancement

As it does not account for specific surface area effects, the $\eta_{1,0}$ criterion is not relevant for evaluating the potentiality of helical pipes or alternative techniques for process intensification, in particular in situations where a large number of flow tubes need to be packed. Such processes include monolith catalytic reactors and printed-circuit heat exchangers, where a dense packing of the flow tubes (i.e. a high specific surface area) is necessary to minimize the volume of the heat/mass exchanger. A convenient criterion in such situations is $\theta_{1,0}$ (following the general form given in Eq. 5.6) which is defined as follows (for heat and mass transfer situations respectively):

$$\theta_{1,0} = \frac{\sigma_{max}^* Nu}{\sigma_{S,max}^* Nu_S} \quad or \quad \theta_{1,0} = \frac{\sigma_{max}^* Sh}{\sigma_{S,max}^* Sh_S} \quad (5.7)$$

$\theta_{1,0}$ represents the ratio of the volumetric heat/mass flux allowed by a given technique/design to that achieved by the base case. For example, a $\theta_{1,0} = 2$ indicates that the enhancement strategy allows obtaining a similar heat/mass flux than the base case while allowing to reduce the volume of the heat/mass transfer device up to a factor 2 (in particular when the heat/mass transfer resistance is mostly located at the inner side of the tube, and in processes involving a heterogeneous chemical reaction, if the reaction is diffusion-controlled). Thus, $\theta_{1,0}$ quantifies the potentiality for miniaturization of an enhancement strategy or design. Since it does not account for the friction factor increase, this criterion is relevant in situations where the available space is the only primary concern.

Figure 5.9 displays contour plots in the (R_H^*, p^*) space of the $\theta_{1,0}$ criterion for Pr (respectively Sc) = 10 and $Re = 100$ and 2 000 (note that different scales are used for figures 5.9a and 5.9a). They are calculated using the correlations of Abushammala et al.(2020) [208] (Equations from chapter 3 (Equation 3.13 and Equation 3.16) whence the discontinuity at $R_H^* = 2$ (see Section 5.2.1). These results reveal that, given their high transfer rate (Figure 5.6a) and specific surface area (Figure 5.5b), HCHPs allow tremendous enhancements of volumetric transfer rates. The performances of HCHPs improve with increasing Re as Dean vortices become more and more intense. Hence, for $Re = 2\,000$ and Pr (respectively Sc) = 10, HCHPs enable a great volume reduction of heat/mass exchangers with more than an 8-fold factor. On the other hand, in the case of ‘classical’ helical pipes, the provided

heat/mass transfer enhancement remains limited and is not always sufficient to compensate the effects of their low packing densities. Hence, ‘classical’ helical pipes may perform even worse than straight tubes (i.e. $\theta_{1,0}$ values lower than one), in particular under low Re conditions.

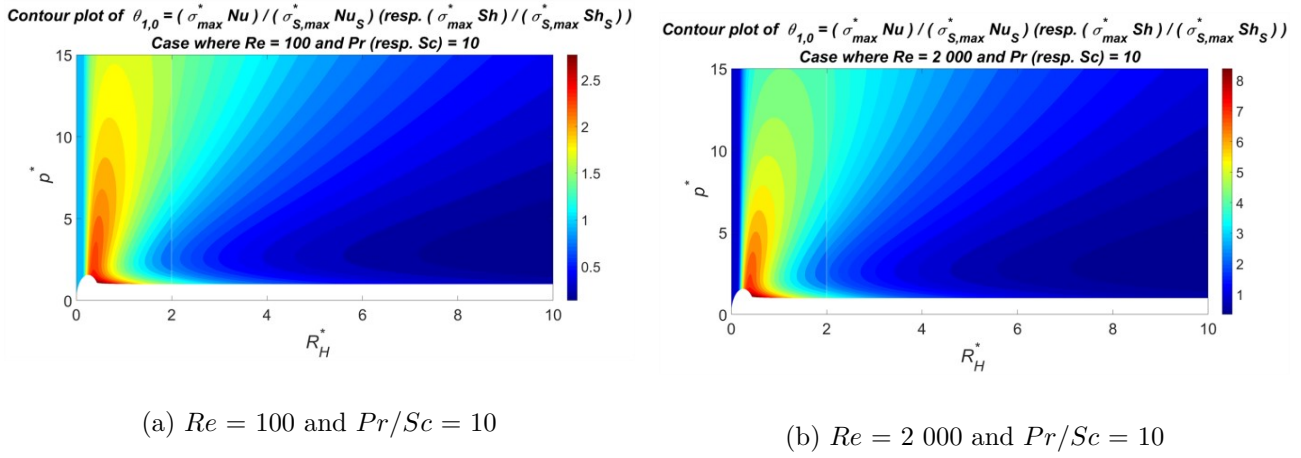


Figure 5.9: Contour plots in the (R_H^*, p^*) of the $\theta_{1,0}$ criterion

Figure 5.10 displays the maximal $\theta_{1,0}$ that can be achieved by helical pipes depending on Re and Pr (respectively Sc) conditions. The discontinuity in the curves at $Re = 400$ is due to the fact that the correlation of Abushammala et al.(2020) [208] for calculating Nu (respectively Sh) relies on different mathematical expressions depending on whether Re is higher or lower than 400. It can be noticed from this figure that, apart for very low Re values, optimal performances are always achieved by HCHPs having a R_H^* between 0.4 and 0.6 and a p^* of about 1.1. In addition, HCHPs intensification potentiality increases with increasing Re and Pr (respectively Sc). For comparison with helical pipe designs, the $\theta_{1,0}$ performance of alternative enhancement methods is also displayed in Figure 5.10. Because of the low specific surface area they develop, all the designs and techniques based on ‘classical’ helical pipe geometries exhibit much inferior performances than HCHPs, and some perform even worse than straight tubes. On the other hand, correctly designed twisted tapes disposed in straight tubes offer impressive intensification potentials, appreciably higher than those obtained with HCHPs. Indeed, on the one hand, twisted tapes lead to great transfer rates (Section 5.4.1), while the straight tube geometry allows developing a high specific surface area. Thus, twisted tapes seem to constitute the most efficient solution for the miniaturization of heat/mass transfer devices. One may wonder if the use of twisted tapes within HCHPs would not allow obtaining even higher intensification potentialities. Finally, it should be kept in mind that twisted tapes present some drawbacks which may limit their usage in some situations. In particular, as they are subject to fouling and scaling, they may lead to significant maintenance and cleaning costs.

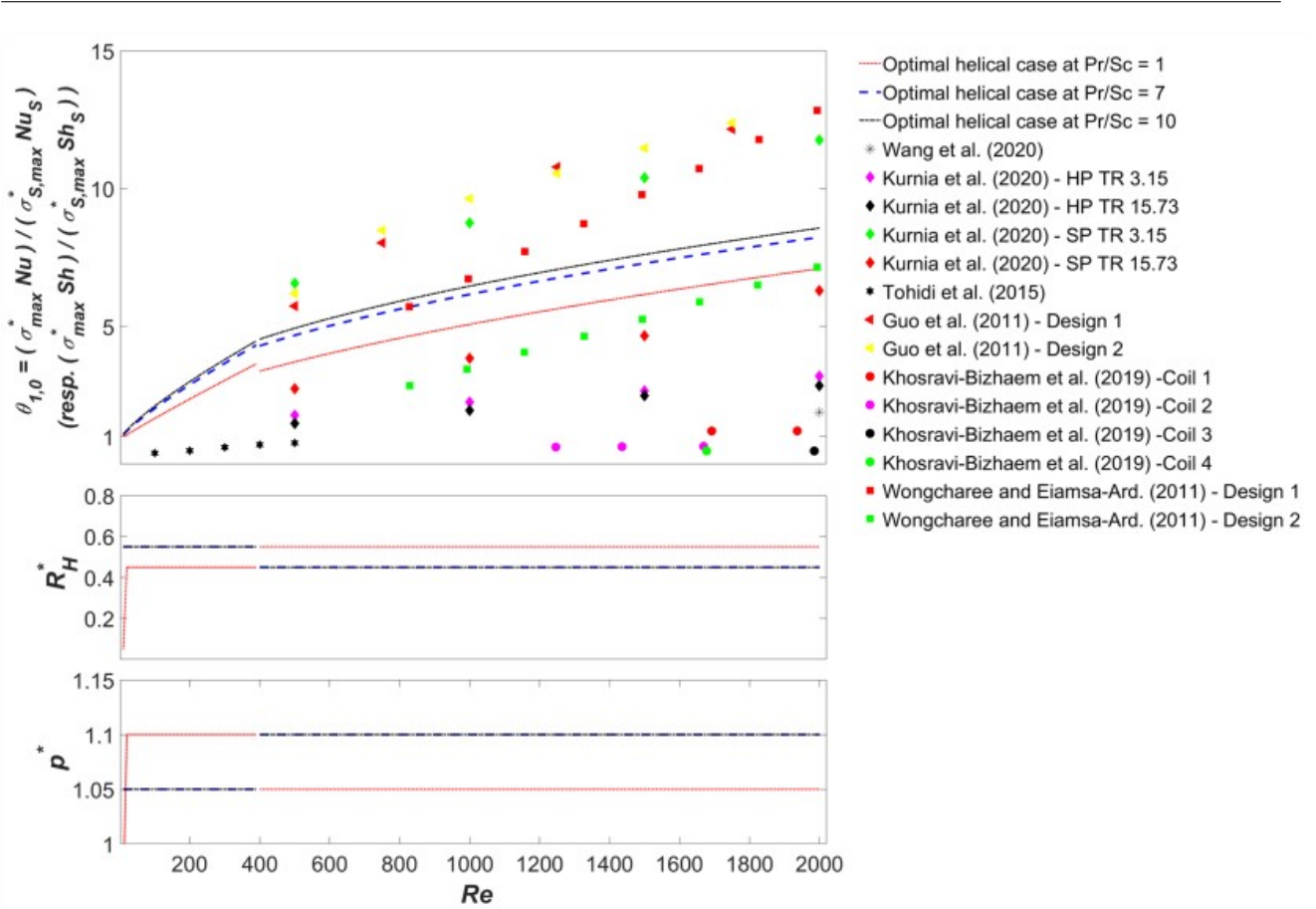
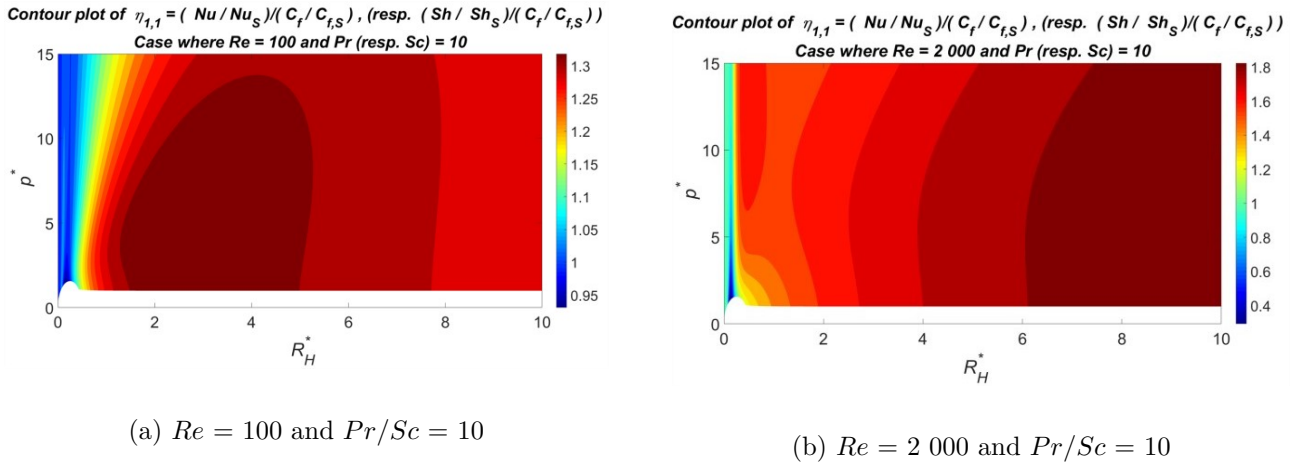


Figure 5.10: Performances of helical pipes and alternative enhancement techniques based on the $\theta_{1,0}$ criterion. In the figure caption, for the data of Kurnia et al. (2020) [240], HP and SP respectively refer to the use of a helical or a straight pipe, while TR refers to the twist ratio of the used twisted tape

5.4.3 Cost-effectiveness of heat/mass transfer enhancement per unit surface

The criteria that have been examined in the previous sections are relevant when the minimization of the exchanger/reactor surface or volume is the sole main objective, while pumping power concerns can be omitted. However, in most situations, to be of industrial relevance, enhancement methods and designs should allow a good trade-off between the minimization of both operating (i.e. pumping power) and purchase (i.e. material mass) costs. One appropriate criterion that enables to simultaneously account for these two conflicting objectives is $\eta_{1,1}$ which is expressed in Eq. 5.2. $\eta_{1,1}$ can be seen as an assessment of the cost-effectiveness of enhancement methods and designs aiming at minimizing exchangers surface. Figure 5.11 presents contour plots in the (R_H^*, p^*) space of the $\eta_{1,1}$ criterion for Pr (respectively Sc) = 10 and $Re = 100$ and 2 000. Both Nu (respectively Sh) and C_f are calculated using the correlations of Abushammala et al. (2020;2019) [191, 208] (see Section 5.2.1). Figure 5.12 displays the maximal $\eta_{1,1}$ that can be achieved by helical pipes depending on Re and Pr (respectively Sc) conditions.

Figures 5.11 and 5.12 reveal that optimal performances in terms of $\eta_{1,1}$ criterion are not achieved by HCHPs, but rather by ‘classical’ helixes. Indeed, as can be seen from Figures 5.6a and 5.6b,

Figure 5.11: Contour plots in the (R_H^*, p^*) of the $\eta_{1,1}$ criterion

although HCHPs do lead to great transfer rates, they also induce relatively high friction losses. On the other hand, it can be noticed that the heat/mass transfer enhancement provided by ‘classical’ helical pipes is significantly higher than the friction factor increase they induce.

Figure 5.12 indicates that at relatively low Reynolds numbers, optimal $\eta_{1,1}$ values are achieved by helices having a R_H^* of about 2 and a moderate to high p^* . On the other hand, for relatively high Reynolds numbers, the highest $\eta_{1,1}$ values are obtained with helices of low p^* and a large R_H^* of 10, which is the highest R_H^* value considered in this study. The significant discontinuity appearing at $Re = 400$ is due to several reasons. First, the fact that both correlations calculating C_f [191] and Nu (respectively Sh) [208] rely on different mathematical expressions depending on whether Re is higher or lower than 400. Second, as can be seen from Figures 5.11a and 5.11b, for a given Re , there is a large range of geometric parameters R_H^* and p^* where helices achieve high performances. From an engineering point of view, given the limited precision of any correlation, all of these helices can be regarded as exhibiting high and similar efficiencies. However, mathematically speaking, the exact R_H^* and p^* coordinates of the helix achieving the highest $\eta_{1,1}$ value may be indeed very sensitive to the correlation expression used, whence the significant discontinuity appearing at $Re = 400$.

Finally, it is noteworthy that, even with the relatively low Pr (respectively Sc) numbers considered in this study, most helical designs allow obtaining $\eta_{1,1}$ values higher than unity (Figure 5.11), which means that the heat/mass enhancement they provide is higher than the friction factor increase they induce. This point is of major importance from a cost-efficiency perspective. Indeed, for achieving a given heat/mass flux, by virtue of their higher Nu (resp. Sh), helical tubes require a shorter pipe length than the base case. The fact that their $\eta_{1,1}$ value is higher than unity implies that the effect of their shorter length on pumping power overcomes the effect of their higher friction factor. Thus, helical pipes prove to be a cost-effective solution that, compared to the base case, allows simultaneously reducing the exchanger surface and the associated pumping costs. Obviously, this conclusion is valid as long as the heat/mass transfer is limited by the convective resistance at the inner flow side.

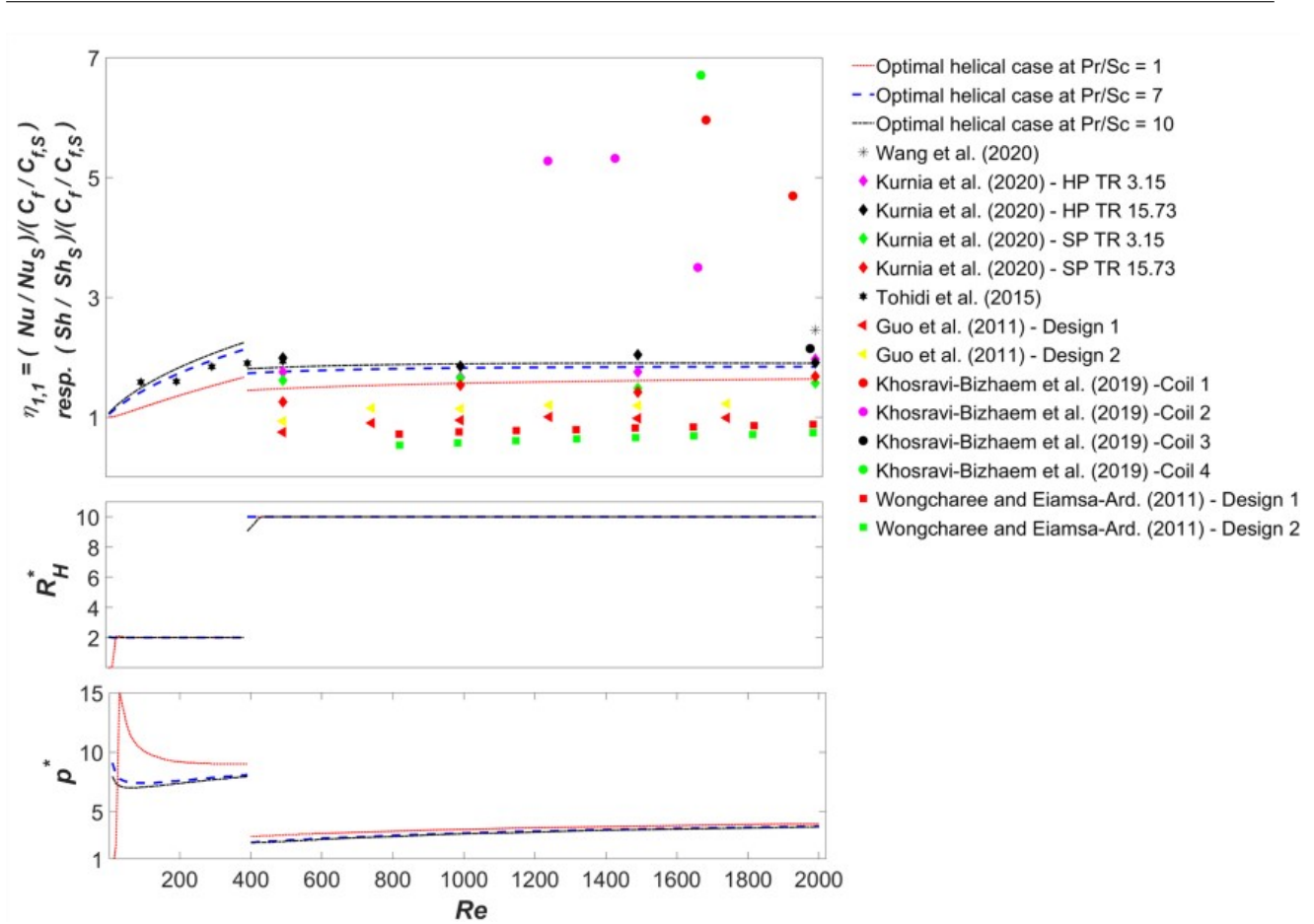


Figure 5.12: Performances of helical pipes and alternative enhancement techniques based on the $\eta_{1,1}$ criterion. In the figure caption, for the data of Kurnia et al. (2020) [240], HP and SP respectively refer to the use of a helical or a straight pipe, while TR refers to the twist ratio of the used twisted tape

Comparison between helical pipes and alternative techniques is carried out in Figure 5.12. The data of Khosravi-Bizhaem et al. (2019) [211] suggest that pulsating flow conditions allow achieving remarkably higher performances than the remaining methods. However, as noted in Section 5.3, pressure drop measurements performed by these authors have probably largely underestimated the friction factor which leads to these surprising results.

Twisted tapes disposed in straight tubes exhibit slightly to much lower performances than helical pipes in terms of $\eta_{1,1}$ criterion. Indeed, although they lead to tremendous enhancement rates (Figure 5.8), they also induce excessive frictional losses.

On the other hand, enhancement methods based upon a helical design constitute energy-efficient solutions for heat/mass transfer augmentation. Hence, the chaotic heat exchanger of Tohidi et al. (2015) [239] and the twisted tapes fitted within a helical tube of Kurnia et al. (2020) [240] display similar performances than helical pipes. The geometry proposed by Wang et al. (2020) [238] seems to be the most effective with regard to the $\eta_{1,1}$ criterion. Unfortunately, these authors mainly focused on turbulent flows and performed a single experimental measurement within the laminar regime (at a Re of about 2 000, see Figure 5.12) only, which limits the comparison.

5.4.4 Cost-effectiveness of volumetric heat/mass transfer enhancement

As it does not account for specific surface area effects, the $\eta_{1,1}$ criterion is not relevant for evaluating the potentiality of helical pipes or alternative techniques for cost-effective process intensification, in particular in situations where a large number of flow tubes need to be used. Such processes include monolith catalytic reactors and printed-circuit heat exchangers, where a dense packing of the flow tubes (i.e. a high specific surface areas) is necessary for minimizing the volume of the heat/mass exchanger. A convenient criterion in such situations is $\theta_{1,1}$ which is defined as follows (for heat and mass transfer situations respectively):

$$\theta_{1,1} = \frac{(\sigma_{max}^* Nu / C_f)}{(\sigma_{S,max}^* Nu_S / C_{f,S})} \quad \text{or} \quad \theta_{1,1} = \frac{(\sigma_{max}^* Sh / C_f)}{(\sigma_{S,max}^* Sh_S / C_{f,S})} \quad (5.8)$$

$\theta_{1,1}$ compares the volumetric heat/mass transfer enhancement allowed by a given strategy to the relative friction factor increase that it induces with respect to the base case. Thus, it allows evaluating the potentiality of a given method in terms of cost-effective miniaturization.

Figure 5.13 presents contour plots in the (R_H^*, p^*) space of the $\theta_{1,1}$ criterion for Pr (resp. Sc) = 10 and $Re = 100$ and 2 000 respectively. The geometric features and thermo-hydraulic performances of helical pipes, σ_{max}^* , Nu (resp. Sh) and C_f , were calculated using the correlations of Abushammala et al. (2020;2019) [191, 208] (that are reported in Equation 2.7, Equation 3.13 and Equation 3.16). Figure 5.14 displays the maximal $\theta_{1,1}$ that can be achieved by helical pipes depending on Re and Pr (resp. Sc) conditions.

Figures 5.13 and 5.14 reveal that the best $\theta_{1,1}$ performances are achieved by helices having a low R_H^* and a high p^* . These designs provide the finest trade-off between a high specific surface area (Figure 5.5b), a good convective transfer rate (Figure 5.6a) and a relatively low friction factor (Figure 5.6b). At high Re values, maximal performances are reached with helices of $p^* = 15$, which is the highest p^* value investigated in this study.

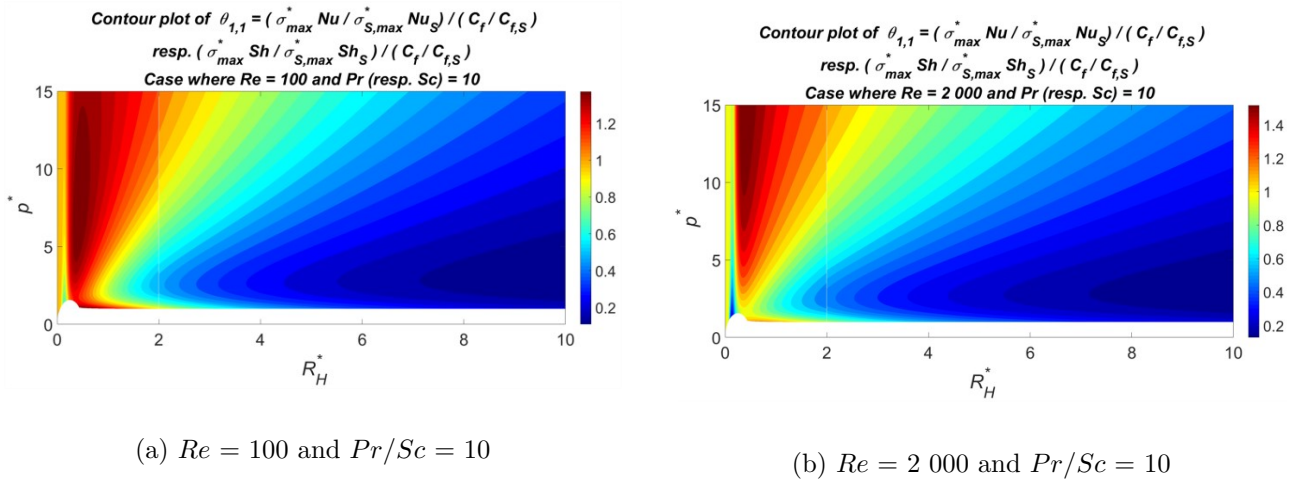


Figure 5.13: Contour plots in the (R_H^*, p^*) of the $\theta_{1,1}$ criterion

These results reveal that elongated helices of low R_H^* allow achieving $\theta_{1,1}$ values higher than unity. Thus, these helix designs are particularly appropriate for conceiving compact units. Indeed, compared to the base case, they simultaneously enable to decrease the required pumping power and to considerably reduce the volume of the heat/mass exchanger or reactor. This conclusion remains valid as long as the heat/mass transfer is limited by the convective resistance at the inner flow side.

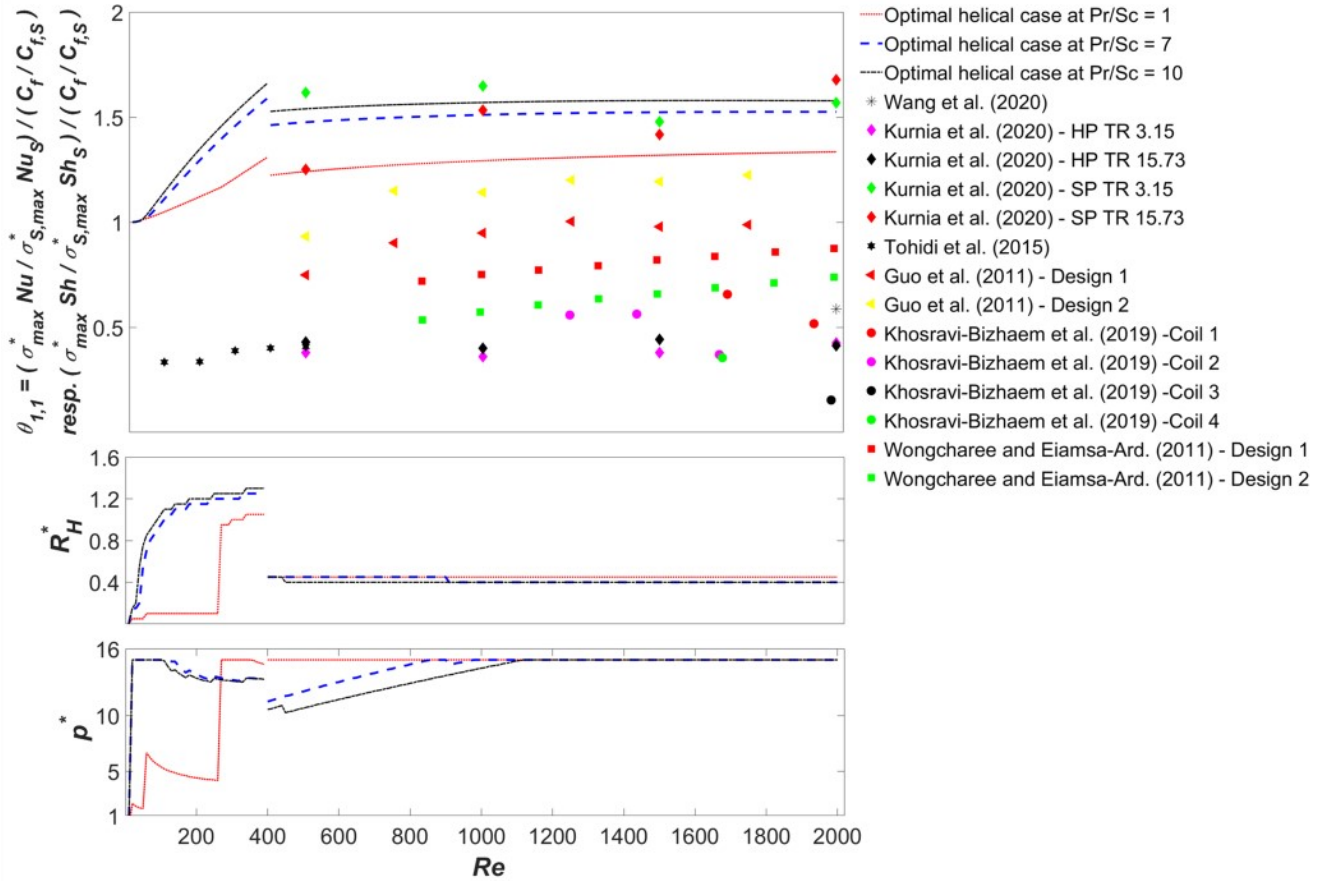


Figure 5.14: Performances of helical pipes and alternative enhancement techniques based on the $\theta_{1,1}$ criterion. In the figure caption, for the data of Kurnia et al. (2020) [240], HP and SP respectively refer to the use of a helical or a straight pipe, while TR refers to the twist ratio of the used twisted tape

Comparison with literature data is carried out in Figure 5.14 which shows that all methods based on a ‘classical’ helix geometry poorly perform with respect to the $\theta_{1,1}$ criterion because of the low specific surface area they develop. Despite their high packing density and convective transfer rate, straight tubes equipped with twisted tapes generally exhibit much lower performances than helical pipes because of the significant friction losses they induce. Only those investigated by Kurnia et al. (2020) [240] achieve comparable or slightly higher potentialities than elongated helix designs.

5.4.5 Cost-effectiveness of volumetric heat/mass transfer enhancement in ‘shell-and-tube’ configurations

As discussed in the previous section, in many applications (e.g. monolith catalytic reactors, printed-circuit heat exchangers), the flow tubes need to be packed as densely as possible in order to minimize the exchanger volume. However, in many other processes, two fluids need to be used, one circulating within the tubes and the other within a calender. Such processes include shell-and-tube heat exchangers, hollow fiber dense membrane contactors, multitubular and monolithic catalytic reactors where temperature is regulated using a heating or cooling fluid, etc.

In such configurations, the tubes packing density should be carefully fixed so as to ensure a good trade-off between intensification purposes and a limited pressure drop at the shell-side. Attributing half of the unit volume to the fluid circulating within the tubes is a good compromise, the remaining half volume being left for the tubes walls and to the fluid circulating within the calender. Thus, at a first approximation, it may be considered that a packing density of 0.5 is the most appropriate in such configurations. As mentioned in Section 5.2.1, the maximal packing density of cylinders is 90.7%, and their dimensionless specific surface area under these dense packing conditions is noted $\sigma_{S,max}^*$. Thus, under a packing density of 50%, the specific surface area developed by straight tubes equals $(0.5/0.907) \times \sigma_{max}^* = 0.55\sigma_{max}^*$. Accordingly, a new criterion, $\chi_{1,1}$, is proposed for assessing the cost-effectiveness of volumetric heat/mass transfer enhancement in exchangers following a shell-and-tube configuration:

$$\chi_{1,1} = \begin{cases} \frac{(\sigma_{max}^* Nu/C_f)}{(0.55 \sigma_{S,max}^* Nu_S/C_{f,S})} = \frac{\theta_{1,1}}{0.55} & \text{or} & \frac{(\sigma_{max}^* Sh/C_f)}{(0.55 \sigma_{S,max}^* Sh_S/C_{f,S})} = \frac{\theta_{1,1}}{0.55} & \text{if } \phi_{max} \leq 0.5 \\ \frac{(\sigma_{0.5}^* Nu/C_f)}{(0.55 \sigma_{S,max}^* Nu_S/C_{f,S})} & \text{or} & \frac{(\sigma_{0.5}^* Sh/C_f)}{(0.55 \sigma_{S,max}^* Sh_S/C_{f,S})} & \text{if } \phi_{max} \geq 0.5 \end{cases} \quad (5.9)$$

With the $\chi_{1,1}$ criterion, the performances of an enhancement technique/design are compared to that of straight tubes disposed with a packing density of 50%, i.e. developing 55% of their highest possible specific surface area, whence the factor 0.55 at the denominator. Designs which maximal packing density is lower than 50% are considered to be packed as densely as possible (i.e. under their maximal possible packing density) since anyway, enough space would be left for the fluid circulating in the calender. On the other hand, geometries which maximal packing density exceeds 50% are considered to be arranged with a packing density of 50% only (and the dimensionless specific surface area they develop is noted $\sigma_{0.5}^*$) so as to keep a sufficient space for the fluid circulating at the shell side. The ratio of the specific surface areas developed by helixes and straight tubes is equal to the ratio of their packing densities (see Eq. 5.5). Therefore, in the case of helical pipes, the expression of

the $\chi_{1,1}$ criterion may be simplified and becomes:

$$\chi_{1,1} = \begin{cases} \frac{(\sigma_{H,max}^* Nu_H / C_{f,H})}{(0.55 \sigma_{S,max}^* Nu_S / C_{f,S})} = \frac{\theta_{1,1}}{0.55} & \text{or} & \frac{(\sigma_{H,max}^* Sh_H / C_{f,H})}{(0.55 \sigma_{S,max}^* Sh_S / C_{f,S})} = \frac{\theta_{1,1}}{0.55} & \text{if } \phi_{max} \leq 0.5 \\ \frac{(Nu_H / C_{f,H})}{(Nu_S / C_{f,S})} = \eta_{1,1} & \text{or} & \frac{(Sh_H / C_{f,H})}{(Sh_S / C_{f,S})} = \eta_{1,1} & \text{if } \phi_{max} \geq 0.5 \end{cases} \quad (5.10)$$

One can notice from Equation 5.10 that for helices exhibiting a maximal packing density higher than 0.5, the expression of $\chi_{1,1}$ becomes the same as that of $\eta_{1,1}$ (Equation 5.2 and Section 5.4.3). Figure 5.15 presents the contour plot in the (R_H^*, p^*) space of the $\chi_{1,1}$ criterion for Pr (resp. Sc) = 10 and $Re = 2\,000$, and Figure 5.16 displays the maximal $\chi_{1,1}$ that can be achieved by helical pipes, depending on Re and Pr (resp. Sc) conditions. It can be noticed that the highest performances are achieved by elongated helices having a low to moderate R_H^* value and a relatively high p^* , up to 15, the maximal p^* value considered in this investigation.

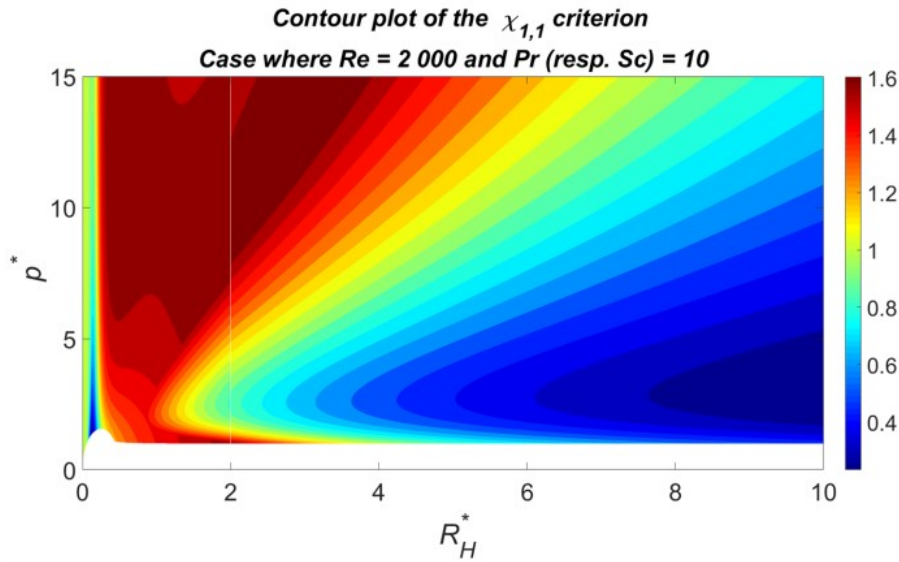


Figure 5.15: Contour plot in the (R_H^*, p^*) of the $\chi_{1,1}$ criterion for $Re = 2\,000$ and $Pr/Sc = 10$

The performances of alternative techniques are represented in Figure 5.16. Despite that with the $\chi_{1,1}$ criterion, the packing density of straight tubes is limited to 55% of its maximal possible value, methods based on a ‘classical’ helix geometry still exhibit relatively low performances because of their very low specific surface area, and generally achieve $\chi_{1,1}$ values lower than unity. On the other hand, as straight tubes lose the advantage of their higher specific surface area, twisted tapes fitted within straight pipes achieve significantly to slightly lower $\chi_{1,1}$ performances than helical pipes. Hence, elongated helical designs allow achieving the highest $\chi_{1,1}$ values and reveal to be the most effective method for an energy-efficient miniaturization of exchangers following a shell-and-tube configuration.

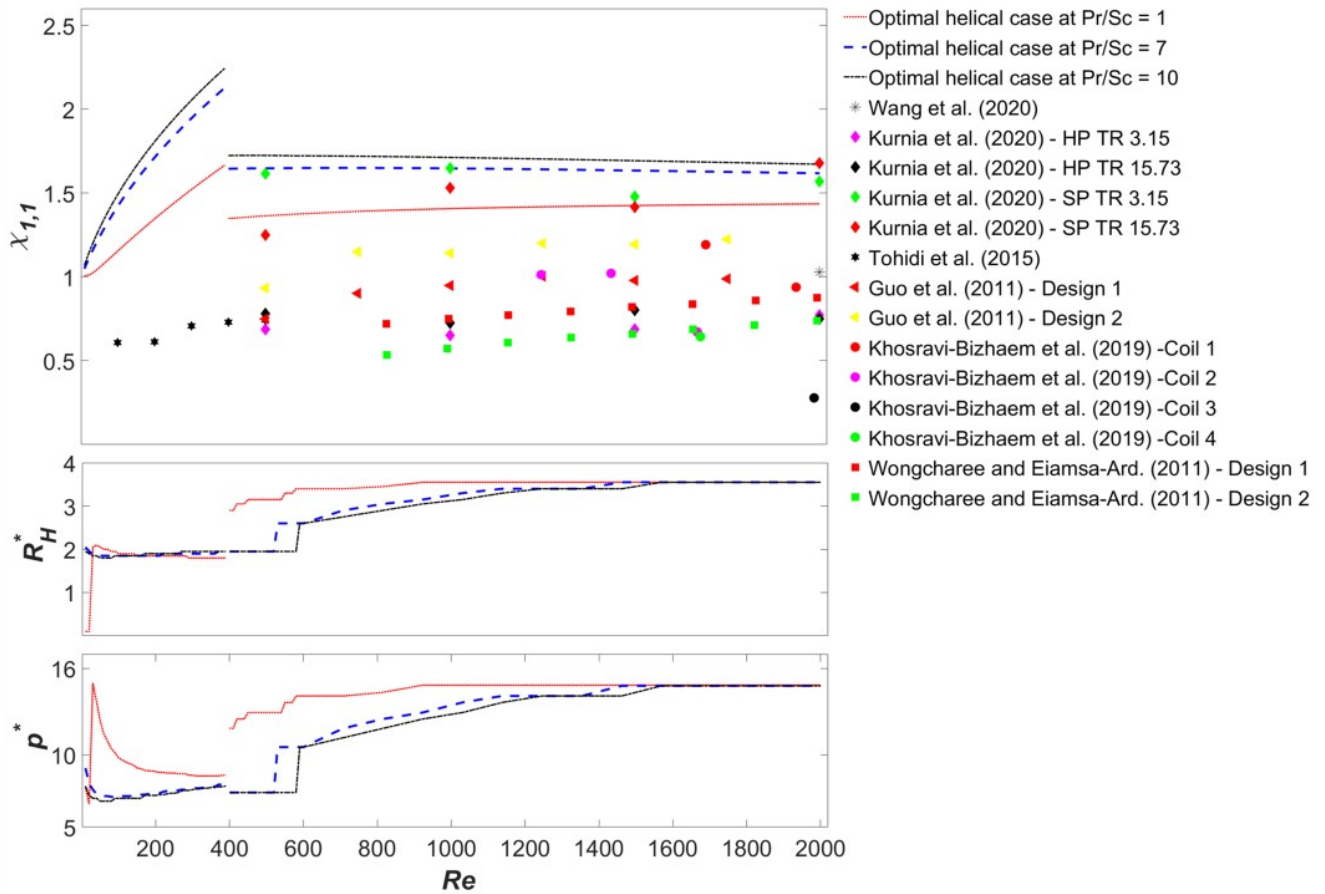


Figure 5.16: Performances of helical pipes and alternative enhancement techniques based on the $\chi_{1,1}$ criterion. In the figure caption, for the data of Kurnia et al. (2020) [240], HP and SP respectively refer to the use of a helical or a straight pipe, while TR refers to the twist ratio of the used twisted tape

5.5 Conclusion

Novel performance criteria accounting for specific surface area effects have been proposed in this chapter for evaluating the intensification potentiality of heat/mass transfer enhancement techniques. For each considered criterion, some particular helix designs have been shown to exhibit good to excellent performances. Highly curved helical pipes reveal to be a very efficient strategy for minimizing the volume of heat/mass exchangers and reactors. However, these geometries induce significant friction losses. On the other hand, elongated helical pipes of low helical radius were shown to allow cost-effective process intensification as they simultaneously enable to decrease the required pumping power and to considerably reduce the volume of reactors and heat/mass exchangers. The performances of alternative techniques of heat/mass transfer enhancement (twisted tape inserts, pulsatile flow operation, and modified helical geometries) have also been analyzed, highlighting the weaknesses and strengths of each strategy. Applying these methods in conjunction with a highly curved or elongated helical design could allow a further improvement of their potentialities. This remains an open question that is worthy of deep investigation in future studies.

Chapter 6

Toward novel coiled heat/mass exchangers designs

Summary

Curved geometries are preferred to other passive techniques because they perform similarly or even better with lower energy consumption and maintenance cost. Accordingly, transport phenomena in helical pipes and other coiled geometries were investigated in numerous numerical and experimental studies. As demonstrated in the previous chapters, highly curved and/or elongated helical pipes offer tremendous potentialities for intensified heat/mass transfer performances as they generate intense Dean-type vortices and can be densely packed.

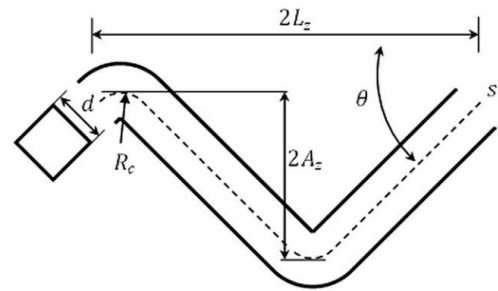
In this chapter, two novel complex coiled designs are proposed and investigated: wavy helical pipes and double helical pipes. The performances of these geometries were evaluated using different criteria accounting for heat/mass transfer enhancement, frictional losses and specific surface area effects. Comparison to helical pipes reveals that these novel designs allow reaching even higher performances in terms of intensified heat/mass transfer.

6.1 Introduction of the Complex helical shapes

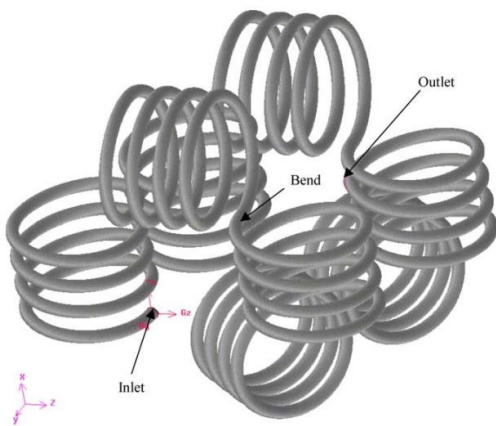
Two methods are used to improve the transfer rate in heat and mass exchangers: active and passive techniques. Active techniques are based on external forces such as pulsed flow, vibration system, etc. to perform the augmentation. They proved to be efficient but they are not always easy to integrate with the other components in a system. They also increase the total cost of the system manufacturing and maintenance. On the other hand, passive techniques involve geometries with elaborate surfaces. These elaborate surfaces are easier and cheaper to integrate and do not interfere with other components in the system. Curved geometries are preferred to other passive techniques because they perform similarly or even better with lower energy consumption and maintenance cost. Their performance is due to the intense Dean-type vortices they generate. In this PhD, helical curved pipes were investigated and shown to provide good trade-off between the achieved enhancement rate and the friction factor increase they induce. In particular, highly curved helical pipes (HCHPs) were proved to perform better than classical helical pipes. HCHPs thus represent a very promising opportunity for heat and mass exchanger applications.



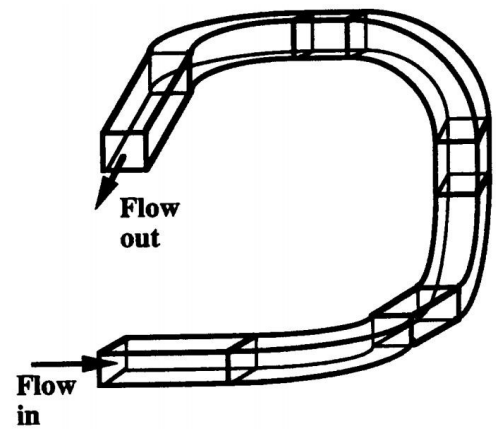
(a) Three-dimensional serpentine by Liu et al. (2000) [243]



(b) Periodic zigzag channels by Zheng et al. (2013) [244]



(c) Bent coil configuration by Kumar and Nigam (2005) [245]



(d) Twisted curved channel by Peerhossaini et al. (1993) [246]

Figure 6.1: Channel structures designed to benefit from Dean vortices and chaotic advection

More complex geometries were also studied in the past, including modified helical shapes. These shapes have been developed in order to generate intense mixing, and in particular chaotic advection, a very efficient mixing occurring at low Reynolds number. Table 6.1 and Figure 6.1 present examples of such complex geometries used in heat/mass exchanger applications.

Two different complex shapes were elaborated and investigated during the present PhD: wavy helical shapes and double helical shapes. CFD simulations were conducted in order evaluate both transfer intensification and pumping cost in these novel designs.

Table 6.1: Performances of heat/mass exchangers processes of complex shape

Authors	Application	Geomtry	Heat/Mass transfer enhancement
Zheng et al. (2013) [244]	Heat exchanger	Periodic zigzag channels	300% compared to the straight pipe case
Moll et al. (2007) [156]	Mass exchanger (Membrane)	Woven fibers	100% compared to the straight pipe case for the same energy supplied
Kumar and Nigam (2005) [245]	Heat exchanger	Bent coil configuration	20 – 30% compared to the helical pipes
Ghogomu et al. (2001) [149]	Mass exchanger (Membrane)	Helical fiber S-fiber Twisted fibers	50% compared to the straight pipe case
Liu et al. (2000) [243]	Heat exchanger	Three-dimensional serpentine channel	16 times compared to the straight pipe case, $Re \leq 70$
Winzeler and Belfort (1993) [43]	Mass exchanger (Membrane)	Coiled half-pipe glued on flat membrane	471%compared to the straight pipe case
Peerhossaini et al. (1993) [246]	Heat exchanger	Twisted curved channel	15 – 18%compared to the helical pipe case

6.1.1 Wavy helical pipes

The first complex helical design is Wavy Helical Pipes (WHP). In this design, the pipe centerline follows a helical path modified by sinusoidal oscillations, which is described by the following parametric equation:

$$\begin{aligned}
 \frac{x}{d} &= R_H^* \cos(t) \\
 \frac{y}{d} &= R_H^* \sin(t) \\
 \frac{z}{d} &= A \sin(Bt) + \frac{p^*}{2\pi} t
 \end{aligned} \tag{6.1}$$

Where A is the sine amplitude, B the number of oscillations per helix turn and t the parameter. Five wavy geometries were designed, Figure 6.2.

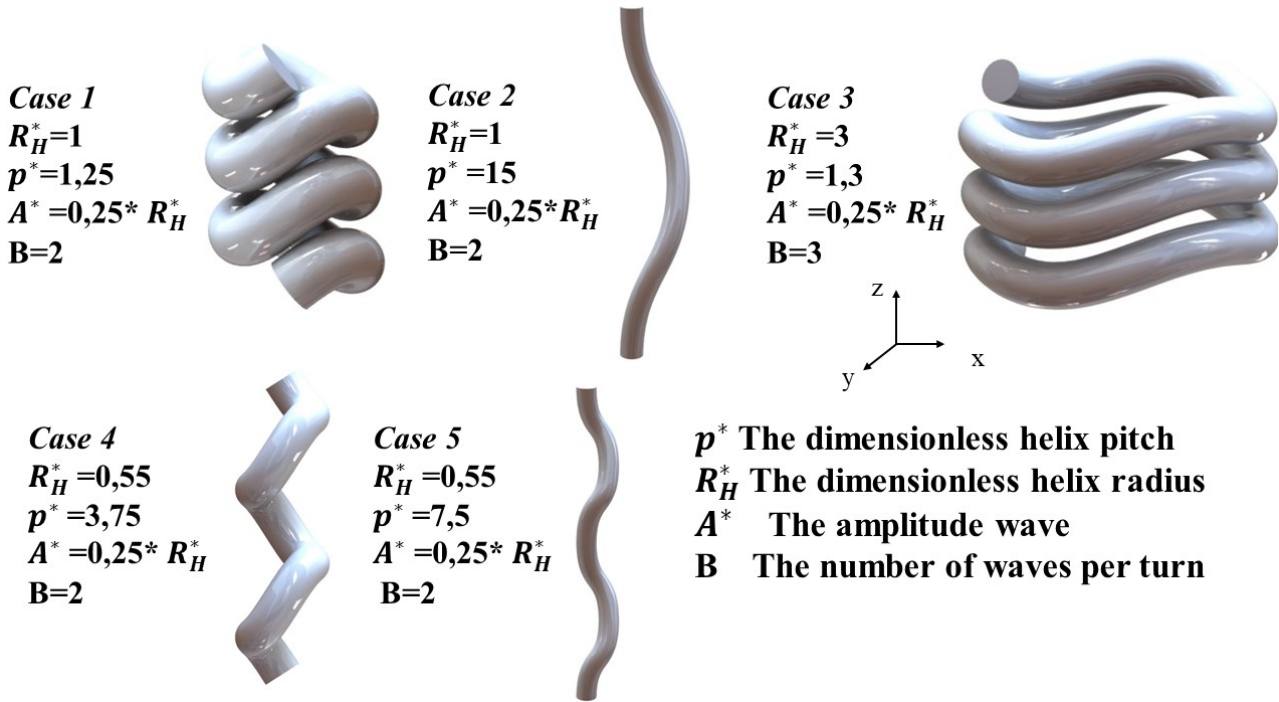


Figure 6.2: The five different wavy helical pipes studied in the present section

CFD simulations were conducted using the commercial code ANSYS Fluent 16. The flow field in the pipe was determined by solving the continuity and Navier-Stokes equations assuming a Newtonian, incompressible, and steady flow and uniform fluid properties. As boundary conditions, a uniform velocity profile was set at the pipe inlet: as the flow rate is imposed and since a uniform fluid density is considered, the gravity force has no effect on the velocity field and therefore this body force term was not included in the Navier-Stokes equations. At the pipe outlet, a uniform pressure condition was used and the no-slip condition was set at the pipe wall. The energy conservation equation was also solved with the following boundary conditions: a uniform fluid temperature was enforced at the inlet, an isothermal wall was considered, and a zero-temperature gradient was imposed at the pipe outlet. The hydrodynamic and energy equations were iteratively solved until convergence. The advective terms were discretized using the QUICK scheme while the diffusive ones were central-differenced. Pressure interpolation was carried out using a second order scheme.

Three different Reynolds numbers were considered $Re = 400, 600$ and 800 , and two Prandtl (Schmidt) values, $Pr/Sc = 1$ and 10 .

For each simulation, the Nusselt number Nu_H , the friction factor $C_{f,H}$, and the maximum compactness $\sigma_{H,max}^*$ were computed. In the following, the performances of wavy helical pipes (WHPs) are evaluated and compared to the best performances obtained with optimal helical pipes (OHPs). First, the performances are analyzed in terms of the heat/mass transfer enhancement factor $\eta_{1,0} =$

Nu_H/Nu_S (resp. Nu_H/Nu_S), Figure 6.3 and Table 6.2 It appears that WHPs are more efficient at high Prandtl number ($Pr/Sc=10$), with four WHPs performing better than OHPs (helical configurations maximizing $\eta_{1,0}$), against only two at low Prandtl number ($Pr/Sc = 1$).

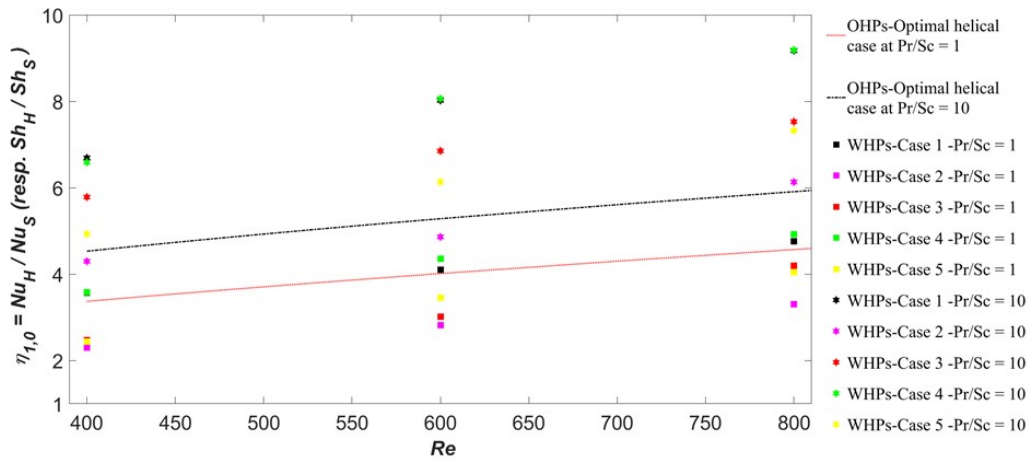












Figure 6.3: Heat/mass transfer enhancement factor $\eta_{1,0}$ vs. Reynolds number for wavy helical pipes (WHPs) and optimal helical pipes (OHPs) at $Pr/Sc=10$ and $Pr/Sc=1$

Table 6.2: Heat/mass transfer enhancement factor $\eta_{1,0}$ ratio of the optimal helical pipes (OHPs) to the wavy helical pipes (WHPs) $(\eta_{1,0})_{OHPs}/(\eta_{1,0})_{WHPs}$

Cases	$Re=400$	$Re=400$	$Re=600$	$Re=600$	$Re=800$	$Re=800$	
	$Pr/Sc=1$	$Pr/Sc=10$	$Pr/Sc=1$	$Pr/Sc=10$	$Pr/Sc=1$	$Pr/Sc=10$	
$(\eta_{1,0})_{OHPs}/(\eta_{1,0})_{WHPs}$							
WHPs-Case 1		0.95	0.76	0.98	0.73	0.93	0.72
WHPs-Case 2		1.64	1.18	1.60	1.22	1.55	1.08
WHPs-Case 3		1.52	0.87	1.49	0.86	1.22	0.88
WHPs-Case 4		0.95	0.77	0.92	0.73	0.89	0.72
WHPs-Case 5		1.54	1.03	1.30	0.96	1.26	0.90

In order to evaluate both the transfer efficiency (via the Nusselt/Sherwood numbers) and the energy cost (via the friction factor), factor $\eta_{1,1} = (Nu_H/Nu_S)/(C_{f,H}/C_{f,S})$ *resp.* $\eta_{1,1} = (Sh_H/Sh_S)/(C_{f,H}/C_{f,S})$, is plotted and compared in Figure 6.4 and Table 6.3 as a function of the Reynolds number, both for WHPs and OHPs (helical configurations maximizing factor $\eta_{1,1}$). At $Pr/Sc=1$, two WHPs (Cases 2 and 5) achieve higher $\eta_{1,1}$ values than the OHPs. At $Pr/Sc=10$, all the tested WHPs beat the OHPs, the most successful being Case 2.

Table 6.3: Performance factor $\eta_{1,1}$ ratio of the optimal helical case (OHPs) to the wavy helical pipes (WHPs) $(\eta_{1,1})_{OHPs}/(\eta_{1,1})_{WHPs}$

Cases	$Re=400$	$Re=400$	$Re=600$	$Re=600$	$Re=800$	$Re=800$
	$Pr/Sc=1$	$Pr/Sc=10$	$Pr/Sc=1$	$Pr/Sc=10$	$Pr/Sc=1$	$Pr/Sc=10$
$(\eta_{1,1})_{OHPs}/(\eta_{1,1})_{WHPs}$						
WHPs-Case 1						
	1.14	0.76	1.23	0.78	1.24	0.78
WHPs-Case 2						
	0.98	0.66	0.94	0.67	0.92	0.59
WHPs-Case 3						
	1.32	0.70	1.35	0.74	1.08	0.74
WHPs-Case 4						
	1.01	0.68	1.00	0.67	1.01	0.66
WHPs-Case 5						
	1.11	0.68	0.94	0.65	0.94	0.62

For many applications, the occupied volume is an important issue. This why the volumetric heat/mass flux $\theta_{1,0} = (\sigma_{H,max}^* Nu_H)/(\sigma_{S,max}^* Nu_S)$ *resp.* $\theta_{1,0} = (\sigma_{H,max}^* Sh_H)/(\sigma_{S,max}^* Sh_S)$ combining the Nusselt/Sherwood ratio with the packing density is computed for wavy helices (WHPs) and compared to the highest $\theta_{1,0}$ values obtained for helical pipes (OHPs), Figure 6.5 and Table 6.4. With this factor, OHPs outreach the WHPs, whatever the Prandtl number value, except at high Reynolds ($Re = 800$) and Prandtl ($Pr = 10$). This is due to the fact that the investigated WHPs are bulkier than the OHPs and cannot be as densely packed.

Finally all three parameters Nusselt/Sherwood, friction factor and maximal compacity ratios are

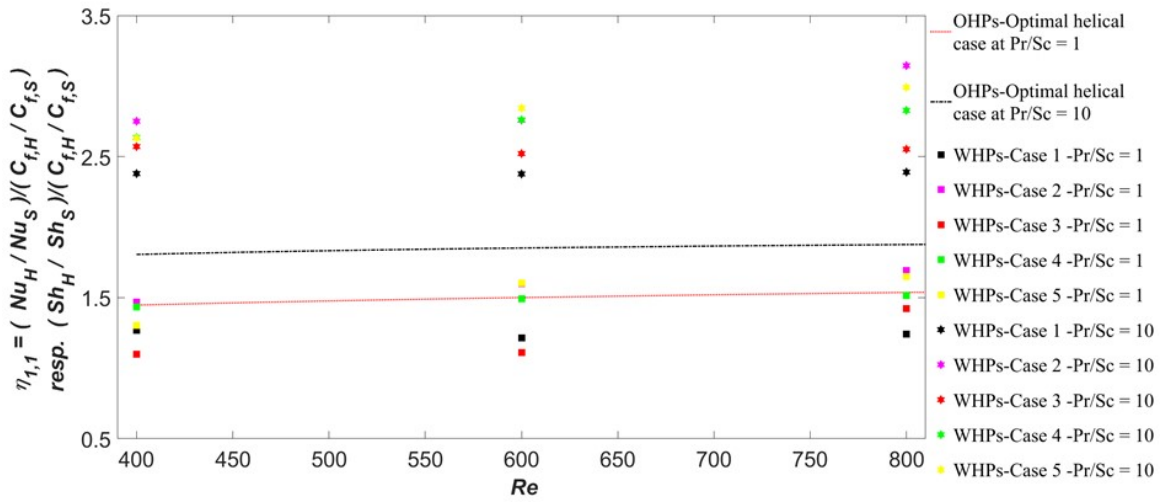


Figure 6.4: Performance factor $\eta_{1,1}$ (comparing transfer enhancement to pumping cost) vs. Reynolds number for wavy helical pipes (WHPs) and optimal helical pipes (OHPs) at $Pr/Sc=10$ and $Pr/Sc=1$

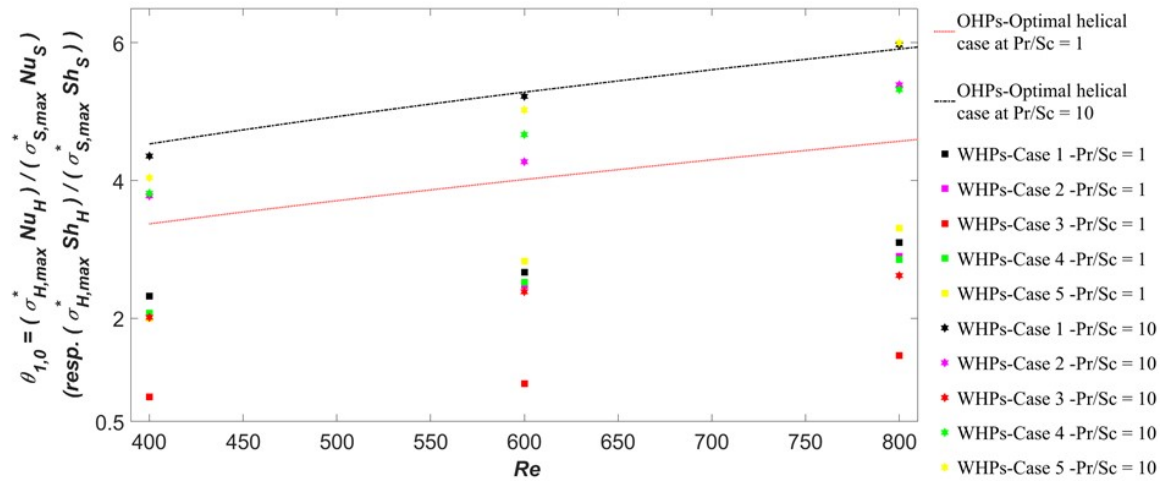












Figure 6.5: The volumetric heat/mass flux $\theta_{1,0}$ vs. Reynolds number for the wavy helical pipes (WHPs) and the optimal helical pipes (OHPs) at $Pr/Sc = 10$ and $Pr/Sc=1$

Table 6.4: The volumetric heat/mass flux $\theta_{1,0}$ ratio of the optimal helical case (OHPs) to the wavy helical pipes (WHPs) $(\theta_{1,0})_{OHPs}/(\theta_{1,0})_{WHPs}$

Cases	$Re=400$	$Re=400$	$Re=600$	$Re=600$	$Re=800$	$Re=800$
	$Pr/Sc=1$	$Pr/Sc=10$	$Pr/Sc=1$	$Pr/Sc=10$	$Pr/Sc=1$	$Pr/Sc=10$
$(\theta_{1,0})_{OHPs}/(\theta_{1,0})_{WHPs}$						
WHPs-Case 1 	1.45	1.04	1.50	1.01	1.47	0.99
WHPs-Case 2 	1.67	1.20	1.62	1.23	1.57	1.09
WHPs-Case 3 	3.91	2.25	3.81	2.21	3.13	2.25
WHPs-Case 4 	1.63	1.18	1.59	1.13	1.60	1.11
WHPs-Case 5 	1.68	1.12	1.41	1.05	1.38	0.98

evaluated together in factor $\theta_{1,1} = \frac{(\sigma_{H,max}^* Nu_H / C_{f,H})}{(\sigma_{S,max}^* Nu_S / C_{f,S})}$ resp. $\theta_{1,1} = \frac{(\sigma_{H,max}^* Sh_H / C_{f,H})}{(\sigma_{S,max}^* Sh_S / C_{f,S})}$ and compared with the maximum $\theta_{1,1}$ values achieved for helical pipes (OHPs), Figure 6.6 and Table 6.5. Two WHPs (Cases 2 and 5) reach higher values than the OHPs, especially at high Prandtl value.

Table 6.5: Performance factor $\theta_{1,1}$ ratio of the optimal helical case (OHPs) to the wavy helical pipes (WHPs) $(\theta_{1,1})_{OHPs} / (\theta_{1,1})_{WHPs}$

Cases	$Re=400$	$Re=400$	$Re=600$	$Re=600$	$Re=800$	$Re=800$
	$Pr/Sc=1$	$Pr/Sc=10$	$Pr/Sc=1$	$Pr/Sc=10$	$Pr/Sc=1$	$Pr/Sc=10$
$(\theta_{1,1})_{OHPs} / (\theta_{1,1})_{WHPs}$						
WHPs-Case 1 	1.48	1.00	1.58	1.03	1.58	1.04
WHPs-Case 2 	0.94	0.64	0.89	0.66	0.85	0.58
WHPs-Case 3 	3.19	1.74	3.24	1.83	2.57	1.82
WHPs-Case 4 	1.47	1.02	1.45	1.00	1.45	0.99
WHPs-Case 5 	1.14	0.72	0.95	0.68	0.95	0.66

This investigation demonstrated that wavy helical pipes have the potentiality to perform even better than helical pipes. In this section five particular wavy helical pipe geometries were studied among an infinity of possible configurations. In order to identify the most performant configurations, it would be necessary to derive correlations giving the Nusselt (Sherwood) number and the friction factor of wavy helical pipes, and to conduct an optimization study, just as was performed for simple helical pipes.

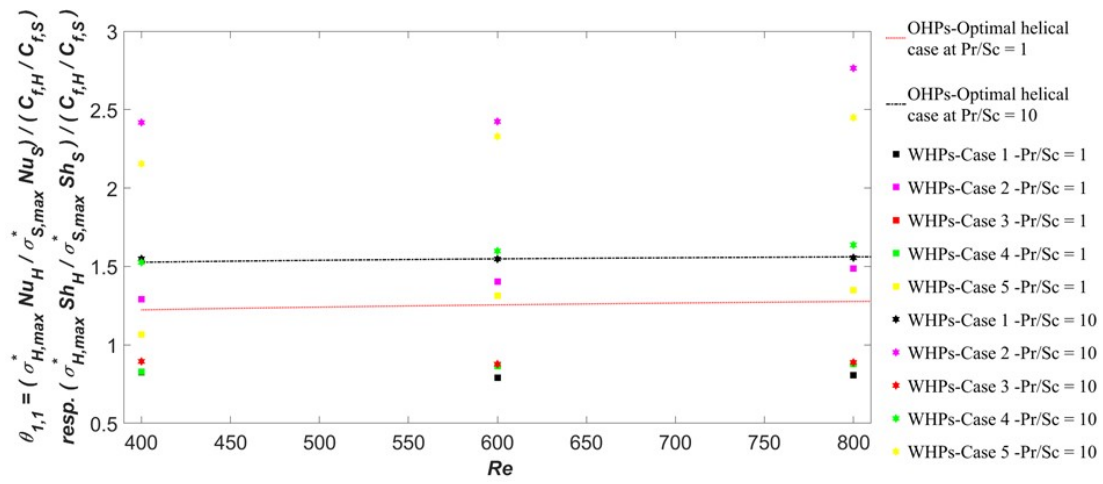


Figure 6.6: Performance factor $\theta_{1,1}$ vs. Reynolds number for the wavy helical pipes (WHPs) and optimal helical pipes (OHPs) at $Pr/Sc=10$ and $Pr/Sc=1$

6.1.2 Double helical pipes

The second complex geometry that was studied is the double helical pipe (DHPs). In this geometry, the pipe is helically wound around a helical line, which is described by the following parametric equation:

$$\begin{aligned} \frac{x}{d} &= [R_H^* + A \cos(Bt)]. \cos(t) \\ \frac{y}{d} &= [R_H^* + A \cos(Bt)]. \sin(t) \\ \frac{z}{d} &= A \sin(Bt) + \frac{p^*}{2\pi} t \end{aligned} \quad (6.2)$$

Seven different DHPs were considered, Figure 6.7.

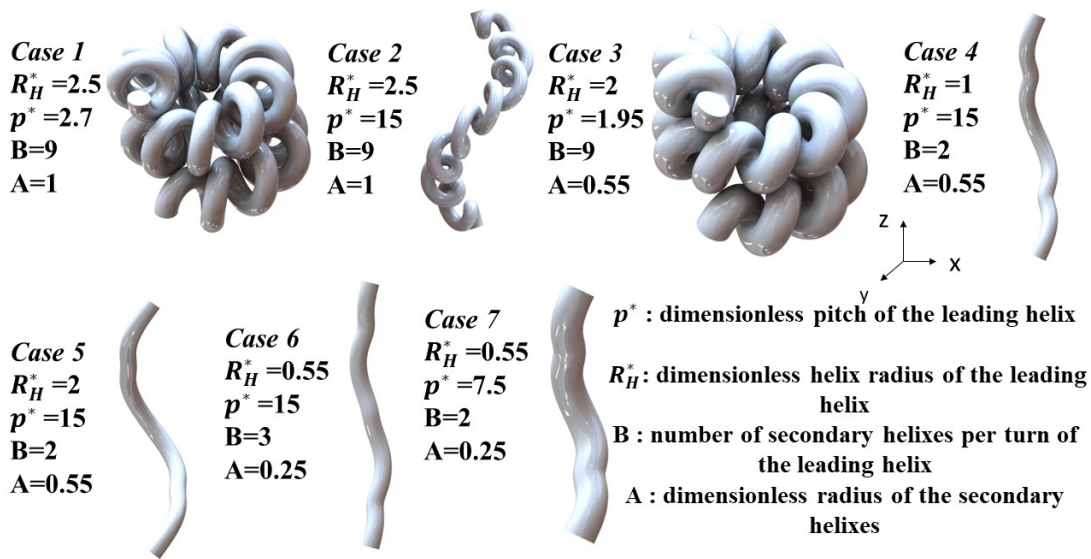









Figure 6.7: Double helical pipe designs considered in this section

Considering $\eta_{1,0} = Nu_H/Nu_S$ (resp. Nu_H/Nu_S) the heat (resp. mass) transfer enhancement, Figure 6.8 and Table 6.6, it appears that most DHPs perform better than OHPs for $Pr=10$, but that optimal helical pipes supplant almost all DHPs for $Pr=1$.

Table 6.6: The heat/mass transfer enhancement $\eta_{1,0}$ ratio of the optimal helical case (OHPs) to the double helical pipe (DHPs) $(\eta_{1,0})_{OHPs}/(\eta_{1,0})_{DHPs}$

Cases	$Re=400$	$Re=400$	$Re=600$	$Re=600$	$Re=800$	$Re=800$
	$Pr/Sc=1$	$Pr/Sc=10$	$Pr/Sc=1$	$Pr/Sc=10$	$Pr/Sc=1$	$Pr/Sc=10$
$(\eta_{1,0})_{OHPs}/(\eta_{1,0})_{DHPs}$						
DHPs-Case 1 	1.20	1.01	1.03	0.71	1.13	0.71
DHPs-Case 2 	1.23	0.93	1.23	0.75	1.35	0.82
DHPs-Case 3 	0.99	0.78	0.98	0.55	1.18	0.63
DHPs-Case 4 	1.22	0.75	1.25	0.73	1.14	0.69
DHPs-Case 5 	1.20	1.14	1.14	1.08	1.25	1.09
DHPs-Case 6 	1.70	1.55	1.54	1.25	1.82	1.33
DHPs-Case 7 	1.10	0.82	0.97	0.70	1.02	0.71

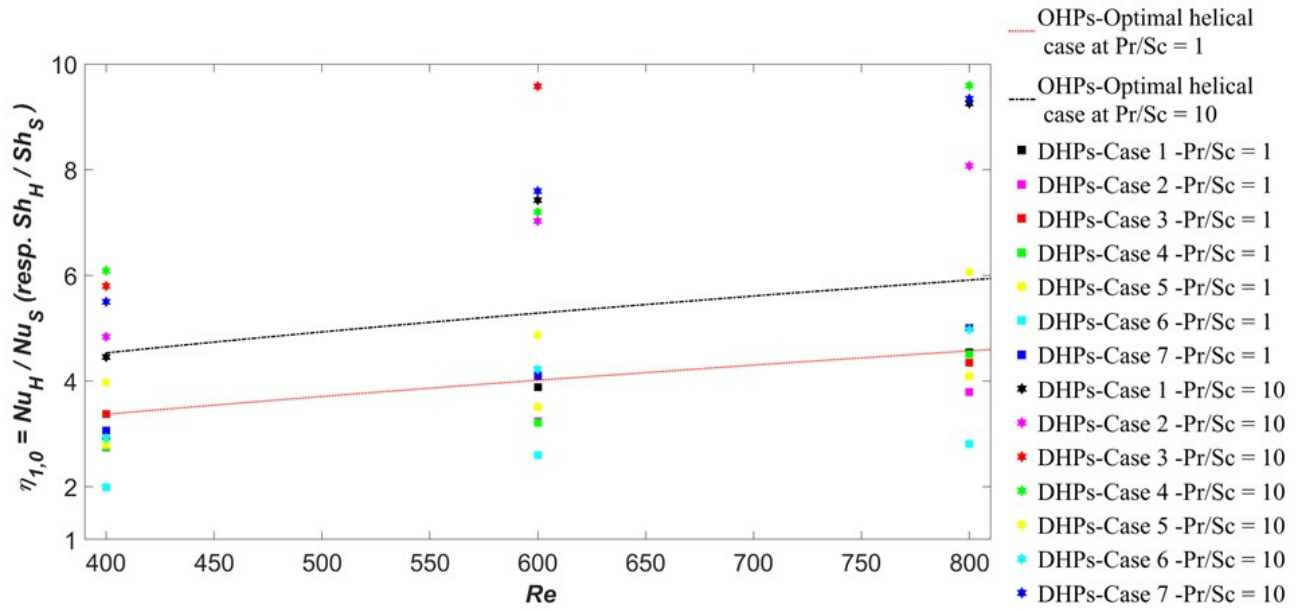


Figure 6.8: The heat/mass transfer enhancement $\eta_{1,0}$ vs. Reynolds number for the double helical pipes (DHPs) and optimal helical pipes (OHPs) at $Pr/Sc=10$ and $Pr/Sc=1$

Factor $\eta_{1,1} = (Nu_H/Nu_S)/(C_{f,H}/C_{f,S})$ resp. $\eta_{1,1} = (Sh_H/Sh_S)/(C_{f,H}/C_{f,S})$, is then examined both for DHPs and optimal helical pipes (helical configurations maximizing factor $\eta_{1,1}$), Figure 6.9 and Table 6.7. At low Prandtl, some DHPs perform better than OHPs (except for Case 4, 5 and 7). At higher Prandtl, however, all DHPs outreach the optimal helical pipes.

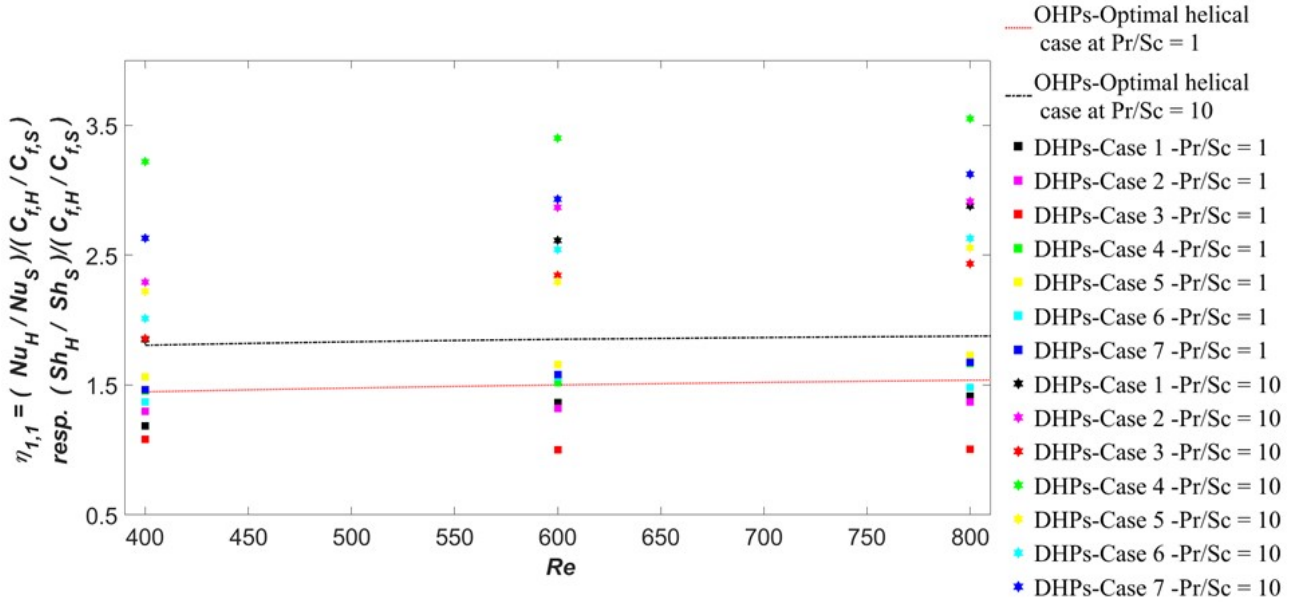









Figure 6.9: Performance factor $\eta_{1,1}$ vs. Reynolds number of the double helical pipes (DHPs) and optimal helical pipes (OHPs) at $Pr/Sc=10$ and $Pr/Sc=1$

Table 6.7: Performance factor $\eta_{1,1}$ ratio of the optimal helical case (OHPs) to the double helical pipe (DHPs) $(\eta_{1,1})_{OHPs}/(\eta_{1,1})_{DHPs}$

Cases	$Re=400$	$Re=400$	$Re=600$	$Re=600$	$Re=800$	$Re=800$
	$Pr/Sc=1$	$Pr/Sc=10$	$Pr/Sc=1$	$Pr/Sc=10$	$Pr/Sc=1$	$Pr/Sc=10$
$(\eta_{1,1})_{OHPs}/(\eta_{1,1})_{DHPs}$						
DHPs-Case 1 	1.22	0.98	1.10	0.71	1.09	0.65
DHPs-Case 2 	1.11	0.78	1.13	0.65	1.12	0.64
DHPs-Case 3 	1.34	0.97	1.50	0.79	1.53	0.77
DHPs-Case 4 	1.00	0.56	0.98	0.55	0.92	0.53
DHPs-Case 5 	0.93	0.81	0.90	0.80	0.89	0.73
DHPs-Case 6 	1.05	0.89	0.96	0.73	1.04	0.71
DHPs-Case 7 	1.00	0.68	0.95	0.63	0.92	0.60

In Figure 6.10 and Table 6.8, the results are presented in terms of the volumetric heat/mass flux $\theta_{1,0} = (\sigma_{H,max}^* Nu_H) / (\sigma_{S,max}^* Nu_S)$ resp. $\theta_{1,0} = (\sigma_{H,max}^* Sh_H) / (\sigma_{S,max}^* Sh_S)$. The optimal helical pipes (helical pipes maximizing factor $\theta_{1,0}$) yield the best performances for $Pr/Sc=1$, regardless of the Reynolds number value. For $Pr/Sc=10$, some DHPs (Cases 3, 4 and 7) are able to outperform the optimal helical pipes.

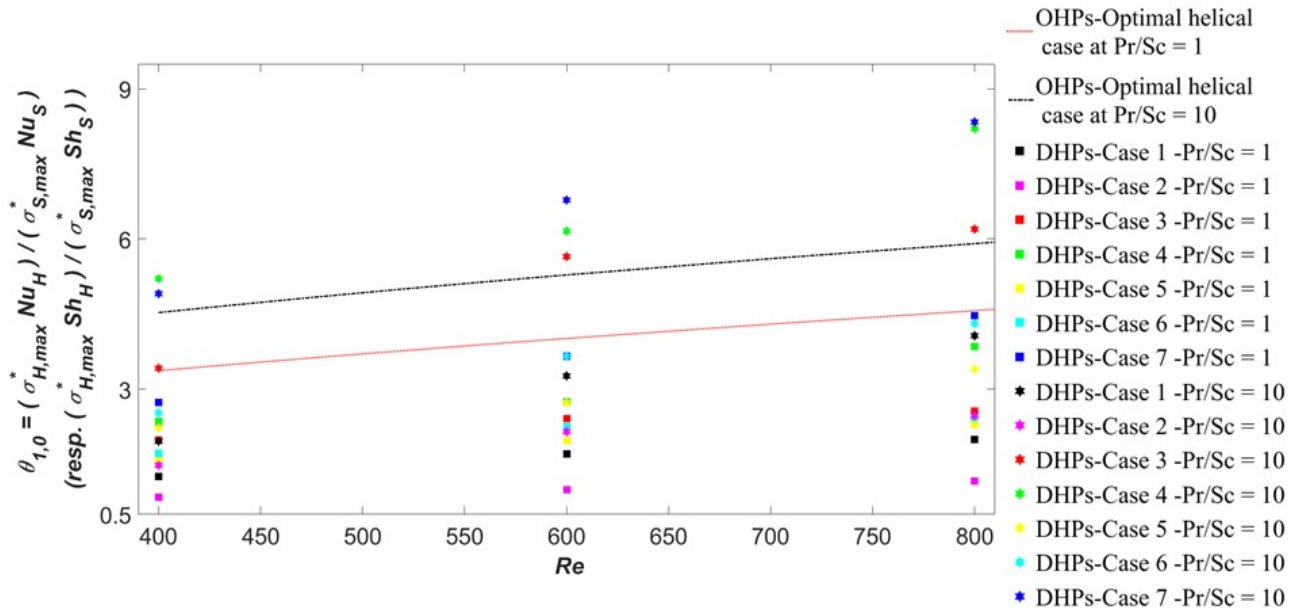









Figure 6.10: The volumetric heat/mass flux $\theta_{1,0}$ vs. Reynolds number for the double helical pipes (DHPs) and optimal helical pipes (OHPs) at $Pr/Sc=10$ and $Pr/Sc=1$

Table 6.8: The volumetric heat/mass flux $\theta_{1,0}$ ratio of the optimal helical case (OHPs) to the double helical pipes (DHPs) $(\theta_{1,0})_{OHPs}/(\theta_{1,0})_{DHPs}$

Cases	$Re=400$	$Re=400$	$Re=600$	$Re=600$	$Re=800$	$Re=800$
	$Pr/Sc=1$	$Pr/Sc=10$	$Pr/Sc=1$	$Pr/Sc=10$	$Pr/Sc=1$	$Pr/Sc=10$
$(\theta_{1,0})_{OHPs}/(\theta_{1,0})_{DHPs}$						
DHPs-Case 1 	2.68	2.31	2.35	1.61	2.28	1.45
DHPs-Case 2 	4.02	3.06	4.04	2.46	3.93	2.39
DHPs-Case 3 	1.69	1.32	1.66	0.93	1.78	0.95
DHPs-Case 4 	1.43	0.86	1.49	0.86	1.18	0.72
DHPs-Case 5 	2.14	2.03	2.03	1.94	1.98	1.74
DHPs-Case 6 	1.95	1.79	1.78	1.44	1.88	1.37
DHPs-Case 7 	1.23	0.93	1.09	0.78	1.02	0.70

Finally, the most comprehensive factor $\theta_{1,1}$, taking into account the transfer intensity through the Nusselt/Sherwood ratio, the power loss through the friction factor ratio, and the maximum possible compacity, is inspected in Figure 6.11 and Table 6.9. Three DHPs (Cases 4, 6 and 7) achieve better results than the optimal helical pipes (helical configurations maximizing factor $\theta_{1,1}$), all the more at higher Prandtl number.

As a conclusion, some double helical pipe geometries, namely Cases 4 and 7, allow to reach better performances than the optimal helical pipes, in particular for fluids when the Prandtl number value is increased. This proves the high potential of double helical shapes. An optimization study should be conducted in order to identify the double helical geometries that produce the highest enhancements.

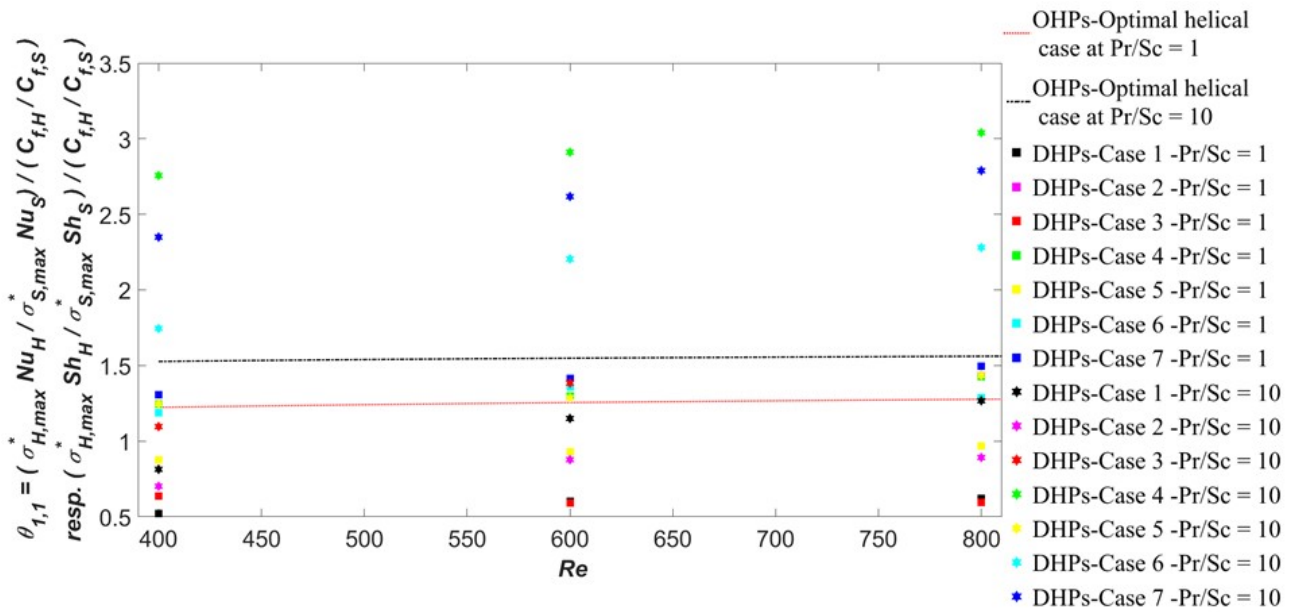









Figure 6.11: Performance factor $\theta_{1,1}$ vs. Reynolds number of the double helical pipes (DHPs) and optimal helical pipes (OHPs) at $Pr/Sc=10$ and $Pr/Sc=1$

Table 6.9: Performance factor $\theta_{1,1}$ ratio of the optimal helical case (OHPs) to the double helical pipes (DHPs) $(\theta_{1,1})_{OHPs}/(\theta_{1,1})_{DHPs}$

Cases	$Re=400$	$Re=400$	$Re=600$	$Re=600$	$Re=800$	$Re=800$
	$Pr/Sc=1$	$Pr/Sc=10$	$Pr/Sc=1$	$Pr/Sc=10$	$Pr/Sc=1$	$Pr/Sc=10$
$(\theta_{1,1})_{OHPs}/(\theta_{1,1})_{DHPs}$						
DHPs-Case 1 	2.34	1.91	2.08	1.39	2.05	1.28
DHPs-Case 2 	3.08	2.21	3.10	1.82	3.04	1.81
DHPs-Case 3 	1.91	1.42	2.12	1.16	2.15	1.12
DHPs-Case 4 	0.98	0.56	0.96	0.55	0.89	0.53
DHPs-Case 5 	1.39	1.25	1.35	1.24	1.31	1.13
DHPs-Case 6 	1.03	0.89	0.92	0.72	1.00	0.71
DHPs-Case 7 	0.94	0.66	0.88	0.61	0.85	0.58

6.2 Conclusion

Optimal performances of helical pipes can be summarized into Pareto fronts. The performances of all helices with R_H^* varying between 0 and 10 (with an increment of 0.05) and p^* varying from the forbidden region until 10 (with an increment of 0.05) were first calculated using the correlations presented in the previous chapters. For given Reynolds and Prandtl/Schmidt numbers, the Pareto front corresponds to the curve enveloping all of these points (Figure 6.12). It is composed of the points of highest $\theta_{1,0}$ value for a given $C_{f,H}/C_{f,S}$ value. All the points (i.e. the helical geometries) of the Pareto front are mathematically optimal: none of them surpasses any other in terms of both objectives.

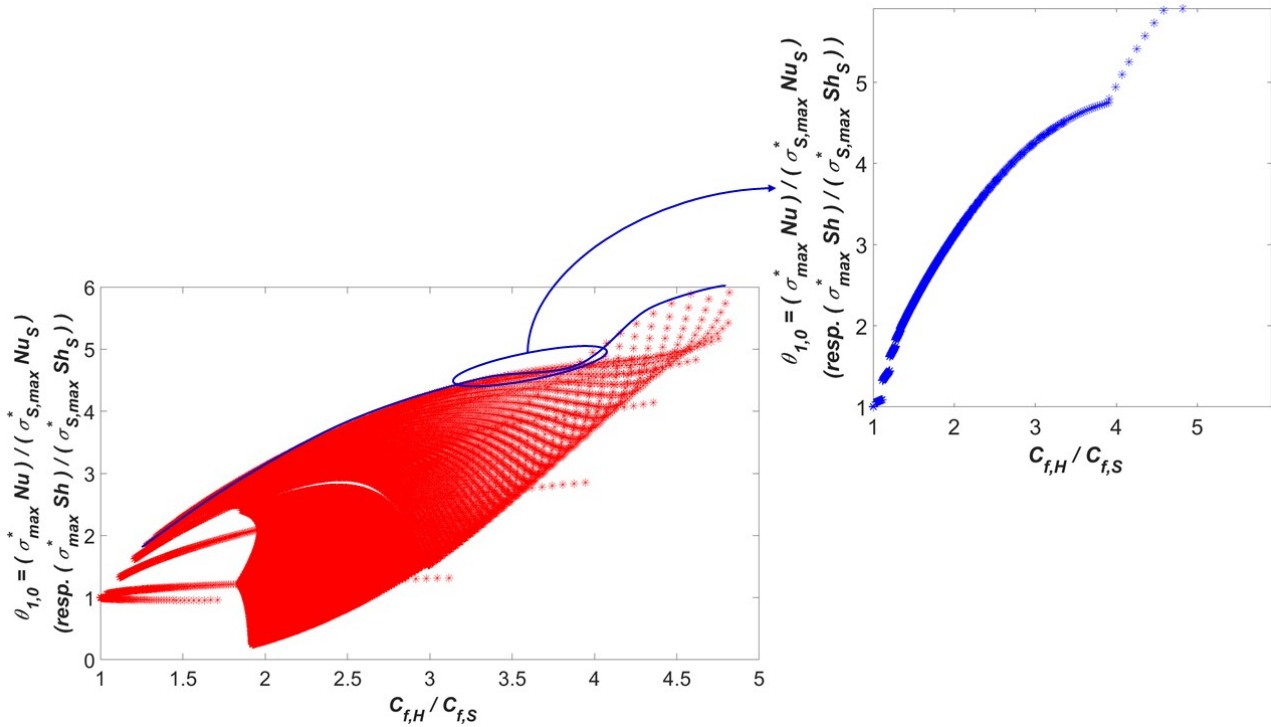


Figure 6.12: The Pareto frontier (blue curve on the left figure) for a multi-objective optimization problem with two objective functions: the enhancement factor and friction factor at $Re=800$ and $Pr/Sc=10$

Figure 6.13 displays the Pareto front for a Reynolds number of 800 and a Prandtl (Schmidt) number of 10. The Pareto front is a good way to compare the performances of wavy and double helical pipes to those that can be achieved by optimal helical pipes. As show in Figure 6.13, many of the novel designs investigated in this chapter surpass helical pipes in terms of Pareto optimality, i.e. for a given pumping power, they allow reaching higher transfer performances (and vice-versa). These results offer perspectives for further research on heat/mass transfer enhancement using coiled geometries.

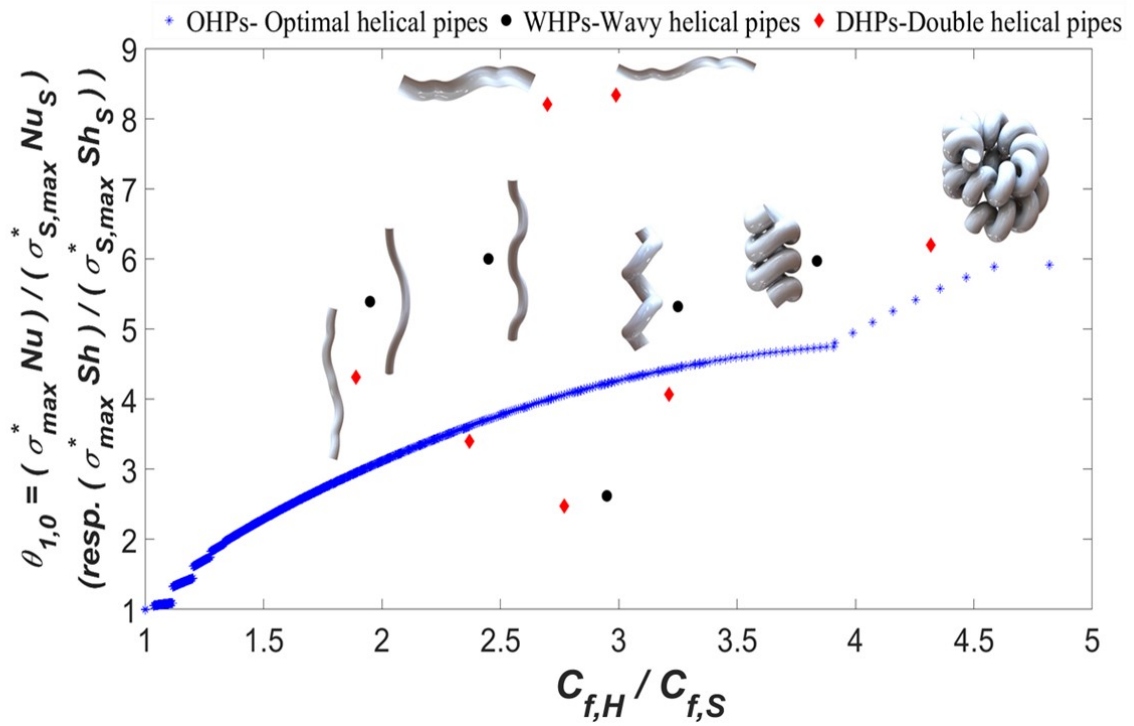


Figure 6.13: The Pareto frontier for a multi-objective optimization problem with two objective functions: the enhancement factor $\theta_{1,0}$ and friction factor of the optimal helical pipes, wavy helical pipes and double helical pipes at $Re = 800$ and $Pr/Sc = 10$

Future work and perspectives

Future work and perspectives

This PhD revealed tremendous potentialities to intensify heat/mass transfer with helical heat/mass exchangers. In particular, highly curved helical pipes (HCHPs) were shown to provide very high performances considering the following factors:

- The achieved mass /heat transfer efficiency (generally expressed by the Sherwood/Nusselt number).
- The involved pressure drops (generally characterized via a friction factor) since pumping constitutes a major operating cost (i.e. energy requirement).
- The packing density or compactness, which represents the highest specific surface area of membrane separators and heat exchangers, i.e. the exchange surface packed within a unit volume.

This thesis opens different perspectives to develop the heat/mass transfer performances of heat/mass exchangers. Particularly, the novelty of HCHPs should be exploited. The present work may be extended in five ways:

Firstly, chapter 6 investigated numerically the possibility of using complex coiled geometries (wavy- and double-helical pipes) in heat/mass exchangers applications where the Prandtl/Schmidt number is low. According to different performance criteria, some cases offered largely better performances than those that could be achieved by helical pipes. So it would be very interesting to study these geometries for different operating conditions and high Prandtl/Schmidt numbers.

Secondly, to the author's best knowledge, no previous study has focused yet on the mixing efficiency in HCHPs geometries. The results of this PhD open powerful opportunities to apply these geometries to micro-mixture application. As an example, Figure 2 shows a T-shaped mixer with a highly curved body, which could be investigated both numerically and experimentally. Indeed, with the development of additive manufacturing, the elaboration of highly curved helical geometries has become easily achievable.

Thirdly, experimental measurements of the heat/mass transfer efficiency in HCHPs should be undertaken for a trustworthy validation of the numerical results. Indeed, as explained in this PhD (Chapter 3 and Chapter 4), such data lacks in the literature since HCHPs were difficult to manufacture using traditional manufacturing techniques, which is now rendered possible thanks to 3D-printing (see appendix A.2). Polymeric models allow flow field measurements using magnetic resonance imaging, and if a transparent material is used, PIV (Particle Image Velocimetry) or μ PIV measurements can be performed. If the polymer is sufficiently permeable, gas-liquid mass transfer experiments can be conducted and the involved Sherwood numbers calculated. On the other hand, metal 3D-printed models allow heat transfer measurements and Nusselt numbers calculation. Unfortunately, the elab-



Figure 1: T-shaped micro-mixer with a HCHP design

oration of an experimental set-up integrating a HCHP heat exchanger was frustrated by the COVID 19 pandemic. It would be very interesting to develop such a set up in the future, in order to confirm the PhD numerical data.

Fourthly, although intense Dean vortices in HCHPs lead to improved heat and mass transfer efficiencies compared to straight tubes, they also induce higher frictional losses per pipe unit length. Although in Chapter 5 these conflicting criteria were merged into single objectives, the best way for assessing the potential of HCHPs remains multi-objective optimization and the computation of the Pareto front which displays the optimal trade-off between the benefits provided by HCHPs and the additional operating costs involved.

Different problems of industrial relevance can be handled via multi-objective optimization: exhaust gas treatment (No_x reduction) via monolith catalytic reactors, printed-circuit heat exchangers, etc. Given the involved fluids properties and flow rates, the correlations for calculating the Nusselt/Sherwood number and friction factor (Chapters 2 and 3) can be used as surrogates in the intended model-based optimization and allow determining the total heat/mass flux and required pumping power for a given reactor/exchanger configuration. Computation of the Pareto front allows displaying the achievable trade-off between pumping power and the reactor/exchanger volume (or mass), i.e. the minimal volume allowing to reach the targeted heat/mass flux for a given pumping cost.

Travaux futurs et perspectives

Cette thèse a révélé l'énorme potentiel des échangeurs hélicoïdaux pour intensifier le transfert de chaleur et de matière. En particulier, les tuyaux hélicoïdaux très incurvés (HCHP) ont montré d'excellentes performances en ce qui concerne:

- L'efficacité du transfert de matière/chaleur obtenue (généralement exprimée par le nombre de Sherwood/Nusselt).
- Les pertes de charge impliquées (généralement caractérisées par le coefficient de frottement) puisque l'énergie de pompage nécessaire pour les compenser constitue un coût de fonctionnement important.
- La densité ou la compacité, qui représente la plus grande surface spécifique d'échange par unité de volume que ces échangeurs/séparateurs permettent de développer.

Cette thèse ouvre différentes perspectives pour améliorer les performances de transfert des échangeurs de chaleur/masse. Il convient en particulier d'exploiter la nouveauté des HCHP. Le présent travail peut être étendu de cinq manières :

Premièrement, le chapitre 6 a adressé la possibilité d'utiliser des géométries hélicoïdales complexes (hélices ondulées et doubles hélices) dans les applications d'échangeurs de chaleur/masse où le nombre de Prandtl/Schmidt est faible. Selon différents critères de performance, ces géométries permettent d'aboutir à des performances largement supérieures à celles qui pourraient être obtenues avec des tuyaux hélicoïdaux simples. Il serait donc très intéressant d'étudier ces géométries pour des conditions d'exploitation différentes et un nombre de Prandtl/Schmidt élevé.



Figure 2: Micro-mélangeur en forme de T avec un design HCHP

Deuxièmement, à la connaissance de l’auteur, aucune étude antérieure ne s’est encore penchée sur l’efficacité du mélange dans les géométries de type HCHP. Les résultats de ce doctorat ouvrent la possibilité d’appliquer ces géométries au micro-mélange. À titre d’exemple, la figure 2 représente un mélangeur en T avec un corps hélicoïdal, qui pourrait être étudié à la fois numériquement et expérimentalement. En effet, avec le développement de la fabrication additive, l’élaboration de géométries hélicoïdales fortement incurvées devient réalisable.

Troisièmement, des mesures expérimentales de l’efficacité du transfert de chaleur/masse dans les HCHP devraient être entreprises pour valider les résultats numériques. En effet, comme expliqué dans cette thèse (chapitre 3 et chapitre 4), ces données manquent dans la littérature car les HCHP sont difficiles à fabriquer en utilisant des techniques de fabrication traditionnelles, ce qui est maintenant rendu possible grâce à l’impression 3D (voir annexe A.2). Des modèles en matériaux polymères permettraient de mesurer le champ d’écoulement à l’aide de l’imagerie par résonance magnétique, et si un matériau transparent était utilisé, des mesures de PIV (vélocimétrie par image de particules) ou de μ PIV pourraient être effectuées. Si le polymère est suffisamment perméable, des expériences de transfert de matière gaz-liquide pourraient être entreprises et les nombres de Sherwood correspondants calculés. D’autre part, des modèles imprimés en 3D en métal permettraient de quantifier le transfert de chaleur dans les HCHP et de calculer les nombres de Nusselt correspondants. Malheureusement, l’élaboration pendant cette thèse d’un dispositif expérimental intégrant un échangeur de chaleur hélicoïdal fortement incurvé a été contrariée par l’épidémie de COVID 19. Il serait très intéressant de développer un tel dispositif à l’avenir, afin de confirmer les données numériques obtenues dans cette thèse.

Quatrièmement, bien que les tourbillons de Dean intenses dans les HCHP entraînent une amélioration des rendements de transfert de chaleur et de masse par rapport aux tubes droits, ils induisent également des pertes par frottement plus élevées par unité de longueur de tube. Au Chapitre 5, ces critères conflictuels ont été réunis en un seul objectif. Mais la meilleure façon de l’évaluation du potentiel des HCHP reste l’optimisation multi-objectifs et le calcul du front de Pareto qui traduit le compromis optimal entre les avantages fournis par les HCHP et les coûts de fonctionnement supplémentaires qu’ils engendrent.

Différents problèmes d’importance industrielle peuvent être traités par optimisation multi-objectifs : traitement des effluents gazeux (réduction des NO_x) par des réacteurs catalytiques monolithiques, échangeurs de chaleur à circuit imprimé, etc. Les propriétés et les débits des fluides étant fixées, les corrélations pour le calcul du nombre de Nusselt/Sherwood et du coefficient de frottement (chapitres 2 et 3) pourront être utilisées comme modèles de substitut dans une optimisation mathématique

et permettront de déterminer le flux total de chaleur/masse et la puissance de pompage nécessaire pour une configuration donnée de réacteur/échangeur. Le calcul du front de Pareto permettra de déterminer le compromis réalisable entre la puissance de pompage et le volume (ou la masse) du réacteur/échangeur, c'est-à-dire le volume minimal permettant d'atteindre le flux de chaleur/matière visé pour un coût de pompage donné.

Appendix

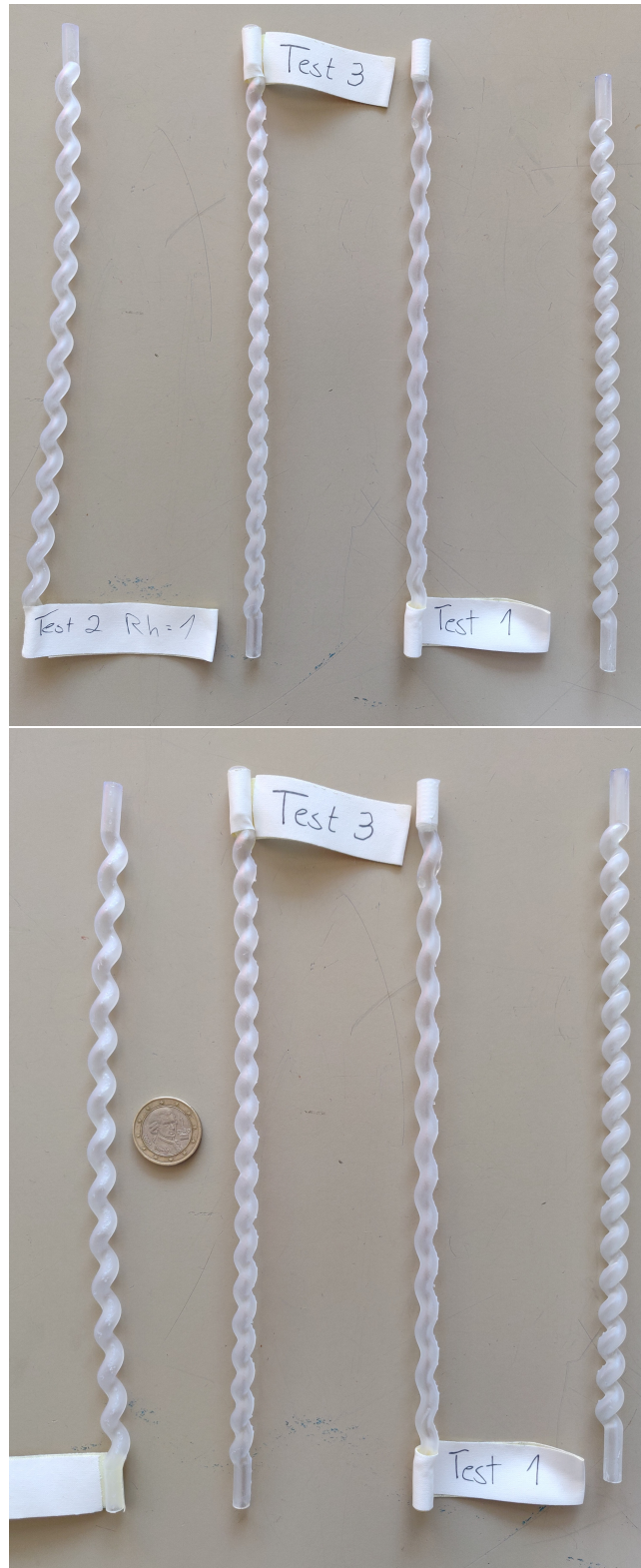
A.1 The CFD data of the friction factor $C_{f,H}^\infty$

R_H^*	p^*	Re	Friction factor $C_{f,H}^\infty$
0.704	4.8	5	13.7
0.704	4.8	10	6.89
0.704	4.8	15	4.63
0.704	4.8	17	4.1
0.704	4.8	20	3.51
0.704	4.8	30	2.344
0.704	4.8	35	2.057
0.704	4.8	40	1.85
0.704	4.8	45	1.68
0.704	4.8	50	1.55
0.25	25	10	6.5
1	25	10	6.42
2.5	25	10	6.42
5	25	10	6.5
2.5	1.25	10	6.52
5	1.25	10	6.43
10	1.25	10	6.57
10	25	10	6.56
0.05	1.25	10	7.3
0.05	3.75	10	6.98
0.05	25	10	6.452
0.55	25	10	6.403
0.25	7.5	10	6.43
0.55	7.5	10	6.463
0.55	3.75	10	6.9
5	3.75	10	6.5
0.55	1.25	10	9.9
5	15	10	6.43
0.65	1.25	10	8.57
2.5	1.25	100	0.825
2.5	3.75	100	0.85
0.55	1.25	100	1.5
0.55	3.75	100	1.07
0.25	3.75	100	0.89
5	1.25	100	0.739
10	1.25	100	0.684
10	25	100	0.7
5	25	100	0.7
2.5	25	100	0.69
1	25	100	0.658
0.25	25	100	0.641
0.25	7.5	100	0.69
0.05	1.25	100	0.714
0.05	25	100	0.6407
0.55	7.5	100	0.8
0.55	25	100	0.646
5	3.75	100	0.745
2.5	7.5	100	0.79
5	7.5	100	0.765

R_H^*	p^*	Re	Friction factor $C_{f,H}^\infty$
5	1.25	100	0.738
5	15	100	0.724
2.5	15	100	0.743
0.55	15	100	0.672
0.65	1.25	100	1.31
2.5	1.25	400	0.31
2.5	3.75	400	0.32
0.55	1.25	400	0.59
0.55	3.75	400	0.44
0.05	3.75	400	0.162
0.25	3.75	400	0.34
5	3.75	400	0.26
0.55	7.5	400	0.305
0.25	7.5	400	0.25
0.55	2.75	400	0.46
0.05	1.25	400	0.176
5	1.25	400	0.265
5	7.5	400	0.274
0.55	15	400	0.234
0.25	15	400	0.2
2.5	15	400	0.27
1	3.75	400	0.377
5	15	400	0.25
2.5	7.5	400	0.299
1	1.25	400	0.423
1	7.5	400	0.319
0.1	3.75	400	0.177
0.2	3.75	400	0.28
1.2	7.5	400	0.322
10	1.25	400	0.234
10	15	400	0.232
0.55	25	400	0.203
0.25	25	400	0.179
10	60	400	0.214
1	25	400	0.219
2.5	25	400	0.242
0.05	25	400	0.167
5	25	400	0.243
0.65	1.25	400	0.535
0.25	25	600	0.126
1	25	600	0.163
2.5	25	600	0.182
5	25	600	0.185
2.5	1.25	600	0.243
5	1.25	600	0.204
10	1.25	600	0.176
10	25	600	0.178
0.05	1.25	600	0.112
0.05	25	600	0.107
0.55	25	600	0.15
0.55	1.25	600	0.467
0.25	7.5	600	0.185
0.55	7.5	600	0.24
0.55	3.75	600	0.33

R_H^*	p^*	Re	Friction factor $C_{f,H}^\infty$
5	3.75	600	0.205
5	15	600	0.195
2.5	15	600	0.207
0.55	15	600	0.176
0.65	1.25	600	0.418
5	1.25	800	0.171
10	1.25	800	0.146
10	25	800	0.148
5	25	800	0.154
2.5	25	800	0.152
1	25	800	0.134
0.25	25	800	0.094
0.05	1.25	800	0.088
0.05	25	800	0.0854
0.55	25	800	0.12
2.5	1.25	800	0.203
1	1.25	800	0.266
0.25	7.5	800	0.155
0.55	7.5	800	0.202
5	3.75	800	0.172
5	15	800	0.162
2.5	15	800	0.174
0.55	15	800	0.146
0.55	1.25	800	0.394
2.5	3.75	800	0.25
0.55	3.75	800	0.278
0.65	1.25	800	0.353
0.65	1.25	2000	0.211
0.25	25	2000	0.052
1	25	2000	0.076
2.5	25	2000	0.086
5	25	2000	0.087
2.5	1.25	2000	0.118
5	1.25	2000	0.098
10	1.25	2000	0.083
10	25	2000	0.084
0.05	25	2000	0.0323
0.55	25	2000	0.067
5	3.75	2000	0.0987
0.55	3.75	2000	0.168
0.55	15	2000	0.084

A.2 The 3D-printed helical pipes



A.3 The experimental results of the friction factor $C_{f,H}^\infty$ and experimental model geometries

The experimental model geometries

Total height helix (m)	1.56E-01
Helix pitch, p (m)	5.80E-03
Helical radius, R_H (m)	8.00E-04
Pipe internal diameter, d (m)	1.25E-03
Length of a straight tube connection (m)	2.20E-02
Number of straight tubes	2.00E+00
Total length of the straight tubes (m)	4.40E-02
Total number of helix turns, n	2.69E+01
Curvilinear length of the helical tub, L (m)	2.06E-01

Solution den- sity (kg/m ³)	Solution viscosity (Pa.s)	Volumetric flow rate (m ³ /s)	Average velocity (m/s)	Re	Total pressure drop, average value of 3 exper- imental measur- ments (Pa)	Standard devi- ation of the total pressure drop mea- sure- ments (Pa)	Calculated pressure drop in the straight tubes (Pa)	Pressure drop across the heli- cal pipe (Pa)	Friction coef- ficient in the helical tube, $C_{f,H}^\infty$
1040	4.48E-02	4.23E-07	3.45E-01	1.00E+01	9.31E+04	8.08E+00	1.39E+04	7.92E+04	7.77E+00
1040	4.48E-02	6.34E-07	5.17E-01	1.50E+01	1.44E+05	1.36E+01	2.09E+04	1.23E+05	5.35E+00
1040	4.48E-02	7.19E-07	5.86E-01	1.70E+01	1.60E+05	9.29E+00	2.37E+04	1.37E+05	4.64E+00
1040	4.48E-02	8.46E-07	6.89E-01	2.00E+01	1.89E+05	1.15E+00	2.78E+04	1.61E+05	3.95E+00
1180	2.85E-02	7.11E-07	5.80E-01	3.00E+01	1.07E+05	5.13E+00	1.49E+04	9.21E+04	2.81E+00
1180	2.85E-02	8.30E-07	6.76E-01	3.50E+01	1.26E+05	1.06E+01	1.74E+04	1.08E+05	2.43E+00
1180	2.85E-02	9.48E-07	7.73E-01	4.00E+01	1.46E+05	3.61E+00	1.98E+04	1.26E+05	2.17E+00
1180	2.85E-02	1.07E-06	8.69E-01	4.50E+01	1.63E+05	1.39E+01	2.23E+04	1.41E+05	1.91E+00
1180	2.85E-02	1.19E-06	9.66E-01	5.00E+01	1.86E+05	1.53E+00	2.48E+04	1.61E+05	1.77E+00
1080	2.41E-02	1.20E-06	9.82E-01	5.50E+01	1.55E+05	1.26E+01	2.13E+04	1.33E+05	1.55E+00
1080	2.41E-02	1.31E-06	1.07E+00	6.00E+01	1.72E+05	7.00E+00	2.33E+04	1.48E+05	1.45E+00
1080	2.41E-02	1.42E-06	1.16E+00	6.50E+01	1.88E+05	5.03E+00	2.52E+04	1.63E+05	1.36E+00

A.4 The CFD data of the asymptotic Nusselt / Sherwood number (Nu/Sh)

R_H^*	p^*	Re	Pr/Sc	Asymptotic Nu/Sh
0.25	3.75	2000	1	12.2
0.25	7.5	2000	1	10.17
0.25	15	2000	1	8.3
0.55	1.25	2000	1	27.7
0.55	3.75	2000	1	24.73
0.55	7.5	2000	1	21.37
0.55	15	2000	1	15.3
1	1.25	2000	1	27.16
1	3.75	2000	1	26.04
2.5	1.25	2000	1	23.33
5	1.25	2000	1	20.4
5	3.75	2000	1	20.4
5	7.5	2000	1	20.6
5	15	2000	1	19.55
10	1.25	2000	1	17.7
10	15	2000	1	17.55
0.25	3.75	2000	5	15.47
0.25	7.5	2000	5	10.98
0.25	15	2000	5	8.86
0.55	1.25	2000	5	33.5
0.55	3.75	2000	5	28.4
0.55	7.5	2000	5	23.25
0.55	15	2000	5	16.94
1	3.75	2000	5	29.34
2.5	1.25	2000	5	25.46
5	1.25	2000	5	22.26
5	3.75	2000	5	22.16
5	7.5	2000	5	22.26
5	15	2000	5	21.12
10	1.25	2000	5	19.07
10	15	2000	5	18.9
0.25	3.75	2000	10	18.8
0.25	7.5	2000	10	11.59
0.25	15	2000	10	9.12
0.55	1.25	2000	10	34.4
0.55	3.75	2000	10	29.3
0.55	7.5	2000	10	24.29
0.55	15	2000	10	17.5
1	1.25	2000	10	31.8
1	3.75	2000	10	30.6
2.5	1.25	2000	10	26.6
5	1.25	2000	10	22.6
5	3.75	2000	10	22.6

R_H^*	p^*	Re	Pr/Sc	Asymptotic Nu/Sh
5	7.5	2000	10	22.65
5	15	2000	10	21.54
10	1.25	2000	10	19.36
10	15	2000	10	19.15
0.05	3.75	800	1	3.68
0.25	3.75	800	1	9.63
0.25	7.5	800	1	8.09
0.25	15	800	1	6.68
0.4	2.75	800	1	17.95
0.55	1.25	800	1	17.47
0.55	3.75	800	1	17.28
0.55	7.5	800	1	14.57
0.55	15	800	1	10.47
1	1.25	800	1	17.37
1	3.75	800	1	16.75
2.5	1.25	800	1	15.16
2.5	7.5	800	1	14.7
2.5	15	800	1	13.38
5	1.25	800	1	13.18
5	3.75	800	1	13.27
5	7.5	800	1	13.4
5	15	800	1	12.65
10	1.25	800	1	11.31
10	15	800	1	11.14
0.25	7.5	800	5	9.2
0.55	1.25	800	5	21.63
0.55	3.75	800	5	19.97
2.5	1.25	800	5	16.8
0.25	7.5	800	10	9.53
0.25	15	800	10	7.35
0.55	1.25	800	10	22.38
0.55	3.75	800	10	20.38
0.55	7.5	800	10	16.63
0.55	15	800	10	12.01
1	15	800	10	13.99
2.5	1.25	800	10	17.16
2.5	7.5	800	10	16.6
5	1.25	800	10	14.96
5	3.75	800	10	15.09
5	7.5	800	10	15.13
5	15	800	10	14.33
10	1.25	800	10	12.9
10	15	800	10	12.71
0.25	3.75	600	1	8.85
0.25	7.5	600	1	7.61
0.25	25	600	1	4.8
0.55	3.75	600	1	15.08
0.55	7.5	600	1	12.64
10	1.25	800	10	12.9
10	15	800	10	12.71
0.25	3.75	600	1	8.85
0.25	7.5	600	1	7.61
0.25	25	600	1	4.8

R_H^*	p^*	Re	Pr/Sc	Asymptotic Nu/Sh
0.55	3.75	600	1	15.08
0.55	7.5	600	1	12.64
0.55	15	600	1	9.01
0.65	1.25	600	1	15.53
2.5	1.25	600	1	13.27
5	1.25	600	1	11.45
5	3.75	600	1	11.55
5	15	600	1	10.96
10	1.25	600	1	9.8
0.05	1.25	600	5	4.22
0.25	3.75	600	5	10.73
0.25	7.5	600	5	9.2
0.25	25	600	5	5.13
0.55	3.75	600	5	17.91
0.55	7.5	600	5	14.83
0.55	15	600	5	10.28
0.65	1.25	600	5	19.89
2.5	1.25	600	5	15.05
5	1.25	600	5	13.047
5	3.75	600	5	13.06
5	15	600	5	12.46
10	1.25	600	5	11.22
0.25	3.75	600	10	11.31
0.25	7.5	600	10	10.79
0.25	25	600	10	5.33
0.55	3.75	600	10	18.97
0.55	7.5	600	10	16.43
0.55	15	600	10	11.11
0.65	1.25	600	10	21.9
2.5	1.25	600	10	15.68
5	1.25	600	10	13.56
5	3.75	600	10	13.56
5	15	600	10	12.97
10	1.25	600	10	11.66
0.05	4.5	400	1	3.68
0.25	7.5	400	1	6.78
0.25	15	400	1	5.2
0.4	2.75	400	1	12.79
0.55	1.25	400	1	12.62
0.55	2.75	400	1	12.61
0.55	3.75	400	1	12.37
0.55	7.5	400	1	10.27
0.55	15	400	1	6.58
1	1.25	400	1	12.53
1	3.75	400	1	11.25
1	7.5	400	1	10.89
1.2	7.5	400	1	10.97
2.5	1.25	400	1	10.85
2.5	3.75	400	1	10.86
2.5	7.5	400	1	10.34
2.5	15	400	1	9.34
5	1.25	400	1	9.37

R_H^*	p^*	Re	Pr/Sc	Asymptotic Nu/Sh
5	3.75	400	1	9.37
5	7.5	400	1	9.45
5	15	400	1	8.88
10	1.25	400	1	8.11
10	15	400	1	7.99
0.25	3.75	400	5	9.21
0.25	7.5	400	5	7.41
0.25	15	400	5	5.6
0.55	1.25	400	5	15.75
0.55	2.75	400	5	15.05
0.55	3.75	400	5	14.4
0.55	7.5	400	5	11.57
0.55	15	400	5	8.32
2.5	1.25	400	5	12.47
2.5	3.75	400	5	14.44
5	1.25	400	5	10.74
5	15	400	5	10.3
0.05	3.75	400	10	3.66
0.1	3.75	400	10	3.85
0.2	3.75	400	10	6.79
0.25	3.75	400	10	9.89
0.25	7.5	400	10	7.84
0.25	15	400	10	5.6
0.4	2.75	400	10	15.81
0.55	1.25	400	10	16.07
0.55	2.75	400	10	15.5
0.55	3.75	400	10	14.99
0.55	7.5	400	10	11.87
0.55	15	400	10	8.49
1	1.25	400	10	15.102
1	3.75	400	10	14.23
1	7.5	400	10	12.74
1	15	400	10	10.07
1.2	7.5	400	10	12.79
2.5	1.25	400	10	12.67
2.5	3.75	400	10	12.8
2.5	7.5	400	10	12.05
2.5	15	400	10	11.07
5	1.25	400	10	11.03
5	3.75	400	10	11.1
5	7.5	400	10	11.16
5	15	400	10	10.6
10	1.25	400	10	9.779
10	15	400	10	9.7
2.5	1.25	200	1	7.74
5	1.25	200	1	7.44
2.5	1.25	200	5	9.28
5	1.25	200	5	8.44
2.5	1.25	200	10	9.73
5	1.25	200	10	8.9
0.25	3.75	100	1	5.18
0.25	7.5	100	1	3.97
0.25	15	100	1	3.71

R_H^*	p^*	Re	Pr/Sc	Asymptotic Nu/Sh
0.55	1.25	100	1	6.55
0.55	3.75	100	1	6.5
0.55	7.5	100	1	4.72
0.55	15	100	1	3.97
2.5	1.25	100	1	5.71
2.5	3.75	100	1	5.88
2.5	7.5	100	1	5.65
5	1.25	100	1	5.21
5	15	100	1	4.5
10	1.25	100	1	4.45
10	15	100	1	4.4
0.25	3.75	100	5	5.8
0.25	7.5	100	5	4.04
0.25	15	100	5	3.749
0.55	1.25	100	5	8.43
0.55	3.75	100	5	8.33
0.55	7.5	100	5	6.27
0.55	15	100	5	4.15
2.5	1.25	100	5	7.55
2.5	3.75	100	5	7.63
2.5	7.5	100	5	7.32
5	1.25	100	5	7.09
5	15	100	5	6.06
10	1.25	100	5	6.51
10	15	100	5	6.4
0.25	3.75	100	10	6.03
0.25	7.5	100	10	4.06
0.25	15	100	10	3.751
0.55	1.25	100	10	8.85
0.55	3.75	100	10	8.62
0.55	7.5	100	10	6.69
0.55	15	100	10	4.21
2.5	1.25	100	10	8
2.5	3.75	100	10	8.08
2.5	7.5	100	10	7.75
5	1.25	100	10	7.61
5	3.75	100	10	7.63
5	15	100	10	6.14
10	1.25	100	10	7.084
10	15	100	10	6.97
0.25	3.75	50	1	4.09
0.25	7.5	50	1	3.71
0.55	1.25	50	1	5.46
0.55	3.75	50	1	4.79
0.55	7.5	50	1	3.95
0.55	15	50	1	3.67
2.5	1.25	50	1	4.29
5	1.25	50	1	3.94
5	15	50	1	3.83
10	1.25	50	1	3.67
0.25	3.75	50	5	4.2

R_H^*	p^*	Re	Pr/Sc	Asymptotic Nu/Sh
0.25	7.5	50	5	3.76
0.55	1.25	50	5	7.25
0.55	3.75	50	5	6.37
0.55	7.5	50	5	4.21
0.55	15	50	5	3.77
2.5	1.25	50	5	6.27
5	1.25	50	5	5.66
5	15	50	5	5.12
10	1.25	50	5	4.77
0.25	3.75	50	10	4.29
0.25	7.5	50	10	3.77
0.55	1.25	50	10	7.8
0.55	3.75	50	10	6.62
0.55	7.5	50	10	4.24
0.55	15	50	10	3.79
2.5	1.25	50	10	6.87
5	1.25	50	10	6.4
5	15	50	10	5.71
10	1.25	50	10	5.74
2.5	1.25	10	1	3.76
2.5	1.25	10	5	3.76
2.5	1.25	10	10	3.79
5	1.25	10	5	3.71
5	1.25	10	10	3.72
0.55	3.75	10	1	3.78
0.55	3.75	10	5	3.72
0.55	3.75	10	10	3.74
0.25	7.5	10	5	3.66
0.25	7.5	10	10	3.67
0.55	7.5	10	5	3.67
0.55	7.5	10	10	3.69
Additional	CFD	data		
2.5	60	600	10	8.72
2.5	60	600	5	8.2
2.5	60	600	1	7.1
2.5	60	400	10	7.85
2.5	60	400	5	7.3
2.5	60	400	1	6.1
4	25	400	10	10.3
4	25	400	5	9.85
4	25	400	1	8.47
20	1.25	400	10	9.05
20	1.25	400	5	8.56
20	1.25	400	1	7.06

A.5 The CAD data of the a_{min}^*

R_H^*	p^*	a_{min}^*
0.05	1	1.06
0.05	1.2	1.01
0.05	1.8	1.01
0.05	2.5	1.01
0.05	3.7	1
0.05	5	1
0.05	7.5	1
0.05	10	1
0.05	12.5	1
0.05	15	1
0.05	17.5	1
0.05	20	1
0.2	1.8	1.19
0.2	2.5	1.12
0.2	3.7	1.06
0.2	5	1.04
0.2	7.5	1.02
0.2	10	1.01
0.2	12.5	1.01
0.2	15	1.01
0.2	17.5	1.01
0.2	20	1.01
0.5	1.2	1.85
0.5	1.8	1.68
0.5	2.5	1.5
0.5	3.7	1.3
0.5	5	1.19
0.5	7.5	1.09
0.5	10	1.05
0.5	12.5	1.03
0.5	15	1.02
0.5	17.5	1.02
0.5	20	1.02
1	1.2	2.83
1	1.8	2.61
1	2.5	2.3
1	3.7	1.87
1	5	1.59
1	7.5	1.31
1	10	1.19
1	12.5	1.12
1	15	1.08
1	17.5	1.06
1	20	1.05

R_H^*	p^*	a_{min}^*
1.5	1.2	3.82
1.5	1.8	3.58
1.5	2.5	3.18
1.5	3.7	2.54
1.5	5	2.07
1.5	7.5	1.6
1.5	10	1.38
1.5	12.5	1.26
1.5	15	1.19
1.5	17.5	1.14
1.5	20	1.11
2	1.2	4.82
2	1.8	4.56
2	2.5	4.08
2	3.7	3.23
2	5	2.6
2	7.5	1.94
2	10	1.61
2	12.5	1.43
2	15	1.31
2	17.5	1.23
2	20	1.18
2.5	1.2	5.83
2.5	1.8	5.55
2.5	2.5	5.01
2.5	3.7	3.96
2.5	5	3.17
2.5	7.5	2.3
2.5	10	1.87
2.5	12.5	1.62
2.5	15	1.46
2.5	17.5	1.35
2.5	20	1.29
3	1.2	6.82
3	1.8	6.54
3	2.5	5.94
3	3.7	4.69
3	5	3.73
3	7.5	2.68
3	10	2.14
3	12.5	1.82
3	15	1.62
3	17.5	1.48
3	20	1.38
3.5	1.2	7.82
3.5	1.8	7.54
3.5	2.5	6.87
3.5	3.7	5.44
3.5	5	4.31
3.5	7.5	3.07
3.5	10	2.42
3.5	12.5	2.04

R_H^*	p^*	a_{min}^*
3.5	15	1.79
3.5	17.5	1.62
3.5	20	1.49
4	1.2	8.82
4	1.8	8.52
4	2.5	7.81
4	3.7	6.18
4	5	4.89
4	7.5	3.46
4	10	2.71
4	12.5	2.26
4	15	1.97
4	17.5	1.77
4	20	1.65
4.5	1.2	9.83
4.5	1.8	9.53
4.5	2.5	8.77
4.5	3.7	6.95
4.5	5	5.49
4.5	7.5	3.87
4.5	10	3.01
4.5	12.5	2.5
4.5	15	2.16
4.5	17.5	1.93
4.5	20	1.75
5	1.2	10.82
5	1.8	10.53
5	2.5	9.72
5	3.7	7.72
5	5	6.09
5	7.5	4.28
5	10	3.31
5	12.5	2.74
5	15	2.35
5	17.5	2.09
5	20	1.89
5.5	1.2	11.83
5.5	1.8	11.53
5.5	2.5	10.68
5.5	3.7	8.49
5.5	5	6.7
5.5	7.5	4.7
5.5	10	3.63
5.5	12.5	2.98
5.5	15	2.56
5.5	17.5	2.25
5.5	20	2.03
6	1.2	12.83
6	1.8	12.52
6	2.5	11.64
6	3.7	9.23
6	5	7.27
6	7.5	5.11

R_H^*	p^*	a_{min}^*
6	10	3.93
6	12.5	3.22
6	15	2.75
6	17.5	2.41
6	20	2.18
6.5	1.2	13.83
6.5	1.8	13.52
6.5	2.5	12.58
6.5	3.7	10
6.5	5	7.86
6.5	7.5	5.5
6.5	10	4.23
6.5	12.5	3.45
6.5	15	2.95
6.5	17.5	2.58
6.5	20	2.31
7	1.2	14.84
7	1.8	14.54
7	2.5	13.58
7	3.7	10.84
7	5	8.52
7	7.5	5.96
7	10	4.58
7	12.5	3.73
7	15	3.17
7	17.5	2.77
7	20	2.46
7.5	1.2	15.84
7.5	1.8	15.54
7.5	2.5	14.54
7.5	3.7	11.59
7.5	5	9.13
7.5	7.5	6.36
7.5	10	4.9
7.5	12.5	3.98
7.5	15	3.38
7.5	17.5	2.94
7.5	20	2.62
8	1.2	16.84
8	1.8	16.54
8	2.5	15.51
8	3.7	12.35
8	5	9.73
8	7.5	6.78
8	10	5.21
8	12.5	4.22
8	15	3.58
8	17.5	3.11
8	20	2.77
8.5	1.2	17.84
8.5	1.8	17.54
8.5	2.5	16.47
8.5	3.7	13.11

R_H^*	p^*	a_{min}^*
8.5	5	10.34
8.5	7.5	7.19
8.5	10	5.52
8.5	12.5	4.49
8.5	15	3.78
8.5	17.5	3.29
8.5	20	2.92
9	1.2	18.83
9	1.8	18.52
9	2.5	17.45
9	3.7	13.96
9	5	10.98
9	7.5	7.64
9	10	5.85
9	12.5	4.74
9	15	4.02
9	17.5	3.49
9	20	3.08
9.5	1.2	19.83
9.5	1.8	19.53
9.5	2.5	18.44
9.5	3.7	14.76
9.5	5	11.62
9.5	7.5	8.11
9.5	10	6.19
9.5	12.5	5
9.5	15	4.24
9.5	17.5	3.65
9.5	20	3.24
10	1.2	20.83
10	1.8	20.53
10	2.5	19.42
10	3.7	15.54
10	5	12.2
10	7.5	8.5
10	10	6.51
10	12.5	5.25
10	15	4.45
10	17.5	3.86
10	20	3.41
Additonal	CAD	data
15	1.25	30.85
15	50	2.45
15	100	1.65
20	3.75	31.9
100	1.25	201
100	150	10.7
500	1000	41.6
500	50000	3.75

Bibliography

- [1] G. Baluais, D. Leclerc, and G. Meriguet. *Dictionnaire de la filtration et des séparation solide-liquide*. IDEXPO, 1986. [9](#), [11](#)
- [2] M Catalina, J Cot, P Celma, A Manich, and A Marsal. Molecular weight separation of collagen-base biomaterials by ultrafiltration. [9](#)
- [3] NP Cheremisinoff. Liquid filtration. application of filtration to wastewater treatment. *Butterworth-Heinemann, USA Desai R, Sahu O (2014) Comparative study of polymer and regular coagulant for municipal waste water treatment. J Appl Chem*, 2(1):82–91, 1998. [9](#)
- [4] Jean-Christophe REMIGY and Sandrine DESCLAUX. Filtration membranaire (oi, nf, uf)-présentation des membranes et modules. *Techniques de l'ingénieur Procédés de traitement des eaux potables, industrielles et urbaines*, 2007. [10](#)
- [5] Jean-Pierre Brun. *Procédés de séparation par membranes: transport, techniques membranaires, applications*. Masson, 1989. [10](#), [11](#)
- [6] R. B. Bird, W. E. Stewart, and E. N. Lightfoot. *Transport phenomena. 2nd*. New York, 2002. [10](#)
- [7] Richard W Baker, EL Cussler, W Eykamp, WJ Koros, RL Riley, and RH Strathman. Membrane separation systems. 1991. [11](#)
- [8] Leonard D Tijing, Woo Yun Chul, Choi June-Seok, Lee Sangho, Kim Seung-Hyun, and Shon Ho Kyong. Fouling and its control in membrane distillation a review. *Journal of Membrane Science*, 475:215–244, 2015. [11](#)
- [9] [12](#)
- [10] Mohsen Sheikholeslami, Mofid Gorji-Bandpy, and Davood Domiri Ganji. Review of heat transfer enhancement methods: Focus on passive methods using swirl flow devices. *Renewable and Sustainable Energy Reviews*, 49:444–469, 2015. [13](#)
- [11] Piyush Kumar Verma. Various techniques for heat transfer enhancement in a heat exchanger using active and passive techniques: A. 2018. [13](#)

- [12] Muhammad Mahmood Aslam Bhutta, Nasir Hayat, Muhammad Hassan Bashir, Ahmer Rais Khan, Kanwar Naveed Ahmad, and Sarfaraz Khan. Cfd applications in various heat exchangers design: A review. *Applied Thermal Engineering*, 32:1–12, 2012. [13](#)
- [13] Ravindra M Ghogare, Vijay G Gore, and AS Shaikh. A review of passive technique used for heat transfer enhancement in heat exchanger. 2018. [13](#)
- [14] Mehdi Ghobadi and Yuri Stephan Muzychka. A review of heat transfer and pressure drop correlations for laminar flow in curved circular ducts. *Heat Transfer Engineering*, 37(10):815–839, 2016. [13](#), [83](#)
- [15] Ahmad S Alsaadi, Lijo Francis, Gary L Amy, and Noredine Ghaffour. Experimental and theoretical analyses of temperature polarization effect in vacuum membrane distillation. *Journal of Membrane Science*, 471:138–148, 2014. [14](#)
- [16] Mohammad Abdul Wahab, Teow YH, Ang WL, Chung YT, Oatley-Radcliffe DL, and Hilal N. Nanofiltration membranes review: Recent advances and future prospects. *Desalination*, 356:226–254, 2015. [14](#)
- [17] RJ Wakeman and CJ Williams. Additional techniques to improve microfiltration. *Separation and Purification Technology*, 26(1):3–18, 2002. [15](#), [19](#)
- [18] Georges Belfort. Fluid mechanics in membrane filtration: recent developments. *Journal of Membrane science*, 40(2):123–147, 1989. [15](#)
- [19] Darko M Krstić, Wilhelm Höflinger, András K Koris, and Gyula N Vatai. Energy-saving potential of cross-flow ultrafiltration with inserted static mixer: Application to an oil-in-water emulsion. *Separation and purification technology*, 57(1):134–139, 2007. [15](#), [16](#)
- [20] BJ Bellhouse, G Costigan, K Abhinava, and A Merry. The performance of helical screw-thread inserts in tubular membranes. *Separation and Purification Technology*, 22:89–113, 2001. [15](#)
- [21] Kausick Auddy, Sirshendu De, and Sunando DasGupta. Performance prediction of turbulent promoter enhanced nanofiltration of a dye solution. *Separation and purification technology*, 43(1):85–94, 2005. [15](#)
- [22] Philip G Drazin and William Hill Reid. *Hydrodynamic stability*. Cambridge university press, 2004. [16](#)
- [23] [16](#)
- [24] Julio M Ottino. *The kinematics of mixing: stretching, chaos, and transport*, volume 3. Cambridge university press, 1989. [16](#)

-
- [25] Abraham D Stroock, Stephan KW Dertinger, Armand Ajdari, Igor Mezić, Howard A Stone, and George M Whitesides. Chaotic mixer for microchannels. *Science*, 295(5555):647–651, 2002. [16](#)
- [26] DM Hobbs and FJ Muzzio. The kenics static mixer: a three-dimensional chaotic flow. *Chemical Engineering Journal*, 67(3):153–166, 1997. [16](#)
- [27] TY Chiu and AE James. Effects of axial baffles in non-circular multi-channel ceramic membranes using organic feed. *Separation and purification technology*, 51(3):233–239, 2006. [16](#)
- [28] Nidal Hilal, Oluwaseun O Ogunbiyi, and Nick J Miles. Experimental investigation on the separation of bentonite using ceramic membranes: Effect of turbulence promoters. *Separation Science and Technology*, 43(2):286–309, 2008. [16](#)
- [29] Y Gençal, EN Durmaz, and PZ Çulfaz-Emecen. Preparation of patterned microfiltration membranes and their performance in crossflow yeast filtration. *Journal of Membrane Science*, 476:224–233, 2015. [16](#)
- [30] T Sugimoto. Ultrafiltration performance of tubular membrane modules fitted with turbulent promoter: twisted tape and static mixer. *Kagaku Kogaku Ronbunshu*, 22:42–48, 1996. [16](#)
- [31] Svetlana Popović and Miodrag N Tekić. Twisted tapes as turbulence promoters in the microfiltration of milk. *Journal of membrane science*, 384(1-2):97–106, 2011. [16](#)
- [32] Vitor Geraldes, Viriato Semião, and Maria Norberta Pinho. Hydrodynamics and concentration polarization in nf/ro spiral-wound modules with ladder-type spacers. *Desalination*, 157(1-3):395–402, 2003. [16](#)
- [33] Zohreh Jalilvand, Farzin Zokae Ashtiani, Amir Fouladitajar, and Hamid Rezaei. Computational fluid dynamics modeling and experimental study of continuous and pulsatile flow in flat sheet microfiltration membranes. *Journal of Membrane Science*, 450:207–214, 2014. [16](#)
- [34] HG Gomaa. Flux characteristics at oscillating membrane equipped with turbulent promoters. *Chemical engineering journal*, 191:541–547, 2012. [16](#), [20](#), [21](#)
- [35] MMK Bhuiya, MSU Chowdhury, M Saha, and MT Islam. Heat transfer and friction factor characteristics in turbulent flow through a tube fitted with perforated twisted tape inserts. *International Communications in Heat and Mass Transfer*, 46:49–57, 2013. [17](#)
- [36] Sompol Skullong, Pongjet Promvong, Chinaruk Thianpong, and Nuthvipa Jayranaiwachira. Thermal behaviors in a round tube equipped with quadruple perforated-delta-winglet pairs. *Applied Thermal Engineering*, 115:229–243, 2017. [17](#)

- [37] Witoon Chingtuaythong, Pongjet Promvonge, Chinaruk Thianpong, and Monsak Pimsarn. Heat transfer characterization in a tubular heat exchanger with v-shaped rings. *Applied Thermal Engineering*, 110:1164–1171, 2017. [17](#)
- [38] Pongjet Promvonge, Sombat Tamna, Monsak Pimsarn, and Chinaruk Thianpong. Thermal characterization in a circular tube fitted with inclined horseshoe baffles. *Applied Thermal Engineering*, 75:1147–1155, 2015. [17](#)
- [39] MMK Bhuiya, Jamal Uddin Ahamed, MSU Chowdhury, MAR Sarkar, B Salam, Rahman Saidur, Haji Hassan Masjuki, and MA Kalam. Heat transfer enhancement and development of correlation for turbulent flow through a tube with triple helical tape inserts. *International Communications in Heat and Mass Transfer*, 39(1):94–101, 2012. [17](#)
- [40] Sibel Gunes, Veysel Ozceyhan, and Orhan Buyukalaca. Heat transfer enhancement in a tube with equilateral triangle cross sectioned coiled wire inserts. *Experimental Thermal and Fluid Science*, 34(6):684–691, 2010. [17](#)
- [41] Smith Eiamsa-ard, Vichan Kongkakitpaiboon, and Kwanchai Nanan. Thermohydraulics of turbulent flow through heat exchanger tubes fitted with circular-rings and twisted tapes. *Chinese Journal of Chemical Engineering*, 21(6):585–593, 2013. [17](#)
- [42] P Murugesan, K Mayilsamy, S Suresh, and PSS Srinivasan. Heat transfer and pressure drop characteristics in a circular tube fitted with and without v-cut twisted tape insert. *International Communications in Heat and Mass Transfer*, 38(3):329–334, 2011. [17](#)
- [43] Heinz B Winzeler and Georges Belfort. Enhanced performance for pressure-driven membrane processes: the argument for fluid instabilities. *Journal of Membrane Science*, 80(1):35–47, 1993. [17](#), [109](#), [136](#)
- [44] L Broussous, Philippe Schmitz, Henri Boisson, E Prouzet, and A Larbot. Hydrodynamic aspects of filtration antifouling by helically corrugated membranes. *Chemical engineering science*, 55(21):5049–5057, 2000. [17](#), [18](#)
- [45] Seung-Yeop Kwak and Dae Woo Ihm. Use of atomic force microscopy and solid-state nmr spectroscopy to characterize structure-property-performance correlation in high-flux reverse osmosis (ro) membranes. *Journal of membrane science*, 158(1-2):143–153, 1999. [18](#)
- [46] BN Prasad and JS Saini. Effect of artificial roughness on heat transfer and friction factor in a solar air heater. *Solar energy*, 41(6):555–560, 1988. [19](#)
- [47] Dhananjay Gupta, SC Solanki, and JS Saini. Heat and fluid flow in rectangular solar air heater ducts having transverse rib roughness on absorber plates. *Solar Energy*, 51(1):31–37, 1993. [19](#)

-
- [48] RP Saini and JS Saini. Heat transfer and friction factor correlations for artificially roughened ducts with expanded metal mesh as roughness element. *International Journal of Heat and Mass Transfer*, 40(4):973–986, 1997. 19
- [49] Abdul-Malik Ebrahim Momin, JS Saini, and SC Solanki. Heat transfer and friction in solar air heater duct with v-shaped rib roughness on absorber plate. *International journal of heat and mass transfer*, 45(16):3383–3396, 2002. 19
- [50] KB Muluwork, JS Saini, and SC Solanki. Studies on discrete rib roughened solar air heaters. In *Proceedings of National Solar Energy Convention, Roorkee*, pages 75–84, 1998. 19
- [51] JL Bhagoria, JS Saini, and SC Solanki. Heat transfer coefficient and friction factor correlations for rectangular solar air heater duct having transverse wedge shaped rib roughness on the absorber plate. *Renewable Energy*, 25(3):341–369, 2002. 19
- [52] Peter Walzel. Effects and new applications of pulsed flow. *Chemical Engineering & Technology*, 36(1):15–21, 2013. 19
- [53] RK Lalrinsanga, Nagesh B Bejgam, and Somenath Ganguly. Effect of pressure pulsing on concentration boundary layer over membrane—a numerical investigation. *Asia-Pacific Journal of Chemical Engineering*, 8(4):519–526, 2013. 20
- [54] Ali Emad, A Ajbar, and I Almutaz. Periodic control of a reverse osmosis desalination process. *Journal of Process Control*, 22(1):218–227, 2012. 20
- [55] G Arroyo and C Fonade. Use of intermittent jets to enhance flux in crossflow filtration. *Journal of membrane science*, 80(1):117–129, 1993. 20
- [56] C Maranges and C Fonade. Flux enhancement in crossflow filtration using an unsteady jet. *Journal of membrane science*, 123(1):1–8, 1997. 20
- [57] JN Kuruzovich and PR Piergiovanni. Yeast cell microfiltration: optimization of backwashing for delicate membranes. *Journal of membrane science*, 112(2):241–247, 1996. 20
- [58] SC Hargrove, H Parthasarathy, and Shamsuddin Ilias. Flux enhancement in cross-flow membrane filtration by flow reversal: a case study on ultrafiltration of bsa. *Separation science and technology*, 38(12-13):3133–3144, 2003. 20
- [59] AP Reverberi, VP Meshalkin, C Cerrato, and Yu O Savina. Dynamics of a reverse osmosis unit with application to pulsating regimes for process optimization. *Theoretical Foundations of Chemical Engineering*, 45(2):190, 2011. 20

- [60] Frank Vinther and Ann-Sofi Jönsson. Modelling of optimal back-shock frequency in hollow fibre ultrafiltration membranes i: Computational fluid dynamics. *Journal of Membrane Science*, 506:130–136, 2016. [20](#)
- [61] Piotr Czekaj, Wendy Mores, Robert H Davis, and Carme Güell. Infrasonic pulsing for foulant removal in crossflow microfiltration. *Journal of Membrane Science*, 180(1):157–169, 2000. [20](#)
- [62] Rishi Sondhi and Ramesh Bhave. Role of backpulsing in fouling minimization in crossflow filtration with ceramic membranes. *Journal of Membrane Science*, 186(1):41–52, 2001. [20](#), [21](#)
- [63] Sumihar HD Silalahi and TorOve Leiknes. High frequency back-pulsing for fouling development control in ceramic microfiltration for treatment of produced water. *Desalination and Water Treatment*, 28(1-3):137–152, 2011. [20](#)
- [64] Bolaji Olayiwola and Peter Walzel. Effects of in-phase oscillation of retentate and filtrate in crossflow filtration at low reynolds number. *Journal of Membrane Science*, 345(1-2):36–46, 2009. [20](#)
- [65] TJ Kennedy, RL Merson, and BJ McCoy. Improving permeation flux by pulsed reverse osmosis. *Chemical Engineering Science*, 29(9):1927–1931, 1974. [21](#)
- [66] P Blanpain-Avet, N Doubrovine, C Lafforgue, and M Lalande. The effect of oscillatory flow on crossflow microfiltration of beer in a tubular mineral membrane system—membrane fouling resistance decrease and energetic considerations. *Journal of Membrane Science*, 152(2):151–174, 1999. [21](#)
- [67] RBEN AMAR, BB Gupta, and MY Jaffrin. Apple juice clarification using mineral membranes: fouling control by backwashing and pulsating flow. *Journal of food science*, 55(6):1620–1625, 1990. [21](#)
- [68] Huimin Ma, Christopher N Bowman, and Robert H Davis. Membrane fouling reduction by backpulsing and surface modification. *Journal of Membrane Science*, 173(2):191–200, 2000. [21](#)
- [69] Tatsuo Nishimura and Shigeki Matsune. Vortices and wall shear stresses in asymmetric and symmetric channels with sinusoidal wavy walls for pulsatile flow at low reynolds numbers. *International Journal of Heat and Fluid Flow*, 19(6):583–593, 1998. [22](#)
- [70] DX Jin, YP Lee, and D-Y Lee. Effects of the pulsating flow agitation on the heat transfer in a triangular grooved channel. *International journal of heat and mass transfer*, 50(15-16):3062–3071, 2007. [22](#)

-
- [71] Mohammad Jafari, Mousa Farhadi, and Kurosh Sedighi. Pulsating flow effects on convection heat transfer in a corrugated channel: A lbm approach. *International Communications in Heat and Mass Transfer*, 45:146–154, 2013. [22](#)
- [72] Unal Akdag, Selma Akcay, and Dogan Demiral. Heat transfer enhancement with laminar pulsating nanofluid flow in a wavy channel. *International Communications in Heat and Mass Transfer*, 59:17–23, 2014. [22](#)
- [73] Channarong Wantha. Effect and heat transfer correlations of finned tube heat exchanger under unsteady pulsating flows. *International Journal of Heat and Mass Transfer*, 99:141–148, 2016. [22](#)
- [74] Tapas K Nandi and Himadri Chattopadhyay. Numerical investigations of simultaneously developing flow in wavy microchannels under pulsating inlet flow condition. *International communications in heat and mass transfer*, 47:27–31, 2013. [22](#)
- [75] Fatih Selimefendigil and Hakan F Öztop. Pulsating nanofluids jet impingement cooling of a heated horizontal surface. *International Journal of Heat and Mass Transfer*, 69:54–65, 2014. [22](#)
- [76] Michel Y Jaffrin. Dynamic shear-enhanced membrane filtration: a review of rotating disks, rotating membranes and vibrating systems. *Journal of Membrane Science*, 324(1-2):7–25, 2008. [22](#), [23](#), [26](#), [27](#)
- [77] G Genkin, TD Waite, AG Fane, and S Chang. The effect of vibration and coagulant addition on the filtration performance of submerged hollow fibre membranes. *Journal of membrane science*, 281(1-2):726–734, 2006. [23](#)
- [78] O Al Akoum, Michel Y Jaffrin, Luhui Ding, Patrick Paullier, and Clotilde Vanhoutte. An hydrodynamic investigation of microfiltration and ultrafiltration in a vibrating membrane module. *Journal of Membrane Science*, 197(1-2):37–52, 2002. [23](#)
- [79] Søren Prip Beier, Maria Guerra, Arvid Garde, and Gunnar Jonsson. Dynamic microfiltration with a vibrating hollow fiber membrane module: filtration of yeast suspensions. *Journal of membrane science*, 281(1-2):281–287, 2006. [23](#)
- [80] Hoang Van Phan, M Bulut Coşkun, Muhsincan Şeşen, Gregory Pandraud, Adrian Neild, and Tuncay Alan. Vibrating membrane with discontinuities for rapid and efficient microfluidic mixing. *Lab on a Chip*, 15(21):4206–4216, 2015. [23](#)
- [81] Po-Hsun Huang, Yuliang Xie, Daniel Ahmed, Joseph Rufo, Nitesh Nama, Yuchao Chen, Chung Yu Chan, and Tony Jun Huang. An acoustofluidic micromixer based on oscillating sidewall sharp-edges. *Lab on a Chip*, 13(19):3847–3852, 2013. [23](#)

- [82] Anusha Kola, Yun Ye, Amy Ho, Pierre Le-Clech, and Vicki Chen. Application of low frequency transverse vibration on fouling limitation in submerged hollow fibre membranes. *Journal of membrane science*, 409:54–65, 2012. [23](#)
- [83] O Akoum, D Richfield, MY Jaffrin, LH Ding, and P Swart. Recovery of trypsin inhibitor and soy milk protein concentration by dynamic filtration. *Journal of membrane science*, 279(1-2):291–300, 2006. [23](#)
- [84] Farhad Zamani, Adrian WK Law, and AG Fane. Hydrodynamic analysis of vibrating hollow fibre membranes. *Journal of membrane science*, 429:304–312, 2013. [23](#)
- [85] C Stewart Slater, Mariano J Savelski, Pavlo Kostetsky, and Max Johnson. Shear-enhanced microfiltration of microalgae in a vibrating membrane module. *Clean Technologies and Environmental Policy*, 17(7):1743–1755, 2015. [23](#)
- [86] HG Gomaa, S Rao, and M Al Taweel. Flux enhancement using oscillatory motion and turbulence promoters. *Journal of Membrane science*, 381(1-2):64–73, 2011. [23](#)
- [87] William B Krantz, Robert R Bilodeau, Marc E Voorhees, and Roger J Elgas. Use of axial membrane vibrations to enhance mass transfer in a hollow tube oxygenator. *Journal of membrane science*, 124(2):283–299, 1997. [23](#)
- [88] Raed A Al-Juboori and Talal Yusaf. Biofouling in ro system: mechanisms, monitoring and controlling. *Desalination*, 302:1–23, 2012. [23](#), [24](#)
- [89] N Hengl, Yun Jin, F Pignon, S Baup, R Mollard, N Gondrexon, A Magnin, L Michot, and E Paineau. A new way to apply ultrasound in cross-flow ultrafiltration: Application to colloidal suspensions. *Ultrasonics sonochemistry*, 21(3):1018–1025, 2014. [23](#)
- [90] Dan Liu, Eugène Vorobiev, Raphaëlle Savoie, and Jean-Louis Lanoisellé. Comparative study of ultrasound-assisted and conventional stirred dead-end microfiltration of grape pomace extracts. *Ultrasonics sonochemistry*, 20(2):708–714, 2013. [23](#)
- [91] Shobha Muthukumaran, Sandra E Kentish, Geoff W Stevens, and Muthupandian Ashokkumar. Application of ultrasound in membrane separation processes: a review. *Reviews in chemical engineering*, 22(3):155–194, 2006. [24](#)
- [92] AL Ahmad, NF Che Lah, S Ismail, and BS Ooi. Membrane antifouling methods and alternatives: ultrasound approach. *Separation & Purification Reviews*, 41(4):318–346, 2012. [24](#)
- [93] HM Kyllönen, P Pirkonen, and M Nyström. Membrane filtration enhanced by ultrasound: a review. *Desalination*, 181(1-3):319–335, 2005. [24](#), [25](#)

-
- [94] Mikko O Lamminen, Harold W Walker, and Linda K Weavers. Mechanisms and factors influencing the ultrasonic cleaning of particle-fouled ceramic membranes. *Journal of membrane science*, 237(1-2):213–223, 2004. [24](#)
- [95] Hathaichanok Duriyabunleng, Jittiwut Petmune, and Chirakarn Muangnapoh. Effects of the ultrasonic waves on microfiltration in plate and frame module. *Journal of chemical engineering of Japan*, 34(8):985–989, 2001. [24](#)
- [96] T Kobayashi, X Chai, and N Fujii. Ultrasound enhanced cross-flow membrane filtration. *Separation and Purification Technology*, 17(1):31–40, 1999. [24](#)
- [97] Takaomi Kobayashi, Tsuyoshi Kobayashi, and Nobuyuki Fujii. Effect of ultrasound on enhanced permeability during membrane water treatment. *Japanese Journal of Applied Physics*, 39(5S):2980, 2000. [24](#)
- [98] A Simon, N Gondrexon, S Taha, J Cabon, and G Dorange. Low-frequency ultrasound to improve dead-end ultrafiltration performance. *Separation Science and Technology*, 35(16):2619–2637, 2000. [24](#)
- [99] Chao Zhu and Guangliang Liu. Modeling of ultrasonic enhancement on membrane distillation. *Journal of Membrane Science*, 176(1):31–41, 2000. [24](#)
- [100] Xijun Chai, Takaomi Kobayashi, and Nobuyuki Fujii. Ultrasound effect on cross-flow filtration of polyacrylonitrile ultrafiltration membranes. *Journal of membrane science*, 148(1):129–135, 1998. [25](#)
- [101] Shobha Muthukumar, Sandra E Kentish, Muthupandian Ashokkumar, and Geoffrey W Stevens. Mechanisms for the ultrasonic enhancement of dairy whey ultrafiltration. *Journal of membrane science*, 258(1-2):106–114, 2005. [25](#)
- [102] Kenji Takahashi and Kazuo Endoh. A new correlation method for the effect of vibration on forced-convection heat transfer. *Journal of chemical engineering of Japan*, 23(1):45–50, 1990. [25](#)
- [103] L Léal, M Miscevic, P Lavieille, M Amokrane, F Pigache, Frédéric Topin, B Nogarède, and L Tadrist. An overview of heat transfer enhancement methods and new perspectives: Focus on active methods using electroactive materials. *International Journal of Heat and Mass Transfer*, 61:505–524, 2013. [25](#)
- [104] TT Chandratilleke, Deepak Jagannatha, and Ramesh Narayanaswamy. Heat transfer enhancement in microchannels with cross-flow synthetic jets. *International journal of thermal sciences*, 49(3):504–513, 2010. [25](#)

- [105] Mangesh Chaudhari, Bhalchandra Puranik, and Amit Agrawal. Heat transfer characteristics of synthetic jet impingement cooling. *International Journal of Heat and Mass Transfer*, 53(5-6):1057–1069, 2010. [25](#)
- [106] KW Li and JD Parker. Acoustical effects on free convective heat transfer from a horizontal wire. 1967. [25](#)
- [107] Jun Cai, Xiulan Huai, Runsheng Yan, and Yanjun Cheng. Numerical simulation on enhancement of natural convection heat transfer by acoustic cavitation in a square enclosure. *Applied Thermal Engineering*, 29(10):1973–1982, 2009. [25](#)
- [108] GI Taylor. Stability of a viscous liquid contained between two rotating cylinders phil. trans. r. soc. lond. a january. 1923. [26](#)
- [109] C David Andereck, SS Liu, and Harry L Swinney. Flow regimes in a circular couette system with independently rotating cylinders. *Journal of Fluid Mechanics*, 164:155–183, 1986. [26](#)
- [110] Fernando Vigo, Claudio Uliana, and Paolo Lupino. The performance of a rotating module in oily emulsions ultrafiltration. *Separation Science and Technology*, 20(2-3):213–230, 1985. [26](#)
- [111] Georges Belfort, Joseph M Pimbley, Anthony Greiner, and Kun Yong Chung. Diagnosis of membrane fouling using a rotating annular filter. 1. cell culture media. *Journal of Membrane Science*, 77(1):1–22, 1993. [27](#)
- [112] Jin Yong Park, Chang Kyun Choi, and Jae Jin Kim. A study on dynamic separation of silica slurry using a rotating membrane filter 1. experiments and filtrate fluxes. *Journal of membrane science*, 97:263–273, 1994. [27](#)
- [113] Ulrich B Holeschovsky and Charles L Cooney. Quantitative description of ultrafiltration in a rotating filtration device. *AIChE Journal*, 37(8):1219–1226, 1991. [27](#)
- [114] Sangho Lee and Richard M Lueptow. Rotating reverse osmosis for water recovery in space: influence of operational parameters on ro performance. *Desalination*, 169(2):109–120, 2004. [27](#)
- [115] Richard M Lueptow and Azardokht Hajiloo. Flow in a rotating membrane plasma separator. *ASAIO journal (American Society for Artificial Internal Organs: 1992)*, 41(2):182–188, 1995. [27](#)
- [116] Samuel Robert Maurice Gardiner and RH Sabersky. Heat transfer in an annular gap. *International Journal of Heat and Mass Transfer*, 21(12):1459–1466, 1978. [27](#)
- [117] M Fénot, E Dorignac, A Giret, and G Lalizel. Convective heat transfer in the entry region of an annular channel with slotted rotating inner cylinder. *Applied Thermal Engineering*, 54(1):345–358, 2013. [27](#)

-
- [118] Saeedreza Zeibi Shirejini, S Rashidi, and JA Esfahani. Recovery of drop in heat transfer rate for a rotating system by nanofluids. *Journal of Molecular Liquids*, 220:961–969, 2016. [27](#)
- [119] Weerapun Duangthongsuk and Somchai Wongwises. An experimental investigation of the heat transfer and pressure drop characteristics of a circular tube fitted with rotating turbine-type swirl generators. *Experimental thermal and fluid science*, 45:8–15, 2013. [27](#)
- [120] Etienne Braak, Marion Alliet, Sylvie Schetrite, and Claire Albasi. Aeration and hydrodynamics in submerged membrane bioreactors. *Journal of membrane science*, 379(1-2):1–18, 2011. [27](#)
- [121] Y Sun, X Huang, F Chen, and X Wen. A dual functional filtration/aeration membrane bioreactor for domestic wastewater treatment. In *Proceedings of the Water Environment-Membrane Technology Conference, Seoul, Korea*, pages 7–10, 2004. [27](#)
- [122] Pierre Le Clech, Vicki Chen, and Tony AG Fane. Fouling in membrane bioreactors used in wastewater treatment. *Journal of membrane science*, 284(1–):17–53, 2006. [27](#)
- [123] T Imasaka et al. Apparatus for membrane separation of wastewater from food industries. *Japanese Patent JP63104610*, 1988. [27](#)
- [124] Takuo Imasaka, Hiroyuki So, Kohnosuke Matsushita, Tomoya Furukawa, and Nobuhiko Kanekuni. Application of gas-liquid two-phase cross-flow filtration to pilot-scale methane fermentation. *Drying Technology*, 11(4):769–785, 1993. [27](#)
- [125] ZF Cui and KIT Wright. Flux enhancements with gas sparging in downwards crossflow ultrafiltration: performance and mechanism. *Journal of Membrane Science*, 117(1-2):109–116, 1996. [28](#)
- [126] M Mercier-Bonin, C Lagane, and C Fonade. Influence of a gas/liquid two-phase flow on the ultrafiltration and microfiltration performances: case of a ceramic flat sheet membrane. *Journal of Membrane Science*, 180(1):93–102, 2000. [28](#)
- [127] C Cabassud, S Laborie, and JM Laine. How slug flow can improve ultrafiltration flux in organic hollow fibres. *Journal of Membrane Science*, 128(1):93–101, 1997. [28](#)
- [128] Tung-Wen Cheng, Ho-Ming Yeh, and Jun-Hsiung Wu. Effects of gas slugs and inclination angle on the ultrafiltration flux in tubular membrane module. *Journal of membrane science*, 158(1-2):223–234, 1999. [28](#)
- [129] Wu Chunrui, Jia Yue, Chen Huayan, Wang Xuan, Gao Qijun, and Lu Xiaolong. Study on air-bubbling strengthened membrane distillation process. *Desalination and Water Treatment*, 34(1-3):2–5, 2011. [27](#), [28](#)

- [130] Xiaoyang Fan, Hui-qiang Li, Ping Yang, and Bo Lai. Effect of c/n ratio and aeration rate on performance of internal cycle mbr with synthetic wastewater. *Desalination and Water Treatment*, 54(3):573–580, 2015. [27](#)
- [131] TW Cheng, TW Cheng, and CT Gau. Enhancement of permeate flux by gas slugs for crossflow ultrafiltration in tubular membrane module. *Separation science and technology*, 33(15):2295–2309, 1998. [27](#)
- [132] Amir Fouladitajar, Farzin Zokaee Ashtiani, Hamid Rezaei, Amin Haghmoradi, and Ali Kargari. Gas sparging to enhance permeate flux and reduce fouling resistances in cross flow microfiltration. *Journal of Industrial and Engineering Chemistry*, 20(2):624–632, 2014. [27](#)
- [133] Qusay F Alsahy, Talib M Albyati, and Mumtaz A Zablouk. A study of the effect of operating conditions on reverse osmosis membrane performance with and without air sparging technique. *Chemical Engineering Communications*, 200(1):1–19, 2013. [27](#)
- [134] Peter B Whalley. Boiling, condensation, and gas-liquid flow. 1987. [28](#)
- [135] ZF Cui, S Chang, and AG Fane. The use of gas bubbling to enhance membrane processes. *Journal of Membrane Science*, 221(1-2):1–35, 2003. [28](#), [29](#)
- [136] L Vera, R Villarroel, S Delgado, and S Elmaleh. Enhancing microfiltration through an inorganic tubular membrane by gas sparging. *Journal of membrane Science*, 165(1):47–57, 2000. [28](#)
- [137] SR Bellara, ZF Cui, and DS Pepper. Gas sparging to enhance permeate flux in ultrafiltration using hollow fibre membranes. *Journal of membrane science*, 121(2):175–184, 1996. [28](#)
- [138] Taha Taha and ZF Cui. Cfd modelling of gas-sparged ultrafiltration in tubular membranes. *Journal of membrane science*, 210(1):13–27, 2002. [29](#)
- [139] Hwal W Sur and Zhanfeng Cui. Experimental study on the enhancement of yeast microfiltration with gas sparging. *Journal of chemical technology and biotechnology*, 76(5):477–484, 2001. [28](#)
- [140] MJ Van der Waal, PM Van der Velden, J Koning, CA Smolders, and WPM Van Swaay. Use of fluidised beds as turbulence promoters in tubular membrane systems. *Desalination*, 22(1-3):465–483, 1977. [28](#)
- [141] Ruey-Hung Chen, Louis C Chow, and Jose E Navedo. Effects of spray characteristics on critical heat flux in subcooled water spray cooling. *International Journal of Heat and Mass Transfer*, 45(19):4033–4043, 2002. [29](#), [30](#)
- [142] Ruey-Hung Chen, Louis C Chow, and Jose E Navedo. Optimal spray characteristics in water spray cooling. *International Journal of Heat and Mass Transfer*, 47(23):5095–5099, 2004. [29](#), [30](#)

-
- [143] Kurt A Estes and Issam Mudawar. Correlation of sauter mean diameter and critical heat flux for spray cooling of small surfaces. *International Journal of Heat and Mass Transfer*, 38(16):2985–2996, 1995. [29](#), [30](#)
- [144] BQ Li, T Cader, J Schwarzkopf, K Okamoto, and B Ramaprian. Spray angle effect during spray cooling of microelectronics: experimental measurements and comparison with inverse calculations. *Applied thermal engineering*, 26(16):1788–1795, 2006. [30](#)
- [145] Issam Mudawar and KaA Estes. Optimizing and predicting chf in spray cooling of a square surface. 1996. [30](#)
- [146] Wen-Long Cheng, Qi-Nie Liu, Rui Zhao, and Han-lin Fan. Experimental investigation of parameters effect on heat transfer of spray cooling. *Heat and mass transfer*, 46(8-9):911–921, 2010. [30](#)
- [147] Yaqing Wang, Minghou Liu, Dong Liu, Kan Xu, and Yiliang Chen. Experimental study on the effects of spray inclination on water spray cooling performance in non-boiling regime. *Experimental Thermal and Fluid Science*, 34(7):933–942, 2010. [30](#)
- [148] Wiliam Reginald Dean. Fluid motion in a curved channel. *Proceedings of the Royal Society of London. Series A, Containing Papers of a Mathematical and Physical Character*, 121(787):402–420, 1928. [30](#)
- [149] JN Ghogomu, C Guigui, JC Rouch, MJ Clifton, and P Aptel. Hollow-fibre membrane module design: comparison of different curved geometries with dean vortices. *Journal of Membrane Science*, 181(1):71–80, 2001. [30](#), [33](#), [136](#)
- [150] Yanfeng Liu, Yaowen Chen, Yong Zhou, Dengjia Wang, Yingying Wang, and Daokun Wang. Experimental research on the thermal performance of pex helical coil pipes for heating the biogas digester. *Applied Thermal Engineering*, 147:167–176, 2019. [30](#), [40](#), [93](#)
- [151] Jatinder Gill and Jagdev Singh. Use of artificial neural network approach for depicting mass flow rate of r134a/lpg refrigerant through straight and helical coiled adiabatic capillary tubes of vapor compression refrigeration system. *International Journal of Refrigeration*, 86:228–238, 2018. [30](#), [40](#), [93](#)
- [152] Igor Pioro. *Handbook of generation IV nuclear reactors*. Woodhead Publishing, 2016. [30](#), [40](#), [93](#)
- [153] MH Abdel-Aziz, IAS Mansour, and GH Sedahmed. Study of the rate of liquid–solid mass transfer controlled processes in helical tubes under turbulent flow conditions. *Chemical Engineering and Processing: Process Intensification*, 49(7):643–648, 2010. [30](#), [41](#), [64](#), [93](#)

- [154] Deisy Lizeth Mejia Mendez, Cécile Lemaitre, Christophe Castel, Maude Ferrari, Herve Simonaire, and Eric Favre. Membrane contactors for process intensification of gas absorption into physical solvents: Impact of dean vortices. *Journal of Membrane Science*, 530:20–32, 2017. [30](#), [41](#), [64](#), [93](#)
- [155] R Ghidossi, D Veyret, and P Moulin. Computational fluid dynamics applied to membranes: State of the art and opportunities. *Chemical Engineering and Processing: Process Intensification*, 45(6):437–454, 2006. [30](#), [41](#), [64](#), [93](#)
- [156] R Moll, D Veyret, F Charbit, and P Moulin. Dean vortices applied to membrane process: Part i. experimental approach. *Journal of Membrane Science*, 288(1-2):307–320, 2007. [30](#), [33](#), [41](#), [93](#), [136](#)
- [157] Michael Mansour, Zhixin Liu, Gábor Janiga, Krishna DP Nigam, Kai Sundmacher, Dominique Thévenin, and Katharina Zähringer. Numerical study of liquid-liquid mixing in helical pipes. *Chemical Engineering Science*, 172:250–261, 2017. [31](#), [41](#), [64](#), [93](#)
- [158] Yasuo Mori and Wataru Nakayama. Study of forced convective heat transfer in curved pipes (2nd report, turbulent region). *International journal of heat and mass transfer*, 10(1):37–59, 1967. [31](#)
- [159] L-J Chang and JM Tarbell. Numerical simulation of fully developed sinusoidal and pulsatile (physiological) flow in curved tubes. *Journal of fluid mechanics*, 161:175–198, 1985. [31](#)
- [160] Ph Moulin, D Veyret, and F Charbit. Dean vortices: comparison of numerical simulation of shear stress and improvement of mass transfer in membrane processes at low permeation fluxes. *Journal of Membrane Science*, 183(2):149–162, 2001. [31](#), [98](#)
- [161] PL Spedding, E Benard, and GM McNally. Fluid flow through 90 degree bends. *Asia-Pacific Journal of Chemical Engineering*, 12(1-2):107–128, 2004. [31](#)
- [162] Hanuman Mallubhotla, Elizabeth Nunes, and Georges Belfort. Microfiltration of yeast suspensions with self-cleaning spiral vortices: Possibilities for a new membrane module design. *Biotechnology and bioengineering*, 48(4):375–385, 1995. [31](#)
- [163] Friedhelm Schönfeld and Steffen Hardt. Simulation of helical flows in microchannels. *AIChE Journal*, 50(4):771–778, 2004. [31](#)
- [164] Heinz B Winzeler and Georges Belfort. Enhanced performance for pressure-driven membrane processes: the argument for fluid instabilities. *Journal of Membrane Science*, 80(1):35–47, 1993. [31](#), [33](#)

-
- [165] C Jonas Bolinder and Bengt Sundén. Flow visualization and ldv measurements of laminar flow in a helical square duct with finite pitch. *Experimental thermal and fluid science*, 11(4):348–363, 1995. [31](#)
- [166] R Moll, D Veyret, F Charbit, and P Moulin. Dean vortices applied to membrane process: Part i. experimental approach. *Journal of membrane science*, 288(1-2):307–320, 2007. [31](#)
- [167] Seyed Pouria Motevalian, Ali Borhan, Hongyi Zhou, and Andrew Zydney. Twisted hollow fiber membranes for enhanced mass transfer. *Journal of Membrane Science*, 514:586–594, 2016. [31](#)
- [168] Ph Moulin, JC Rouch, C Serra, MJ Clifton, and P Aptel. Mass transfer improvement by secondary flows: Dean vortices in coiled tubular membranes. *Journal of Membrane Science*, 114(2):235–244, 1996. [31](#), [66](#), [68](#), [82](#)
- [169] Kun Yong Chung, William A Edelstein, and Georges Belfort. Dean vortices with wall flux in a curved channel membrane system.: 6. two dimensional magnetic resonance imaging of the velocity field in a curved impermeable slit. *Journal of membrane science*, 81(1-2):151–162, 1993. [32](#)
- [170] Subhashini Vashisth, Vimal Kumar, and Krishna DP Nigam. A review on the potential applications of curved geometries in process industry. *Industrial & Engineering Chemistry Research*, 47(10):3291–3337, 2008. [32](#)
- [171] G Yang, ZF Dong, and MA Ebdadian. Laminar forced convection in a helicoidal pipe with finite pitch. *International Journal of Heat and Mass Transfer*, 38(5):853–862, 1995. [32](#)
- [172] RC Xin and MA Ebdadian. The effects of prandtl numbers on local and average convective heat transfer characteristics in helical pipes. 1997. [32](#), [34](#), [68](#)
- [173] Anup Kumer Datta, Shinichiro Yanase, Toshinori Kouchi, and Mohammed ME Shatat. Laminar forced convective heat transfer in helical pipe flow. *International Journal of Thermal Sciences*, 120:41–49, 2017. [32](#)
- [174] Romeo L Manlapaz and Stuart W Churchill. Fully developed laminar convection from a helical coil. *Chemical Engineering Communications*, 9(1-6):185–200, 1981. [33](#), [68](#)
- [175] André Lévêque. *Les Lois de la transmission de chaleur par convection, par André Lévêque,...* Dunod, 1928. [33](#), [101](#)
- [176] Eckehard F Schmidt. Wärmeübergang und druckverlust in rohrschlangen. *Chemie Ingenieur Technik*, 39(13):781–789, 1967. [33](#), [34](#)

- [177] Venugopala Kubair and NR Kuloor. Heat transfer to newtonian fluids in coiled pipes in laminar flow. *International Journal of Heat and Mass Transfer*, 9(1):63–75, 1966. [34](#)
- [178] Arun Nilkanth Dravid, KA Smith, EW Merrill, and PLT Brian. Effect of secondary fluid motion on laminar flow heat transfer in helically coiled tubes. *AIChE Journal*, 17(5):1114–1122, 1971. [34](#), [68](#), [80](#)
- [179] Cengiz Yildiz, Yaşar Biçer, and Dursun Pehlivan. Heat transfer and pressure drop in a heat exchanger with a helical pipe containing inside springs. *Energy conversion and management*, 38(6):619–624, 1997. [34](#), [68](#)
- [180] S Rainieri, F Bozzoli, and G Pagliarini. Experimental investigation on the convective heat transfer in straight and coiled corrugated tubes for highly viscous fluids: Preliminary results. *International Journal of Heat and Mass Transfer*, 55(1-3):498–504, 2012. [34](#)
- [181] Shijie Liu and Jacob H Masliyah. A decoupling numerical method for fluid flow. *International journal for numerical methods in fluids*, 16(8):659–682, 1993. [34](#)
- [182] AV Kirpikov. Heat transfer in helically coiled pipes. *Trudi. Moscov. Inst. Khim. Mashinojtrojenija*, 12:43–56, 1957. [34](#)
- [183] RA Seban and EF McLaughlin. Heat transfer in tube coils with laminar and turbulent flow. *International journal of heat and mass transfer*, 6(5):387–395, 1963. [34](#)
- [184] M Moawed. Experimental study of forced convection from helical coiled tubes with different parameters. *Energy Conversion and Management*, 52(2):1150–1156, 2011. [34](#)
- [185] CE Kalb and JD Seader. Heat and mass transfer phenomena for viscous flow in curved circular tubes. *International Journal of Heat and Mass Transfer*, 15(4):801–817, 1972. [34](#)
- [186] F Jiang, KS Drese, S Hardt, M Küpper, and F Schönfeld. Helical flows and chaotic mixing in curved micro channels. *AIChE journal*, 50(9):2297–2305, 2004. [33](#), [35](#)
- [187] May May Teoh, Sina Bonyadi, and Tai-Shung Chung. Investigation of different hollow fiber module designs for flux enhancement in the membrane distillation process. *Journal of membrane science*, 311(1-2):371–379, 2008. [33](#)
- [188] Dongfei Li, Rong Wang, and Tai-Shung Chung. Fabrication of lab-scale hollow fiber membrane modules with high packing density. *Separation and purification technology*, 40(1):15–30, 2004. [33](#)
- [189] Scott W Jones, Oran M Thomas, and Hassan Aref. Chaotic advection by laminar flow in a twisted pipe. *Journal of Fluid Mechanics*, 209:335–357, 1989. [33](#), [35](#)

-
- [190] Brahim Timité, Cathy Castelain, and Hassan Peerhossaini. Mass transfer and mixing by pulsatile three-dimensional chaotic flow in alternating curved pipes. *International Journal of Heat and Mass Transfer*, 54(17-18):3933–3950, 2011. [33](#)
- [191] Omran Abushammala, Rainier Hreiz, Cécile Lemaitre, and Éric Favre. Laminar flow friction factor in highly curved helical pipes: Numerical investigation, predictive correlation and experimental validation using a 3d-printed model. *Chemical Engineering Science*, 207:1030–1039, 2019. [37](#), [65](#), [66](#), [67](#), [93](#), [94](#), [112](#), [113](#), [116](#), [117](#), [120](#), [125](#), [126](#), [128](#)
- [192] Wo R Dean. Xvi. note on the motion of fluid in a curved pipe. *The London, Edinburgh, and Dublin Philosophical Magazine and Journal of Science*, 4(20):208–223, 1927. [40](#)
- [193] WR Dean. Lxxii. the stream-line motion of fluid in a curved pipe (second paper). *The London, Edinburgh, and Dublin Philosophical Magazine and Journal of Science*, 5(30):673–695, 1928. [40](#)
- [194] P Mishra and SN Gupta. Momentum transfer in curved pipes. 1. newtonian fluids. *Industrial & Engineering Chemistry Process Design and Development*, 18(1):130–137, 1979. [41](#), [42](#), [51](#), [54](#), [55](#), [56](#), [57](#), [120](#)
- [195] CM White. Streamline flow through curved pipes. *Proceedings of the Royal Society of London. Series A, Containing Papers of a Mathematical and Physical Character*, 123(792):645–663, 1929. [42](#)
- [196] Yasuo Mori and Wataru Nakayama. Study of forced convective heat transfer in curved pipes (2nd report, turbulent region). *International journal of heat and mass transfer*, 10(1):37–59, 1967. [42](#)
- [197] Eckehard F Schmidt. Wärmeübergang und druckverlust in rohrschlangen. *Chemie Ingenieur Technik*, 39(13):781–789, 1967. [42](#), [54](#), [68](#)
- [198] P.S Srinivasan, S.S Nandapurkar, and F.A Holland. Pressure drop and heat transfer in coils. *The Chem. Eng*, 218:113–119, 1968. [42](#)
- [199] Shaukat Ali. Pressure drop correlations for flow through regular helical coil tubes. *Fluid dynamics research*, 28(4):295, 2001. [42](#)
- [200] J Hart, J Ellenberger, and PJ Hamersma. Single-and two-phase flow through helically coiled tubes. *Chemical Engineering Science*, 43(4):775–783, 1988. [42](#), [54](#), [120](#)
- [201] Sylwester Przybył and Piotr Pierański. Helical close packings of ideal ropes. *The European Physical Journal E*, 4(4):445–449, 2001. [43](#), [65](#), [93](#), [112](#)

- [202] O Abushammala, R Hreiz, C Lemaître, and E Favre. Maximizing mass transfer using highly curved helical pipes: A cfd investigation. *6th International Conference on Fluid Flow, Heat and Mass Transfer (FFHMT'19)*, 2019. [44](#), [91](#), [95](#), [116](#)
- [203] D Kaufhold, F Kopf, C Wolff, S Beutel, L Hilterhaus, M Hoffmann, T Scheper, M Schlüter, and A Liese. Generation of dean vortices and enhancement of oxygen transfer rates in membrane contactors for different hollow fiber geometries. *Journal of membrane science*, 423:342–347, 2012. [44](#), [66](#), [74](#), [85](#), [110](#)
- [204] Massimo Cardone and Bonaventura Gargiulo. Design and experimental testing of a mini channel heat exchanger made in additive manufacturing. *Energy Procedia*, 148:932–939, 2018. [44](#)
- [205] Ze-Xian Low, Yen Thien Chua, Brian Michael Ray, Davide Mattia, Ian Saxley Metcalfe, and Darrell Alec Patterson. Perspective on printing of separation membranes and comparison to related unconventional fabrication techniques. *Journal of Membrane Science*, 523:596–613, 2017. [44](#)
- [206] Jacopo De Amicis, Antonio Cammi, Luigi PM Colombo, Marco Colombo, and Marco E Ricotti. Experimental and numerical study of the laminar flow in helically coiled pipes. *Progress in Nuclear Energy*, 76:206–215, 2014. [56](#), [57](#), [83](#)
- [207] Mehdi Ghobadi and Yuri Stephan Muzychka. A review of heat transfer and pressure drop correlations for laminar flow in curved circular ducts. *Heat Transfer Engineering*, 37(10):815–839, 2016. [56](#), [66](#)
- [208] Omran Abushammala, Rainier Hreiz, Cécile Lemaitre, and Eric Favre. Optimal design of helical heat/mass exchangers under laminar flow: Cfd investigation and correlations for maximal transfer efficiency and process intensification performances. *International Journal of Heat and Mass Transfer*, 153:119610, 2020. [61](#), [113](#), [114](#), [115](#), [116](#), [117](#), [121](#), [123](#), [124](#), [125](#), [126](#), [128](#)
- [209] Tabish Alam and Man-Hoe Kim. A comprehensive review on single phase heat transfer enhancement techniques in heat exchanger applications. *Renewable and Sustainable Energy Reviews*, 81:813–839, 2018. [64](#), [109](#)
- [210] Lu Qiu, Hongwu Deng, Jining Sun, Zhi Tao, and Shuqing Tian. Pressure drop and heat transfer in rotating smooth square u-duct under high rotation numbers. *International journal of heat and mass transfer*, 66:543–552, 2013. [64](#)
- [211] Hamed Khosravi-Bizhaem, Abbas Abbassi, and Amir Zivari Ravan. Heat transfer enhancement and pressure drop by pulsating flow through helically coiled tube: An experimental study. *Applied Thermal Engineering*, 160:114012, 2019. [64](#), [119](#), [120](#), [122](#), [127](#)

-
- [212] S Jaisankar, TK Radhakrishnan, and KN Sheeba. Experimental studies on heat transfer and friction factor characteristics of thermosyphon solar water heater system fitted with spacer at the trailing edge of twisted tapes. *Applied Thermal Engineering*, 29(5-6):1224–1231, 2009. [64](#)
- [213] Kenan Yakut, Bayram Sahin, Cafer Celik, Nihal Alemdaroglu, and Aslihan Kurnuc. Effects of tapes with double-sided delta-winglets on heat and vortex characteristics. *Applied energy*, 80(1):77–95, 2005. [64](#)
- [214] Muhammad Ilyas and Fatih Aydogan. Steam generator performance improvements for integral small modular reactors. *Nuclear Engineering and Technology*, 49(8):1669–1679, 2017. [64](#)
- [215] Rithy Kong, Thoranis Deethayat, Attakorn Asanakham, and Tanongkiat Kiatsiriroat. Heat transfer phenomena on waste heat recovery of combustion stack gas with deionized water in helical coiled heat exchanger. *Case studies in thermal engineering*, 12:213–222, 2018. [64](#)
- [216] Hossein Javadi, Seyed Soheil Mousavi Ajarostaghi, Mohsen Pourfallah, and Mohammad Zaboli. Performance analysis of helical ground heat exchangers with different configurations. *Applied Thermal Engineering*, 154:24–36, 2019. [64](#)
- [217] Marina Sabelfeld and Sven-Uwe Geißen. Effect of helical structure on ozone mass transfer in a hollow fiber membrane contactor. *Journal of membrane science*, 574:222–234, 2019. [66](#)
- [218] Charles E Kalb and JD Seader. Fully developed viscous—flow heat transfer in curved circular tubes with uniform wall temperature. *AIChE Journal*, 20(2):340–346, 1974. [68](#), [80](#)
- [219] Mehdi Ghobadi and Yuri Stephan Muzychka. Fully developed heat transfer in mini scale coiled tubing for constant wall temperature. *International Journal of Heat and Mass Transfer*, 72:87–97, 2014. [68](#), [83](#), [84](#)
- [220] A Sheeba, CM Abhijith, and M Jose Prakash. Experimental and numerical investigations on the heat transfer and flow characteristics of a helical coil heat exchanger. *International Journal of Refrigeration*, 99:490–497, 2019. [68](#), [82](#), [83](#), [84](#)
- [221] F Kreith, RF Boehm, GD Raithby, and KG anHollands. Heat and mass transfer handbook, 2000. [70](#), [95](#)
- [222] Hamid Saffari, Rouhollah Moosavi, Nourooz Mohammad Nouri, and Cheng-Xian Lin. Prediction of hydrodynamic entrance length for single and two-phase flow in helical coils. *Chemical Engineering and Processing: Process Intensification*, 86:9–21, 2014. [70](#), [98](#)
- [223] W Nusselt. The dependence of the heat-transfer coefficient on tube length. *Zeit. VDI*, 54:1154–1158, 1910. [71](#), [73](#)

- [224] N Jamshidi, M Farhadi, D Domeiry Ganji, and K Sedighi. Experimental analysis of heat transfer enhancement in shell and helical tube heat exchangers. *Applied Thermal Engineering*, 51(1-2):644–652, 2013. [82](#)
- [225] Dengxi Wu and JA Howell. Calculation of the entrance length of the concentration boundary layer in ultrafiltration and its influence on scale-up. *Journal of membrane science*, 74(1-2):37–49, 1992. [98](#)
- [226] MJ Clifton, N Abidine, P Aptel, and V Sanchez. Growth of the polarization layer in ultrafiltration with hollow-fibre membranes. *Journal of Membrane Science*, 21(3):233–245, 1984. [98](#)
- [227] Subhashini Vashisth and KDP Nigam. Prediction of flow profiles and interfacial phenomena for two-phase flow in coiled tubes. *Chemical Engineering and Processing: Process Intensification*, 48(1):452–463, 2009. [98](#)
- [228] Larry R Austin and JD Seader. Entry region for steady viscous flow in coiled circular pipes. *AIChE Journal*, 20(4):820–822, 1974. [98](#), [99](#)
- [229] Y Agrawal, L Talbot, and K Gong. Laser anemometer study of flow development in curved circular pipes. *Journal of Fluid Mechanics*, 85(3):497–518, 1978. [98](#)
- [230] L-S Yao and SA Berger. Entry flow in a curved pipe. *Journal of Fluid Mechanics*, 67(1):177–196, 1975. [98](#)
- [231] Woo Yung Soh and SA Berger. Laminar entrance flow in a curved pipe. *Journal of Fluid Mechanics*, 148:109–135, 1984. [99](#)
- [232] B Zheng, CX Lin, and MA Ebadian. Combined laminar forced convection and thermal radiation in a helical pipe. *International journal of heat and mass transfer*, 43(7):1067–1078, 2000. [99](#)
- [233] KC Cheng and Mitsunobu Akiyama. Laminar forced convection heat transfer in curved rectangular channels. *International Journal of heat and mass Transfer*, 13(3):471–490, 1970. [99](#)
- [234] Hanbin Shi, Nathalie Di Miceli Raimondi, David F Fletcher, Michel Cabassud, and Christophe Gourdon. Numerical study of heat transfer in square millimetric zigzag channels in the laminar flow regime. *Chemical Engineering and Processing-Process Intensification*, 144:107624, 2019. [100](#), [103](#)
- [235] Shuli Liu and M Sakr. A comprehensive review on passive heat transfer enhancements in pipe exchangers. *Renewable and sustainable energy reviews*, 19:64–81, 2013. [109](#)
- [236] Rambir Bhadouriya, Amit Agrawal, and SV Prabhu. Experimental and numerical study of fluid flow and heat transfer in an annulus of inner twisted square duct and outer circular pipe. *International Journal of Thermal Sciences*, 94:96–109, 2015. [109](#)

-
- [237] RL Webb and ERG Eckert. Application of rough surfaces to heat exchanger design. *International Journal of Heat and Mass Transfer*, 15(9):1647–1658, 1972. [110](#)
- [238] Guanghui Wang, Talib Dbouk, Dingbiao Wang, Yuanshuai Pei, Xu Peng, Honglin Yuan, and Sa Xiang. Experimental and numerical investigation on hydraulic and thermal performance in the tube-side of helically coiled-twisted trilobal tube heat exchanger. *International Journal of Thermal Sciences*, 153:106328, 2020. [117](#), [118](#), [119](#), [122](#), [127](#)
- [239] A Tohidi, SM Hosseinalipour, M Shokrpour, and AS Mujumdar. Heat transfer enhancement utilizing chaotic advection in coiled tube heat exchangers. *Applied Thermal Engineering*, 76:185–195, 2015. [118](#), [119](#), [122](#), [127](#)
- [240] Jundika C Kurnia, Benitta A Chaedir, and Agus P Sasmito. Laminar convective heat transfer in helical tube with twisted tape insert. *International Journal of Heat and Mass Transfer*, 150:119309, 2020. [119](#), [120](#), [122](#), [123](#), [125](#), [127](#), [129](#), [132](#)
- [241] Jian Guo, Aiwu Fan, Xiaoyu Zhang, and Wei Liu. A numerical study on heat transfer and friction factor characteristics of laminar flow in a circular tube fitted with center-cleared twisted tape. *International Journal of Thermal Sciences*, 50(7):1263–1270, 2011. [119](#), [120](#), [123](#)
- [242] K Wongcharee and S Eiamsa-Ard. Friction and heat transfer characteristics of laminar swirl flow through the round tubes inserted with alternate clockwise and counter-clockwise twisted-tapes. *International Communications in Heat and Mass Transfer*, 38(3):348–352, 2011. [119](#), [120](#), [123](#)
- [243] Robin H Liu, Mark A Stremmer, Kendra V Sharp, Michael G Olsen, Juan G Santiago, Ronald J Adrian, Hassan Aref, and David J Beebe. Passive mixing in a three-dimensional serpentine microchannel. *Journal of microelectromechanical systems*, 9(2):190–197, 2000. [135](#), [136](#)
- [244] Zhanying Zheng, David F Fletcher, and Brian S Haynes. Chaotic advection in steady laminar heat transfer simulations: Periodic zigzag channels with square cross-sections. *International Journal of Heat and Mass Transfer*, 57(1):274–284, 2013. [135](#), [136](#)
- [245] Vimal Kumar and KDP Nigam. Numerical simulation of steady flow fields in coiled flow inverter. *International journal of heat and mass transfer*, 48(23-24):4811–4828, 2005. [135](#), [136](#)
- [246] H Peerhossaini, C Castelain, and Y Le Guer. Heat exchanger design based on chaotic advection. *Experimental thermal and fluid science*, 7(4):333–344, 1993. [135](#), [136](#)

Abstract

Optimal helical tube design for intensified heat / mass exchangers

The search for technological solutions aimed at minimizing the size of a device, known as intensification, is a classic objective of process engineering. In this thesis, the intensification possibilities offered by helical tubes are studied, both for heat and mass exchangers. The use of helical tubes instead of straight tubes is indeed of interest both in terms of increasing the exchange surface per unit volume between the two fluids circulating in the exchanger and by the possibility of increasing the transfers by generating Dean vortices in the tubes. A set of CFD (Computational Fluid Dynamics) type simulations was carried out and compared with experimental results. In the end, on the basis of a systematic approach using correlations, a volume reduction of a factor of 8 was obtained, both for heat exchangers and for membrane contactors.

Keywords: Simulation, exchangers, transfer, intensification, CFD, helical tubes, design, optimisation

Résumé

Design optimal pour l'intensification des échangeurs de chaleur et matière à tubes hélicoïdaux

La recherche de solutions technologiques visant à minimiser la taille d'un dispositif, qualifiée d'intensification, est un objectif classique du génie des procédés. Dans ce mémoire, les possibilités d'intensification offertes par des tubes hélicoïdaux sont étudiées, à la fois pour des échangeurs de chaleur et de matière. L'utilisation de tubes hélicoïdaux en lieu et place de tubes droits présente en effet un intérêt à la fois en termes d'augmentation de la surface d'échange par unité de volume entre les deux fluides circulant dans l'échangeur et par la possibilité d'augmentation des transferts par génération de vortex de Dean dans les tubes. Un ensemble de simulations de mécanique des fluides numérique a été réalisé et confronté à des résultats expérimentaux. Au final, sur la base d'une démarche systématique faisant appel à des corrélations, une réduction volumique d'un facteur 8 est obtenue, tant pour les échangeurs de chaleur que pour les contacteurs à membranes.

Mots-clés: Simulation, échangeurs, transferts, intensification, CFD, tubes spirales, design, optimisation

